

A Study on Aerosol Transport Dynamics over the Indian Landmass and the Adjoining Oceanic Regions Using Satellite Data

Thesis submitted to the

Cochin University of Science and Technology

In partial fulfillment of the requirements for the award of the degree of

Doctor of Philosophy

In

Physics

UNDER THE FACULTY OF SCIENCE

by

Marina Aloysius



SPACE PHYSICS LABORATORY

VIKRAM SARABHAI SPACE CENTRE

THIRUVANANTHAPURAM-695 022

KERALA, INDIA

JANUARY 2010

DECLARATION

This to declare that the work presented in this thesis was carried out at the Space Physics Laboratory, Vikram Sarabhai Space Centre, Thiruvananthapuram for the award of the degree of Doctor of Philosophy of Cochin University of Science and Technology, India. The results reported herein are entirely original and have not formed the basis for the award of any degree or diploma by any other University or Institution.

January 2010
Thiruvananthapuram


Author

(Marina Aloysius)

भारत सरकार
अंतरिक्ष विभाग
विक्रम साराभाई अंतरिक्ष केन्द्र
तिरुवनन्तपुरम-695 022
केरल, भारत
फोन : (0471) 2562070
फैक्स : (0471) 2706535
तार/Gram : SPACE



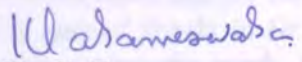
Government of India
Department of Space
Vikram Sarabhai Space Centre
Thiruvananthapuram-695 022
Kerala, INDIA
Telephone : (0471) 2562070
Fax : (0471) 2706535
Email: k_parameswaran@vssc.gov.in

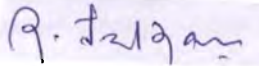
SPACE PHYSICS LABORATORY

CERTIFICATE

Certified that the thesis entitled "A Study on Aerosol Transport Dynamics over the Indian Landmass and the Adjoining Oceanic Regions Using Satellite Data" submitted by Ms. Marina Aloysius, to Cochin University of Science and Technology, Cochin, embodies the original results of the investigations carried out at the Space Physics Laboratory, Vikram Sarabhai Space Centre, Thiruvananthapuram, under my guidance. The work presented in this thesis has not been submitted for the award of any other degree or diploma to any other University or Institution.

Thiruvananthapuram
January 2010


Dr. K. Parameswaran
(Thesis Supervisor)


Countersigned
Prof. R. Sridharan
Director
Space Physics Laboratory



भारतीय अंतरिक्ष अनुसंधान संगठन



Indian Space Research Organisation

Acknowledgement

Thanks to God the Divine who continues to make the impossible possible

No words to describe how much I am indebted to those who have supported my journey at SPL and led to the successful completion of my PhD thesis. I humbly take this opportunity to express my heartfelt gratitude for their love and care.

First and foremost, my sincere gratitude to my thesis guide, Dr. K. Parameswaran, for his wholehearted support provided throughout the work. His extra-ordinary patience and sincerity shown throughout the period of thesis correction will be cherished forever. His suggestions, advices and comments have immensely helped me cast this thesis into the final form. I am also thankful to CSIR for granting scientistship under its Emeritus Scientist scheme to Dr. K. Parameswaran, thereby enabling me to continue the work in his guidance.

Words fall short to convey my gratitude to my 'Guru', Dr. Mannil Mohan who introduced me to the field of space research. It was his valuable ideas and meticulous guidance that lead to the successful culmination of this doctoral thesis. During the five years of my research tenure, he incessantly encouraged me and taught me a lot many things which I will cherish and treasure my entire life. His passion for physics was truly inspiring and I believe he was the one who made me 'love' my work.

I sincerely thank the Indian Space Research Organization, for the fellowship provided to me to carry out my research activities at SPL. My heartfelt gratitude to Dr. Sridharan, Director SPL for his constant encouragement and for the facilities provided for the work.

I am extremely thankful to the ISRO Geosphere Biosphere Programme Committee and especially to Dr. K. Krishna Moorthy, Project Director, ARFI and Dr. C.B.S Dutt, Programme Director, ISRO-GBP, for giving me a worthy opportunity to participate in the ICARB cruise. I acknowledge Dr.K. Krishna Moorthy also for the data provided for my thesis work and for the useful discussions and support extended during my research tenure. My special thanks to Dr. Prabha R. Nair for sharing the data and for her loving support I felt during the work. I specially acknowledge Dr. K. Rajeev for the fruitful discussions and valuable advices. Thanks to Dr. P.K. Kunhikrishnan, Dr. C.V. Devasia, Dr. Sudha Ravindran, Dr. Geetha Ramkumar, Dr. Anil Bhardwaj, Dr. C. Suresh Raju, Dr. Tarun Kumar Pant, Dr. Radhika Ramachandran, Dr. S.M. Ahmed, Dr. Rajkumar Choudhary for their feedbacks, advices and criticism, especially during annual reviews which helped me in shaping my thesis better. I would like to thank the Atmospheric Technology Division of SPL, particularly Mr. S.V. Mohan Kumar, Mr. P. Pradeep Kumar, Ms. Sreelatha, Mr. T.P. Das, Mr. Dinakar Prasad Vajja, Mr. G.S. Pramod, Mr. Ajeesh, Mr. Anumod, Mr. Sam Das, Mrs. Santhi and Mrs. Mable for their wholehearted support and care extended throughout. Special thanks to Dr. Siji Kumar, Dr. D. Bala Subrahmanyam, Dr. K. Kishore Kumar, Dr. Kiran Kumar, Dr. Mukunda Gogoi, Dr. Satheesh Thampi, Dr. G. Manju, Dr. Siddharth, Dr. Debadatta and all other scientists in SPL for their help and directions at the times I needed.

I would like to acknowledge my doctoral and research committee members, Dr. C.K. Rajan, Dr. V.C. Kuriakose and other members from Cochin University of Science and Technology for their yearly assessments, fruitful comments and encouragement which helped me to improve the work. My special thanks to the office staff of Cochin University who helped me, especially during my visits to the campus.

I specially acknowledge NASA MODIS team for providing me with the large amount of MODIS data used for the analysis. I am also thankful to the NOAA for the NCEP data available from their website, <http://www.esrl.noaa.gov/psd>.

Sincere thanks to the library staff of VSSC for the service rendered for literature collection during my research work. I thank Ms. P.R. Suseela, Ms. Geetha C., Mr. Jayakumar S., Mr. Hari Krishna Kishore, Mr. Watson, Jihasa, Raji, Jomon, Shamna, Arya and Mr. T. K. Vijayan for the administrative and logistic support I have received during my research tenure. I also acknowledge Mr. Asokan Kumar G.S. for printing the posters for my presentations in various symposia.

I thankfully remember my seniors, Dr. Suresh Babu, Dr. Sandhya K. Nair, Dr. Smitha V. Thampi, Dr. Deepa V. and Dr. S.V. Sunil Kumar for their valuable advices, discussions and love which continued throughout the work. My hearty thanks to my beloved seniors, Dr. Susan George, Dr. Indira Rani, Dr. Korak Saha, Dr. Maria Antonita, Dr. C. Vineeth, Abish and Sreeja who have helped me through useful discussions and extended their care and help. My heartfelt gratitude to my proud batchmates Sreeja, Meenu, Naseema, Vijaya Kumar, Denny and Bijoy for their enduring friendship, outstanding support and help. My special thanks to my loving juniors Prijith, Sherine, Anish, Sumod, Veena, Liji, Lijo, Raghu, Sonal, Jai, Ambili, Anu, Tinu, Asha and Arun. I must appreciate the way Prijith has devoted his time for helping his senior. I thankfully remember my friends Pramod, Dhanya, Neha, Manoj, Rosmy, Lali, Dr. Uma and Vaishnavi for their love and friendship.

I extend my gratitude to all my teachers, especially at St. Aloysius College, Edathua who loved me and boosted me up in my career. My sincere gratitude to all my teachers at the Dept. of Physics, Kariavattom for their guidance. I would like to thank Dr. Sreekumar, ISAC with whom I worked for my M.Sc. Project, for his guidance and support.

I cannot forget my dearest uncle, Mr. K.J. Mathew who really directed me to the Physics stream. I stayed with his family for almost four years during my research tenure. My heartfelt gratitude to him, to my aunt, Mrs. Daisy Mathew, and to my cousins Goju, Ria and Anniemol for their love, support and encouragement which was an immense strength for me. My heartfelt thanks to Mrs. Sreekumary and family, Mr. Issac and family, Mrs. Beena and family and Mrs. Shyla and family for the love and care I received during my research period. I thank Fr. Mathew Moonnattumukham and Fr. Joy Chencheril and all other beloved fathers and my well-wishers for their prayers and support.

Special thanks to my dearest friend, Abhilash who gave me enduring support all through these years from the time of my graduation.

I express my love and gratitude to my parents who were there to support me in all my endeavours throughout my life. Their pains and prayers were always my strength. My special thanks to my sister, Rose and brother-in-law, Sony and all my uncles, aunts and cousins for their love and support to this day. I gratefully acknowledge my in-laws for all the support, prayers and understanding which really helped me especially during the final stages of my work. With overwhelming gratitude, I remember my husband, Vijay, who stood by my side with his myriad ways of support rendered all through...

*Marina Aloysius
(Author)*

Contents

Preface	i
Symbols Used	iv
Frequently used Acronyms	vii

Chapter 1: An overview on atmospheric aerosols and their transport

1.1 Introduction	1
1.2 Aerosol generation in the atmosphere	2
1.2.1 Natural aerosol sources	2
1.2.1.1 Oceans.....	2
1.2.1.2 Deserts/Arid regions.....	3
1.2.1.3 Volcanoes.....	4
1.2.1.4 Biological debris.....	5
1.2.2 Anthropogenic aerosol sources	5
1.3 Properties of aerosols	6
1.3.1 Aerosol size	7
1.3.2 Aerosol size distribution	7
1.3.2.1 Power law distribution.....	8
1.3.2.2 Gamma distribution.....	9
1.3.2.3 Log-normal distribution.....	9
1.3.3 Different forms of size distribution	10
1.3.4 Shape of aerosols	11
1.4 Aerosol Sink processes	11
1.5 Aerosol Residence time	12
1.6 Major aerosol transformation processes	13
1.6.1 Coagulation	14
1.6.2 Effect of relative humidity	14
1.7 Interaction of aerosols with radiation	16
1.7.1 Scattering and absorption	17
1.7.1.1 Scattering/absorption/extinction coefficients.....	19
1.7.1.2 Aerosol optical depth.....	20
1.7.1.2.1 Angstrom exponent.....	21
1.7.1.3 Single scattering albedo.....	22
1.7.1.4 Scattering phase function.....	22
1.7.1.5 Asymmetry parameter.....	22
1.8 Radiative effects of aerosols	23
1.8.1 Radiative forcing of aerosols	24

1.8.2	Some examples of the effects of aerosols.....	25
1.9	Monitoring of atmospheric aerosols.....	26
1.9.1	Ground-based measurements.....	26
1.9.2	Space-borne remote sensors.....	27
1.9.2.1	AVHRR.....	28
1.9.2.2	TOMS & OMI.....	28
1.9.2.3	CZCS.....	29
1.9.2.4	SAM & SAGE.....	29
1.9.2.5	ATSR.....	30
1.9.2.6	MOS.....	31
1.9.2.7	POLDER.....	31
1.9.2.8	OCTS.....	32
1.9.2.9	SeaWiFS.....	32
1.9.2.10	OCM.....	32
1.9.2.11	MISR.....	33
1.9.2.12	MODIS.....	33
1.9.2.13	SCIAMACHY.....	33
1.9.2.14	GLI.....	34
1.9.2.15	MERIS.....	34
1.9.2.16	GLAS.....	34
1.9.2.17	CALIPSO.....	35
1.10	Radiative transfer in the atmosphere.....	35
1.10.1	Aerosol sensing from space.....	36
1.11	Transport of tropospheric aerosols.....	38
1.12	Importance of vertical distribution of aerosols.....	40
1.13	Objectives of the present study.....	41

Chapter 2 : Data and Methodology

2.1	Introduction.....	43
2.2	Aerosol properties from MODIS.....	44
2.2.1	Sensor details.....	44
2.2.2	Inversion algorithms.....	46
2.2.2.1	Algorithm over the land.....	47
2.2.2.1.1	Recent modifications in the land algorithm.....	47
2.2.2.1.2	Parameterization of the land surface reflectance.....	48
2.2.2.1.3	Inversion procedure.....	49
2.2.2.1.4	Correction for Rayleigh optical depth.....	50
2.2.2.1.5	Inversion procedure for dark pixels.....	51
2.2.2.1.6	Inversion procedure for brighter pixels.....	52

2.2.2.2	Algorithm over the ocean.....	53
2.2.3	Cloud screening in MODIS.....	55
2.2.4	Calibration of MODIS.....	55
2.2.5	Levels of MODIS products.....	56
2.2.6	Uncertainties in MODIS retrieval.....	56
2.2.7	MODIS data used for the present study.....	57
2.3	Aerosol optical depth from surface measurements.....	59
2.3.1	Principle of operation of Microtops II	59
2.3.2	Estimation of AOD using Microtops II.....	59
2.3.3	Errors and precautions.....	61
2.4	NCEP reanalysis of meteorological fields.....	62
2.5	Ocean surface wind from QuikSCAT.....	62
2.5.1	QuikSCAT sensor and measurement technique.....	62
2.5.2	Retrieval uncertainties & difficulties.....	64
2.5.3	Details of wind data from QuikSCAT	65
2.6	Meteorological parameters influencing the aerosol properties..	65
2.6.1	Horizontal wind convergence.....	65
2.6.2	Vorticity.....	66
2.6.3	Vertical wind.....	66
2.6.4	Relative Humidity.....	66
2.7	Investigation of aerosol source strength and continuity equation.....	67
2.7.1	Aerosol flux continuity equation.....	67
2.8	Summary.....	69

Chapter 3 : Aerosol generation and transport over the Ganga Basin during Boreal winter : ISRO-GBP Land Campaign II

3.1	Introduction.....	70
3.2	Land Campaign - II.....	72
3.3	Database.....	73
3.4	Comparison of MODIS derived AOD with ground measurements.....	74
3.5	Aerosol distribution and synoptic circulation over the Ganga Basin.....	75
3.6	Day-to-day variability in AOD over the Ganga Basin during the campaign.....	78
3.7	Role of dynamics on the day-to-day variations of AOD.....	80
3.8	Estimation of net aerosol source strength.....	81
3.9	Estimation of aerosol source strength (aerosol production rate) and its spatial distribution over the Ganga Basin.....	83
3.10	Estimation of actual source strength incorporating	

the loss term.....	84
3.11 Results and discussions.....	85
3.12 Summary.....	88

Chapter 4 : Investigation on aerosol transport over the South East Arabian Sea during the pre-monsoon period: ARMEX – II

4.1 Introduction.....	90
4.2 ARMEX-II.....	91
4.3 Data used for the study.....	92
4.4 Comparison of AOD and Angstrom exponent from MODIS with cruise measurements.....	93
4.5 Comparison of mass concentration measurements.....	96
4.6 Role of atmospheric circulation in the spatial distribution of AOD.....	97
4.7 Temporal characteristics of AOD during ARMEX-II.....	101
4.8 Influence of circulation and RH on the day-to-day variation of AOD over the ARMEX domain.....	103
4.8.1 Discussion of the results.....	106
4.9 Summary.....	110

Chapter 5: Influence of circulation parameters on aerosol distribution over the Bay of Bengal during the pre-monsoon period: ICARB (Phase I)

5.1 Introduction.....	112
5.2 Integrated Campaign for Aerosols, gases and Radiation Budget (ICARB).....	113
5.3 Data.....	114
5.4 Comparison of AOD from MODIS with ship measurements...	115
5.5 Circulation variables and spatial distribution of aerosols over the BoB.....	116
5.6 Aerosol transport over the BoB.....	120
5.7 An episodic AOD event during the campaign.....	122
5.7.1 Influence of transport dynamics on the aerosol distribution over the BoB during the episode.....	123
5.8 Influence of wind convergence and vorticity on AOD perturbation.....	126
5.8.1 Estimation of aerosol flux convergence and vorticity.....	126
5.8.2 Aerosol extinction profile derived from CALIPSO.....	126
5.8.3 Association of AOD modulation with convergence and vorticity.....	128

5.9 Contribution of <i>in situ</i> production on the observed AOD.....	130
5.10 Summary.....	131

Chapter 6 : Transport dynamics of aerosols over the Arabian Sea during the pre-monsoon period : ICARB (Phase II)

6.1 Introduction.....	133
6.2 A comparison of MODIS derived AOD with cruise measurements over the Arabian Sea.....	134
6.3 Spatial distribution of AOD over the Arabian Sea during the campaign.....	136
6.4 Influence of circulation on the spatial distribution of AOD.....	137
6.5 Variations in aerosol distribution during the campaign.....	140
6.6 An observational evidence for the influence of transport dynamics on the spatial distribution of AOD: Cluster movement, a case study.....	144
6.6.1 Role of dynamics in the formation, drift and dispersal of the aerosol cluster.....	147
6.6.1.1 Formation of the cluster.....	147
6.6.1.2 Movement of the cluster along the west coast.....	150
6.6.1.3 Dispersal of the cluster.....	151
6.6.2 Evidence from Lidar observations in support of the transport dynamics of aerosol cluster.....	153
6.6.3 Supporting evidence from aerosol chemical analysis for the source of aerosols in the cluster.....	154
6.7 Influence of wind convergence on AOD variations.....	155
6.7.1 Estimation of flux convergence	155
6.7.2 Aerosol extinction profile from CALIPSO.....	156
6.7.3 Association between day-to-day variations in AOD and wind convergence.....	157
6.8 Estimation of aerosol source strength over the Arabian Sea.....	158
6.9 Summary.....	160

Chapter 7: Summary and Future Scope

7.1 Summary.....	162
7.2 Scope for future investigation.....	167

References.....	168
List of Publications.....	195
Symposium Presentations.....	196

Preface

Atmospheric aerosols are intricately linked to the earth's climate and it is now well recognized that they are crucial elements in "climate change". They perturb the radiative balance of the earth-atmosphere system by directly scattering and absorbing the solar short wave and the terrestrial long wave radiation and indirectly through modifying the optical properties and life span of clouds.

On a global basis, about 90% of the aerosol loading is caused primarily by the natural sources, mainly consisting of sea-salt and dust. The rest of the aerosol burden is contributed by anthropogenic activities such as industrial and vehicular emissions, forest fire, bio-mass burning, fossil fuel combustion etc. This diversity in the sources leads to pronounced variation in their physical and chemical properties. Large spatial heterogeneity of sources and their temporal non-uniformity along with the short residence time (typically few days in the troposphere), of aerosols leads to pronounced spatio-temporal variations in their distribution. Long-range transport is another important factor that influences the spatio-temporal variability. These heterogeneities in the aerosol distribution and properties challenge the quantification of their impact on the climate system.

Satellite remote sensing is an ideal tool for the regular monitoring of the global distribution of aerosols. Launch of new satellite-borne sensors with enhanced capabilities in the recent years brought a revolution in the understanding of global aerosol distribution and their long range transport. The multi-spectral satellite sensor, "MODIS" is a unique instrument capable of synoptic scale monitoring of aerosols with fine spatial resolution, on a daily basis. In order to assess the aerosol variations due to source and transport activities, NCEP reanalysis is a reliable source of prevailing meteorology and dynamics in the earth-atmosphere system.

In the present study, an attempt is made to investigate the transport dynamics of aerosols at different geographical environments over the Indian sub-

continent and the adjoining oceanic regions, mainly by using aerosol data from MODIS and reanalysis winds from NCEP. The study also aims to identify the sources of aerosols and estimate their strengths, using an aerosol flux continuity equation. This theme presented in the thesis opens up a distinct phase in the study of aerosols.

The thesis is organized in seven chapters. Chapter 1 outlines an overview on the atmospheric aerosols with emphasis on the importance of studies on aerosol transport. A review on the space-borne aerosol remote sensing and their advantage in addressing the transport dynamics of aerosols are discussed in this chapter. The specification details of MODIS sensor, a brief description on MODIS aerosol retrieval algorithm and a summary of the NCEP reanalysis data are presented in Chapter 2. This is followed by brief accounts on other instruments additionally used in the present study. The mathematical approaches adopted for the analysis of aerosol transport dynamics and for the estimation of aerosol source strength using the flux continuity equation are also detailed in this chapter.

Chapter 3 discusses the transport features of aerosols over the Ganga Basin in the winter period (December, 2004), when ISRO-GBP Land Campaign –II was conducted in this region. This study reveals the association between day-to-day changes in the spatial distribution of AOD and wind convergence at lower altitude (below 1 km) over the Ganga Basin. The aerosol flux continuity equation is used to identify the major sources prevailing in this region.

In Chapter 4 the aerosol transport dynamics over the South East Arabian Sea (SEAS) during the pre-monsoon period (ARMEX-II campaign, March 14-April 10, 2003) is presented. The observed day-to-day variation of AOD in the cruise is connected to the day-to-day changes in the spatial distribution of aerosols over the SEAS. AOD data from MODIS is used for this purpose. The role of atmospheric circulation variables and relative humidity in the spatio-temporal variations of aerosol distribution are examined in detail in this chapter.

The transport dynamics of aerosols over the Bay of Bengal (BoB) during the pre-monsoon period (first phase of ICARB, March 18 – April 12, 2006) is detailed in Chapter 5. Wind field variables at different altitudes are analysed to establish the transport mechanism of aerosols over the BoB during this period. The influence of flux convergence and flux vorticity in governing the day-to-day variation of mean AOD over the BoB especially through the higher altitudes winds (above 3 km), is brought out clearly in this chapter. Computations with the flux continuity equation show weak sources of aerosols over the BoB at the locations of moderately high surface wind speeds.

A detailed analysis of the aerosol transport over the Arabian Sea during the pre-monsoon period (second phase of ICARB, April 18 – May 11, 2006) is presented in Chapter 6. Wind field variables are examined to delineate the processes which are responsible for the observed spatial variation of AOD over the Arabian Sea. The mechanism governing an episodic event marked by the appearance of an aerosol cluster off the Maharashtra coast, its southward movement along the Indian west coast and its final dispersal after reaching the southern end of Indian peninsula, is studied in detail. This chapter also brings out the influence of flux convergence at an upper level (~ 3 km) on the day-to-day variations of AOD over the Arabian Sea.

The major findings in the work presented are summarized in Chapter 7. This chapter also outlines the future scope of research in the field of aerosol transport dynamics.

Symbols Used

a_n	<i>Mie coefficient</i>
A	<i>Constant in Deirmendjian size distribution</i>
b_n	<i>Mie coefficient</i>
b_{ss}	<i>Wind index</i>
B	<i>Constant in Deirmendjian size distribution</i>
$B_\lambda(T)$	<i>Planck's function</i>
c	<i>Constant in the aerosol residence time relation</i>
C	<i>Constant in Junge power law distribution</i>
C_1	<i>Constant in Junge modified power law distribution</i>
C_2	<i>Constant in Junge modified power law distribution</i>
d	<i>Density of the hydrated particle</i>
d_0	<i>Relative density of dry particle to that of water</i>
d_r	<i>Particle density</i>
d_w	<i>Density of water</i>
D	<i>Aerosol residence time</i>
D_{wet}	<i>Aerosol residence time resulting from wet removal processes</i>
e	<i>Empirical constant in the coagulation equation</i>
f_{ac}	<i>Aerosol flux convergence</i>
f_{av}	<i>Aerosol flux vorticity</i>
F_λ	<i>Normalized downward flux for zero surface reflectance at wavelength, λ</i>
F_λ^f	<i>Normalized downward flux for zero surface reflectance for fine aerosol model</i>
F_λ^c	<i>Normalized downward flux for zero surface reflectance for coarse aerosol model</i>
g	<i>Asymmetry parameter</i>
G	<i>Slant path radiation</i>
h_n	<i>Spherical Bessel function</i>
H_a	<i>Aerosol scale height</i>
i	<i>Number of modes appearing in the log-normal distribution</i>
i_{\parallel}	<i>Intensity distribution function for the parallel polarized radiation, in Mie Theory</i>
i_{\perp}	<i>Intensity distribution function for the perpendicular polarized radiation, in Mie theory</i>
I	<i>Intensity of the radiation</i>
j_n	<i>Spherical Bessel function</i>
k	<i>Boltzman constant</i>
k_1	<i>Constant in Deirmendjian size distribution</i>
k_2	<i>Constant in Deirmendjian size distribution</i>
K_t	<i>Turbulent diffusion coefficient</i>
l_m	<i>Molecular mean free path</i>
L	<i>Flux radiance</i>
$m_d(r)$	<i>Mass size distribution</i>
m_w	<i>Mass of condensed water</i>
m_0	<i>Dry particle mass</i>
M	<i>Optical air mass considered in the radiative transfer equation for satellites</i>
M_v	<i>Optical air mass in the satellite viewing direction</i>

M_0	<i>Optical air mass in the sun illumination direction</i>
M_a	<i>Optical air mass used in the Microtops sunphotometer retrieval algorithm</i>
$n(r)$	<i>Number of particles per unit volume, per unit radius interval in the logarithmic scale</i>
N	<i>Number of particles per unit volume</i>
N_0	<i>Number of particles per unit volume at time $t = 0$</i>
$NDVI_s$	<i>Normalised Difference Vegetation Index at shortwave infra red wavelength</i>
N_{mi}	<i>Total number density of particles in the i^{th} mode of the log normal size distribution</i>
p	<i>Level of significance</i>
P	<i>Scattering phase function</i>
Q_s	<i>Scattering efficiency</i>
Q_a	<i>Absorption efficiency</i>
Q_e	<i>Extinction efficiency</i>
Q	<i>Actual source strength (aerosol production rate)</i>
r	<i>Particle radius</i>
r_{mi}	<i>Mode radius for the i^{th} mode in the log normal size distribution</i>
r_a	<i>Particle radius at a given RH</i>
r_0	<i>Dry particle radius</i>
R_t	<i>Aerosol removal rate</i>
R	<i>Correlation coefficient</i>
s_λ	<i>Atmospheric backscattering ratio for wavelength, λ</i>
s_λ^f	<i>Atmospheric backscattering ratio for fine aerosol model, for the wavelength, λ</i>
s_λ^c	<i>Atmospheric backscattering ratio for coarse aerosol model, the wavelength, λ</i>
$s_d(r)$	<i>Surface area size distribution</i>
s_0	<i>Strength of aerosol source corresponding to a particular height</i>
S	<i>Column integrated net source strength</i>
T_λ	<i>Upward total transmission into the satellite for the wavelength, λ</i>
T_λ^f	<i>Upward total transmission into the satellite for fine aerosol model</i>
T_λ^c	<i>Upward total transmission into the satellite for coarse aerosol model</i>
t	<i>Time</i>
T	<i>Temperature (in Kelvin)</i>
u	<i>Zonal component of horizontal wind field</i>
U	<i>Wind speed</i>
v	<i>Meridional components of horizontal wind field</i>
$v_d(r)$	<i>Volume size distribution</i>
V	<i>Three dimensional vector wind</i>
V_t	<i>Settling velocity</i>
V_λ	<i>Voltage measured at the wavelength λ</i>
$V_{0\lambda}$	<i>Extraterrestrial voltage at wavelength λ corrected for mean sun-earth distance</i>
X	<i>Size parameter in the scattering theory</i>
z	<i>Atmospheric altitude</i>
Δ	<i>Error defined in the MODIS aerosol retrieval algorithm over ocean</i>
Φ	<i>Turbidity coefficient</i>

Ω	<i>Solid angle</i>
α	<i>Angstrom exponent</i>
β_s	<i>Scattering coefficient</i>
β_a	<i>Absorption coefficient</i>
β	<i>Total extinction coefficient</i>
ε	<i>Error defined in the MODIS aerosol retrieval algorithm over land</i>
ϕ	<i>Azimuth of the direction of observation</i>
ϕ_d	<i>Azimuth difference between solar incident and satellite viewing directions</i>
γ	<i>Scattering angle</i>
η	<i>Fine mode fraction</i>
λ	<i>Electromagnetic wavelength</i>
λ_p	<i>Wavelength corrected for surface elevation in the MODIS aerosol retrieval</i>
μ	<i>Complex refractive index</i>
μ_0	<i>Refractive index of dry particle</i>
μ_w	<i>Refractive index of water</i>
μ_{vis}	<i>Viscosity of air</i>
ν	<i>Size index in the power law size distribution</i>
π_n	<i>Angular function in Mie theory</i>
θ	<i>Zenith angle of the direction of observation</i>
θ_s	<i>Solar zenith angle</i>
θ_v	<i>Satellite zenith angle</i>
ρ_λ^*	<i>Top of the atmosphere reflectance (TOA) at λ, over the land computed by Look up Table</i>
ρ_λ^a	<i>Atmospheric path reflectance at λ</i>
ρ_λ^s	<i>Angular surface reflectance at wavelength λ</i>
ρ_λ^m	<i>TOA reflectance measured by satellite</i>
ρ_λ^{*f}	<i>TOA reflectance for fine aerosol model</i>
ρ_λ^{*c}	<i>TOA reflectance for coarse aerosol model</i>
ρ_λ^{af}	<i>Atmospheric path reflectance at wavelength, λ for the fine aerosol model</i>
ρ_λ^{ac}	<i>Atmospheric path reflectances at wavelength, λ for coarse aerosol model</i>
ρ_λ^{ray}	<i>Atmospheric path reflectance contributed by Rayleigh scattering</i>
σ_s	<i>Angular scattering cross section</i>
σ_a	<i>Absorption cross section</i>
σ_{mi}	<i>Standard deviation of i^{th} mode in the lognormal distribution</i>
τ_n	<i>Angular function in Mie theory</i>
τ	<i>Aerosol optical depth</i>
τ_0	<i>Aerosol optical depth at zero wind speed</i>
$\tau_{O3\lambda}$	<i>Ozone optical depth at wavelength, λ</i>
$\tau_{R,\lambda}$	<i>Rayleigh optical depth at wavelength, λ</i>
τ_{ss}	<i>Sea-salt optical depth</i>
τ_{λ}	<i>Sum of the optical depths of aerosol, ozone, and Rayleigh</i>
τ_{MODIS}	<i>Optical depth derived from MODIS</i>
$\tau_{Microtops}$	<i>Optical depth derived from Microtops</i>
ν	<i>Size index in the power law size distribution</i>
ω	<i>Single scattering albedo</i>

Frequently used Acronyms

AERONET	Aerosol Robotic Network
AOD	Aerosol Optical Depth
ARMEX	Arabian Sea Monsoon Experiment
AVHRR	Advanced Very High Resolution Radiometer
BC	Black Carbon
BoB	Bay of Bengal
BPC	Bulk-to-Particle Conversion
CALIPSO	Cloud Aerosol Lidar and Infrared Pathfinder Satellite Observations
cmAOD	Coarse mode aerosol optical depth
C004	Collection 004 MODIS products
C005	Collection 005 MODIS products
DMS	Dimethyl sulphide
FMF	Fine Mode Fraction
fmAOD	Fine mode aerosol optical depth
GHG	Green House Gas
GPC	Gas-to-Particle Conversion
ICARB	Integrated Campaign for Aerosols, gases and Radiation budget
IGP	Indo-Gangetic Plain
ISRO-GBP	Indian Space Research Organisation – Geosphere Biosphere Programme
IST	Indian Standard Time
INDOEX	Indian Ocean Experiment
Lidar	Light detection and ranging
LUT	Look-Up-Table
LMT	Local Mean Time
MODIS	Moderate Resolution Imaging Spectroradiometer
NCEP	National Centers for Environmental Prediction
NDVI	Normalised Difference Vegetation Index
ORV	Oceanographic Research Vessel
QAC	Quality Assurance Confidence
QCM	Quartz Crystal Microbalance
QuikSCAT	Quick Scatterometer
RH	Relative Humidity
SWIR	Short Wave Infra Red
TOA	Top of the Atmosphere
UV	Ultra Violet
UTC	Coordinated Universal Time

Chapter 1

An overview on atmospheric aerosols and their transport

1.1 Introduction

Intergovernmental Panel for climate change [IPCC, 2007], reports that the current global warming based on the build up of green house gases (GHGs) from the industrial era is $\sim 0.8^\circ\text{C}$, which is smaller by a factor of 3 to 4 as against the expected value of $\sim 2.4^\circ\text{C}$ [Ramanathan and Feng, 2009]. Further, studies have indicated that this discrepancy between the observed and the estimated value, is mainly due to the effect of ‘**Atmospheric Aerosols**’, which are capable of partly nullifying the warming effect caused by the GHGs [Santer *et al.*, 1996; Kaufman *et al.*, 1997a; Haywood *et al.*, 1999]. It was only in the early 1990’s the significance of aerosols in the climate change was recognized, even though it was speculated in the early sixties and seventies [McCormick and Ludwig, 1967; Mitchel, 1970]. Unlike the GHGs, the perturbation due to these relatively short lived species (aerosol) on the radiative balance of the earth-atmosphere system [Charlson *et al.*, 1992; Haywood and Boucher 2000] is difficult to estimate primarily because of their large **spatio-temporal heterogeneity** in (i) **concentrations**, (ii) **optical and chemical properties** and (iii) **vertical distribution**. After more than two decades of scientific investigation in this area, studies still project them as the most variable component in the atmosphere responsible for the greatest uncertainty in the climate prediction models [IPCC, 2007].

1.2 Aerosol generation in the atmosphere

Atmospheric aerosols are tiny solid or liquid particles suspended in the air with size ranging between 10^{-3} and 10^2 μm . A major factor responsible for the heterogeneity of aerosols is the wide variety of their generation mechanisms, which can be broadly classified as **primary** and **secondary processes**.

In the primary generation mechanism, aerosol particles are produced directly from the sources. Wind generated dust over arid and desert regions and sea-salt particles over the ocean surface are examples of this mechanism, which is also called '**Bulk-to-Particle Conversion**' (BPC) process. In the secondary production mechanism, aerosols are created under different meteorological conditions through chemical reactions of gases emitted from industries, vehicular transportation, etc. This is termed '**Gas-to-Particle Conversion**' (GPC) process [Prospero *et al.*, 1983; Jaenicke, 1984]. Falling in one of these mechanisms, aerosol generation by different sources is either natural or anthropogenic.

1.2.1 Natural aerosol sources

About 90% of the total aerosol burden in the atmosphere is of natural origin, which includes sea salt particles from the oceans, soil dust from deserts and other arid regions, smoke from wild peat and forest fires, volcanic emissions, etc.

1.2.1.1 Oceans

The agitation of sea surface by winds with speeds greater than around $3 - 4 \text{ ms}^{-1}$, generates air bubbles on the sea surface which then burst give rise to jets of water that break into fine droplets [Blanchard and woodcock, 1957; Monahan, 1971]. Each bursting bubble produces between one to ten jet drops (radii $< 10 \mu\text{m}$) and several hundred smaller film droplets (radii $< 1 \mu\text{m}$) [Woolf *et al.*, 1988]. These drops and droplets get equilibrated to the ambient relative humidity and become sea-salt particles or sea-salt solution droplets. For wind speeds exceeding 10 ms^{-1} the mechanical disruption of wave crests leads to spume drops with sizes $> 10 \mu\text{m}$ radius [Wang and Street 1978; Monahan *et al.*, 1986]. Sea-salt particles produced over the oceans constitute the single largest contributor to the global aerosol burden with a production rate of $\sim 1000 - 10,000 \text{ Tgyr}^{-1}$ [Blanchard, 1983; Winter and Chylek, 1997] amounting to about 30 – 75% of the natural aerosols [Blanchard and Woodcock, 1980]. The abundance and size spectrum of the sea-salt aerosols are strongly

influenced by the wind speed [Woodcock, 1953; Blanchard, 1963]. It is speculated that the sea-salt production increases by about 10 times for each 4 ms^{-1} increase in wind velocity [Tsunogai *et al.*, 1972]. The major chemical species constituting the sea salt particles are chlorine (Cl^-), sodium (Na^+), sulphur (SO_4^{2-}), magnesium (Mg^{2+}), calcium (Ca^{2+}), and potassium (K^+) [Wilson, 1975].

Oceans also produce secondary aerosols in the ultra-fine size range primarily in the form of non sea-salt sulphate (nss) and organic types, through the GPC processes of the gaseous emissions from phytoplanktons [O'Dowd *et al.*, 1996]. Almost all the species of the marine phytoplankton during senescence or when grazed release dimethyl sulphide (CH_3SCH_3) vapour. The dimethyl sulphide (DMS) in the air gets oxidised in the presence of OH to form methane sulphononic acid ($\text{CH}_3\text{SO}_3\text{H}$) and SO_4^{2-} [Fitzgerald, 1991]. These GPC processes are important in shaping the sub-micron part (radius $< 0.5 \mu\text{m}$) of the marine aerosol size distribution [Fitzgerald and Hoppel, 1988; Hoppel *et al.*, 1990]. Concentration of DMS in the ocean follows the seasonal cycles of oceanic primary productivity [Prospero, 2002]. In the regions of ocean upwelling where productivity is large, the concentration of sub-micron sulphate particles has been found (at times) to exceed that of sea-salt sulphate particles [Fitzgerald, 1991]. But, in clean maritime situations, sulphate (from GPC) contributes less than 25% of aerosol mass while the rest is predominantly contributed by sea-salt particles in all the size ranges [O'Dowd and Smith, 1993], mainly produced by BPC.

1.2.1.2 Deserts/ Arid regions

Deserts which cover almost one-third of the earth's land surface with a contribution of 30 – 50% are the next major producer of naturally occurring tropospheric aerosols [d'Almeida *et al.*, 1991]. When wind blows over the arid regions, the momentum from wind is transferred to the soil particles and they will be easily dislodged from the surface. The emission of dust from soil depends upon its moisture content, surface wind speed and soil conditions (vegetated or bare soil) [Tegen and Miller, 1998; Miller *et al.*, 2004]. Though the dust predominantly consists of large aerosols with maximum radii around $100 \mu\text{m}$, studies by d'Almeida and Schutz [1983] have demonstrated the presence of smaller particles ($\sim 0.01 \mu\text{m}$ radius) with number size distribution peaking around $0.1 \mu\text{m}$ in the accumulation mode. Estimates of annual dust emission range from 1000 to 3000 Tgyr^{-1} [Cakmur *et al.*, 2006]. Principal elements constituting mineral dust are Si, Al, Ca and Fe as carbonates and oxides

[*Malm et al.*, 1994]. Soil-derived dust accounts for more than 50% of the total Cr, Mn and V emissions, as well as for 20-30% of the Cu, Mo, Ni, Pb, Sb and Zn released annually into the atmosphere [*Pacyna*, 1998].

Hotspots of dust are centred mostly around the topographical ‘lows’ which were flooded with water around 2 million years back. On a global scale, the dominant sources of mineral dust are all located in the northern hemisphere, mainly in the North Africa, the Middle East, Central Asia, and the Indian subcontinent [*Herman et al.*, 1997; *Prospero et al.*, 2002]. There is a large spatial variability in dust emission scenario with changing seasons. In North Africa, dust activity during winter which is quite large in low latitudes shifts to higher latitudes as the year progresses. Around 3 Tg of mineral dust is injected into the troposphere annually from the Saharan desert [*Prospero*, 1996]. In the Middle East, the activity peaks in late spring and summer and is minimum during winter. Over the Indian subcontinent, the dust activity peaks during spring and decreases in summer, with the onset of the southeast monsoon. In Asia, dust activity peaks in spring [*Prospero et al.*, 2002]. Mineral aerosols from West and Central Africa accounts for nearly 50% of the global dust loading [*Luo et al.*, 2004] and therefore is responsible for about 20% of the global aerosol optical thickness [*Tegen et al.*, 1997]. Droughts also cause increase in mineral dust concentration on a synoptic scale [*Prospero and Nees*, 1977].

1.2.1.3 Volcanoes

Volcanic eruptions eject large amounts of materials mainly as precursor gases for GPC process, water insoluble dust and ash into the atmosphere [*Parameswaran*, 1998]. This is the most important source of aerosols in the stratosphere. The primary particles that are ejected into the atmosphere, being larger in size, settle down very fast. But the gases like SO₂ reach up to the stratospheric altitudes and undergo chemical reactions such as oxidation of SO₂ to SO₃, hydration, direct GPC conversion and reactions with water vapour to form sulphuric acid (H₂SO₄) [*Hoffman*, 1988]. Very small size of these particles and the absence of any major loss processes in the stratosphere favour to extent their life time up to around 2 years or even more, favouring an easy distribution all over the globe [*Farlow and Ferry*, 1979]. Volcanic aerosols also serve as surfaces for heterogeneous chemical reactions that destroy stratospheric ozone [*Robock*, 2000].

The importance of volcanic activities varies depending on the strength of the eruptions, but on an average, they contribute 15 – 90 Tgyr⁻¹ [*Parameswaran*, 1998]. For

instance, the famous Mt. Krakatoa eruption in the East Indies in 1883, was so severe, that it produced a veil of volcanic dust in the stratosphere causing considerable reduction of sunlight around the world for months together, resulting in a cooling of the earth's surface. The Katmai (Alaska) in 1912, Mount Agung (Indonesia) in 1963, El Chichon (Mexico) in 1982 and Mount Pinatubo (Philippines) in 1991 were some of the strong volcanic eruptions in the 20th century which produced notable impacts on climate [Robock, 2000].

1.2.1.4 Biological debris

Biological processes are also important sources of natural aerosols. Particulates of biological origin are derived from living organisms such as protein-containing cells, microorganisms and fragments of living things [Jaenicke, 1993]. This includes a wide range of biogenic particles, such as small viruses, bacteria, algae, pollen grains, plant debris like leaf litter and terpenes consisting of unsaturated hydrocarbons found in essential oils and oleoresins of plants such as conifers. Coarse size aerosols dominate in the size distributions of these particles. Biological processes account for aerosol emission around 25 - 80 Tgyr⁻¹ [d'Almeida *et al.*, 1991].

1.2.2 Anthropogenic aerosol sources

About 10% of global atmospheric aerosol mass is contributed by human activities. They are mainly concentrated in the immediate vicinity of the sources and along the downwind direction. Industrial effluents, exhausts from vehicles, fossil fuels and biofuel combustion, biomass burning, etc, are the major anthropogenic sources of aerosol emission. Anthropogenic burning of agricultural and crop wastes has tremendously increased in the past two decades and is contributing to around 95% of the total biomass emissions [Hewitt and Jackson, 2003; Streets *et al.*, 2003; Bond *et al.*, 2004,]. Although the per-capita usage of biofuels in the developing countries is declining, with the usage of more efficient commercial energy sources, the total consumption still shows an increasing trend [Hall *et al.*, 1994] due to the increase in population. Seasonal and inter-annual variability in the open-burning has been studied using the active-fire-count data from satellites [Duncan *et al.*, 2003; Reddy and Boucher, 2004]. Both fossil fuel and biomass burning contribute to primary aerosols by emitting particles like fly ash, dust, black carbon (BC) and organic carbon (OC) while precursor gases such as SO₂, NO_x and volatile organic compounds form

secondary aerosols through GPC processes [Andrea and Crutzen, 1997]. Central South America, South Africa and South Asia are among the major biomass-burning regions in the world [Streets et al., 2004].

Fossil fuel combustion in the thermal power plants, other industrial activities and exhaust from vehicles are important sources of sulphates and nitrates. Aerosol emission from industrial activities is estimated to be nearly 100Tgyr^{-1} [Hewitt and Jackson, 2003]. By around 1960, the natural emissions of sulphur in the atmosphere was exceeded by anthropogenic SO_2 emissions, predominantly from fossil fuel burning (about 72%) [Moller, 1984] with a small contribution (about 2%) from biomass burning [IPCC, 2007]. Pollution aerosols were modelled first exclusively as sulphates [Kiehl and Briegleb, 1993], but the new chemical measurements [Novakov et al., 1997] made downwind of the eastern United States show that the contribution of carbonaceous material to aerosol optical depth (around 30%) is double that of sulphates (around 16%) which arises mainly from incomplete combustion activities. Globally, biomass and biofuel burning contribute about 65% and fossil fuel about 35% to the emission of BC [Bond et al, 2004].

Increase of SO_2 emissions in India during the years 1979 – 2000 has been reported to be 47% per decade and is attributed to the increase in population over these years [Massie et al., 2004]. Anthropogenic sources such as biomass burning and fossil fuel combustion contribute above 75% of the aerosols observed over the Indian subcontinent which is further confirmed by their high BC content and absorbing nature [Gabriel et al., 2002]. These are blamed for the extensive Atmospheric Brown Cloud (ABC) over the South Asia [Gustaffson et al., 2009].

Soil and desert dust also can be considered partly pseudo-anthropogenic because of the human impact on land cover and desertification [Tucker et al., 1991]. Some studies have reported that the anthropogenically contributed dust can be as high as 30 to 50% of total dust production even though these estimates have large uncertainties [Tegen and Fung, 1995; Sokolik and Toon, 1996]

1.3 Properties of aerosols

Atmospheric aerosols influence the radiative energy balance of the earth-atmosphere system, through their interaction with the solar short wave and terrestrial long wave radiation [Charlson and Pilat, 1969; Twomey, 1977; Coakley et al., 1983; Lubin et

al., 1996]. This interaction is basically determined by the physical properties of aerosols such as size, shape, concentration and their chemical composition.

1.3.1 Aerosol size

Aerosols in the atmosphere are polydisperse in nature. Based on the particle size, they are generally classified into three categories [Junge, 1963]: (i) Aitken particles (radius $< 0.1\mu\text{m}$) (ii) large particles (radius $\sim 0.1\mu\text{m}$ to $1\mu\text{m}$) and (iii) giant particles (radius $> 1\mu\text{m}$). In terms of the mechanism of aerosol production these categories respectively fall into (i) nucleation (radius ~ 0.001 to $0.1\mu\text{m}$) mode (ii) accumulation mode and (iii) coarse mode particles [Whitby, 1978].

As discussed in the previous section, large amount of volatile gases are released into the atmosphere through the combustion processes, transportation, industries etc. These gases, through GPC processes under different atmospheric conditions give rise to ultra fine and sub-micron particles termed as '**nucleation mode aerosols**'. The '**accumulation mode aerosols**' are formed mainly through the coagulation of nucleation mode particles and further by the condensation of water vapour on them [Prospero *et al.*, 1983]. Particles comprising the nucleation and accumulation size ranges are mostly the anthropogenic aerosols. On the other hand, the primary particles that are formed through BPC processes are termed the '**coarse mode particles**' and comprise mostly of natural aerosols. Soil and mineral dust from the deserts and sea-salt from the ocean surface are the major component of particles in coarse mode.

1.3.2 Aerosol size distribution

In a poly-disperse system where different particle sizes co-exist, the size distribution is modelled using different functional forms. Size distribution of aerosols is a core physical parameter that determines the properties like mass and number density or optical scattering in different size ranges [Harrison and Van Grieken, 1998]. The size distribution at a location depends not only on the source mechanisms, but also on the removal processes as well as the prevailing meteorological conditions (these aspects will be discussed later) [Vaveka *et al.*, 2000].

Since the size range of aerosols varies over several orders of magnitude, it is usually expressed in the logarithmic scale. The number size distribution $n(r)$ is defined as the number density of particles for unit radius interval in the logarithmic scale as,

$$n(r) = \frac{dN}{d \ln(r)} \quad (1.1)$$

where dN is the number of particles per unit volume in the radius range $d \ln(r)$ centered around $\ln(r)$. The size distribution is modelled using different analytical forms matching with the observed size distribution.

1.3.2.1 Power law distribution

Based on the measurements of the continental aerosols, *Junge* [1963] found that the number of aerosols decrease with increase in size for $r > 0.1 \mu\text{m}$ and the variation can be fairly well represented by a power-law as

$$n(r) = C r^{-\nu} \quad (1.2)$$

where C is a constant depending on the total number of particles and ν is the 'size index', which is an indicator of the relative dominance of larger particles over the smaller ones. The value of ν generally varies between 2 and 5. However, this type of distribution is not valid for particles $< 0.1 \mu\text{m}$. It is mainly because the ultra fine particles are rapidly transformed into larger ones by coagulation and have very short residence time; sometimes of the order of minutes. Hence in the aitken range, the size distribution would not increase indefinitely with decrease in size, but reaches a maximum around $0.01 \mu\text{m}$ and then decreases for further decrease in size. *McClatchey et al.* [1972] has suggested a modification of the Junge power law defined by,

$$\begin{aligned} n(r) &= C_1 10^{-\nu} & 0.02\mu\text{m} < r < 0.1\mu\text{m} \\ n(r) &= C_2 r^{-\nu} & 0.1\mu\text{m} < r < 10\mu\text{m} \\ n(r) &= 0 & r < 0.02\mu\text{m} \text{ and } r > 10\mu\text{m} \end{aligned} \quad (1.3)$$

where C_1 and C_2 are constants decided by the continuity of the distribution and total amount of aerosols. This model of aerosol size distribution is found to be fairly well suited for describing the optical effects of aerosols.

1.3.2.2 Gamma distribution

Deirmendjian [1969] has proposed a size distribution which is widely accepted to describe haze and cloud particles. This is in the form of a modified Gamma distribution function given by

$$n(r) = A r^{k_1} \exp(-B r^{k_2}) \quad (1.4)$$

where A , B , k_1 and k_2 are positive constants. The radius intervals in this function can be chosen as large as required to include the lower and higher size ranges. The maximum of the distribution occurs at r_m , at which the different constants are related as,

$$k_1 = B k_2 r_m^{k_2} \quad (1.5)$$

1.3.2.3 Log-normal distribution

The most commonly used functional form for the size distribution is the multi-modal **log-normal distribution** [*Deepak and Box*, 1982; *d'Almeida et al.*, 1991]. The general form of this distribution is given by,

$$n(r) = \sum_{i=1}^n \frac{N_{mi}}{\sqrt{2\pi}\sigma_{mi}} \exp \left[-\frac{(\log r - \log r_{mi})^2}{2\sigma_{mi}^2} \right] \quad (1.6)$$

where r_{mi} is the mode radius, σ_{mi} is the standard deviation, N_{mi} is the total number density for the i^{th} mode. Summation is carried out over 'n' individual lognormal distributions. This form of the aerosol size distribution is widely used for all types of naturally occurring aerosols in the atmospheric boundary layer and troposphere. Different modes included in Eq.(1.6) represent the contributions from distinctly different aerosol sources (anthropogenic, marine, etc.). In practice a summation of three individual lognormal modes is sufficient to characterize most of the naturally occurring aerosol systems. Figure.1.1 shows lognormal number size distributions of different species detected after the Kuwait oil fires [*Parungo et al.*, 1992]. Though each species has a mono-modal distribution, the composite is fairly well represented by a bi-modal lognormal distribution.

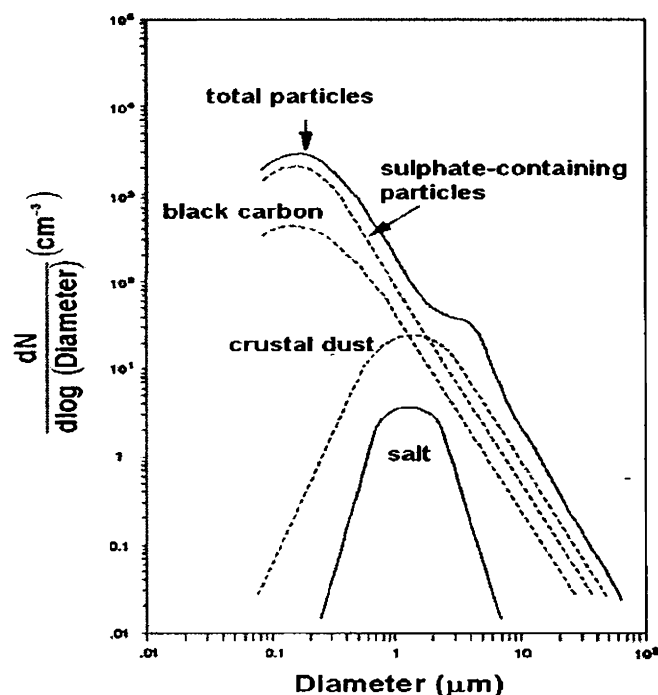


Fig.1.1. Size distributions of various kinds of particles collected after the Kuwait oil fires [Parungo et al., 1992].

1.3.3 Different forms of size distribution

Depending on the physical phenomena of interest, aerosol size distribution is expressed in three different ways: in terms of surface area [$s_d(r)$], volume [$v_d(r)$] or mass concentration [$m_d(r)$]. These are related to number size distribution through the following expressions.

$$\begin{aligned}
 s_d(r) &= 4\pi r^2 n(r) \\
 v_d(r) &= (4/3)\pi r^3 n(r) \\
 m_d(r) &= d_r v_d(r)
 \end{aligned}
 \tag{1.7}$$

where d_r is the particle density.

Aerosol distribution expressed in terms of surface area is important in the context of chemical reactions as well as the effects of scattering. Expressing in terms of volume or mass concentration is more relevant for describing the extinction properties of aerosols (or aerosol loading in the atmosphere). In the total aerosol content, nucleation mode particles contribute mainly to the number, while the accumulation and coarse modes mainly contribute respectively to the surface area and the volume or mass concentrations [Parameswaran, 1998].

1.3.4 Shape of aerosols

On the basis of shape, aerosols are generally classified as Isometric particles (whose all the three dimensions are roughly the same), platelets (with two dimensions long and the third dimension small) and fibres (with one dimension long and the other two short). But in practice, aerosols do not have regular geometric shapes except in very rare cases [Twomey, 1977]. However, for the sake of simplicity, spherical shape is assumed in most of the cases, notwithstanding the fact that in recent years, attempts are being made to incorporate non-sphericity to describe their scattering property [Mishchenko and Travis, 1997].

1.4 Aerosol sink processes

The major removal processes of aerosols in the troposphere are either dry or wet deposition. Dry deposition includes scavenging of the particulate matter by sedimentation, impaction on various surfaces or transfer to the surface through diffusion. Sedimentation is another removal process in which the particles fall under the gravity. About 10 – 20% of the mass of the total aerosols is lost through this process which is mostly the case for particles greater than a few micrometers in size. Loss through impaction on the vegetation, buildings and other objects is the most important mechanism for particles in the size range less than few micrometers, but it is also governed by the wind speed [Slinn and Slinn, 1980]. In addition to the particle size, the aerosol removal efficiency by this process is also governed by the nature of the underlying surface. For example, the removal is more effective over rough surfaces such as forests and urban areas, than over the smooth surfaces such as water and grass lands.

Wet deposition of aerosols involves rainout and washout processes [Prospero *et al.*, 1983]. In the rain out process - also called nucleation scavenging - the particles act as cloud condensation nuclei (CCN) and get removed from the atmosphere through precipitation. In the washout process, aerosols are removed through incorporation into precipitation as a consequence of processes occurring below the cloud base [Prospero *et al.*, 1983]. The aerosol mass removed by washout is several orders of magnitude lower than the nucleation scavenging.

The ratio of wet-to-dry removal of aerosols containing ocean derived elements (eg. Na, Cl, Br, I) are found 3 to 5 times more than that containing crustal or pollution derived elements (Fe, Al, Pb) [Duce *et al.*, 1979; 1980]. Jaenicke [1984] has shown that in the 0.1 μm particle size range, wet removal is 30 times more effective than dry removal processes. For giant particles in the atmosphere, wet removal is not very efficient and particles larger

than 10 μm are removed mainly by dry removal processes [*Whelpdale*, 1982; *Jaenicke*, 1984].

1.5 Aerosol residence time

The two opposing processes of production and loss combine to give the aerosols a definite life time in the atmosphere. Residence time refers to the mean time of a particle to remain air-borne. It decides how far the aerosol particles generated at a particular location will travel and where they will be deposited [*Prospero et al.*, 1983]. The residence time can also be defined as the time required for the particle population to decrease by a factor of $\exp(-1)$ of the initial concentration.

For a first order removal process, the concentration of aerosol at any time t , $N(t)$ can be described by the equation

$$N(t) = N_0 \exp(-R_r t) = N_0 \exp(-t/D) \quad (1.8)$$

where N_0 is the concentration in the source or at time $t=0$, R_r is the removal rate (s^{-1}) and D is the residence time.

But it is not possible to generalize the residence time of aerosols, as it varies with altitude as well as with the particle size. In general, the aerosol residence time varies from a few hours near the surface to a few years at higher altitudes (e.g. stratosphere). Residence time of particles in specific regions will vary depending on the meteorological and climatological conditions. For example, the residence time of particles could be significantly large in the Arctic region compared to the mid-latitudes. Decreased precipitation and increased air mass stability are two possible reasons for this feature. Further, the removal by impaction will be ineffective over the relatively smooth snow covered surface over the Arctic as against the rough and vegetated surface in the mid-latitudes [*Prospero et al.*, 1983].

As the nucleation mode number concentration rapidly decrease through coagulation and coarse mode aerosols are removed fast by sedimentation, both these types of particles are rather short lived compared to the accumulation mode particles. Hence the accumulation mode particles will have a large residence time making them the dominant species in the atmosphere [*Jaenicke*, 1984]. In their size range, where the removal is mainly

controlled by the wet processes, *Jaenicke* [1984] has developed a semi-empirical relation for aerosol residence time given by

$$\frac{1}{D} = \frac{1}{c} \left(\frac{r}{r_n} \right)^2 + \frac{1}{c} \left(\frac{r}{r_n} \right)^{-2} + \frac{1}{D_{\text{wet}}} \quad (1.9)$$

where D is the residence time, r is the particle radius, r_n is the normalization radius ($0.3 \mu\text{m}$, because it has the longest residence time), c is a constant ($1.28 \times 10^8 \text{ s}$) and D_{wet} is the residence time resulting from wet removal processes. This yields a maximum residence time of about a week in the lower troposphere, which increases to several weeks in the upper troposphere. In the stratosphere, residence times are typically of the order of 12 months for volcanic aerosols. The residence time of aerosols as a function of size and altitude within the tropospheric region is depicted graphically in Fig.1.2.

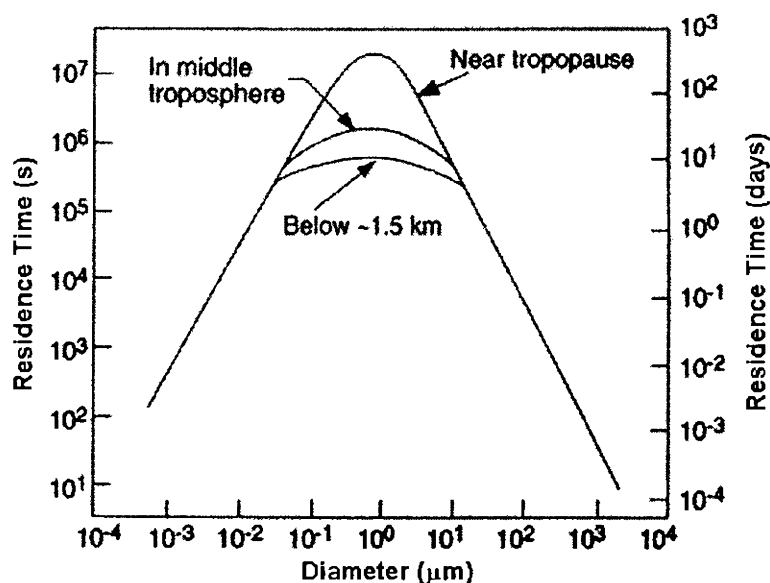


Fig.1.2 Estimates of residence times of aerosols as a function of their diameters [Hobbs, 2000]

1.6 Major aerosol transformation processes

Certain processes in the atmosphere shift the aerosol particles from one size regime to another. This change in size spectrum will influence optical and radiative properties of the aerosol system. Two such important processes are coagulation and condensation.

1.6.1 Coagulation

Coagulation is the process in which small particles collide each other through turbulent diffusion and coalesce together to form larger ones. This leads to an increase in the number of larger particles at the expense of smaller particles without affecting the total mass concentration. Coagulation principally affects the large population of small particles more than the small population of large particles.

In a unit volume of air containing N particles in two size groups with radii r_1 and r_2 , the rate of coagulation is given in modelled as [McCartney, 1976]

$$\frac{dN}{dt} = - \frac{k T f_r}{6\mu_{\text{vis}}} \frac{(r_1 + r_2)^2}{r_1 r_2} \left(1 + \frac{e l_m}{r} \right) N^2 \quad (1.10)$$

where r is the mean value of r_1 and r_2 , k is the Boltzman constant, T is the temperature in Kelvin, μ_{vis} is the viscosity of air ($1.8 \times 10^{-4} \text{ g cm}^{-1} \text{ sec}^{-1}$), e is empirical constant (0.9 cm) and l_m is the molecular mean free path [6×10^{-6}]. f_r is expressed as

$$f_r = \frac{\text{radius of sphere of particle influence (capture)}}{\text{radius of particle}}$$

$f_r = 2$ implies that any two colliding particles will coalesce on touching at any contact angle from head-on to grazing incidence.

The rate of coagulation is minimum for two particles of the same size and it increases with increase in size difference [McCartney, 1976; Pruppacher and Klett, 1978]. According to Byers [1965], particles of radius $0.01 \mu\text{m}$ coagulate 3 times faster with particles of radius $0.1 \mu\text{m}$ than with particles of the radius $0.02 \mu\text{m}$ and 30 times faster with the particles of radius $1 \mu\text{m}$. In natural aerosols, the effect of coagulation is to make the maximum of the distribution to lie between radii of $0.01 \mu\text{m}$ and $0.1 \mu\text{m}$ [McCartney 1976]. Figure 1.3(a) shows the effect of coagulation on the time evolution of particle size distribution.

1.6.2 Effect of relative humidity

Relative humidity (RH) is the ratio of the amount of water vapor present in the atmosphere to the amount that it can hold (without precipitating) at the prevailing temperature. In other words, it is the ratio of ambient water vapour pressure to the saturation vapour pressure expressed in percentage. Depending upon the geography of the

location, atmospheric RH can vary significantly from station to station. When RH increases, water vapour condenses on the particles to maintain equilibrium with the ambient RH so that the physical parameters like size, mean density, refractive index etc. of the particles change thereby altering their radiative properties [*Hanel et al.*, 1976]. The size of the hygroscopic particles grow due to RH according to [*Hanel et al.*, 1976]

$$r_a = r_0 \left[1 + d_0 \frac{m_w}{m_0} \right]^{1/3} \quad (1.11)$$

where r_a is the radius of the particle at a given RH, r_0 the dry particle radius, d_0 the relative density of dry particle to that of water, m_w the mass of condensed water decided by the water activity of the particle, which is a function of its composition and m_0 the dry particle mass.

The particle density change due to hydration is described by

$$d = d_w + (d_0 - d_w) (r_0 / r_a)^3 \quad (1.12)$$

where d is the humid relative density of the particle and d_w the density of water.

Equivalently, the effective refractive index of a hydrated particle can be written as

$$\mu = \mu_w + (\mu_0 - \mu_w) (r_0 / r_a)^3 \quad (1.13)$$

The effect of RH on aerosol properties is non-linear and becomes significant for RH above 70% depending strongly on the size distribution and chemical composition [*Hanel et al.*, 1976; *Parameswaran*, 1996]. For example, oceanic mineral salts like Na and Mg have high affinity to water, while industrial effluents which include soot exhibit very little affinity [*Parameswaran and Vijayakumar*, 1994]. An increase in RH from 40 to 80%, doubles the scattering cross section of sulphate dominated aerosols, whereas it increases only 10 – 40% for smoke aerosols [*Hobbs et al.*, 1997; *Kaufman et al.*, 1998]. *Parameswaran* [1996] has reported that as the RH increases from 70% to 90%, aerosol size index decreases from around 4.7 to 3.5 indicating an increase in the relative abundance of larger size particles.

Effect of RH on the absorption coefficient is uncertain though some theoretical studies indicate that it is much smaller than that on the scattering coefficient [Redemann *et al.*, 2001]. As the ambient RH decreases, condensed water will evaporate resulting in the reduction of particle size. But recent studies have shown that the dependence of particle size during the increasing phase of RH is not retraced in the decreasing phase (especially for solution droplets) - an effect called the hysteresis effect [Rood *et al.*, 1987]. Figure 1.3 (b) shows the particle diameter change for various aerosol compositions [Tang *et al.*, 1977; Tang and Munkelwitz, 1977; Tang 1980].

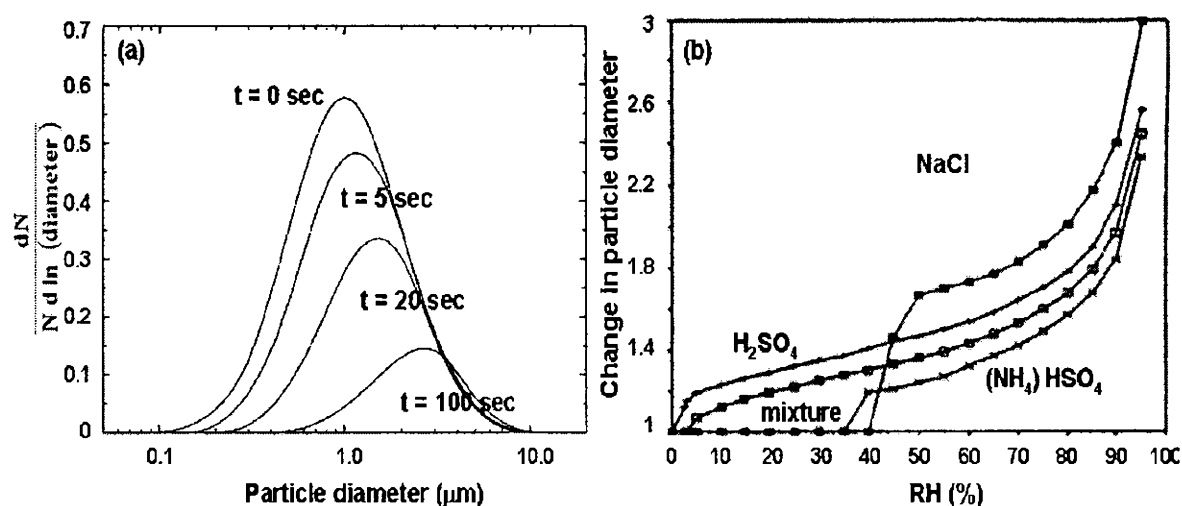


Fig.1.3. Effect of coagulation on particle size distribution, $N_0 = 10^8 \text{ cm}^{-3}$, median diameter = $1 \mu\text{m}$ and initial geometric standard deviation = 2 [Baron and Willeke, 2001 from Hinds, 1999] (a) Equilibrium aerosol diameters as a function of relative humidity for various aerosol compositions. The values for NaCl, H_2SO_4 and $(\text{NH}_4)\text{HSO}_4$ are based on work of Tang *et al.* [1977]; Tang and Munkelwitz [1977]; and Tang [1980]. The line shown for the mixture is based on the laboratory experiments with various molar ratios of $(\text{NH}_4/\text{SO}_4)$ ranging from 0 to 1 [Porter and Clarke, 1997] (b)

1.7 Interaction of aerosols with radiation

Aerosols interact with the short wave solar radiation and long wave terrestrial radiation through scattering and absorption, leading to the attenuation of the incident radiation. This extinction depends on the physical and chemical properties of aerosols, their concentration as well as the frequency of the incident beam itself [Bohren and Huffman, 1983].

1.7.1 Scattering and absorption

Scattering is the process by which a particle redistributes the incident radiant energy into the total solid angle centered at the particle. Atmospheric scattering falls mainly into two categories, **Rayleigh** and **Mie** scattering. Rayleigh scattering occurs when the particles are much smaller than the wavelength of the electromagnetic wave, like air molecules in the atmosphere. In this case, equal amount of radiant energy is scattered into the forward and backward hemispheres and the total energy scattered varies inversely as the fourth power of wavelength.

When the particle sizes are greater than about one-tenth of the wavelength of the incident radiation, electrical multipoles are induced within the scatterer. These multipoles produce higher order partial waves. Since the size of the particle is comparable to the incident wavelength the phase of the primary wave will not be uniform over the particle resulting in phase differences between the various partial waves. The constructive and destructive interferences caused by these partial waves give rise to a complicated scattering pattern. Scattering by aerosols in the atmosphere falls in this category. If the particles are spherical, the scattering pattern is described through Mie theory, which depends on the relative size (or radius, r) of the particle with respect to the wavelength (λ) of the incident radiation and can be expressed by the size parameter (X) as

$$X = 2\pi r/\lambda \quad (1.14)$$

As the value of X becomes larger than around 0.5, the scattering deviates from the Rayleigh characteristics and more energy is scattered in the forward direction. Intermediate maximas and minimas (side lobes) appear in the scattering pattern. The intensity of scattered radiation is a function of X , complex refractive index (μ) of the scattering particles and the scattering angle (γ) [angle between incident and scattered directions]. Mie theory expresses the intensity of scattered radiation polarised in the perpendicular and parallel directions with respect to the scattering plane in terms of two functions i_{\perp} and i_{\parallel} defined as [*Hansen and Travis, 1974; McCartney, 1976*]

$$i_{\perp}(X, \mu, \gamma) = \left| \sum_{n=1}^{\infty} \frac{2n+1}{n(n+1)} [a_n \pi_n(\cos \gamma) + b_n \tau_n(\cos \gamma)] \right|^2 \quad (1.15)$$

$$i_{\parallel}(X, \mu, \gamma) = \left| \sum_{n=1}^{\infty} \frac{2n+1}{n(n+1)} [b_n \pi_n(\cos \gamma) + a_n \tau_n(\cos \gamma)] \right|^2$$

where a_n and b_n are the Mie coefficients which are functions of X and μ expressed in terms of spherical Bessel functions, j_n and h_n as

$$a_n = \frac{j_n(X)[\mu X j_n(\mu X)] - \mu^2 j_n(\mu X)[X j_n(X)]}{h_n(X)[\mu X j_n(\mu X)] - \mu^2 j_n(\mu X)[X h_n(X)]} \quad (1.16)$$

$$b_n = \frac{j_n(X)[\mu X j_n(\mu X)] - j_n(\mu X)[X j_n(X)]}{h_n(X)[\mu X j_n(\mu X)] - j_n(\mu X)[X h_n(X)]}$$

π_n and τ_n are functions of γ given by

$$\pi_n(\cos \gamma) = \frac{1}{\sin \gamma} P_n^1(\cos \gamma) \quad \text{and} \quad \tau_n(\cos \gamma) = \frac{d}{d\gamma} P_n^1(\cos \gamma) \quad (1.17)$$

where P_n^1 are associated Legendre polynomials of the first kind.

For unit irradiance of an unpolarised beam of radiation the scattered intensity [McCartney, 1976] in the direction γ is

$$I(\gamma) = \frac{\lambda^2}{4\pi^2} \left(\frac{i_{\perp} + i_{\parallel}}{2} \right) \quad (1.18)$$

Although the theory is strictly applicable only to isotropic spheres, it is customary to employ it to particles which are irregular in shape but in random orientation. Rayleigh scattering is a special case of Mie scattering in the limit of very small size parameter. In this case the expression for scattered radiation reduces to

$$I_{\text{ray}} = \frac{8\pi^4 r^6}{\lambda^4} \left[\frac{(\mu^2 - 1)}{(\mu^2 + 2)} \right]^2 (1 + \cos^2 \gamma) \quad (1.19)$$

where r is the particle radius and μ its refractive index.

Figures 1.4(a), (b) and (c) show respectively the scattering patterns for particles of sizes one-tenth the wavelength, one-fourth the wavelength and larger than the wavelength of light.

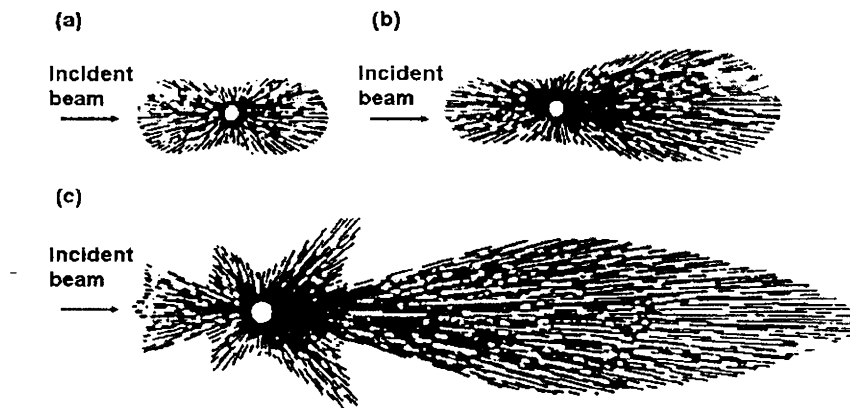


Fig.1.4. Angular patterns of scattered intensity from (a) Small particles ($r < \lambda/10$) (b) large ($r \sim \lambda/4$) (c) larger particles ($r > \lambda$) [Brumberger et al., 1968; McCartney, 1976]

Besides scattering a small portion of the incident radiation can be absorbed by the particle to change its internal energy, which may be re-emitted at other wavelengths and/or utilized to increase its thermal energy. But unlike scattering, absorption is spectrally selective and discontinuous. The real part of the complex refractive index (μ) determines the scattering properties and the imaginary part, the absorption properties. Both scattering and absorption processes result in the removal of energy from the incident beam of radiation and are jointly called extinction process [McCartney, 1976; Bohren and Huffman, 1983].

Interaction of a particle with radiation in general can be described in terms of the parameters such as; scattering/absorption/extinction coefficients, optical depth, single scattering albedo, scattering phase function and asymmetry parameter, all of which vary independently with wavelength.

1.7.1.1. Scattering/absorption/extinction coefficients

Angular scattering cross section [$\sigma_s(\theta, \phi)$] is defined as the cross section of the incident wave, acted upon by the particle, having an area such that the power flowing across it is equal to the power scattered per steradian into the direction (θ, ϕ) . The **total scattering cross section** is defined as the angular scattering cross section integrated over all the 4π directions. In a poly disperse system, if $n(r)$ is the number of scatterers per unit

volume per radius range between r_1 and r_2 , the **scattering coefficient** (per unit volume) is defined as,

$$\beta_s = \int_{r_1}^{r_2} \int_0^{4\pi} \sigma_s(r, \theta, \phi) n(r) d\Omega dr \quad (1.20)$$

where $d\Omega$ is the elemental solid angle. Since the scattering and absorption processes are additive, the total attenuation can be expressed through the **extinction coefficient** as

$$\beta = \beta_s + \beta_a \quad (1.21)$$

where β_a is the absorption coefficient. The extinction coefficient (whose unit is reciprocal of length), can be considered as the fraction of the radiant flux lost from the incident beam when it passes unit distance in the atmosphere, due to scattering and absorption by aerosols.

The scattering or absorption cross-section can be smaller or larger than the geometric cross-section of the particle. The concept of the efficiency factor (Q) is used to express the effective cross-sectional area of the particle with respect to its geometric cross-section [McCartney, 1976]. It is defined as the ratio of the actual scattering or absorption cross-section (σ_s and σ_a respectively) to the geometric cross section (πr^2) of the particle. The scattering (Q_s), absorption (Q_a) and extinction (Q_e) efficiencies are defined respectively as

$$Q_s = \frac{\sigma_s}{\pi r^2}, \quad Q_a = \frac{\sigma_a}{\pi r^2} \quad \text{and} \quad Q_e = Q_s + Q_a \quad (1.22)$$

In a poly disperse system of aerosols, the total extinction coefficient can thus be expressed in terms of Q as

$$\beta = \int_{r_1}^{r_2} \pi r^2 Q_e(r) n(r) dr \quad (1.23)$$

1.7.1.2 Aerosol optical depth

The radiance lost from a beam of radiation while passing through a distance ds can be expressed as,

$$dL = -\beta L ds \quad (1.24)$$

where L is the radiance of the beam.

Integrating over a distance s , the radiance left in the original beam can be obtained as

$$L_s = L_0 \exp\left(-\int_0^s \beta(s') ds'\right) \quad (1.25)$$

where L_0 is the radiance at $s = 0$. This means that radiation gets attenuated exponentially as it traverses the medium. This fundamental law of extinction is called **Lambert - Beer's Law**.

In the atmosphere, the extinction suffered by the incident radiation as it passes through the entire vertical column of aerosols can be expressed as

$$L_s = L_0 \exp\left(-\int_0^\infty \beta dz\right) \quad (1.26)$$

where $\tau = \int_0^\infty \beta dz$ is called the **aerosol optical depth (AOD)**.

1.7.1.2.1 Angstrom exponent

The AOD, in general, displays a wavelength dependence which can be approximated by a power law as

$$\tau_\lambda = \Phi \lambda^{-\alpha} \quad (1.27)$$

where τ_λ is the AOD at wavelength λ (expressed in μm), Φ is the 'turbidity coefficient' which is a measure of the total aerosol loading and can be expressed as AOD at 1 μm wavelength and α is the wavelength exponent known as the 'Angstrom exponent' [Angstrom, 1964].

The Angstrom exponent indicates the columnar size distribution of aerosols. A steep increase in AOD towards shorter wavelengths is a sign of increased abundance of fine (sub-micron) aerosols [Angstrom, 1929]. Generally, values of $\alpha \leq 1$ indicate aerosol distributions dominated by coarse mode particles (radii $\geq 0.5 \mu\text{m}$), typically associated with dust and sea-salt, while $\alpha \geq 2$, indicates size distribution dominated by fine mode particles (radii $\leq 0.5 \mu\text{m}$) usually associated with urban pollution and biomass burning [Westphal and Toon, 1991; Eck et al., 1999].

1.7.1.3 Single scattering albedo

The relative importance of scattering and absorption of the radiation by the particles can be expressed in terms of single scattering albedo (ω), which is the fraction of the radiation that is scattered with respect to the total amount that is scattered and absorbed,

$$\omega = \frac{\sigma_s}{\sigma_s + \sigma_a} \quad (1.28)$$

The value of ω ranges from 0 for purely absorbing particles to 1 for purely scattering ones. Generally at visible wavelengths, the single scattering albedo decreases with wavelength for non-dust aerosols and increases for dust aerosols [Dubovik *et al.*, 2002a]. Typical values for soot particles are around 0.2 and for dust, around 0.8.

1.7.1.4 Scattering phase function

The angular dependence of scattering with respect to the incident direction of radiation is described using the scattering phase function, $P(\theta, \phi)$, where θ is the scattering angle and ϕ is the angle made by the azimuth of the scattered radiation. It is defined as the ratio of the energy scattered per unit solid angle in a given direction (θ, ϕ) with respect to the average energy scattered per unit solid angle in all the directions. This definition requires that the integral of the phase function be normalized to unity such that,

$$\frac{1}{4\pi} \int_0^{4\pi} P(\theta, \phi) d\Omega = 1 \quad (1.29)$$

where

$$P(\theta, \phi) = \frac{\beta_s(\theta, \phi)}{\frac{1}{4\pi} \int_0^{4\pi} \beta_s(\theta, \phi) d\Omega} \quad (1.30)$$

For a spherical particle, the phase function is independent of ϕ .

1.7.1.5 Asymmetry parameter

The asymmetry parameter (g) is an index used for expressing the asymmetry in scattering in the forward/backward hemispheres, for a spherical particle. It is defined as the cosine weighted mean of the angular scattering phase function,

$$g = \frac{\int_0^{4\pi} P(\theta) \cos(\theta) d\Omega}{\int_0^{4\pi} P(\theta) d\Omega} \quad (1.31)$$

The value of this parameter ranges from -1 for entirely back-scattering case to +1 for entirely forward-scattering case. For isotropic scattering, its value is 0. The absolute value of g decreases with increase in wavelength because of the decrease in the scattering efficiency of the particle [Hansen and Travis, 1974].

1.8 Radiative effects of aerosols

Aerosols as a result of their interaction with the radiation, affect the radiative balance of the earth-atmosphere system through their direct and indirect effects. The direct effect refers to the scattering or absorption of the radiation by the aerosol particles. Scattering of solar radiation enhances the albedo of the earth and cools the climate system while absorption of the solar short wave and terrestrial long wave radiations causes heating of the atmosphere. This can weaken convection activities and introduce changes in the atmospheric circulation [McCormick and Ludwig, 1967; Charlson and Pilat, 1969; Coakley et al., 1983; King et al., 1999].

The role of aerosols in altering the earth's energy budget through modification of cloud microphysics by acting as cloud condensation nuclei (CCN) is termed the **indirect effect** of aerosols. This can be split into two components. The first one is the increase in the CCN for a fixed amount of water vapour, leading to a decrease in cloud droplet size but an increase in number of cloud droplets, which in turn causes an increase in the cloud albedo [Twomey, 1974; 1977]. This is also called the **cloud albedo effect** or **Twomey effect** which results in cooling due to reduction in the incoming solar radiation. Studies over polluted regions have reported reduction in cloud droplet size by 20–30% accompanied by an increase in cloud reflectance of sunlight by up to 25% [Coakley et al., 1987; Kaufman and Fraser, 1997; Nakajima et al., 2001]. The second one refers to the reduction in cloud droplet size leading to lowering of the precipitation efficiency [Feingold et al., 1997] thereby extending the cloud lifetime [Albrecht, 1989] and increasing the cloud thickness [Pincus and Baker, 1994]. This is also called **cloud life time effect**. Many investigators could demonstrate this indirect effect based on observations on the influence of aerosols from forest fires and urban pollution in suppressing the rain and snow fall [Rosenfeld, 1999; 2000; Mircea et al., 2005].

Furthermore, the direct absorption of radiation by absorbing particles in the atmosphere can modify the atmospheric temperature structure by evaporating the low level clouds. This effect is called **semi-direct effect** [Hansen *et al.*, 1997]. Recent model studies have indicated the evaporation of low clouds (eg. Stratocumulus and trade cumulus) by solar heating in the presence of soot emitted from biomass burning and fossil fuel combustion [Kiehl *et al.*, 1999; Ackerman *et al.*, 2000].

1.8.1 Radiative forcing of aerosols

Aerosol radiative forcing can be stated in simple terms, as the difference in the radiative flux between an initial state and a perturbed aerosol loading state, at a specified layer in the atmosphere. This can be evaluated at the surface, within the atmosphere, or at the top-of-the atmosphere (TOA) [Chin *et al.*, 2009]. As aerosols in the atmosphere reduce the flux reaching the earth's surface, this forcing will always be negative in sign at the surface. Difference between the TOA forcing and the surface forcing is the atmospheric forcing. A negative value for radiative forcing at TOA, implies a net loss of energy to the earth-atmosphere system leading to a cooling effect, whereas a positive value would mean addition of energy resulting in a warming effect [Haywood and Boucher, 2000; Yu *et al.*, 2006; Chin *et al.*, 2009]. The question whether aerosols warm or cool the planet depends on the particle chemical composition and relative contribution of various chemical species constituting the aerosol system. For example, aerosols such as sulphates, nitrates, sea-salt particles and certain organic compounds are known to produce a negative radiative forcing at the TOA, while the absorbing species like black carbon particles are considered to be positive radiative forcing agents [Charlson *et al.*, 1990; 1992; Haywood and Shine, 1997; Jacobson, 2001]. Determining the strength and sign of the forcing is not very simple, as it is also governed by the altitude of the clouds relative to the aerosols [Haywood and Shine, 1997; Heitzenberg *et al.*, 1997; Satheesh *et al.*, 2008] and also by the reflectance of the underlying surface [Haywood and Ramaswamy, 1998; Haywood and Boucher, 2000]. The mixing states of the aerosols (internal as well as external mixing) also strongly influence the radiative effects of the aerosols [Jacobson, 2001; Chandra *et al.*, 2004].

On a global scale basis, the sum of the direct and indirect radiative forcing is found to be negative implying a cooling effect, which can offset the positive forcing, produced by the greenhouse gases [IPCC, 2001; Yu *et al.*, 2006]. But because of the large spatial and temporal non-uniformity in aerosols, their effects are felt on a regional scale depending on the regional dominance of aerosol species. Hence impacts of aerosols on climate have to be assessed beyond the limited scope of globally averaged radiative forcing.

The results from the fourth assessment of IPCC [IPCC, 2007] indicate substantial advancement from the previous assessments on the aerosol radiative forcing. However, due to the incomplete knowledge on the seasonal and regional variations in the aerosol concentrations, their physical and chemical properties as well as their indirect effects, large uncertainties still exist in accurately determining their climate sensitivity [IPCC, 2007]. A comprehensive assessment of aerosol properties over the globe to minimize these uncertainty limits.

1.8.2 Some examples of the effects of aerosols

Natural aerosols can introduce variability in the climate system and also be part of its feedbacks mechanisms, e.g. larger amount of dust generated during drought conditions in the Sahel [Prospero and Lamb, 2003] can cool the earth's surface and bring about changes in the drought conditions. Anthropogenic aerosols, on the other hand, can be considered as an external cause to climate change [Charlson *et al.*, 1992]. Several climate model studies have indicated that the inclusion of aerosol forcing can possibly explain the decrease in Indian monsoon rainfall [Chung *et al.*, 2002; Vinoj *et al.*, 2004a; Ramanathan *et al.*, 2005; Meehl *et al.*, 2007; Lau *et al.*, 2008] and the north-south shift in east Asian rainfall [Menon *et al.*, 2002]. Transported BC over the Arctic is found to reduce the albedos in fresh snow by 1–3% and further by a factor of 3 as the snow ages and the BC becomes more concentrated [Clarke and Noone, 1985]. Krishnamurthi *et al.* [2009] has reported the influence of pollution over the southern Arabian Sea on the reduction of winter monsoon rains over the south east coast of India. Studies by Lau *et al.* [2006] show that increased dust loading coupled with BC from local sources in northern India during late spring may advance the rainy periods and further intensify summer monsoon leading to the suppression of rainfall over East Asia and the adjacent oceanic regions.

Increased pollution over many urban locations has resulted in intense haze, fog and smog events during the winter period, causing very poor visibility [Ali *et al.*, 2004]. Certain aerosol species when inhaled create severe health problems related to respiratory system, and cause allergies and infections. Inhalation of soot is a major public health issue. For example, in India, it is estimated inhalation of indoor smoke is responsible for over 400,000 deaths annually (mostly among women and children; Smith, [2000]). Chameides *et al.* [1999] demonstrated that over China, reduction of solar radiation by aerosols can lower the crop yields.

1.9 Monitoring of atmospheric aerosols

Detailed global measurements over the land and the ocean from satellites, further supported by measurements from ground-based networks of instruments, and comprehensive regional field experiments in clean and polluted environments fed into global aerosol and climate models is essential for a good understanding on aerosols and their climatic effects.

1.9.1 Ground-based measurements

Historically, scientific studies on atmospheric aerosols started with ground-based measurements on aerosol properties such as size distribution, optical characteristics, chemical composition, vertical profiles, etc. either performed continuously for a long period at a selected site, or specifically as part of intensive field campaigns for short periods over a particular region. The conventional methods of aerosol measurements include two distinct techniques: *in situ* and **remote sensing**. The *in situ* measurement involves direct collection of aerosols from the ambient air on a substrate or in a chamber and carrying out measurements on their properties. This technique more-or-less provides best information on the aerosol properties as they do not involve any major assumptions in deriving the required information. High volume samplers, multi-stage impactors, particle counters, aethelometers, nephelometers, etc are a few among these instruments used for direct measurement of aerosol properties such as size distribution, size-segregated mass concentration, BC mass concentration, scattering coefficients etc. These measurements are also carried out from air-borne platforms like balloons or aircrafts to measure the aerosol properties at different altitudes.

In remote sensing the particle properties are inferred by observing their interaction with radiation. In this case measurements are made without making a direct contact with the particles. Remote sensing techniques mainly measure radiometric parameters, the inversion of which using a radiative transfer theory provides information on aerosol properties. This includes both active and passive methods. While the former use naturally available radiation (solar, lunar, stellar or terrestrial), the latter use an artificial source to illuminate the desired target under study. The simplest example of a passive remote sensor is a radiometer which measures solar radiation reaching the ground for determining the AOD at different wavelengths. Lidar (Light detection and ranging) is an active sensor, which probes the atmosphere with laser pulses to derive the vertical profile of aerosol distribution.

Remote sensing of aerosols is carried out almost throughout the globe at different locations from a variety of platforms over the land, the ocean as well as in the air. Though these measurements can provide a wealth of information on the aerosol physical and chemical properties, their spatial and temporal coverage is rather limited, especially over the oceans and remote land areas, which could introduce biases in the aerosol radiative forcing estimation. Aerosols being highly dynamic both spatially and temporally, integration of all these measurements is still far from providing synoptic information on aerosols, that too at short time scales. On the other hand, remote sensing measurements from satellites can quite well characterize the spatial and temporal heterogeneities of aerosol distribution on a global scale [King *et al.*, 1999].

1.9.2 Space-borne remote sensors

Remote sensing of aerosols from space was initiated more than two decades back [King *et al.*, 1999]. In those days retrievals were limited to the oceanic areas which are dark in the visible and IR parts of the spectrum [Stowe *et al.*, 1997; Mishchenko *et al.*, 1999]. In recent years, with the advent of improved retrieval procedures and new measurement technologies, satellite remote sensing of aerosols has been extended over to the land also. Sensors with improved capabilities are being planned for implementation in the coming decades [Lee *et al.*, 2006; Mishchenko *et al.*, 2007; Chin, *et al.*, 2009], promising the scientific community with more accurate retrieval of aerosol properties and their spatio-temporal variations.

In mid 1972, it was found that a 1% change in radiance in the 0.75 μm channel of Landsat-MSS (Multi Spectral Scanner) satellite sensor resulted from a 1.5% change in aerosol content [Griggs, 1975]. Later, Griggs [1979] investigated the technique of aerosol detection over the low reflectance surface like the ocean for implementation in other satellites like GOES (Geostationary Operational Environmental Satellites) and AVHRR (Advanced Very High Resolution Radiometer). Aerosol amount in the atmosphere was assessed from the relationship between aerosol content and the upwelling visible radiance. The AOD data as an operational product became first available from NOAA (National Oceanic and Atmospheric Administration) AVHRR (Advanced Very High Resolution Radiometer) satellites launched in 1978. Later, a series of satellites for aerosol measurements with advanced technologies supported with efficient retrieval procedures were launched to measure the aerosol properties with better accuracies.

1.9.2.1 AVHRR (Advanced Very High Resolution Radiometer)

NOAA (National Oceanic Atmospheric Administration) - POES (Polar Orbiting Environmental Satellite) series carrying the cross-track scanning AVHRR sensors commenced operation with the launch of TIROS-N in 1978. Towards the end of the life time of each AVHRR sensor, the next sensor is put into orbit to provide uninterrupted data since the launch of the first sensor. There are about 15 satellites launched so far in this series, of which presently about eight of them are in operation [<http://www.oso.noaa.gov/poesstatus>]. AVHRR measures AOD over the ocean at regular intervals [Husar *et al.*, 1997; Ignatov and Stowe, 2002]. Having a swath of about 2400 km, it covers the whole globe in a single day with a spatial resolution of $\sim 1 \text{ km} \times 1 \text{ km}$. The AVHRR channels are spectrally wide, and vary from one satellite to the other. But on an average, they are confined in the range $0.58 - 12.5 \text{ }\mu\text{m}$, of which the wavelength at $\sim 0.63 \text{ }\mu\text{m}$ is used to derive AOD [Husar *et al.*, 1997]. Mishchenko *et al.* [1999] and Geogdzhayev *et al.* [2002] proposed a two-channel (0.65 and $0.85 \text{ }\mu\text{m}$) procedure to derive the Angstrom exponent in addition to AOD over the oceans and was extended later for application over other dark backgrounds such as forests and lakes [Soufflet *et al.*, 1997]. By generating of a multi-decadal climatology on AOD, the AVHRR sensor has significantly contributed to the understanding of global distribution of aerosols [Husar *et al.*, 1997; Mishchenko *et al.*, 1999; 2003; Nair *et al.*, 2005].

1.9.2.2 TOMS (Total Ozone Mapping Spectrometer) & OMI (Ozone Monitoring Instrument)

The TOMS sensor launched in October 1978, on the Nimbus-7 polar sun-synchronous satellite, measures the UV- absorbing aerosols both over the land and the ocean [Heath *et al.*, 1975; Herman *et al.*, 1997], even though its main objective was to retrieve the ozone parameters. Measurement of aerosols is based on the high sensitivity of UV channels to aerosol absorption with a low sensitivity to surface reflectance, even over the land. Detailed procedure of aerosol detection by TOMS is discussed by Torres *et al.* [1998]. It provides Aerosol Index (colour of the scene in the UV with respect to that for a purely Rayleigh scattering atmosphere), optical depth of absorbing aerosols and aerosol single scattering albedo. But the large footprint (about 50 km) of this sensor hampered a good quantitative analysis of aerosol [Torres *et al.*, 1998]. Towards the end of its life time (about 14.5 years), a second non sun synchronous TOMS was launched on board the Russian Meteor 3 satellite which provided data from 1991 to 1994 [Herman and Larko,

1994]. Later, a modified version of this instrument was launched in 1996, onboard NASA's Earth Probe in a sun-synchronous low altitude orbit for better detection of aerosols. In the same year, additional sensors similar to Nimbus-7/TOMS were launched in the Japanese satellite ADEOS (Advanced Earth Observing Satellite). Although the retrieval is done using two different pairs of wavelengths depending on the instrument (i.e., 0.34 and 0.38 μm for Nimbus-7 and Meteor 3 and 0.33 and 0.36 μm for the others), the results are reported at 0.38 μm to keep the continuity of the longer Nimbus-7/TOMS record [Torres *et al.*, 2002]. The TOMS mission was extremely successful in monitoring biomass burning smoke and dust [Herman *et al.*, 1997; Massie *et al.*, 2004] along with the aerosol single scattering albedo [Torres *et al.*, 2005] from space.

OMI on board NASA's EOS satellite Aura launched in July 2004 follows the TOMS measurements on aerosol parameters. The retrieval algorithm uses spectral information from both the visible and the UV part of the spectrum, improving the distinction between weakly absorbing aerosols, biomass burning aerosols and desert dust aerosols. With a swath of 2600 km, it provides daily global information on aerosols with a fairly good spatial resolution of 13 x 24 km at nadir [Veihelmann *et al.*, 2007].

1.9.2.3 CZCS (Coastal Zone Color Scanner)

The Nimbus-7 satellite also carried the first ocean colour sensor, CZCS which initiated a new era of ocean colour monitoring [Hovis *et al.*, 1980]. The scan width of the sensor was 1556 km, observing with a spatial resolution of 825 m at nadir. CZCS operated at six wavelength channels, in the range 0.44 – 12.5 μm primarily meant for detecting chlorophyll, suspended sediments and other ocean related parameters. The spectral channel at 0.67 μm employed for the atmospheric correction was used to estimate AOD over the ocean. To avoid sun-glint, the scanner mirror was provided with a tilting arrangement by about $\pm 20^\circ$ from nadir on ground command. Due to the power demands of the various on-board experiments the CZCS sensor was operated intermittently and collected data only for two hours per day on an average during its observation period till 1986.

1.9.2.4 SAM (Stratospheric Aerosol Measurement) & SAGE (Stratospheric Aerosol and Gas Experiment)

SAM, the first satellite borne sensor focussed for the study of stratospheric aerosols from space, was launched in 1975 during Apollo-Soyuz Test Project. The altitude profile of aerosol extinction was obtained by solar occultation technique. Motivated by the success, it

was followed by SAM-II and SAGE programmes. SAM-II was launched on October 1978, on board Nimbus 7 satellite which made measurements till 1991. It measured the aerosol extinction in 1 μm wavelength at all the occultation points which were confined to the polar regions [McCormick *et al.*, 1979]. Later, the limb viewing, SAGE –I satellite was launched onboard the Application Explorer mission- B (AEM-B) in February 1979, which continued its successful operation till 1981. Operating in four spectral channels between 0.38 and 1.0 μm , this instrument produced for the first time, the atmospheric extinction profiles on a global basis for aerosols and trace gases such as ozone and nitrogen dioxide [McCormick *et al.*, 1979]. The SAGE II began operation with the launch of Earth Radiation Budget Satellite (ERBS) in October, 1984. It had additional three channels ranging from 0.385 to 1.02 μm [Yue *et al.*, 1986; Kent *et al.*, 1998] intended for a better parameterization of aerosols. The vertical resolution of this sensor was 1 km and horizontal resolution, 200 km. However, the altitude profiles were restricted to above 6 km because of the interference from clouds in the limb viewing direction. The SAGE II data helped scientists to understand the causes and effects of Antarctic ozone hole, and has made valuable scientific contributions in studying the stratospheric aerosols during the Mt. Pinatubo eruption [Antuna *et al.*, 2002]. SAGE II was followed by SAGE III, launched on board Meteor-3 in December, 2001 [Kent *et al.*, 1997]. It was designed to make aerosol measurements in eight wavelengths in the spectral band, 0.38 - 1.55 μm . The longest wavelengths are particularly useful for upper tropospheric aerosol studies and also down to the surface, in the absence of clouds [Kent *et al.*, 1997].

1.9.2.5 ATSR (Along Track Scanning Radiometer)

In April 1991, the European Space Agency (ESA) launched a new type of multi-angle conically scanning sensor, called the ATSR on board their first European Remote Sensing Satellite (ERS-1) to test the ‘along track scanning’ concept. This sensor operated only in IR channels. An enhanced version of ATSR, ATSR-2 was successfully launched on board ERS-2 spacecraft on April 1995, with additional channels in the visible wavelengths. It could make AOD measurements by remotely sensing the visible and near-infrared wavelengths at nadir and oblique forward scan angles (both within a two-minute interval) [Mackay *et al.*, 1998]. The 512 km swath at a spatial resolution 1 km x1 km, allows a global coverage in 6 days [King *et al.*, 1999]. A modified version of the sensor, called the

Advanced Along Track Scanning Radiometer (AATSR), launched in 1995 aboard ERS-2, was fully operational till 2003.

1.9.2.6 MOS (Modular Optoelectronic Scanner)

German sensor MOS was launched onboard polar sun-synchronous (Indian Remote Sensing) IRS - P3 satellite on March 1996 with a long gap of around 10 years after the lifetime of CZCS. It was the second mission dedicated to cater the needs of ocean colour community. The MOS sensor had three spectrometers of which the MOS-A sensor was meant for the detection of aerosol layers. It was basically designed to measure radiance in O₂A absorption bands around 0.76 μm (in 4 narrow channels) and made use of the differential penetration of radiation in the atmosphere to separate aerosols in different layers. It could be used for stratospheric aerosol loading after volcanic eruptions. The atmospheric correction bands in ocean colour sensing sensor MOS-B had the capability of detecting the columnar AOD over the ocean. With a narrow swath of 200 km, both MOS A and B, performed global coverage only at a time period of 24 days, but with good ground resolution of 500m.

1.9.2.7 POLDER (Polarization and Directionality of the Earth Reflectances)

Measurements of radiance at one or more viewing angles in addition to the state of polarisation can give more handle to explore the complex properties of atmospheric aerosols [*Mishchenko and Travis, 1997*]. POLDER was conceived with this idea in mind. Launched onboard ADEOS in 1996, POLDER was a polarimetric instrument which, during its orbital motion, viewed the same target on the earth surface from different directions in three spectral channels in the range 0.44 – 0.86 μm . This instrument had a swath width of 220 km and a spatial resolution of 7 km x 6 km. Due to the solar panel failure, the ADEOS mission ended prematurely after eight months of its launch. But the mission was followed by POLDER 2 onboard ADEOS-II in 2002. The new sensor also worked for only five months. Main advantage of this sensor is that it could distinguish aerosols and molecules in the atmosphere from the earth's surface in terms of the polarization of TOA radiances at the short wavelengths [*Leroy et al., 1997*]. Through the bidirectional capability of POLDER, the microphysical properties of aerosols like effective radius and refractive index could be derived in addition to the AOD [*King et al., 1999; Goloub et al., 2001*]. A similar POLDER sensor launched in December 2004 on board the PARASOL (Polarisation and Anisotropy

of Reflectances for Atmospheric Sciences coupled with Observations from a Lidar) satellite operating at channels 0.44 – 1.02 μm is currently operational in its orbit.

1.9.2.8 OCTS (Ocean Colour and Temperature Scanner)

Launched in 1996, along with POLDER in ADEOS, OCTS was an ocean colour sensor, which could be successfully used for aerosol retrieval over the ocean [Zion, 1983]. The retrieval algorithm used the radiance measured in two channels at 0.66 and 0.86 μm to derive AOD and Angstrom exponent [Mukai *et al.*, 1998]. It had a primary resolution of 700 m and a swath of 1400 km, covering the entire globe in 3 days. Due to the failure of ADEOS spacecraft, this mission ceased after 8 months of successful operation.

1.9.2.9 SeaWiFS (Sea viewing Wide Field of view Sensor)

SeaWiFS is another cross-track scanning ocean color sensor developed by NASA launched onboard OrbView-2 in August 1997. SeaWiFS employs two near-infrared (0.765 and 0.865 μm) bands, to estimate the aerosol optical properties and extrapolate to visible channels [Gordon and Wang, 1994] for applying the atmospheric correction in the chlorophyll retrieval algorithm. With a swath width of 2801 km, it provides daily global coverage with a spatial resolution of 1.1 km at nadir. This sensor (like the OCTS), has the tilt capability for avoiding sun-glint. SeaWiFS regularly generates AOD at 0.865 μm and Angstrom exponent products over the global oceans.

1.9.2.10 OCM (Ocean Colour Monitor)

The first Indian satellite dedicated for oceanographic applications, IRS-P4 (Oceansat-1) launched in May, 1999 carried the OCM which is capable of estimating of AOD over the oceans. This sensor operates in eight narrow spectral channels from 0.41 to 0.86 μm and uses the atmospheric correction channels at 0.765 and 0.865 μm to derive AOD and Angstrom exponent [Das *et al.*, 2002]. With a swath width of 1420 km, it covers the entire globe once in every 2 days with a spatial resolution of 360 m. The follow up of Oceansat (i.e. Oceansat -2) launched very recently in September, 2009 also carries an OCM (OCM-2) to supplement OCM-I. The OCM-2 configuration is very similar to that of OCM-1 except for some minor shift in the two spectral channels mainly intended to provide a better parameterization of aerosols and suspended sediments.

1.9.2.11 MISR (Multi-angle Imaging Spectroradiometer)

The NASA instrument, MISR was launched on board the EOS Terra satellite in a polar sun-synchronous orbit in 1999. With nine CCD-based push broom cameras, it views the earth's surface in four spectral bands (0.44 – 0.86 μm channels) at nine angles, spread in the forward and aftward directions ($\pm 70.5^\circ$, $\pm 60.0^\circ$, $\pm 45.6^\circ$, and $\pm 26.1^\circ$) along the flight path within a few minutes [Diner *et al.*, 1998], thereby under almost the same atmospheric conditions. The wide range of along track view makes it feasible to retrieve aerosol over the ocean as well as over the land including the bright desert surfaces and the glint regions over the oceans which would otherwise be masked for mono-directional instruments [Diner *et al.*, 1998; Martonchik *et al.*, 1998]. It is one among the new instruments unique with a combination of high spatial resolution (275 m - 1.1 km) and high calibration accuracy [Diner *et al.*, 1998]. MISR retrieves AOD, Angstrom exponent and aerosol type at 17.6 km spatial resolution. The data obtained from sampling at different scattering angles ranging from about 60° to 160° E in mid-latitudes, can be effectively used to extract information about particle size and shape [Kahn *et al.*, 1998; Kalashnikova and Kahn, 2006; Chen *et al.*, 2008]. Evaluation studies have shown that the 2/3 of the MISR-retrieved AOD values fall within ± 0.05 or 0.2τ of the AERONET for both land and dark water retrievals [Abdou *et al.*, 2005]. Because of a narrow swath of around 360 km, it accomplishes a full global coverage once in a week.

1.9.2.12 MODIS (Moderate Resolution Imaging Spectroradiometer)

Launched on board two different platforms; first on Terra in 1999 and later on Aqua in 2002, MODIS is a unique passive remote sensor with 36 channels that monitors aerosols over both the land and the ocean. These two satellites having a spatial resolution of 250-500 m covers almost the entire globe within a day. Out of its 36 spectral channels, seven are dedicated for aerosol retrieval. The major aerosol parameters retrieved are spectral AOD, Angstrom exponent, fine mode fraction, effective radius etc. More details of this sensor and its uniqueness are presented in Chapter 2.

1.9.2.13 SCIAMACHY (SCanning Imaging Absorption spectroMeter for Atmospheric CHartography)

SCIAMACHY is a spectrometer which flies on board ESA's ENVISAT (Environment Satellite) launched in March 2002. Operating in the wavelength range

between 0.24 and 2.38 μm [Bovensman *et al.*, 1999], the primary scientific objective of SCIAMACHY is the global measurement of various trace gases in the troposphere and the stratosphere. With the spatial resolution of 30 km x 60 km in the UV to visible channels, and 30 km x 240 km in the near-IR it takes around 6 days to cover the entire globe. This can provide Absorbing Aerosol Index (AAI) from its UV channels [de Graaf and Stammes, 2005].

1.9.2.14 GLI (Global Imager)

This sensor was launched along with POLDER 2 onboard ADEOS-2. It is an optical imager working in 36 spectral channels ranging from visible to IR wavelengths. The visible channels dedicated to ocean colour observations could also be used to detect aerosols. Having a wide swath of 1600 km, it produced global aerosol information with spatial resolutions 250 m and 1 km in different channels. Because of the early power failure of ADEOS-II, GLI could not succeed in achieving its mission objectives.

1.9.2.15 MERIS (Medium Resolution Imaging Spectrometer)

ESA's ENVISAT launched in 2002 carries on board the sensor, MERIS. The primary objective of this mission is oceanographic observations, but it also provides aerosol information over the ocean. The specialty about MERIS is that its 15 channels spread over the spectral range 0.40 – 1.05 μm are programmable in the central wavelengths and band widths (ranging from 0.00125 to 0.03 μm) by ground command [Kaufman *et al.*, 1997a]. This sensor has a swath width of 1150 km with a spatial resolution of 300 m allowing global coverage once in every 3 days [Rast *et al.*, 1999].

1.9.2.16 GLAS (Geoscience Laser Altimeter System)

Global profiling of aerosols with space borne Lidars started with the launch of GLAS on board the polar orbiting satellite, ICESat (Ice, Cloud and land Elevation Satellite) in 2003. GLAS consists of a non-scanning Nd:YAG lidar nominally operating in a nadir-viewing mode at 0.532 and 1.064 μm wavelengths [Spinhirne *et al.*, 2005]. It yields vertical profiles at 76.2 m resolution at every 172 m spacing along the orbit track. This pioneering effort for lidar in space could demonstrate the capability of detecting and discriminating multiple cloud layers, atmospheric boundary layer aerosols as well as elevated aerosol layers [Hart *et al.*, 2005; Spinhirne *et al.*, 2005]. Due to the problems related to the lasers

onboard, its operation is restricted to one month in an interval of 3 to 6 months, which is a limitation for uninterrupted data over long periods.

1.9.2.17 CALIPSO (Cloud-Aerosol Lidar and Infra-red Pathfinder Satellite Observations)

The lidar CALIOP (Cloud Aerosol Lidar with Orthogonal Polarization) is currently operational onboard the sun-synchronous satellite CALIPSO launched in April, 2006. This sensor uses Nd:YAG diode pumped laser in the visible (0.532 μm) and near IR (1.064 μm) wavelengths. CALIOP measures ‘attenuated aerosol backscatter profiles’ in the two wavelengths along with polarization in the visible wavelength [*Winker et al.*, 2003; 2007]. With the capability of depolarization measurements, CALIPSO can discriminate dust from other types of aerosols [*Liu et al.*, 2008]. The horizontal resolution of the sensor is about 333 m and vertical resolution is 30 - 60 m.

Global measurements from satellites have begun to improve the performance of aerosol models and hence the assessment of their radiative effects. However, a substantial reduction of uncertainties in the quantification of aerosol forcing is possible only through an integrated approach which must include measurements from ground networks, aircrafts, balloons and ships in addition to space-based observations [*Kaufman et al.*, 2002; *IPCC*, 2007; *Chin et al.*, 2009].

1.10 Radiative transfer in the atmosphere

When radiation passes through the atmosphere it gets attenuated as described by the Lambert – Beer’s law (Sect.1.7.1.2), which is the simplest form of radiative transfer. This expression is strictly valid when the optical depth is small and the effects of multiple scattering and surface reflectances can be neglected. A complete description of the passage of radiation in the atmosphere must include all the following processes [*Kidder and Vonder Haar*, 1995]:

- (a) Attenuation due to absorption in the atmosphere
- (b) Enhancement due to emission in the atmosphere
- (c) Attenuation due to scattering from the beam into other directions
- (d) Enhancement due to scattering from the other directions into the beam

Consider an amount of radiance L_λ (radiant energy per unit area per unit solid angle per unit wavelength interval) passing through a medium of length ds in the atmosphere [Fig.1.5]. The processes (c) and (d) described above are illustrated in this figure.

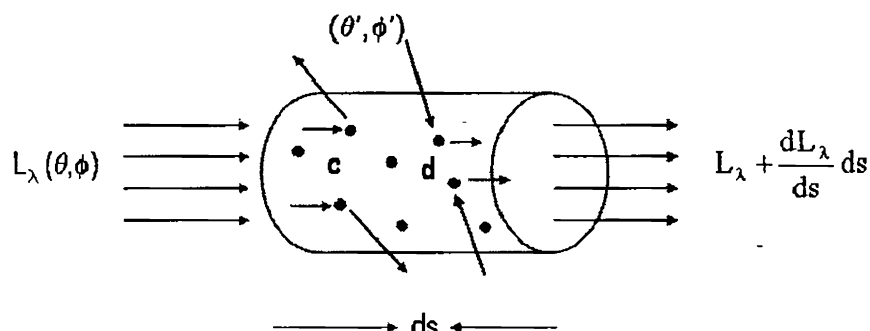


Fig.1.5. Schematic diagram showing the different processes taking place when a radiation enters and emerges through a medium.

Incorporating all the above four processes the rate of increment of L_λ per unit distance is given by the radiative transfer equation as [Kidder and Vonder Haar, 1995]

$$\frac{dL_\lambda}{ds} = -\beta_a L_\lambda + \beta_a B_\lambda(T) - \beta_s L_\lambda + \frac{\beta_s}{4\pi} \int_0^{2\pi} \int_0^\pi L_\lambda(\theta', \phi') P(\gamma) \sin \theta' d\theta' d\phi' \quad (1.32)$$

where $B_\lambda(T)$ is the Planck's function dependent on the temperature T (in °K) of the medium, (θ', ϕ') is the direction of other radiations which is scattered into the beam direction (θ, ϕ) (shown in Fig.1.5). $P(\gamma)$ is the scattering phase function for the scattering angle γ [angle between (θ, ϕ) and (θ', ϕ')] defined by

$$\cos \gamma = \cos \theta \cos \theta' + \sin \theta \sin \theta' \cos(\phi - \phi') \quad (1.33)$$

1.10.1 Aerosol sensing from space

Consider a beam of radiation upwelling through a thin atmospheric layer ' ds ' (between s_1 and s_2) on its way to the satellite at a zenith angle, θ_v [Fig. 1.6]. In the case of radiation in visible and near IR wavelengths (which interact more with aerosols) the Planck emission term [$B_\lambda(T)$] can be neglected (since its contribution in the atmosphere will be only in thermal IR) and the radiative transfer equation becomes,

entered into water and undergone multiple scattering and absorption by the water constituents. After properly accounting for the effects of Rayleigh scattering and water leaving radiance, AOD can be accurately derived from the sensor measured radiances in different wavelengths.

Over the land, the sensor detected radiance will be highly contaminated by the inhomogeneous reflectance of the land surface. Different sensors adopt different techniques like multi-spectral, multi-viewing or polarimetric capabilities to identify the contamination from underlying surface so as to eliminate its effect to retrieve AOD over land.

1.11 Transport of tropospheric aerosols

In the vicinity of aerosol sources particle properties are closely related to the nature of the sources. But, being light weight and air-borne, aerosols during their short residence time can travel long distances far away from their sources carried by wind and affect distant locations as well. Seasonal and regional meteorological conditions are the major factors which govern the extent of their dispersion. For instance, a mean wind velocity of $\sim 5\text{ms}^{-1}$ can carry an airborne particle in the atmosphere as much as to around 3000 km in a week [*Chin et al.*, 2009].

Though the dust sources are geographically confined, their influence can be felt over thousands of square kilometers around the source through long-range transport [*Duce*, 1995; *Gao et al.*, 2001; *Prospero et al.*, 2002]. Dust plumes generally cover large areas, and are more persistent than those associated with anthropogenic pollution [*Husar et al.*, 1997]. The areal extent of a desert and the intensity of winds decide the amount of dust mobilized and heights to which it is lofted. Of the aerosols generated over the desert only those with size less than $5\ \mu\text{m}$ are transported to large distances by prevailing winds [*Arimoto*, 2001; *Prospero*, 2003].

During the North African summer, when dust activity is maximum, large quantities of Saharan dust is carried across the Mediterranean to Europe and Middle East [*Moulin et al.*, 1998; *Kalvitis et al.*, 2007], across the Atlantic to the Caribbean [*Prospero and Nees*, 1986; *Prospero and Lamb*, 2003] and the southern United States [*Prospero et al.*, 1981; *Perry et al.*, 1997] and also to the Arabian Sea through higher altitude winds between 3 – 10 km [*Gobbi et al.*, 2000]. Space-borne remote sensing is the most efficient tool for

monitoring long-range transport of aerosols. Depicted in Fig 1.7(a) is an event of dust that originated in the Saharan desert on August 17, 2007 and transported over the Atlantic reaching Mexico by August 28, 2007, captured by CALIPSO. Similarly, dust particles from

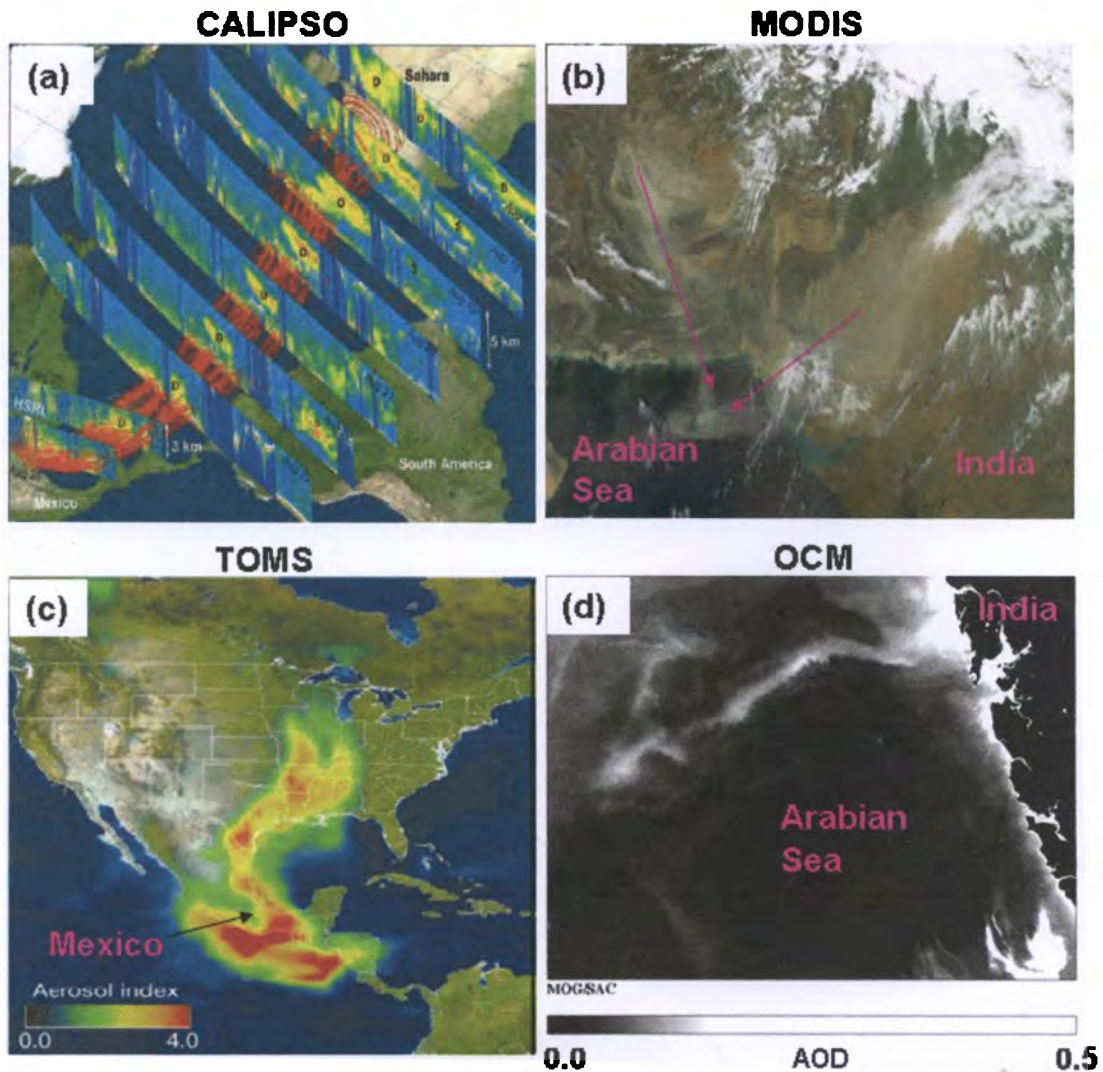


Fig.1.7 Dust originating from the Saharan desert on August 17, 2007 being transported to reach the Gulf of Mexico by August 28, 2007 [taken from Chin et al., 2009] (a) MODIS image showing dust transport from India, Pakistan and Afghanistan getting mixed up over the Arabian Sea on April 9, 2006 (b) Transport of heavy smoke to North America from large wild fires in Mexico on May 15, 1998 observed by TOMS [taken from Kaufman et al., 2002] (c) OCM image on December 13, 1999, showing an aerosol plume extending from the Mumbai coast towards the Arabian Sea [taken from Das, 2004]

the Asian continent are also frequently transported over to neighbouring countries and oceanic regions. Long-range transport of aerosols from West Asia and south-east Asia is known to significantly modify the aerosol properties over the Arabian Sea [Jha and Krishnamurti, 1999; Moorthy and Satheesh, 2000; Satheesh and Srinivasan, 2002]. A

MODIS image of April 9, 2006 showing the transport of dust from India, Pakistan and Afghanistan over to the Arabian Sea is presented in Fig.1.7(b). The high AOD over the Ganga basin in India, during the pre-monsoon and monsoon period, is partly attributed to the large influx of dust from the north western Indian desert (Thar), Pakistan, Arabia etc [Middleton, 1986; Dey *et al.*, 2004; El-Askary *et al.*, 2006].

Several studies have reported the long-range transport of anthropogenic aerosols. Smoke particles from forest fires in Canada are found at ~2- 3 km altitude over Greece [Formenti *et al.*, 2001] and those from California are observed over the north eastern US at altitudes below 7 km [Hoff *et al.*, 2005]. Fig.1.7(c) shows the transport of heavy smoke from wild fires in Mexico to North America on 15 May 1998 as observed by TOMS satellite. Frequently observed haze events over the Arctic region, where there are very limited local sources, are found to be associated with the long-range transport of polluted air from the southern latitudes [Quinn *et al.*, 2007; Tomasi *et al.*, 2007]. Haze layers due to the biomass burning over the Amazon basin are known to spread horizontally up to 1000 km and vertically from the surface to about 3 km in altitude [Heitzenberg *et al.*, 2002].

Pollution of the pristine oceanic environments over the northern Indian Ocean, Arabian Sea and Bay of Bengal by the aerosols advecting from the south and south east Asian regions are reported by many investigators on different occasions [Moorthy and Satheesh; 2000; Lelieveld *et al.*, 2001, Moorthy *et al.*, 2001; Ramanathan *et al.*, 2001; Quinn *et al.*, 2002; Rajeev *et al.*, 2004]. Figure 1.7(d) shows an OCM image on December 13, 1999 depicting an aerosol plume stretching several hundreds of kilometers into the Arabian Sea from the coast of the highly industrialized city of Mumbai [Das and Mohan, 2003]. The above are a few examples highlighting the efficiency of the space-borne sensors for the study of aerosol transport

1.12 Importance of vertical distribution of aerosols

Aerosols generated from the earth's surface due to various natural and anthropogenic processes are carried to higher altitudes through convection and turbulent diffusion, while the processes such as sedimentation, subsidence and deposition bring them to lower altitudes. The balance of these processes leads to a steady state vertical distribution of aerosols which can be modeled by an exponentially decreasing function of the form

$$n = n_0 \exp(-V_t z/K_t) = n_0 \exp(-z/H_a) \quad (1.36)$$

where n and n_0 are the number densities at the altitude z and at the surface respectively. V_t is the settling velocity, K_t is the turbulent diffusion coefficient and the ratio, $H_a = V_t/K_t$ is the aerosol scale height which can be different at different locations. This expression, however, does not account for the layer formation in the atmosphere arising from stratified turbulence [Parameswaran *et al.*, 1997].

Several investigators have attempted to study the altitude structure of aerosols using lidars at different parts of the globe [Devara *et al.*, 1994; Jayaraman *et al.*, 1995; Ansmann *et al.*, 1997; Parameswaran, 1998] and tried to model them with reasonable accuracy. In practise, the vertical structure may differ substantially from the exponential model [Eq.(1.36)] regionally and seasonally under the influence of a variety of atmospheric processes [Yu *et al.*, 2006]. For example, there are distinct differences between the vertical layers of dust over the Atlantic and the Mediterranean, even though both originate from the North African region [Hamonou *et al.*, 1999; Gobbi *et al.*, 2000; Di Sarra *et al.*, 2001; Koren *et al.*, 2003]. This is mainly due to the differences in the nature of convection as well as the features of the synoptic circulation [Barkan *et al.*, 2005].

Along with the optical properties and chemical composition, vertical distribution of aerosols is an important factor influencing their radiative effects. In the case of absorbing aerosols such as soot, the altitude of the aerosol layer as well as the altitude and type of clouds become important [Heitzenberg *et al.*, 1997; Satheesh, 2002]. But even in the case of those aerosols which are not absorbing or rather weakly absorbing the effect of layered structure cannot be neglected, if they are located above 7-8 km [Ding and Gordon, 1995]. Hence, along with gaining a better understanding on the spatial variation and temporal evolution of aerosol distribution, one needs to acquire information on the aerosol vertical profiles with a reasonably good accuracy.

1.13 Objectives of the present study

India is a unique region, strongly influenced by aerosols of different types, locally generated as well as brought by winds from near and far away places. Aerosols in this region display significant variations in their type and spatial distribution, depending on the season and geography of the location. Due to the high density of population and the associated anthropogenic activities, the Ganga Basin is a heavily polluted region where the occurrence of fog and haze are very frequent during the winter months. Long-range

transport of aerosols from the surrounding landmasses over to the adjoining oceanic regions, the Arabian Sea and the Bay of Bengal, give rise to significant aerosol loading over these environments. Additionally, the spatial distribution of aerosols also exhibits pronounced day-to-day variability. Synoptic scale daily aerosol information from MODIS and reanalysis global circulation fields from NCEP supported with ground-based measurements can efficiently be utilized to study the transport features and source activity of aerosols over these regions.

The present study mainly addresses a relatively less explored, but a very important facet of the aerosol science, that is, the dynamics of aerosol transport. The work presented in this compilation are for different specific cases of aerosol transport over the Ganga Basin, the Arabian Sea and the Bay of Bengal during different periods of the year. The strength of aerosol sources, spatio-temporal distribution of aerosols and their transport characteristics are examined employing the flux continuity equation, circulation variables like wind speed, convergence, vorticity, up/downdrafts and atmospheric relative humidity.

Chapter 2

Data and Methodology

2.1. Introduction

A study on the time evolution of synoptic scale distribution of aerosols essentially requires detailed information on aerosols over a large geographical region on a routine basis. Space borne remote sensing is the most effective means for this purpose. The Moderate Resolution Imaging Spectroradiometer (MODIS) onboard the Earth Observing Satellite (EOS) Terra and Aqua is a unique sensor with capabilities to attain nearly a full global coverage every day both over the land and the ocean. The specifications of MODIS for the aerosol measurement are unmatched by any other orbiting sensor at present.

The next most important parameter required for studying the aerosol transport is the atmospheric wind field. Reanalyzed wind field generated using the global circulation model by the National Centres for Environmental Prediction (NCEP) is highly reliable and well suited for this purpose. Wind over the ocean surface, measured by QuikSCAT (Quick Scatterometer) is sufficiently accurate to estimate the in-situ production of sea-salt aerosols. An appropriate combination of these data is effective in studying the role of dynamics that governs the aerosol distribution. Incorporating these into the aerosol flux continuity equation, proves to be an ideal technique to identify the major sources of aerosols and assess their strengths. This chapter provides a brief outline of the data sets used for the

present study and the methodologies adopted for addressing the aerosol transport dynamics and for the estimation of the strength of aerosol sources.

2.2 Aerosol properties from MODIS

2.2.1 Sensor details

MODIS sensor is the first of its kind which can characterize the spatial variation of aerosol properties over the land and ocean globally on a daily basis. The features of this sensor onboard the polar sun-synchronous satellites Terra (descending node, 10:30 am, equatorial crossing local time) launched in December, 1999 and Aqua (ascending node, 1:30 pm, equatorial crossing local time) launched in May, 2002, are far superior to those of any other space-borne aerosol sensor till date. From an altitude of 705 km, at an inclination of 98.2° and field of view $\pm 55^\circ$, the sensor's swath is about 2330 km. This makes it possible to cover almost the entire globe once in a day. Exact revisit over a particular region occurs once in every 16 days. Onboard calibrators are used to perform regular radiometric, spatial and spectral calibrations. Figure 2.1 shows the visible image (composite of red, green and blue wavelengths) of MODIS from Terra satellite on a typical day, April 19, 2000. This shows the capability of MODIS in acquiring almost full global coverage in a single day except for a few gaps between 30°N and 30°S .



Fig.2.1. True colour RGB image from MODIS sensor onboard Terra on April 19, 2000 showing its near daily global coverage capability.

MODIS operates at 36 spectral channels ranging from 0.42 to 14.24 μm , out of which seven (0.47, 0.55, 0.66, 0.86, 1.2, 1.6, 2.1 μm) are dedicated for aerosol retrieval. The primary resolutions of these seven bands range between 250 - 500m. The spectral stability of MODIS sensor is better than 0.002 μm . Further details of the spectral channels are summarized in the Table 2.1.

Table 2.1. Characteristics of MODIS channels used in aerosol retrieval. ρ is the spectral reflectance and $NE\Delta\rho$ is the 'Noise equivalent differential spectral reflectance' and SNR is the 'Signal-to-Noise Ratio' of the sensor.

Band /Channel	Wavelength band (μm)	Spatial Resolution (m)	$NE\Delta\rho$ ($\times 10^{-4}$)	SNR
1	0.620 – 0.670	250	3.39	128
2	0.841 – 0.876	250	3.99	201
3	0.459 – 0.479	500	2.35	243
4	0.545 – 0.565	500	2.11	228
5	1.230 – 1.250	500	3.12	74
6	1.628 – 1.652	500	3.63	275
7	2.105 – 2.155	500	3.06	110

In agreement with common references in aerosol literature the central wavelengths of the bands (or channels) 1 – 7 are identified respectively as 0.66, 0.86, 0.47, 0.55, 1.2, 1.6 and 2.1 μm . To retrieve aerosol parameters from MODIS data, independent algorithms are used over the ocean and over the land. The principal aerosol parameter retrieved by MODIS is the spectral AOD at six bands corresponding to 0.55, 0.66, 0.86, 1.2, 1.6, 2.1 μm over the ocean and at two bands corresponding to 0.47 and 0.66 μm over the land. The wide spectral coverage of the sensor provides an opportunity to determine different aerosol parameters such as the spectral optical depth, the fine mode fraction (FMF), the angstrom exponent, the effective radius and the column integrated mass concentration. The parameter FMF is specified for 0.55 μm which is the fraction of AOD contributed by the fine (small) mode particles to the total AOD, where fine mode and coarse mode comprise of particles with effective radii in the ranges, 0.1 – 0.25 μm and 1 – 2.5 μm respectively. Over the land, Angstrom exponent is derived from the AODs at 0.47 and 0.66 μm wavelengths while over

the ocean, two Angstrom exponents are derived; one using the wave lengths 0.55 and 0.86 μm and the other using 0.86 and 2.1 μm .

2.2.2 Inversion algorithms

Details of the aerosol retrieval algorithm over the land and the ocean are documented by *Kaufman et al.* [1997b] and *Tanre et al.* [1997]. The basic formulation of the retrieval method has not changed since its initial inception except that it has been upgraded [*Levy et al.*, 2003; *Remer et al.*, 2005; 2008] a few times by incorporating appropriate changes in the aerosol models, surface reflectance characteristics and radiative transfer computations. These changes could refine the algorithm to a great extent. The MODIS data are classified into ‘collections’, where the collection number corresponds to data produced by a definite version of the algorithm. The evaluations of Collection 002 (C002) and Collection 003 (C003) products [*Chu et al.*, 2002; *Remer et al.*, 2002] led to the generation of Collection 004 (C004) with a few improvements in this version of the algorithm. A comprehensive evaluation of regional and global C004 aerosol products [*Remer et al.*, 2005] resulted in a complete overhaul of the retrieval algorithm over the land and a few upgradings for the retrieval over the ocean incorporated into the Version 5.2 that forms the C005 products.

Each MODIS pass is split into individual scenes called ‘granules’, containing measurements for an interval of 5 minutes. Before processing, the calibrated and geolocated radiances in each granule (termed the Level 1B products) are first organized into nominal 10 km \times 10 km boxes, each corresponding to 20 by 20 pixels in the case of 500 m resolution channels. Reflectances in channels with 250 m resolution are degraded to 500 m resolution and are also organized into 10 km \times 10 km boxes. Each of the 20 by 20 (= 400) pixels in the box is first checked for cloudiness, snow/ice or water, using MODIS cloud mask (MOD/MYD35) which contains all the masking information. Ocean algorithm is implemented only if all the pixels in the box are identified as water otherwise the land algorithm is followed. Note that the quality of aerosol retrieval along the coast will be rather poor as the domain box considered in this case will contain pixels over water as well as over the land.

2.2.1 Algorithm over the land

The reflectance measured at the top of the atmosphere (TOA) is a function of all the successive orders of interaction within the coupled surface-atmosphere system. According to *Kaufman et al.* [1997b], this can be approximated as

$$\rho_{\lambda}^* (\theta_s, \theta_v, \phi_d) = \rho_{\lambda}^a (\theta_s, \theta_v, \phi_d) + \frac{F_{\lambda} (\theta_s) T_{\lambda} (\theta_v) \rho_{\lambda}^s (\theta_s, \theta_v, \phi_d)}{1 - s_{\lambda} \rho_{\lambda}^s (\theta_s, \theta_v, \phi_d)} \quad (2.1)$$

where ρ_{λ}^a is the ‘atmospheric path reflectance’, F_{λ} is the ‘normalized downward flux for zero surface reflectance’, T_{λ} is the ‘upward total transmission’ into the satellite, s_{λ} is the ‘atmospheric backscattering ratio’ and ρ_{λ}^s is the ‘angular surface reflectance’, all corresponding to the wavelength, λ . These are functions of solar zenith angle, satellite zenith angle and relative azimuth angle (azimuth difference between solar incident and satellite viewing directions) represented here as θ_s , θ_v and ϕ_d respectively. All the terms in Eq.(2.1), except surface reflectance, are functions of aerosol type and its concentration. A ‘look-up-table’ (LUT) is generated through simulation of the satellite detected radiances for a range of aerosol and surface properties. The TOA reflectance is computed for seven aerosol loadings ($\tau = 0, 0.25, 0.5, 1.0, 2.0, 3.0, 5.0$), nine solar zenith angles (between 0.0° and 66.0°), 16 sensor zenith angles (between 0.0° and 66.0°) and 16 relative azimuth angles (between 0.0° and 180.0°). For aerosols, the algorithm assumes a fine (spherical) particle dominated model and a coarse (spheroid) particle dominated model, each comprising of multiple log normal size distribution combined with proper weightage, to represent the ambient aerosols over the target. The algorithm works by comparing the satellite observed radiances with the computed radiances in the LUT to retrieve the aerosol conditions which mimics best, the observed radiation field.

2.2.2.1.1 Recent modifications in the land algorithm

Evaluation of C004 algorithm with measurements from 132 Aerosol Robotic Network (AERONET) stations located at different parts of the globe showed very good agreement in most of the cases. However, the retrieved AOD showed a systematic bias which varied from place to place over the land [*Remer et al.*, 2005]. At many places the bias was positive when the AOD values were relatively low and negative when the AOD

values were high [Ichoku *et al.*, 2003; 2005; Levy *et al.*, 2005]. Moreover, the FMF retrieved over the land showed significant deviations in many cases. These problems indicated the need of incorporating region and season specific refinements in surface reflectance and aerosol optical properties to improve the aerosol retrieval. For certain viewing and solar illumination geometries, neglecting the effect of polarization in the radiative transfer calculation was also found to be a source of error in the estimated TOA reflectance. This can lead to discrepancies greater than 10% in the retrieved values of AOD [Levy *et al.*, 2004].

In the MODIS C005 algorithm, a basic change is incorporated in the parameterization of land surface reflectance. Besides, a vector radiative transfer code, RT3 [Evans and Stephens, 1991] is implemented in the generation of the LUT instead of the scalar code used in C004 and the aerosol scattering phase functions are calculated using MIEV Mie code [Wiscombe *et al.*, 1980] or the T-matrix kernel code [Dubovik *et al.*, 2002b; 2006] depending on the spherical and spheroidal model for the aerosols. Further, the Rayleigh optical depth which was assumed same everywhere as at the sea level, is corrected for the elevation of the surface [Fraser *et al.*, 1989]. In addition to these modifications in the algorithm, the sensor calibration coefficients are also updated in C005.

2.2.2.1.2 Parameterization of the land surface reflectance

Up to the C004 algorithm, the retrieval philosophy of MODIS over the land, had assumed aerosols to be transparent at 2.1 μm channel over vegetated surfaces which appear darker in the mid-IR wavelengths. Based on observations over vegetated and dark soil surfaces, Kaufman and colleagues [Kaufman *et al.*, 1997b; Kaufman *et al.*, 1997c] had arrived at the following relations between the surface reflectances in different wavelengths:

$$\rho_{0.47}^s = 0.25 \rho_{2.1}^s \quad \text{and} \quad \rho_{0.66}^s = 0.5 \rho_{2.1}^s \quad (2.2)$$

where ρ_{λ}^s denotes the surface reflectance at the wavelength λ

Later, after extensive validations of MODIS derived AOD [Chu *et al.*, 2002; Remer *et al.*, 2002; Levy *et al.*, 2005] and surface reflectance measurements in the visible (VIS) and short wave IR (SWIR) [Gatebe *et al.*, 2001], it was observed that the ratio VIS/SWIR vary according to the surface type, scattering geometry and vegetation of the surface

expressed in terms of NDVI_s (Normalised Difference Vegetation Index) [Gatebe *et al.*, 2001; Remer *et al.*, 2001; Levy *et al.*, 2007]. NDVI_s is defined as

$$\text{NDVI}_s = \frac{(\rho_{1.2}^m - \rho_{2.1}^m)}{(\rho_{1.2}^m + \rho_{2.1}^m)} \quad (2.3)$$

where $\rho_{1.2}^m$ and $\rho_{2.1}^m$ are MODIS measured reflectances in 1.2 and 2.1 μm channels respectively which are not very much influenced by the aerosols.

Values of NDVI_s > 0.6 correspond to dense vegetation while NDVI_s < 0.2 indicates sparse vegetation. An increase in NDVI_s indicates increase in the density of vegetation near the surface. Thus the values of $\rho_{0.66}^s$ and $\rho_{0.47}^s$ used in C005 algorithm, are modified as functions of $\rho_{2.1}^s$, NDVI_s and scattering angle γ , defined as

$$\rho_{0.66}^s = f_1(\rho_{2.1}^s, \text{NDVI}_s, \gamma) = \rho_{2.1}^s \times \text{slope}_{0.66/2.1} + \text{y int}_{0.66/2.1} \quad (2.4)$$

$$\rho_{0.47}^s = f_2(\rho_{0.66}^s) = \rho_{0.66}^s \times \text{slope}_{0.47/0.66} + \text{y int}_{0.47/0.66}$$

where

$$\begin{aligned} \text{slope}_{0.66/2.1} &= \text{slope}_{0.66/2.1}^{\text{NDVI}_s} + 0.002\gamma - 0.27, \\ \text{y int}_{0.66/2.1} &= 0.00025\gamma + 0.033, \\ \text{slope}_{0.47/0.66} &= 0.49, \\ \text{y int}_{0.47/0.66} &= 0.005 \end{aligned} \quad (2.5)$$

where in turn

$$\begin{aligned} \text{slope}_{0.66/2.1}^{\text{NDVI}_s} &= 0.48; \text{ for } \text{NDVI}_s < 0.25, \\ \text{slope}_{0.66/2.1}^{\text{NDVI}_s} &= 0.58; \text{ for } \text{NDVI}_s > 0.75, \\ \text{slope}_{0.66/2.1}^{\text{NDVI}_s} &= 0.48 + 0.2(\text{NDVI}_s - 0.25); \\ &\text{ for } 0.25 \leq \text{NDVI}_s \leq 0.75 \end{aligned} \quad (2.6)$$

2.2.2.1.3 Inversion procedure

The C005 land algorithm combines fine and coarse particle dominated models to match with the sensor detected spectral reflectance. By simultaneously inverting aerosol

and surface information in the three channels 0.47, 0.66 and 2.12 μm , three output parameters; τ and FMF (η) at 0.55 μm and the surface reflectance $\rho_{2.12}^s$ are derived. It has been shown by *Remer et al.* [2005] that η can be used to express the TOA spectral reflectance (ρ_{λ}^*) as a weighted sum of the spectral reflectances from a combination of fine (ρ_{λ}^{*f}) and coarse (ρ_{λ}^{*c}) dominated aerosol models in the form

$$\rho_{\lambda}^* = \eta \rho_{\lambda}^{*f} + (1 - \eta) \rho_{\lambda}^{*c} \quad (2.7)$$

where ρ_{λ}^{*f} and ρ_{λ}^{*c} are composed of surface reflectance and atmospheric path reflectance [as described by Eq. (2.1)] of separate aerosol models. These parameters are defined as

$$\rho_{\lambda}^{*f} = \rho_{\lambda}^{\text{af}} + \frac{F_{\lambda}^f T_{\lambda}^f \rho_{\lambda}^s}{(1 - s_{\lambda}^f \rho_{\lambda}^s)} \quad (2.8)$$

$$\rho_{\lambda}^{*c} = \rho_{\lambda}^{\text{ac}} + \frac{F_{\lambda}^c T_{\lambda}^c \rho_{\lambda}^s}{(1 - s_{\lambda}^c \rho_{\lambda}^s)}$$

where $\rho_{\lambda}^{\text{af}}$ and $\rho_{\lambda}^{\text{ac}}$ are the atmospheric path reflectances for the fine mode and coarse mode aerosols, F_{λ}^f and F_{λ}^c are normalized downward fluxes for zero surface reflectance, T_{λ}^f and T_{λ}^c represent upward total transmission in the satellite field of view, s_{λ}^f and s_{λ}^c are atmospheric backscattering ratios. In the retrieval procedure the value of η is varied in discrete steps of 0.1 from -0.1 to 1.1 . The details of the procedure are described by *Levy et al* [2007].

2.2.2.1.4 Correction for Rayleigh optical depth

In the C005 algorithm the Rayleigh optical depth is computed considering the elevation of the surface [*Dutton et al.*, 1994; *Bodhaine et al.*, 1999] as,

$$\tau_{R,\lambda} = 0.00877 \lambda_p^{-4.05} \quad (2.9)$$

In the computation of $\tau_{R,\lambda}$ the surface elevation z is incorporated in Eq. (2.9) through λ_p using the expression [Fraser *et al.*, 1989],

$$\lambda_p(z) = \lambda \exp (z/34) \quad (2.10)$$

where λ is the true wavelength of the desired channel.

Combining Eq.(2.9) and (2.10), the Rayleigh optical depth is estimated in the algorithm as

$$\tau_{R,\lambda} = 0.00877[\lambda \exp (z/34)]^{-4.05} \quad (2.11)$$

2.2.2.1.5 Inversion procedure for dark pixels

The reflectance data in the 400 pixels encompassed over a domain of 10 km \times 10 km [described in Sect. (2.2.2)] is screened based on the value of surface reflectance for each pixel. Dark pixels are those with dense vegetation for which the value of $\rho_{2.1}$ will be small while for the pixels with unvegetated and partly vegetated surface the value of $\rho_{2.1}$ will be large. With this assumption only those pixels which satisfy $0.01 < \rho_{2.1} < 0.25$ are considered for deriving the aerosol parameters over the land. In order to reduce the possible cloud and surface contaminations, the darkest 20% and brightest 50% of the pixels in the 0.66 μm band are also discarded. After this, if the number of pixels remaining is 12 or more, the average of the reflectances at 0.47, 0.66, 2.1 and 1.2 μm channels and the NDVI_s are computed. Depending on the number of the screened in pixels, a Quality Assurance Confidence (QAC) value between 0 and 3 is assigned for each box. In the algorithm, the fine dominated aerosol model is selected based on the geography and season at the respective region while the coarse dominated model (dust) is always kept fixed. The fine mode (spherical) model include either of the three models viz ‘absorbing/heavy smoke’, ‘neutral/generic’ and ‘non-absorbing/urban-industrial’ depending on the case applicable with appropriate single scattering albedos, refractive indices and scattering phase functions [Remer *et al.*, 2006; Levy *et al.*, 2007].

The values of the parameters ρ^a , F, T and s for fine as well as coarse models are interpolated from the LUT for the solar illumination and sensor viewing angles corresponding to seven values of AOD (0, 0.25, 0.5, 1.0, 2.0, 3.0 and 5.0) indexed at 0.55 μm . The algorithm then solves for $\tau_{0.55}$, and $\rho^s_{2.12}$ for each of the 13 values of η ranging

from -0.1 to 1.1 in interval of 0.1, to match exactly the MODIS measured reflectances at 0.47 μm ($\rho_{0.47}^m$) and 2.1 μm ($\rho_{2.1}^m$) with those obtained from the LUT ($\rho_{0.47}^*$, $\rho_{2.1}^*$) [Remer *et al.*, 2005; Levy *et al.*, 2007]

$$|(\rho_{0.47}^* - \rho_{0.47}^m) / \rho_{0.47}^m| = 0 \quad (2.12)$$

$$|(\rho_{2.1}^* - \rho_{2.1}^m) / \rho_{2.1}^m| = 0$$

The final solution for $\tau_{0.55}$ and $\rho_{2.1}^s$ is arrived at iteratively using different values of η such that the error ε defined by,

$$|(\rho_{0.66}^* - \rho_{0.66}^m) / \rho_{0.66}^m| = \varepsilon \quad (2.13)$$

is reduced to a minimum value.

2.2.2.1.6 Inversion procedure for brighter pixels

If the number of screened in pixels is less than 12 in the above procedure, the domain is considered to be less vegetated and the pixels within the box are too bright to support the standard retrieval procedure for darker pixels. In this case, the upper limit of $\rho_{2.1}^m$ is relaxed to increase as a function of slant path as

$$0.25 < \rho_{2.1}^m < 0.25G < 0.40 \quad (2.14)$$

where $G = 0.5 ((1/M_v) + (1/\sqrt{M_0}))$, $M_v = \cos(\theta_v)$ and $M_0 = \cos(\theta_s)$ represents the slant path of radiation.

According to this criterion, as the path traversed by the radiation increases, more energy is scattered from the atmosphere, and the contribution from the surface reflectance becomes less significant. This is especially true at the 0.47 μm channel where atmospheric signal is maximum and the surface is very dark. For this reason this alternative path of inversion retrieves aerosol only in the 0.47 μm channel [Remer *et al.*, 2005]. If a minimum number of 12 pixels satisfying the above condition is available in the domain, this inversion procedure for the brighter pixels is followed. Otherwise the procedure ends with no retrieval. In this case, the Quality Assurance Confidence (QAC) is set 0, indicating that data quality is 'poor'.

Because of the greater retrieval uncertainty over these brighter surfaces as well as due to the fact that the retrieval is made only in one wavelength (unlike the case over the darker pixels), a simple ‘continental model’ is used for the retrieval purpose. The AOD and flux are derived from the LUT for 0.47 μm and are then extrapolated to 0.55 and 0.66 μm using the spectral dependence of the continental model [Remer *et al.*, 2005]. The same VIS to SWIR reflectance relation [given in Eq.(2.4) to (2.6)] used in the earlier method is assumed for this case also and the aerosol properties are indexed to 0.55 μm . Over and above, since a single spheroid aerosol model is used for retrieval, the first term of Eq.(2.7) alone (i.e., $\eta = 1.0$) is used in this case. The primary products derived are $\tau_{0.55}$ and $\rho_{2.1}^s$ [Levy *et al.*, 2007].

2.2.2.2 Algorithm over the ocean

Aerosol retrieval algorithm over the ocean employs six MODIS spectral channels (i.e. all except channel 3 in Table.2.1) to derive aerosol properties only under cloud free [Ackerman *et al.*, 1998; Martins *et al.*, 2002], glint free and sediment free [Li *et al.*, 2003] conditions. The 400 pixels, after being screened for clouds, glint and sediment, are sorted in ascending order to avoid the darkest and brightest 25% pixels to eliminate the possible residual clouds, glint and cloud shadow effects. The retrieval algorithm will proceed only if there are at least 10 good pixels at 0.86 μm channel within the 10 km \times 10 km domain. A LUT generated using the radiative transfer code by Ahmad and Fraser [1982] consists of TOA reflectances at six wavelengths computed by incorporating the sun glint effect [Cox and Munk, 1954], reflection by white caps [Koepke, 1984] for a surface wind speed 6 ms^{-1} and a Lambertian reflectance from under water scattering. The water leaving radiance is assumed to be negligible in all the wavelengths except 0.55 μm for which a fixed value of 0.005 is assumed. The LUT further adopts a bimodal lognormal distribution function for aerosol size distribution with nine basic modes including ‘four’ fine modes and ‘five’ coarse modes combined with a weighting parameter (η) which is the FMF such that,

$$\rho_{\lambda}^{\text{LUT}} = \eta \rho_{\lambda}^{\text{f}} + (1 - \eta) \rho_{\lambda}^{\text{c}} \quad (2.15)$$

The LUT is computed for the 20 combinations of fine mode and coarse mode for 6 AOD values (0, 0.2, 0.5, 1.0, 2.0 and 3.0), 9 solar zenith angles (between 6.0° and 72.0°),

16 satellite zenith angles (between 0.0° and 72.0°) and 16 relative sun/satellite azimuth angles (between 0.0° and 180.0°) for a total of 2304 angular combinations. For each of the 20 combinations the inversion finds the pair of $\tau_{0.55}$ and η that minimizes the deviation defined as,

$$\Delta = \sqrt{\frac{\sum_{\lambda=1}^6 N_{\lambda} \left(\frac{\rho_{\lambda}^m - \rho_{\lambda}^{\text{LUT}}}{\rho_{\lambda}^m - \rho_{\lambda}^{\text{ray}} + 0.01} \right)^2}{\sum_{\lambda=1}^6 N_{\lambda}}} \quad (2.16)$$

where N_{λ} is the sum of good pixels at wavelength λ , ρ_{λ}^m is the MODIS measured reflectance at λ , $\rho_{\lambda}^{\text{ray}}$ is the reflectance contributed by Rayleigh scattering and $\rho_{\lambda}^{\text{LUT}}$ is that provided in the LUT. A fixed value of 0.01 is included in this equation to prevent division by zero for longer wavelength under clean conditions [Tanre et al., 1997]. The $\rho_{0.87}^{\text{LUT}}$ is made to fit exactly with the measured reflectance at this wavelength, as this channel is least affected by variability in water leaving radiance but exhibits strong influence by aerosols. Best fits to other five wavelengths are arrived at using the relation Eq.(2.16). The combination of the modes with accompanying $\tau_{0.55}$ and η that minimizes Δ , gives the best solution. The ‘average’ solution is the average of the solutions with $\Delta < 3\%$. If no solution has $\Delta < 3\%$, the average of three best solutions is taken.

To identify dust events over the glint, an additional check is performed in the inversion procedure. Heavy dust activity over glint shows a distinct spectral signature because of increased absorption at blue wavelength. Hence if glint angle is $< 40^\circ$, and $\rho_{0.47}/\rho_{0.66}$ is < 0.95 , it is identified as heavy dust and retrieval is done, instead of masking the (glint) pixel.

The theory and strategy of C005 aerosol retrieval over the ocean remains the same as that for C004 described above except for a change in the sea salt refractive index in the coarse aerosol model. The primary retrieved products of ocean algorithm are AOD and FMF. From these primary data, other products like effective radius, mass concentration etc. are derived [Remer et al., 2005].

2.2.3 Cloud screening in MODIS

Ackerman et al. [1998] and *Gao et al.* [2002] have developed an excellent cloud masking scheme for MODIS by making use of a combination of 14 wavelength bands involving about 40 different tests. These different tests confirm the elimination of all types of clouds including thick high clouds, thin clouds, low clouds, upper tropospheric thin clouds and cirrus. But as these tests are clear sky conservative (error towards more clouds), thick aerosol features could be misidentified as clouds. Later *Martins et al.* [2002] additionally implemented spatial variability test which further produce satisfactory difference between aerosols and clouds. Because of this specialized cloud masking scheme and high spatial resolution, MODIS retrieves aerosol properties near the clouds better than many other sensors.

2.2.4 Calibration of MODIS

The MODIS sensor has an efficient in-built system for performing the radiometric, spectral and spatial calibration of the instrument onboard. This system includes

1. Black Body (BB): Primary source for the calibration of thermal bands located between 3.5 μm and 14.4 μm
2. Solar Diffuser (SD): The source for the calibration of visible, near IR and short wave IR bands.
3. Solar Diffuser Stability Monitor (SDSM): A device which tracks changes in the reflectance of SD in reference to the sun, so that the changes in calibration source will not be incorrectly attributed to the instrument error.
4. Spectro-Radiometric Calibration Assembly (SRCA): This provides in-flight spectral, radiometric and spatial calibration.

Two additional calibration techniques used by MODIS are the viewing of the moon and the deep space. The advantage of "looking" at the moon is that it enables MODIS to view an object that is roughly the same brightness as that of the Earth. Like the on-board Solar Diffuser, the moon is illuminated by the sun. Besides, unlike the Solar Diffuser or the Earth, the moon reflectance is not expected to change over the lifetime of the MODIS mission. "Looking" at the moon provides a second method for tracking degradation of the Solar Diffuser. "Looking" at deep space provides a near zero signal condition, which will

is used as an additional point of reference for calibration (stars are too dim for MODIS to sense).

2.2.5 Levels of MODIS products

The aerosol products retrieved by processing Level 1B data (discussed in Section 2.2.2) at $10 \text{ km} \times 10 \text{ km}$ resolution (at nadir) are called the Level-2 products. Global composites of Level 2 granule products for a day, geometrically corrected and gridded to $1^\circ \times 1^\circ$ resolution for an earth based coordinate system are termed Level-3 daily products [Masouka *et al.*, 1998]. During the re-gridding, the data quality is ascertained by appropriately weighting the Level 2 data based on its quality flags. It should be noted that each grid square in a Level 3 product can contain multiple orbits and hence are not synchronous in time, but is a better representation of daily average. From Level 2, weekly and monthly Level 3 global products are also generated.

2.2.6 Uncertainties in MODIS retrieval

Extensive exercises for the validation of MODIS have been carried out using data from AERONET stations distributed over the globe. The expected error bars were within $\pm 0.03 \pm 0.05\tau$ over the ocean and $\pm 0.05 \pm 0.15\tau$ over the land [Remer *et al.*, 2005]. These errors, designated for $0.55 \mu\text{m}$ are assumed to be applicable to all other channels also. Retrieval results for C005 products over the ocean at $0.55 \mu\text{m}$ fall within the expected uncertainty 60% of the time. These results are similar to those reported for C004. While over the land, more than 72% of the observations are within the error (against the 68% in the case of C004). High values of bias encountered over the land reduced as much as $\sim 0\%$ for Terra and $\sim 7\%$ for Aqua (keeping in mind that the expected errors are higher than that over ocean). Over the ocean, even though the implementation of C005 did not show significant effect on the derived AOD, it reduced the positive bias associated with the FMF [Remer *et al.*, 2008].

In the vicinity of clouds (for cloud fraction $> 80\%$), there is a drastic increase in the measured AOD (almost double) both over the land and the ocean, most probably caused by the cloud contamination [Zhang *et al.*, 2005]. However, this condition occurs only 2%

times over the ocean and less than 1% times over the land. It could also be due to factors like 3-D effects [Wen *et al.*, 2006; 2007] and the increased humidity around clouds [Koren *et al.*, 2007; Remer *et al.*, 2008].

In the case of FMF, it does not have a fixed error attached to it. But it shows good correlations with AERONET measurements of fine aerosol weighting defined by O'Neill *et al.* [2003]. Large bias in FMF over the ocean reported by Kleidman *et al.* [2005] has now been reduced by improving the aerosol models used for the inversion in the new version of C005. Hence at present, this is in closer agreement with AERONET observations [Remer *et al.*, 2008]. As the FMF under low AOD conditions (AOD<0.2) is highly uncertain, it is not reported under such conditions. In general on an average, an uncertainty up to 30% can exist for MODIS derived FMF over the ocean and is higher in the case of naturally occurring aerosols like sea salt and mineral dust [Kaufman *et al.*, 2005; Kleidman *et al.*, 2005; Bellouin *et al.*, 2005]. The uncertainty of FMF over the land is still larger and hence it is suggested that the values should be used only for a qualitative analysis and that too on a global mean basis. Even though during some occasions the FMF values are closer to the expected ones, they cannot properly represent the transformation of one aerosol type to the other [Jethva *et al.*, 2007]. Hence FMF over the land could be used with caution after a thorough evaluation and validation. A better option for representing sub-micron sized aerosol contribution is fine AOD which is the product of FMF and AOD. The uncertainties associated with this are almost comparable to that of the AOD. This quantity can be used as an indicator for the anthropogenic contribution to the measured AOD [Kaufman *et al.*, 2005].

2.2.7 MODIS data used for the present study

As the present study involves an investigation on the day-to-day variations in the spatial distribution of AOD over a large domain comprising the Indian subcontinent and adjoining oceans, the Level 3 daily data at $1^\circ \times 1^\circ$ grid resolution from both Terra and Aqua satellites are used optimally. Gaps between the satellite passes and presence of clouds reduce the coverage of a satellite sensor. But in the case of MODIS, this can be improved considerably by combining data from Terra and Aqua. The inclinations of the tracks of these satellites on the day side are different and there is a time gap of around 3 hours

between their passes over a given location. Combining data from both the satellites, the difference in their inclination helps to reduce the gaps between the passes of each satellite. In addition to this, the movement of clouds during the time gap between the two satellites would reduce data loss due to clouds. Therefore, in order to achieve maximal spatial coverage and better representation of the daily aerosol properties, the data from Terra and Aqua are combined optimally. For doing this, the pixels are divided into three types in terms of data content: (i) those having data from both Terra and Aqua (ii) those having data from either Terra or Aqua (iii) those with data from neither. In the case of pixels having data from both the satellites, the mean is taken and for those having data from one satellite, that data is retained. The pixels with no data from either of the satellites are left blank. Figure 2.2 shows a typical example of MODIS derived AOD on March 20, 2006, over the Indian subcontinent and the surrounding oceanic areas (between 0° - 30° N and 40° - 100° E), from Terra and Aqua satellites separately and that obtained through optimal combination as described above. One can notice the considerable improvement in the spatial coverage achieved.

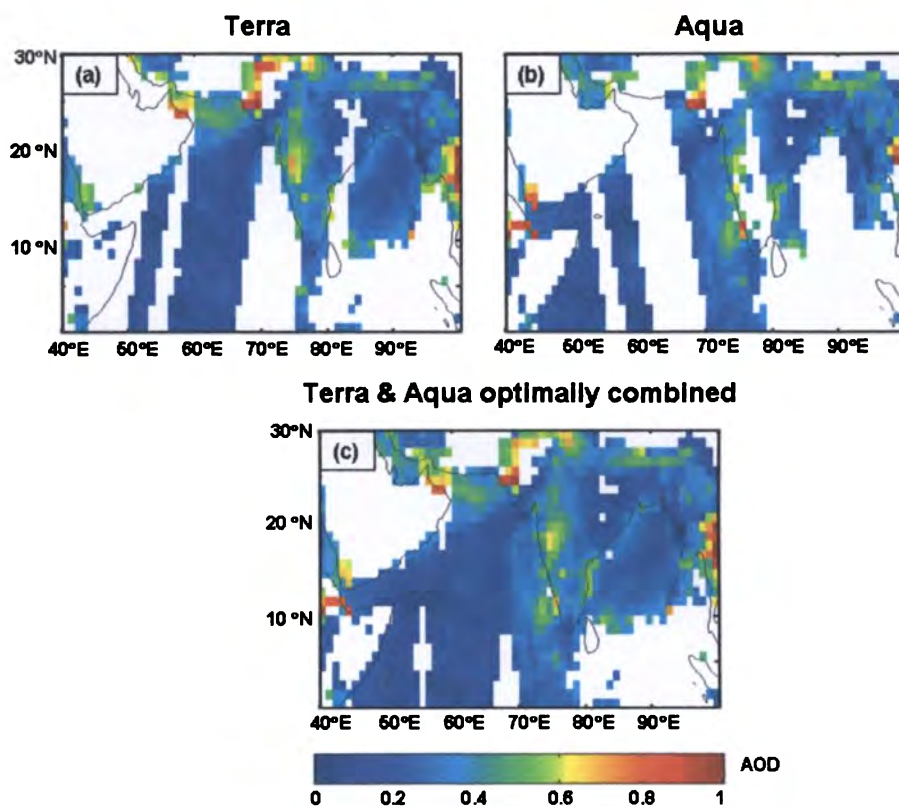


Fig.2.2. Spatial distribution of Level 3 AOD data from MODIS on board Terra (a) Aqua (b) and that obtained by the optimal combination of data from both Terra and Aqua (c) for March 20, 2006

2.3 Aerosol optical depth from surface measurements

Microtops II Sunphotometer (Solar Light Company, Inc., USA) is a multi-channel hand held instrument, that measures direct solar radiation the attenuation of which in different wavelengths is used to derive the AOD in those wavelengths. This instrument, being portable, is widely used for the measurement of AOD from ground.

2.3.1 Principle of Operation of Microtops II

Microtops-II measures solar irradiance in five user defined wavelength channels with a set of five accurately aligned optical collimators having a full field of view of 2.5°. A narrow-band interference filter (with a typical full width at half maximum band pass of 0.01 μm) and a photodiode optimized for the respective wavelength are fitted to each of these channels.

A sun target and pointing assembly is permanently attached to the laser aligned optical block of the instrument to ensure precise alignment with each of the optical channels. All the optical channels are oriented accurately towards the solar disk by focusing the sun exactly on the cross hairs screen provided on the instrument. Radiation entering the collimators is detected by a photodiode after passing through the interference filters. The anode current of the photodiode is proportional to the radiant power received. These signals are further amplified and converted to digital signals using a high resolution A/D converter. Microtops has built-in pressure and temperature sensors. A GPS (Global Positioning System) associated with this system provides the exact geographical coordinates as well as the time information for each of the observations. Using all these parameters recorded by the instrument, a built-in microprocessor computes AOD along with the column integrated concentrations of ozone or water vapor in real time and displays on an LCD screen. [Morys *et al.*, 2001; Porter *et al.*, 2001].

2.3.2 Estimation of AOD using Microtops II

The computation of AOD by the instrument from the ground reaching solar radiation in the visible to near IR wavelengths is based on the Lambert – Beer's law

$$V_{\lambda} = V_{0\lambda} \exp(-\tau_{\lambda} M_a) \quad (2.17)$$

where, V_λ is the signal measured at the wavelength, λ

$V_{0\lambda}$ is the extraterrestrial signal at wavelength, λ corrected for mean sun-earth distance

τ_{λ} is the total optical depth = $\tau_\lambda + \tau_{R\lambda} + \tau_{O3\lambda}$ where

τ_λ , $\tau_{R\lambda}$ and $\tau_{O3\lambda}$ are optical depths for aerosols, molecules and ozone respectively

M_a is the optical air mass

Optical air mass (M_a) is defined as the ratio of the actual path length traversed by the radiation as it reaches the detector to the corresponding vertical path length. This is expressed in terms of the solar zenith angle (θ_s) as

$$M_a = \sec \theta_s - 0.0019167 (\sec \theta_s - 1) - 0.002875 (\sec \theta_s - 1)^2 - 0.0008083 (\sec \theta_s - 1)^3 \quad (2.18)$$

For the estimation of AOD, Rayleigh and Ozone optical depths, $\tau_{R\lambda}$ and $\tau_{O3\lambda}$ defined (based on atmospheric models) through the following relation are to be subtracted from the total measured AOD by the instrument.

$$\tau_{R\lambda} = R_4 \exp [-z / (273/29.3)] \quad (2.19)$$

$$\tau_{O3\lambda} = \text{Ozabs} \times \text{DOBS}/1000 \quad (2.20)$$

where,

z is the altitude of the place of observation in meters

$$R_4 = 28773.6 \times \{R_2 \times (2 + R_2) \times \lambda^{-2}\}^2$$

$$R_2 = 10^{-8} \times \{8342.13 + 2406030 / (130 - \lambda^{-2}) + 15997 / (38.9 - \lambda^{-2})\}$$

Here, λ is the wavelength of radiation in microns [Edlén, 1966; Teillet, 1990; Bodhaine *et al.* 1999]

Ozabs is the Ozone absorption cross section, obtained from a LUT based on wavelength [e.g., Vigroux, 1953; Molina and Molina, 1986],

DOBS is the columnar Ozone amount in Dobson unit, extracted from a LUT based on latitude and date of observation [e.g., London *et al.*, 1976]

From Eq.(2.17), AOD (τ_λ) can be derived as

$$\tau_\lambda = [\ln(V_{0\lambda}) - \ln(V_\lambda)] / M_a - (\tau_{R\lambda} + \tau_{O3\lambda}) \quad (2.21)$$

$V_{0\lambda}$ is obtained by calibrating the instrument through the extrapolation of Langley plot ($\ln V_\lambda$ against M_a) [Shaw *et al.*, 1973] for zero air mass on clear days at a high altitude location.

2.3.3 Errors and precautions

1. Sufficient care has to be taken during the sunphotometer measurements to avoid cloud contamination. Any cloud patch close to the line of sight of the sun can lead to unreasonably high values in AOD. In fact, measurements should be restricted to maintain at least an angular distance of 30° between sun and the nearest cloud patch [Ichoku *et al.*, 2002].
2. The instrument should be pointed accurately towards the Sun such that the centre of solar disk exactly coincides with the centre of cross hairs. Capturing the Sun's image away from the optical axis increases AOD exponentially [Ichoku *et al.*, 2002].
3. The measurements must be made closer to the local noon to avoid optical distortions arising at larger solar zenith angles.
4. The quartz window of the instrument in the front side has to be cleaned periodically to avoid false measurements (unreal high values of AOD).
5. Being a hand held instrument, pointing accuracy is very critical, especially on moving platforms such as ships, which has been discussed extensively in Porter *et al.* [2001]. In such cases, it is advised to make 4-5 measurements continuously in quick succession and select the least value among them as the real optical depth. This is because pointing inaccuracies will always lead to decrease in the collected radiance thereby erroneously leading to an apparent increase in the measured AOD.
6. Sunphotometers have to be calibrated at regular intervals (once a year) and well cleaned before measurements to get accurate values of AOD.

With all these precautions, this instrument is expected to provide AOD with an accuracy of ± 0.03 .

2.4 NCEP reanalysis of meteorological fields

The National Centers of Environmental Prediction (NCEP) / National Center for Atmospheric Research (NCAR) are collaboratively working for a project called ‘reanalysis’ which produces a global record of atmospheric fields for the use of research and climate prediction communities. The basic aim of the project is to use a frozen state-of-art forecast system and execute assimilation of a large collection of data from 1957 onwards. The collection includes data from land surface measurements, rawinsonde, aircraft, satellite and all other possible measurements [Kalnay *et al.*, 1996].

NCEP/NCAR provides several meteorological fields at $2.5^\circ \times 2.5^\circ$ resolution for 17 atmospheric levels from 1000 hPa to 10 hPa. In order to investigate the effects of wind field on aerosols which are mainly confined within the lower troposphere, the data of the lowest seven levels (1000 – 400 hPa) are sufficient. Hence NCEP data of the lowest seven levels are used in the present analysis. The meteorological parameters from NCEP reanalysis used for the present study are the zonal, meridional and vertical components of vector wind and relative humidity.

2.5 Ocean surface wind from QuikSCAT

‘SeaWinds’ is a scatterometer housed in the NASA’s Quick scatterometer (termed QuikSCAT). The scientific objective of this sensor is to carry out high resolution, continuous, all weather measurement of near-surface winds over the ice-free global oceans. The name ‘quik’ is added to this sensor because this satellite was launched with a ‘quick’ planning in 1999 to fill the data gap of the NASA scatterometer (NSCAT), which lost its power in June 1997 while in orbit.

2.5.1 QuikSCAT sensor and measurement technique

QuikSCAT orbits at an altitude 803 km in a Sun-synchronous orbit inclined at 98.6° inclination and has a rotating dish antenna operating in the Ku-band (13.4 GHz) with two pencil beams sweeping the ground in two circles. The inner beam oriented at 40° (angle of incidence) and outer beam at 46° polarized horizontally and vertically respectively produce a wide swath of around 1800 km covering almost 90% of the global oceans in a single day. The centimeter scale or the capillary waves generated by the winds on the

ocean surface scatter back the radar power primarily through Bragg resonance modulated by the roughness of the surface. This scattered radiation received by the satellite is used for estimating the vector wind. The measurement geometry of the QuikSCAT is shown in Fig. 2.3

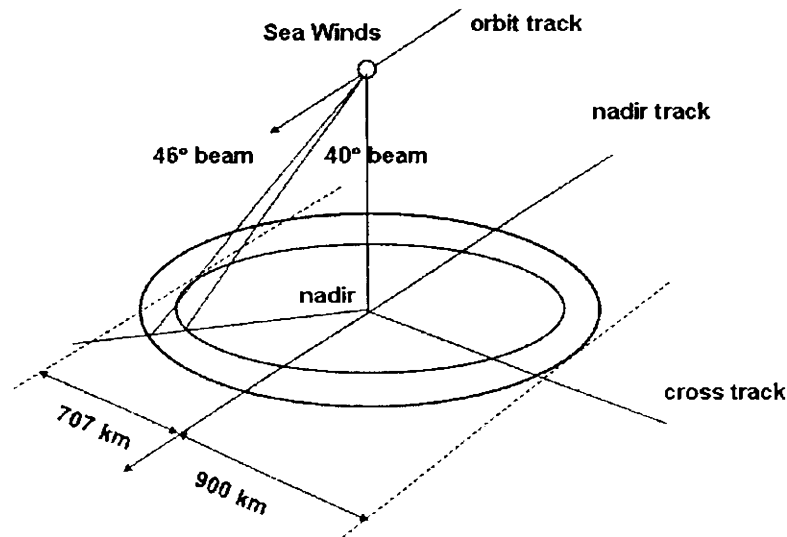


Fig.2.3. Measurement geometry of QuikSCAT scatterometer

The concept of pencil beam Scatterometry was introduced by *Kirimoto and Moore* [1985]. Because of the helical scan pattern swept out by the two pencil beams [as shown in Fig.2.4(a)] of the scatterometer, each measurement cell within the radius of the inner beam will be sampled in four directions: first by the outer beam (T1) followed by the inner beam, looking ahead of the space craft (T2) and later when the two beams look backwards, the inner beam scans first (T3) and the outer beam (T4) follows. The typical geometry of these four scans are presented in Fig.2.4(b). These multiple collated measurements from different directions can be used to determine wind speed and direction simultaneously [*Kramer*, 1994]. Most of the time, four wind solutions are found to be consistent with the observed backscatter at each measurement cell. From these, the absolute wind speed and direction at 10m height from the surface are derived using the 'Geophysical Model Function (GMF)'. These are empirical relations derived based on number of experiments for wide range of incidence angles, frequencies, polarization and azimuth angles. The GMF was first developed for NSCAT [*Wentz and smith*, 1999] and later modified to suit QuikSCAT [*Lungu*, 2001].

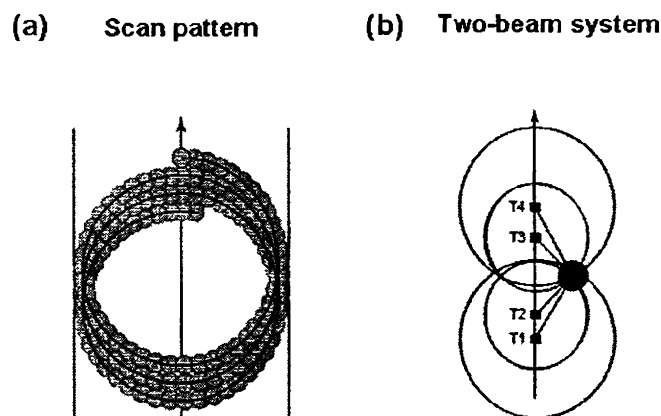


Fig.2.4 The helical scan pattern swept out by the QuikSCAT scatterometer (a) and two beam system which shows a single point being looked at from four different directions (T_1 , T_2 , T_3 and T_4) (b)

2.5.2 Retrieval uncertainties & difficulties

Maximum uncertainty in the QuikSCAT retrieval is when the wind speed is very low ($< 3 \text{ m/s}$), and the spatial variation in wind direction is high. At low wind speed, the backscattered signal will be too low to separate it from noise. For wind speeds in the range $3 - 20 \text{ ms}^{-1}$, the accuracy is within 2 ms^{-1} and in the range $20 - 30 \text{ ms}^{-1}$, it is within 10%. The wind direction can be measured within an uncertainty of 20° [Freilich, SeaWinds Algorithm Basis Theoretical Document]. The GMF tuned with buoy observations and weather forecast models is found to underestimate the wind speed when it is very large. Hence the ambiguity for wind speed $> 25 \text{ ms}^{-1}$ is large compared to that for the low winds [Hoffman and Leidner, 2005].

Rain also introduces contamination in the retrieved wind data as it affects the ocean surface roughness, and attenuates and scatters the radiation. Hence QuikSCAT cannot retrieve accurate ocean winds during moderate to heavy rain conditions. Hoffman and Leidner [2005] have shown that this condition arises when vertically integrated rain rate (estimated from SSM/I) exceeds 2 km mm hr^{-1} .

The data retrieved in the mid swath lying in the range 200 to 700 km on either sides of nadir will be sufficiently accurate since this region is viewed for maximum different viewing geometry. But the data from regions very near to nadir as well as far from the swath region are expected to be inferior in quality.

2.5.3 Details of wind data from QuikSCAT

For the present study, daily data of meridional and zonal components of the ocean surface winds gridded at $0.25^\circ \times 0.25^\circ$ resolution from QuikSCAT are used. Each data file contains individual data sets for both ascending and descending nodes of the satellite pass. Data from both these passes at every $0.25^\circ \times 0.25^\circ$ grid are optimally combined to represent the daily average value of wind at that location. This has been done similar to the case of combining data optimally from MODIS Terra and Aqua satellites, discussed in Sect.2.2.7.

2.6 Meteorological parameters influencing the aerosol properties

Atmospheric aerosols are highly heterogeneous in their spatial distribution and also show significant temporal variation. The wide range of aerosol generation mechanism, their varying strengths and their long range transport through atmospheric circulation are the influencing factors responsible for these spatio-temporal variabilities. The day-to-day variations in the spatial distribution of AOD through atmospheric circulation cannot be attributed entirely to wind speed and/or wind direction. It is also influenced by other features of wind such as wind convergence, vorticity and up/down drafts. In addition to these dynamical features of transport, the prevailing atmospheric relative humidity also plays an important role in determining the AOD at a particular location at a given time [Nair and Moorthy, 1998]. The influence of each of these parameters on AOD is detailed below.

2.6.1 Horizontal wind convergence

Wind field in lower atmosphere is not a well organized stream line flow. It is highly turbulent with speed and direction significantly varying from place to place depending on many atmospheric parameters as well as topography. This can lead to convergences and divergences in the wind field which varies with time. Being buoyant, aerosols are carried over long distances, up to thousands of kilometers from their sources depending on the nature of wind. During the transport, dynamical features of wind such as divergence and convergence can influence the spatial distribution of these aerosols. When there is a convergence in horizontal wind, the aerosols accumulate leading to an increase in the concentration even in the absence of sources. Similarly when there is a divergence aerosols

get dispersed very fast even in the presence of an intense aerosol source. The convergence of horizontal wind can be expressed as

$$\text{Wind convergence} = - \left(\frac{\partial u}{\partial x} + \frac{\partial v}{\partial y} \right) \quad (2.22)$$

where u and v are zonal and meridional components of the horizontal wind field. The positive and negative values indicate convergence and divergence respectively.

2.6.2 Vorticity

Another important parameter relevant to aerosol transport is the vertical component of wind vorticity. Locations of positive and negative vorticities and their strengths are indicators of pressure distributions in the atmosphere, which block and guide the flow of aerosols by the winds. Winds flow faster around localized strong pressure gradients. Thus spatial distribution of vorticity becomes very helpful in identifying the origin and transport pathways of aerosols. Vorticity is defined as

$$\text{Vorticity} = \frac{\partial v}{\partial x} - \frac{\partial u}{\partial y} \quad (2.23)$$

2.6.3 Vertical wind

Vertical component of wind influences the vertical distribution of aerosols. The up lift of aerosols to higher altitudes and their subsidence to lower altitudes are also governed by this component of vector wind. In several cases, the elevated aerosol layers in the atmosphere are formed as a consequence of change in the direction of the vertical wind.

In the NCEP reanalysis, the vertical wind is expressed in Pascal per second (Pas^{-1}) with positive and negative signs representing downdraft and updraft respectively. Note that if the vertical velocity is expressed in terms of ms^{-1} , the opposite will be the case.

2.6.4 Relative Humidity

The effect of RH on the aerosol optical properties are detailed in Chapter 1, Sect. 1.6.2. As the RH in the atmosphere increases water vapour condenses on the aerosol particles leading to a change in their size, density and refractive index thereby modifying

their optical properties. All these effects, lead to an increase in the aerosol extinction coefficient and hence, the AOD. Oceanic aerosols which consist mostly of salt particles, generally show high affinity towards water [Parameswaran and Vijayakumar, 1994]. Hence RH will have a substantial influence on the AOD over the oceanic environment. Hygroscopic growth of aerosols however, is found significant only when RH exceeds around 70% [Hanel., 1976; Parameswaran, 1996].

2.7 Investigation of aerosol source strength and continuity equation

The spatial distribution of aerosols is governed by source activities and features of prevailing circulation. Thus, in order to identify the actual role of sources, it is essential to eliminate the influence of wind field. For this, an analysis using an aerosol flux continuity equation is very effective. Using this the spatial distribution of sources can be derived and their strengths can be estimated.

2.7.1 Aerosol flux continuity equation

The dynamics of aerosol transport and generation /loss processes can be described using the aerosol flux continuity equation

$$\frac{\partial \beta}{\partial t} + \nabla \cdot [\beta \mathbf{V}] = s_0 \quad (2.24)$$

where β is the aerosol extinction coefficient, \mathbf{V} is the three dimensional vector wind and s_0 the strength of aerosol source which are in general, functions of the space co-ordinates and time (x, y, z and t). The aerosol parameter provided by the satellite is the columnar AOD which is related to β as

$$\tau(x, y) = \int_0^{\infty} \beta(x, y, z) dz \quad (2.25)$$

Integrating Eq.(2.24) over z ,

$$\frac{\partial \tau}{\partial t} + \frac{\partial}{\partial x} \left[\int_0^{\infty} \beta u dz \right] + \frac{\partial}{\partial y} \left[\int_0^{\infty} \beta v dz \right] = S(x, y, t) \quad (2.26)$$

here u and v are the zonal and meridional components of the wind and S is the column integrated net source strength. By incorporating the daily values of AOD (from MODIS) and the daily wind field at different atmospheric altitudes (from NCEP reanalysis) into this equation, the strength of aerosol source/sink can be estimated.

As the spatial resolution of NCEP wind field is $2.5^\circ \times 2.5^\circ$, MODIS derived AOD at $1^\circ \times 1^\circ$ resolution is first degraded to match the resolution of the winds. This degrading is performed by imposing the condition that the AOD values must be available over 60% of the area covered by the NCEP wind field grid. Otherwise, the grid is kept blank.

A time interval of one day is considered for the first term on the LHS of Eq.(2.26) which represents the change in AOD in each pixel from one day to the next. The second and the third terms together constitute aerosol flux divergence. The aerosol flux at different pressure levels are expressed through the product of aerosol extinction coefficient at those altitudes with the corresponding NCEP winds. Appropriate models for the altitude distribution of aerosol extinction are adopted (depending on the region and period of interest) based on available information.

In the present study, as the time resolution of AOD data is one day, the mean of the flux divergences for the two successive days are considered along with the day-to-day changes in AOD for solving Eq.(2.26). It should be noted that to compute the LHS of this equation, the AOD for a given pixel has to be available on the two successive days along with the condition that data from at least one adjacent pixel in the zonal and meridional directions should also be available (for estimating the flux divergence terms). In the divergence terms, the latitude and longitude grid sizes are converted to corresponding distances taking into account the earth's curvature. The vertical integration of the flux term is carried out over seven levels (from 1000 hPa to 400 hPa) following the standard Lagrangian interpolation scheme [Jain *et al.*, 1993] by dividing the entire altitude range into three sections with three sub-pressure levels in each.

On the RHS of the Eq.(2.26), S is the net aerosol generation expressed in terms of AOD change per day. This will include aerosol generation from all sources present (natural and anthropogenic) like wind blown dust, sea-salt particles, industrial exhaust, fuel/biomass burning etc., and loss due to removal processes such as dry/wet deposition, impaction, coagulation, diffusion, etc. The sign of the net source will determine the net change in aerosol loading at a particular location. If the value of net source is zero it suggests that the

aerosol generation is fully compensated by the prevailing loss processes, while positive value of S suggests that the aerosol generation is dominating the loss processes and negative value indicates that the loss process is dominating.

In the present study, the flux continuity equation is used to identify major sources of aerosol generation (with positive values of S) and to quantify their strength at different locations over the Indian subcontinent as well as over the adjacent oceanic regions. The use of the flux continuity equation in different study domains are explained in the following chapters.

2.8 Summary

This chapter mainly deals with different sources of data used for the present study (the transport dynamics of aerosols and its influence on the spatio-temporal distribution of aerosols over the Indian subcontinent and the adjoining oceans). The major database required for this study is the spatial distribution of AOD, aerosol size distribution, wind field and atmospheric relative humidity on a synoptic scale. The primary source of aerosol data is MODIS onboard Aqua and Terra satellites from which AOD and FMF are optimally combined to study the spatio-temporal variations. The details of MODIS data and algorithm used for inversion (from the observed upwelling radiance) are briefly described along with the assumptions involved as well as the sources and magnitude of possible errors. Before using the MODIS data it is to be validated (in each case) with ground based observations, for which Microtops II is used. The principle used in this measurement and its possible errors are also described. Synoptic wind field (on a daily basis) from NCEP reanalysis is used for studying the aerosol transport features. The details of NCEP data are briefly discussed. The ocean surface wind from QuikSCAT is used to examine the marine aerosol production over the oceanic regions. The measurement technique used in this space-borne sensor and the probable errors associated with the data are also briefly described. Finally, the wind variables used for studying the transport dynamics and the method adopted for evaluating the source strength using the flux continuity equation are described. These are implemented effectively for studying the spatio-temporal variation in aerosol properties, the results of which are detailed in subsequent chapters.

Chapter 3

Aerosol generation and transport over the Ganga Basin during Boreal winter: ISRO-GBP Land Campaign II

3.1 Introduction

The Indo Gangetic Plain (IGP) is a wide valley stretching along the north western India up to the Head Bay of Bengal covering a vast region from around 22° to 32° N in latitude, across 72° to 92° E in longitude. Occupied by the rivers Ganga, Yamuna and their tributaries, the Ganga basin (~ 22° - 29°N and 75° - 92°E) forms a major portion of IGP. It is a gigantic fluvial plain which makes it the largest agriculturally productive region in South Asia. This fertile land attracted dense human settlement which now amounts to more than 460 million. Uncontrolled urbanisation and industrialisation of this region lead to high levels of atmospheric pollution [*Ramanathan and Ramana, 2005; Prasad et al., 2006*]. Several studies in recent years, using satellite and ground-based measurements have shown heavy aerosol loading (AOD > 0.5) over the Ganga Basin, during the winter period [*Dey et al., 2004; Girolamo et al., 2004; Singh et al., 2004; Jethva et al., 2005*]. Persistent fog and haze has become a common feature in this region during the winter months. Figure 3.1 shows a true colour Terra image, on December 4, 2001 when intense fog was reported over many locations along the Ganga Basin resulting from the pollution over this area.

topography of the region, lead to confinement of aerosol particles in the valley [Girolamo *et al.*, 2004; Gautam *et al.*, 2007]. As the possibility of dust storm and burning of biomass is minimal during the winter, the heavy aerosol loading could be associated more with other anthropogenic activities [Niranjan *et al.*, 2006; Dey and Tripathi, 2007; Gautam *et al.*, 2007]. Winter season thus offers an ideal situation for the investigation of the properties of anthropogenic aerosols and the sources responsible for their production.

3.2 Land Campaign -II

A Land Campaign (LC-II) was organized under the Indian Space Research Organisation – Geosphere Biosphere Programme (ISRO-GBP) to characterize the physical and chemical properties of aerosols over the IGP. In this campaign, extensive measurements on aerosol properties were carried out from December 1 to 31, 2004 at eight fixed locations (Hisar, Delhi, Agra, Kanpur, Allahabad, Jaduguda and Kharagpur spread over the Ganga Basin and Nainital, a remote high-altitude station located in the central part of lower Himalayas) using a variety of ground-based instruments. These measurements include AOD, aerosol mass concentration, BC mass concentration, aerosol number size distribution and chemical compositions. Results from these observations confirmed high anthropogenic contribution in the aerosol loading over this region during winter [Niranjan *et al.*, 2006; Tare *et al.*, 2006; Dey and Tripathi, 2007; Nair *et al.*, 2007].

To estimate the actual source strength (rate of aerosol production) from the measured aerosol concentration over a region, the role played by transport should be properly accounted. The present work is mainly oriented to examine the generation and transport of aerosols over a confined geographical region, $20^{\circ} - 27.5^{\circ}$ N in latitude and $75^{\circ} - 87.5^{\circ}$ E in longitude (referred as the study domain hereafter). This is done using the aerosol flux continuity equation (described in Chapter 2, Sect. 2.7) by incorporating synoptic data of AOD from MODIS and the meteorological wind fields from NCEP reanalysis. Before proceeding to the main part of the work, the MODIS derived AOD is validated through a detailed inter-comparison with these measurements using ground based radiometer measurements from two fixed locations over this region.

3.3 Database

Microtops Sunphotometer was used to estimate the columnar AOD at Kharagpur from the measured direct solar irradiance at 1.02 μm . These observations were carried out at regular intervals (15 minutes) from 08:30 IST to 16:00 IST, by strictly following the procedures laid down for operating this instrument (see Chapter 2, Sect.2.3.3), subject to the sky conditions. Along with this, multi-spectral AOD measurements by radiometer at the Aerosol Robotic Network (AERONET) station at Kanpur also is used.

AERONET is a network of ground-based auto tracking solar radiometer (CIMEL Electronic CE-318 Sun-sky radiometers), distributed at different sites over the globe [Holben *et al.*, 1998, 2001; Eck *et al.*, 2005] installed by NASA. Most of the AERONET stations are programmed to operate at 15 minutes interval during the day at eight wavelengths: 0.34, 0.38, 0.44, 0.50, 0.675, 0.87, 0.94 and 1.02 μm (nominal wave lengths). From the measured solar irradiance at the above wavelengths, the radiometer computes spectral AOD with an accuracy of about ± 0.01 to ± 0.02 [Holben *et al.*, 1998, 2001].

The AOD data at 0.50 μm , obtained by the AERONET station at Kanpur (26.5°N, 80.4°E) and the Microtops measurements at 1.02 μm , from Kharagpur (22.3°N, 87.3°E) are used for a direct comparison and validation of MODIS derived AOD during the campaign period. All the measurements over a day from Microtops and AERONET are averaged to estimate the mean AOD for that day. This value of AOD is compared with the MODIS Level 3 AOD data optimally combined from Terra and Aqua (as explained in Chapter 2, Sect. 2.2.7).

To study the role of transport in aerosol loading at a particular location it is necessary to know the nature of prevailing synoptic circulation, as the mean life time of tropospheric aerosols is of the order of few days. Since the present study is mainly with the columnar aerosols (AOD) whose major contribution comes from lower altitudes, less than 10 km, the NCEP reanalysis winds from the first seven pressure levels (1000, 925, 850, 700, 600, 500 and 400 hPa) only are used for the analysis. From this, the circulation variables are estimated as detailed in Chapter 2, Sect. 2.6. The spatial pattern of these circulation variables along with the spatial maps of AOD are used for the study.

3.4 Comparison of MODIS derived AOD with ground measurements

AOD data obtained from AERONET station at Kanpur and that from Microtops measurements conducted at Kharagpur are used to examine the accuracy of MODIS data. The daily mean AOD at 0.55 μm from MODIS over a grid size of $1^\circ \times 1^\circ$ around the two locations are first adjusted (or normalized) to the wavelengths corresponding to the ground measurements. The spectral AOD values from MODIS at wavelengths 0.47, 0.55 and 0.66 μm are used to derive the angstrom exponent (α) by performing a least square fit between the logarithms of spectral AODs and wavelengths (Eqn.1.26, Chapter 1). Using this value of α , the MODIS derived AOD is normalized to the Microtops wavelength (at Kharagpur) and the AERONET wavelength (at Kanpur) using the relation

$$\tau_2 = \tau_1 (\lambda_2 / \lambda_1)^{-\alpha} \quad (3.1)$$

where τ_1 is the MODIS derived AOD at wavelength λ_1 (0.55 μm) and τ_2 is the estimated value of AOD at the desired wavelength λ_2 (1.02 μm for Kharagpur and 0.50 μm for Kanpur).

The normalized MODIS derived AOD values are then compared with the corresponding ground measurements. Figures 3.2(a) and (b) show respectively the time series of MODIS derived AOD adjusted to appropriate wavelengths along with Microtops measurements at Kharagpur and with the AERONET measurements at Kanpur. The MODIS derived AOD agree fairly well with the ground measurements at both these locations. The corresponding linear correlation coefficients estimated for these two data sets are 0.94 and 0.90 respectively, which are significant at $p < 0.01$ [Fisher, 1970]. It is also seen that on an average MODIS has overestimated AOD at Kharagpur by 0.03 and underestimated at Kanpur by 0.12 with respect to the ground measurements. These deviations are respectively $\sim 4\%$ and $\sim 17\%$ of the mean AOD at these two places during the study period and are well within the uncertainties associated with MODIS retrieval [Remer *et al.*, 2005].

It would be interesting in this context to note that Tripathi *et al.*, [2005] reported a detailed comparison of AERONET measurements with MODIS derived Level 2 AOD at Kanpur which in general showed a good agreement between the two with a correlation of

0.71 and mean absolute difference around 0.12. Results of the present inter-comparison matches well with that reported by *Tripathi et al.*[2005].

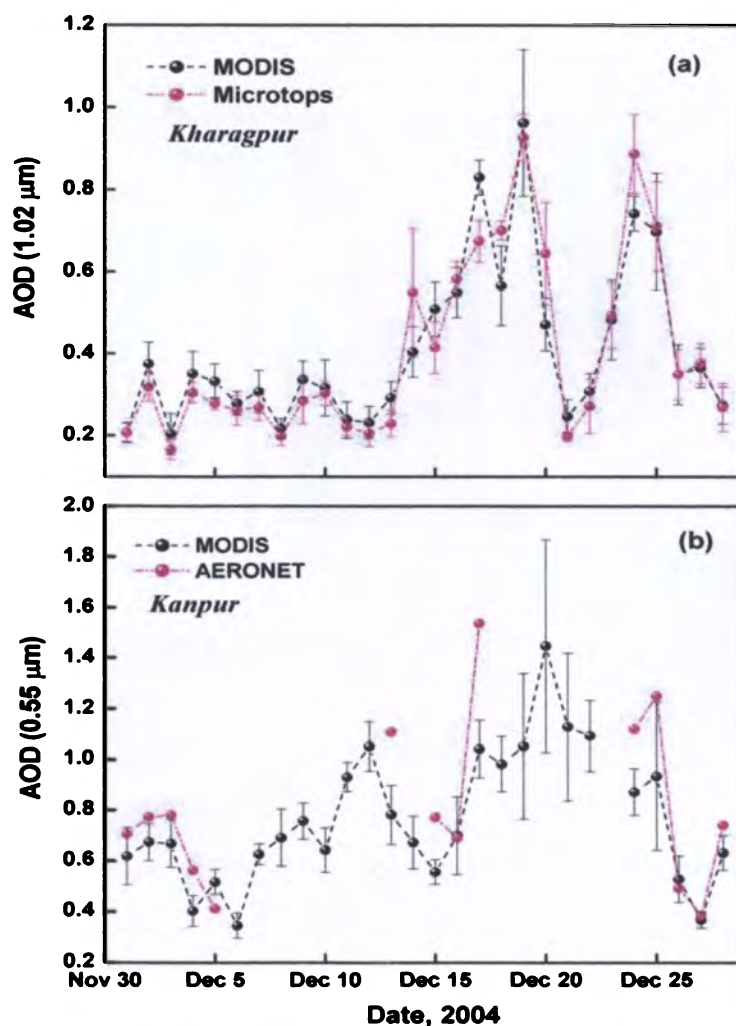


Fig.3.2. Time series plots of MODIS derived AOD normalized to $1.02 \mu\text{m}$ along with Microtops measured AOD at $1.02 \mu\text{m}$ for Kharagpur (a) and MODIS derived AOD normalized to $0.5 \mu\text{m}$ along with the AERONET retrieved AOD at $0.5 \mu\text{m}$, for Kanpur (b) during LC-II. Vertical bars indicate the respective standard deviations.

3.5 Aerosol distribution and synoptic circulation over the Ganga Basin

The MODIS derived AOD and the fine mode fraction (FMF) averaged for the LC-II period are presented in the Fig.3.3(a) and (b) respectively. Figure 3.3(a) clearly shows high aerosol loading over the Ganga Basin during the campaign period. It may also be noted that the FMF exceeds 0.6 in most of the regions along the plain. Increase in fine mode fraction is an indicator for increased contribution from anthropogenic sources. While the

eastern part of the subcontinent up to the tip of the peninsula is dominated by submicron particles (large FMF values), the western part is dominated by large size particles (low FMF values).

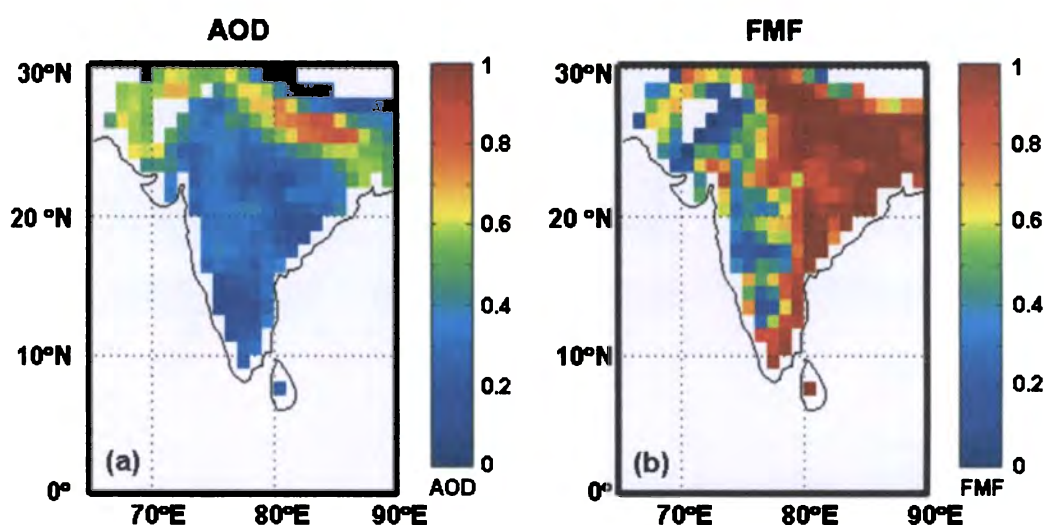


Fig.3.3. Mean spatial distribution of MODIS derived AOD at $0.55 \mu\text{m}$ (a) and FMF (b) for December, 2004.

The AOD distributions during the campaign period shows pronounced spatial heterogeneities which vary from day-to-day. This probably can be attributed to the diversity in the aerosol generation mechanisms as well as to the changes in the prevailing meteorological conditions affecting the dispersal of aerosols. Aerosol particles are lifted up in the air and carried over long distances by wind. During this process, particles can get accumulated at a particular location or disperse fast depending on the convergence of wind and the atmospheric pressure pattern over the region. Figure 3.4(a) - (c) show the mean wind field, wind convergence and vorticity at 925 hPa over the study domain during the campaign period.

Since the horizontal wind speed over the Ganga Basin near the surface, as seen from Fig.3.4, is very low ($\sim 2 \text{ ms}^{-1}$) the possibility of wind generated dust (dust storm) rising up in the atmosphere is far remote. At the same time, a moderate convergence in winds and a slight positive vorticity prevailing in this region is conducive for the particles to get trapped. Over and above, the low wind conditions help the aerosols to remain in this region undispersed.

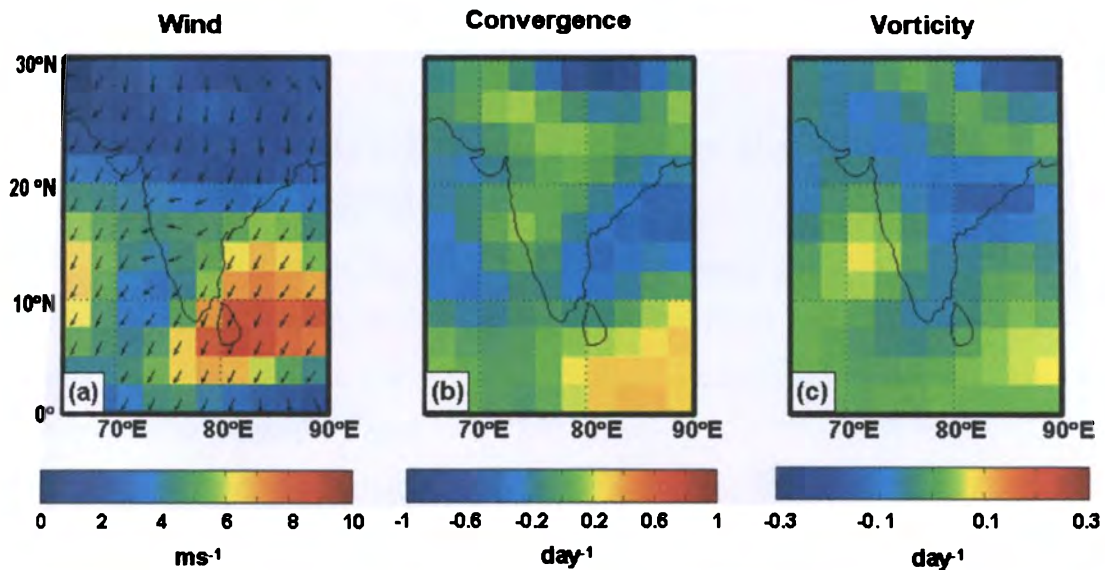


Fig.3.4. Mean spatial distribution of wind speed at 925 hPa (a) wind convergence at 925 hPa (b) and vorticity at 925 hPa (c) for December, 2004 derived from NCEP data.

Note that, the AOD can also be affected by changes in relative humidity (RH) especially when it crosses 70% (see Chapter 2, Sect.2.6). To study the effect of humidity, the altitude profile of RH in this region is examined. Figure 3.5 shows the mean profile of RH over the study domain for the campaign period. As the mean values of RH are well

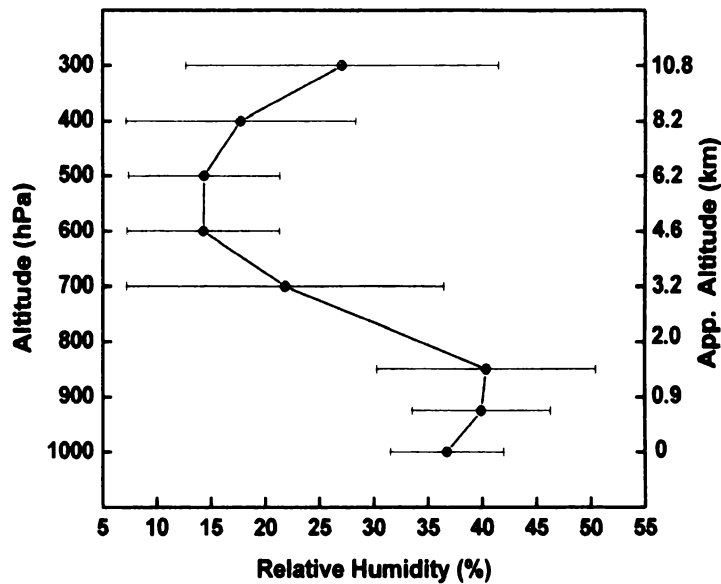


Fig.3.5. Altitude profile of mean Relative humidity profile derived from NCEP during the LC-II averaged over the study domain, along with the standard deviations. Note that the altitude scale on the left axis is shown in pressure levels and the corresponding approximate values in km are shown on the right axis.

below 50% (considering the standard deviations), there is hardly any possibility for it influencing the day-to-day variations of AOD.

3.6 Day-to-day variability in AOD over the Ganga Basin during the campaign

Temporal variation of the mean AOD over the study domain during the campaign period is shown in Fig.3.6. It can be seen that the AOD exhibit oscillations with a periodicity of ~ 4 to 8 days. The amplitude of these oscillations increases significantly in the second half of December, 2004.

After an initial decrease from 0.49 to 0.32 in the first four days, the AOD shows two discernible oscillations during December 5 to 13, 2004. The amplitudes of these oscillations are relatively small compared to those occurred during the second half of December. After December 13, the AOD increases steadily reaching a peak value ~ 0.97 on December 19 followed by a sudden decrease to ~ 0.35 on December 22 and a sharp increase to ~ 0.99 on the very next day. On many of the days in which AOD show high values, fog conditions prevailed in different parts of the Ganga Basin [Tripathi *et al.*, 2006; Nair *et al.*, 2009].

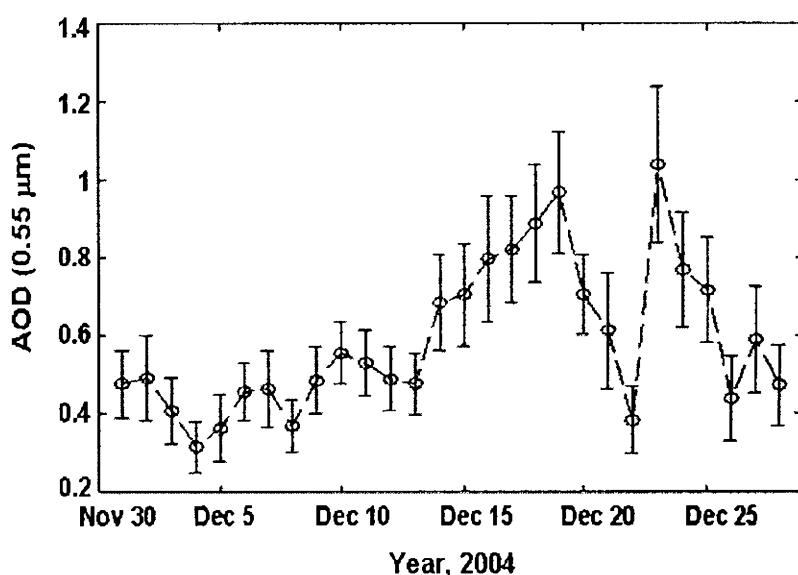


Fig.3.6. Daily variation of mean MODIS AOD ($0.55 \mu\text{m}$) over the study domain during LC-II

It can be seen from Fig.3.2(a) and (b) that the time variations of AOD at Kharagpur and Kanpur do not match well with each other. This indicates that the high and low AOD conditions do not cover the whole Ganga Basin on the same day. They appear and disappear in these two places at different times. This clearly shows the heterogeneity in

aerosol transport in this region. This aspect is further examined in detail by studying the day-to-day variations in the spatial distribution of AOD over the Ganga Basin using the MODIS data

A detailed investigation on the daily variations of the spatial distribution of AOD over the IGP reveals the appearance of localized clusters of high AOD, some of which moving along the plain and growing in size, while others get weakened after an initial growth. The life span of these aerosol clusters varies from a few days to a week. These are illustrated in the sequence of AOD images presented for a few days in Fig.3.7.

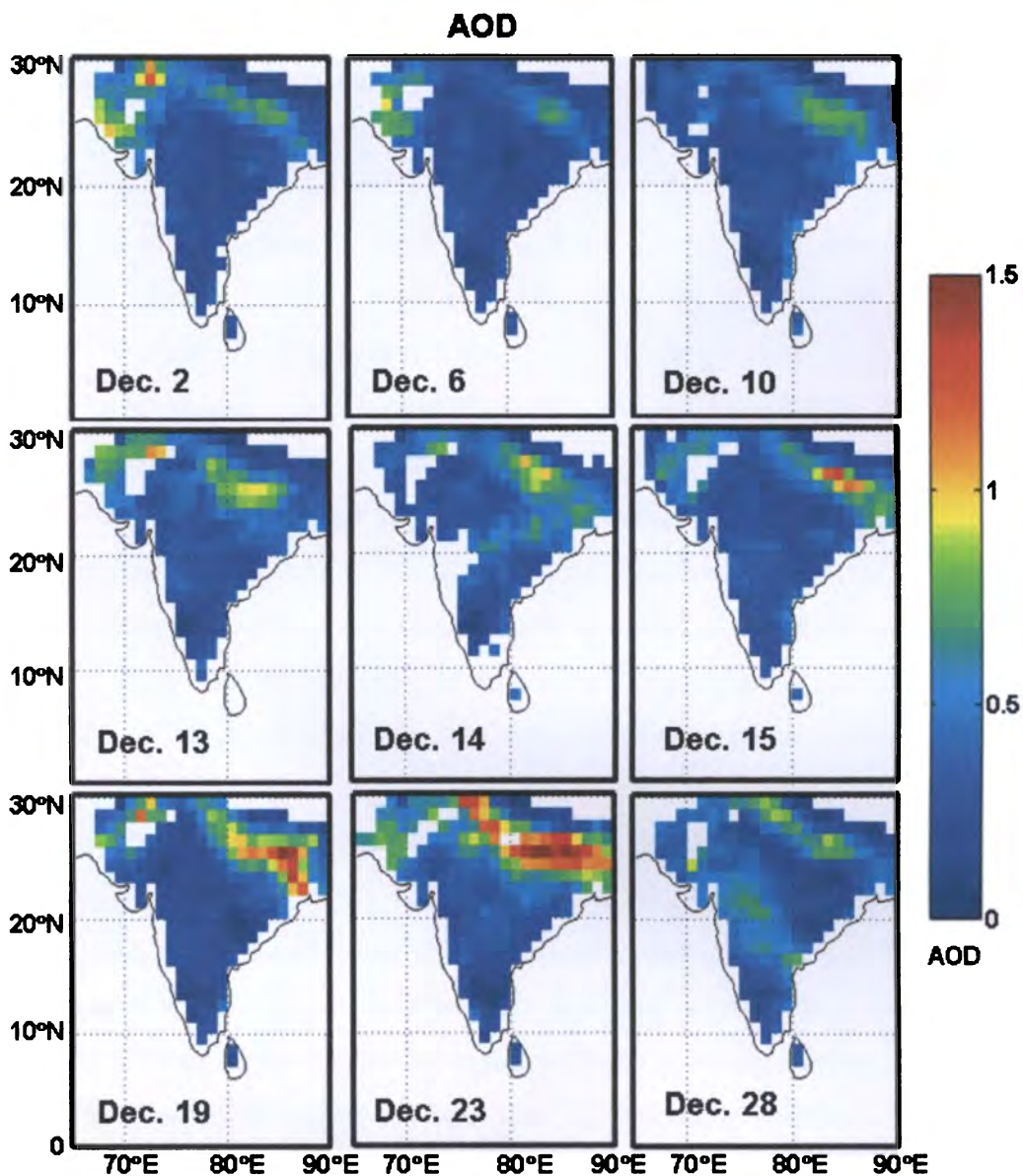


Fig.3.7. Daily distribution of MODIS derived AOD over the Indian region on the days, December 2,6,10, 13, 14, 15, 19, 23 and 28 of 2004.

It can be seen that even though the aerosol loading is generally high over IGP, there are marked variations in their distribution and concentration on different days. On December, 02 the AOD is high all along IGP especially towards its western end. Then after a few days, on December 06 the aerosol loading is found to be low over the entire region except over some small localized regions along the valley. On December 10 again the aerosol spreads and the loading increases. During the three consecutive days from December 13 to 15 a cluster of high AOD moves from the western end to the eastern end along the IGP. The intensification of the aerosol cluster observed during this period continues till December 19 to reach its peak followed by a slight decrease. After this the AOD values again start increasing till December 23 and weakens thereafter reaching low values towards the end of the campaign.

3.7 Role of dynamics on the day-to-day variations of AOD

Day-to-day variations of AOD over IGP are examined in terms of the prevailing features of circulation. The wind speed at 925 hPa [Fig.3.4 (a)] and at 1000 hPa levels over IGP are fairly uniform and generally less than 4ms^{-1} . No pronounced spatial gradient is observable in wind speed. But the spatial pattern of wind convergence shows significant day-to-day variability.

The wind convergences at 925 hPa level on the days in which the AOD distributions are shown in Fig.3.7 are displayed in Fig.3.8. A pronounced variation in the location as well as in the intensity of convergences along the IGP is observable on different days. It is also interesting to note that the positions of strong convergence generally coincide with the locations of high AOD. This indicates that strong wind convergence favours accumulation of aerosols. As seen from these figures, the temporal variation of convergence matches well with the evolution of AOD distribution. For example, the high wind convergence observed at the western end of IGP on December 02, 2004 decreases on subsequent days. Correspondingly, the cluster of high AOD localized in this region (Fig.3.7) also decreases. Similar changes are observable on other days also. But on some days, the magnitude of increase in AOD can be more than that expected from the increase in convergence. Such a feature is observed on December 23. Note that the amount of mismatch is more than the uncertainty ($\pm 0.15\tau \pm 0.05$) in MODIS derived AOD. That is, the high AOD and high convergence do not match exactly in all the cases though there is an overall correspondence between the two. This is expected since the change in AOD can be exclusively attributed to

the change in convergence only in the absence of localized aerosol sources. The amount of mismatch between the convergence and AOD could be an indicator of the presence of aerosol sources/sinks

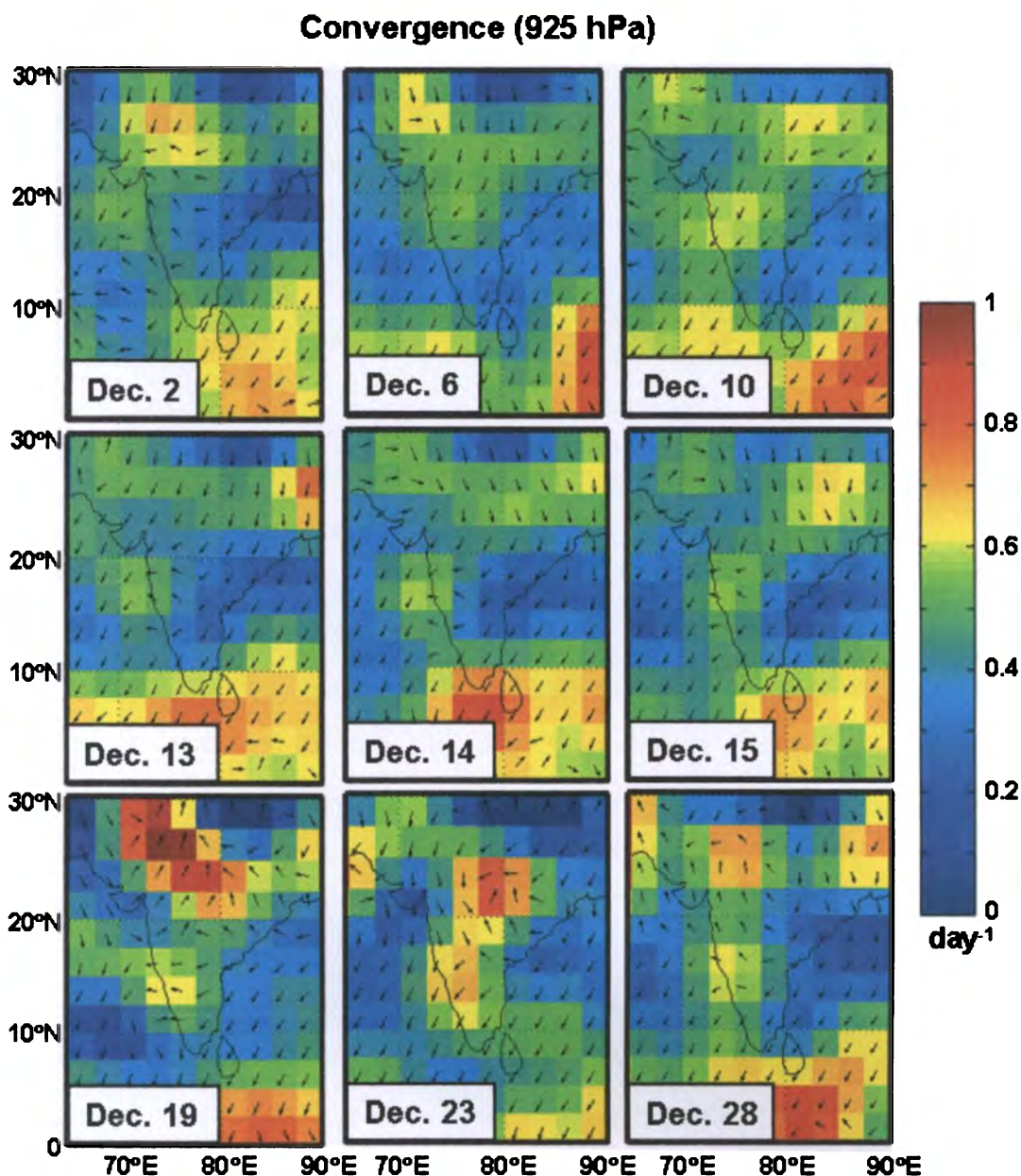


Fig.3.8. Daily distribution of wind convergence at 925 hPa derived from NCEP over the Indian region on the days, December 2,6,10, 13, 14, 15, 19, 23 and 28 of 2004.

3.8 Estimation of net aerosol source strength

As the aerosol properties at a location is not only influenced by the local source characteristics but also by the dynamics of wind field, any realistic description of aerosol distribution should be accounted through the flux continuity equation with a source/sink

term (representing aerosol generation/loss) [Chapter 2, Eq.(2.26)]. By introducing the spatial distribution of AOD from satellites and wind field from an appropriate atmospheric circulation model into the continuity equation, locations of major aerosol sources (and sinks) can be identified and their strengths can be quantified.

For the above analysis, daily values of AOD from MODIS and daily mean wind field at seven pressure levels (from 1000 to 400 hPa) from NCEP reanalysis in the study domain (20°-27.5°N, 75°-87.5°E) are incorporated into the continuity equation (see Chapter 2, Sect.2.7) ,

$$\frac{\partial \tau}{\partial t} + \frac{\partial}{\partial x} \left[\int_0^{\infty} \beta u \, dz \right] + \frac{\partial}{\partial y} \left[\int_0^{\infty} \beta v \, dz \right] = S(x,y,t) \quad (3.2)$$

where τ is the AOD, β is the extinction coefficient, u and v are the zonal (x) and meridional (y) components of wind, z is the altitude and t is the time (in days for the present case).

In order to estimate the gradient terms in Eq.(3.2) for the edge pixels in the study domain, an outer domain 17.5°-30°N, 72.5°-90°E is selected as background. Since the spatial resolution of NCEP data is 2.5°× 2.5°, MODIS data is also degraded from its 1° × 1° to this grid size. It should be noted that as MODIS employs different algorithms for the retrieval of AOD over the land and over the ocean, the coastal pixels will be affected by the edge effect at the land-ocean interface [Kaufman *et al.*, 1997a; 1997b]. To avoid any artifact arising out of this, entering into the source estimation, all the coastline pixels are excluded from this analysis.

Aerosol flux vectors for a pixel at different pressure levels are represented in terms of the product of aerosol extinction at that altitude (defined by a prescribed vertical distribution) in that pixel and the mean of the winds at the four corners of the pixel. More details on the computations of Eq.(3.2) are presented in Chapter 2, Sect.2.7. Flux computations require the altitude variation of aerosol extinction in the lower troposphere the contribution from which is significant for the columnar AOD. A close examination of altitude profiles of aerosol backscatter in the first few kilometres obtained using lidar at Kharagpur during the campaign period [Niranjan *et al.*, 2006] showed decreasing aerosol extinction with increasing height with maximum contribution from 1.5 to 2 km. Hence, the

aerosol extinction profile is modelled by an exponentially decreasing function of altitude in the form,

$$\beta = \beta_0 \exp \left(-\frac{z}{H_a} \right) \quad (3.3)$$

where β_0 ($= \tau/H_a$) is the extinction coefficient at the ground and H_a is the aerosol scale height parameter. On the basis of lidar observation at Kharagpur [Niranjan *et al*, 2006] a value of 2 km is found reasonable for H_a which is adopted for the present computation.

The RHS of Eq.(3.2) represents the net rate of aerosol generation in terms of AOD change per day at every pixel. By incorporating the daily AOD data from MODIS and winds from NCEP reanalysis, the source strength, S is estimated for the campaign period over the study region. Note that a positive value of S indicates the dominance of aerosol generation (or production) and a negative value, the dominance of aerosol loss.

3.9 Estimation of aerosol source strength (aerosol production rate) and its spatial distribution over the Ganga basin

Aerosol source strength over the study domain is estimated for all the days of LC-II using the aerosol continuity equation. Its average over the campaign period is shown in Fig.3.9. In this figure, the blank pixels in the north eastern portion of the study domain results from the masking of data in the original MODIS derived AOD over the highly reflecting Himalayan snow regions. In the south eastern part, the blank pixels are due to the

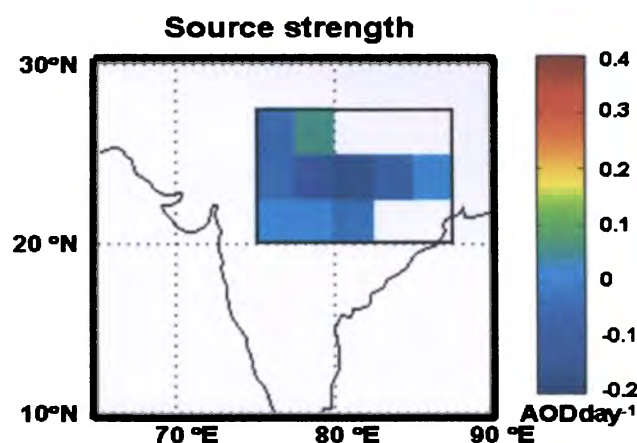


Fig.3.9. Mean source strength distribution over the study domain for December, 2004

exclusion of data over the coastal pixels in the computations. In the remaining part of the domain, one can see that the positive values are located over the west of centre-north, the eastern end and the south western corner. The central region however, shows negative values indicating aerosol loss. The uncertainty in the source strength due to the standard deviation in MODIS AOD (~15%) and the uncertainty in aerosol scale height (~25% or 0.5 km) is ~30%.

3.10 Estimation of the actual source strength incorporating the loss term

As stated above, the term 'S' on the right hand side of Eq.(3.2) represents net source, that is, the resultant aerosol production over aerosol loss through various removal mechanisms such as dry/wet deposition, impaction, sedimentation, diffusion, etc. By modeling these loss processes and compensating them with an appropriate sink term a more realistic estimate of the actual aerosol production rate can be accomplished. As there was no precipitation and pronounced meteorological events during the campaign period in the study region, one can assume a more-or-less steady loss of aerosols, the rate of which depends on the prevailing aerosol concentration. This loss can be represented as an exponential decrease in τ with time, in terms of the mean residence time of aerosols in the lower troposphere. In the absence of any source for aerosol production and transport from adjacent regions, the AOD at a given location should decrease depending on the residence time alone. One can then write

$$\tau(x, y, t) = \tau_0(x, y) \exp(-t/D) \quad (3.4)$$

where $\tau_0(x, y)$ is the value of AOD at the location (x, y) at $t=0$ and $\tau(x, y, t)$ is the value of AOD at time t and D is the residence time of aerosols. This yields the time rate of change of AOD as

$$\frac{\partial \tau}{\partial t} = \tau_0 \left(-1/D\right) \exp(-t/D) = -\tau/D \quad (3.5)$$

Eq.(3.5) represents the rate of decrease of τ (because of the removal processes) in the absence of sources and horizontal transport. Now to describe the general situation which includes horizontal transport as well as aerosol production, the appropriate terms for aerosol flux convergence (negative of divergence) also are to be added. In such a case Eq.(3.5) will be modified as

$$\frac{\partial \tau}{\partial t} = -\frac{\tau}{D} - \frac{\partial}{\partial x} \left[\int_0^{\infty} \beta u \, dz \right] - \frac{\partial}{\partial y} \left[\int_0^{\infty} \beta v \, dz \right] + Q(x,y,t) \quad (3.6)$$

where τ/D represents the absolute value of aerosol loss (which is a function of x, y and t) and $Q(x,y,t)$ is the rate of aerosol production after compensating for the aerosol loss processes. By rearranging the terms in Eq.(3.6) it becomes a modified continuity equation

$$\frac{\partial \tau}{\partial t} + \frac{\tau}{D} + \frac{\partial}{\partial x} \left[\int_0^{\infty} \beta u \, dz \right] + \frac{\partial}{\partial y} \left[\int_0^{\infty} \beta v \, dz \right] = Q(x,y,t) \quad (3.7)$$

Note that if Q is positive it is an indication that the aerosol production is actually dominating, which leads to an increase in AOD. But if it is negative, aerosol loss is more dominating. By using a typical value of 2 days for the average residence time of aerosols in the lower troposphere, Eq.(3.7) is used to estimate mean value of Q over the study domain for the month of December 2004. This result is presented in Fig.3.10. As can be seen, the weak sources depicted in Fig.3.9 emerge out very prominently in this figure, as a result of incorporating the loss processes in the flux continuity equation.

3.11. Results and discussion

The Ganga Basin is a densely populated region with abundant, industrial activities and high bio-fuel consumption. To meet the energy demands for industries, this region harbours a large number of coal fired thermal power plants. Out of ~ 80 thermal power plants in India, about 40% of them are located in the Ganga Basin. The high ash content of the Indian coal and its inefficient combustion in the plants make them a major source of black carbon, nitrate and sulphate particles [http://envfor.nic.in/soer/2001/ind_air.pdf; Reddy and Venkataraman, 2002; Prasad et al., 2006]. With this background, the location

of thermal power plants and their association with high aerosol source strength are examined in detail.

The modified source strength distribution averaged for the campaign period superimposed with the locations of thermal power plants (represented by black dots) in and around study region is presented in Fig.3.10. The total uncertainty in the estimated source strength arising from the standard deviation of MODIS AOD (~15%), uncertainty in the assumed aerosol residence time (half a day) [Jaenicke, 1980] and uncertainty in the aerosol scale height (~ 0.5 km) [Niranjan, et al., 2006] is ~ 38%.

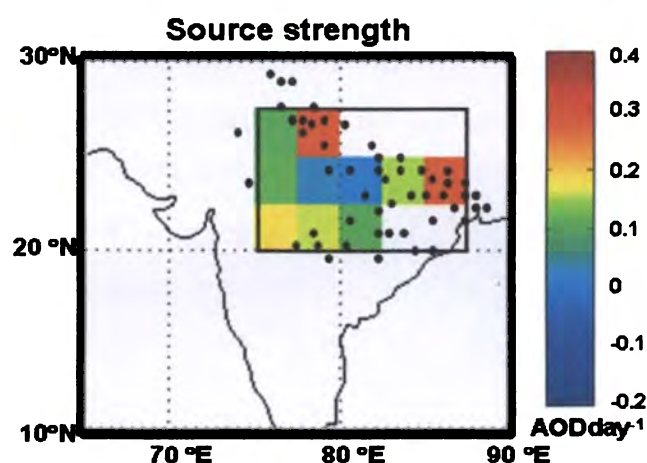


Fig.3.10. Mean source strength distribution over the study domain for December, 2004 after incorporating aerosol sink model. Black dots indicate the location of thermal power plants.

It must be remembered however, that the estimated source strength could also have contributions from effects like variations in relative humidity (RH) and coagulation of particles. As RH over the study domain remained within 30 – 45% throughout the campaign period (Fig. 3.5), any major effect of hygroscopic growth of aerosols and consequent changes in AOD can be ruled out. In the case of coagulation, two or more small particles stick together to form larger particle (Chapter 1, Sect.1.6.1). This leads to an increase in the number of large particles at the expense of smaller ones. Taking this effect into consideration, the computations [McCartney, 1976] with an aerosol size distribution corresponding to a typical polluted urban area [Jaenicke, 1980] shows that the change in AOD per day due to coagulation is $\leq 7.5\%$, near the major sources of aerosol in the study domain.

As is quite evident from Fig.3.10, the locations of high aerosol source strength are seen close to the regions where the thermal power plants are concentrated. The thermal power plants, with an average emission of ~ 700 kg of soot and ~ 85 tons of SO_2 per day from each plant (<http://www.osc.edu/research/pcrm/emissions/thermalemissions.shtml>), contribute substantially towards the anthropogenic aerosol load in this region. Fig. 3.10 shows a moderately strong aerosol source region in the south western parts of the study domain (shown in yellow colour) where the concentration of thermal power plants is small. This could be due to the increased anthropogenic activities associated with the dense population of this region (lying partly in Maharashtra and partly in Madhya Pradesh), which is adding to the emission from the existing thermal plants.

A more quantitative comparison between the number of thermal power plants and source strength is attempted by counting the number concentration of thermal power plants within a circle of influence defined with a diameter 2.5° with its centre in the middle of the each $2.5^\circ \times 2.5^\circ$ grid. Figure 3.11 shows the scatter plot between power plant concentration and source strength, which gives a correlation coefficient, 0.85 supporting the earlier suggestion that the thermal power plants is a significant source of aerosol production over the Ganga basin.

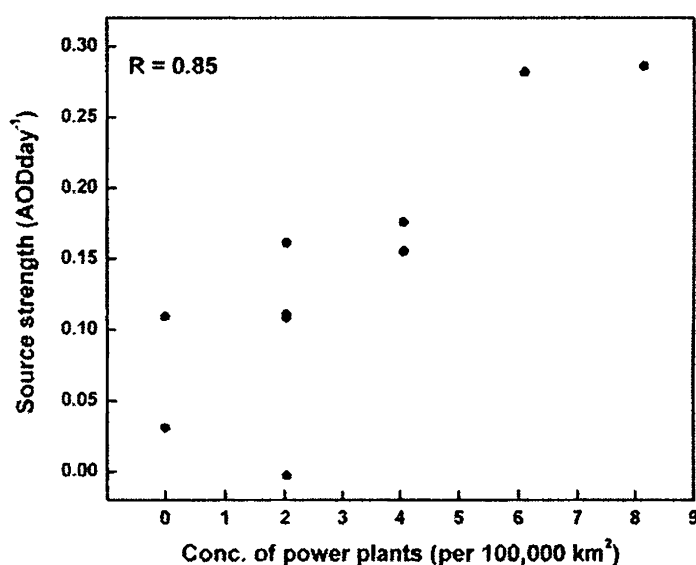


Fig.3.11. Scatter plot between the concentration of thermal power plants and aerosol source strength over the study domain

Further, the level of environmental pollution could also be an index of the particulate loading near the surface. Central Pollution Control Board (CPCB) is a statutory

organization entrusted with the responsibility of controlling the environmental pollution both in the air and water (and preventing when it exceeds the standard limits). In order to assess the air quality and its trend, CPCB has set up monitoring stations at different locations within the country. Measurements on RSPM (Respirable Suspended Particulate Matter), NO_2 and SO_2 are performed regularly at these sites and the data is used for their assessments. This data available for public use in the website <http://www.cpcb.nic.in>, is used to check the inference of aerosol sources derived from the present analysis (Fig.3.10). Figure.3.12 shows the spatial distribution of mean RSPM in the PM_{10} size range, and the gases SO_2 and NO_2 (pollutants) within the study domain for December 2004 obtained from the CPCB data. The data cover about 29 locations in and around the study domain where regular monitoring was carried out (at least for more than 15 days). A perusal of this map reveals a good correspondence between the distributions of RSPM concentration and the source strength presented in Fig 3.10.

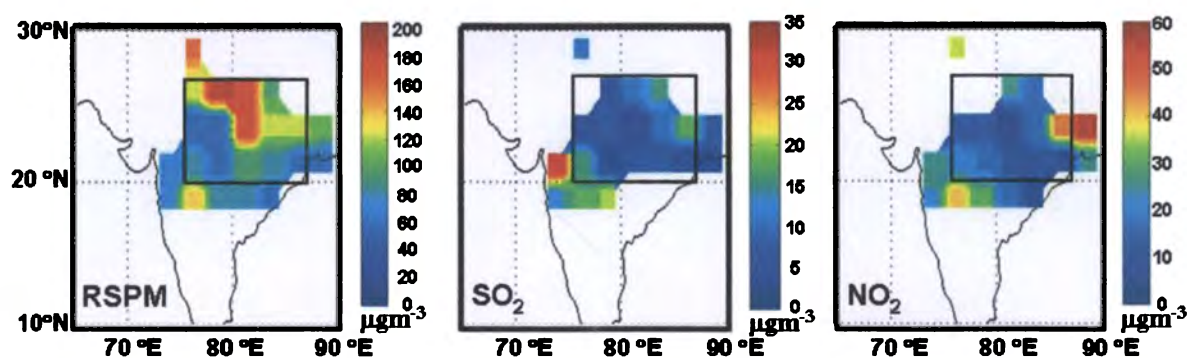


Fig.3.12. Mean spatial distribution of RSPM, SO_2 and NO_2 obtained from CPCB data over the study domain for December, 2004.

3.12. Summary

The main objective of this study is to investigate the generation and transport of aerosols in a confined geographical location ($20^\circ - 27.5^\circ \text{N}$, $75^\circ - 87.5^\circ \text{E}$) over the Ganga Basin where the LC-II campaign was carried out during December, 2004. As a prelude, MODIS data over the study period used in the present study, is compared with ground measurements at two sites in the study domain. This shows a very good agreement between the two. A close examination of the daily AOD distribution derived from MODIS and the wind field at 925 hPa from NCEP reanalysis point towards wind convergence as a plausible factor responsible for the accumulation of aerosols over the Ganga Basin. Incorporating

MODIS derived AOD and the NCEP reanalysis wind field into the aerosol continuity equation, this analysis could reveal the locations where the aerosol sources are very prominent. Further, by incorporating the aerosol loss model (with a residence time of 2 days) in the continuity equation, the sources become more distinct. A fairly good agreement observed between the aerosol sources and the locations of the coal fired thermal power (with a correlation of 0.85 between source strength and power plant concentration) indicates that the power plants could be a major contributor to the increased aerosol loading over the Ganga basin. The spatial distribution of RSPM, SO₂ and NO₂ obtained from CPCB data also confirms this inference.

Chapter 4

Investigation on aerosol transport over the South East Arabian Sea during the pre-monsoon period: ARMEX-II

4.1 Introduction

The oceanic environment around the Indian peninsula is strongly influenced by the intrusion of aerosols from the adjacent landmass through atmospheric circulation. Large scale change in the synoptic circulation from winter (dry) to summer (monsoon) associated with the changes in synoptic meteorology characteristic to this region show corresponding variations in the physical properties and chemical composition of aerosols.

Systematic observation on aerosol properties over the Arabian Sea started since 1995 with regular monitoring of AOD over Minicoy island using MWR [Satheesh *et al.*, 2006a]. This was followed by ship borne observations as part of various satellite (IRS) validation experiments and dedicated campaigns. A major oceanic expedition, Indian Ocean Experiment (INDOEX) carried out in 1998 and 1999, was effective in understanding the spatial distribution of aerosols in this region and their impact on the radiative forcing [Moorthy *et al.*, 2001; Ramanathan *et al.*, 2001; Quinn *et al.*, 2002] of the earth-atmosphere system. These observations which covered mostly the north-east monsoon season showed for the first time, the large scale intrusion of continental (including anthropogenic) aerosols into the pristine atmosphere of the equatorial central Arabian Sea. Most of these aerosols were found to originate from the West Asia, north east Africa and

east/south east Asian regions. They are brought over to the equatorial Arabian Sea through long range transport [Moorthy and Saha, 2000; Lelieveld *et al.*, 2001; Ramanathan *et al.*, 2001; Li and Ramnathan, 2002; Ball *et al.*, 2003; Vinoj and Satheesh, 2003].

The south eastern part of the Arabian Sea adjacent to the west coast of Peninsular India, called the South East Arabian Sea (SEAS) is of special interest as aerosol concentration (detected in terms of AOD) in this region is significantly high during the Asian dry (pre-monsoon) period. Based on a comprehensive study using NOAA-AVHRR data of the period 1996 to 2003, Rajeev *et al.*, [2004] and Nair *et al.*, [2005] showed that the mean AOD over the SEAS, increases steadily from November to April. This was attributed to the advection of aerosols from the Indian subcontinent and the arid regions of Arabia through the lower troposphere. Aerosol observations during the pre-monsoon phase of the second Arabian Sea Monsoon Experiment (ARMEX-II) conducted in 2003 over the SEAS provided further confirmation of this long-range transport of aerosols from Arabia and West Asia to the Arabian Sea [Moorthy *et al.*, 2005].

Prime objective of the present study is to understand the role of synoptic meteorology and atmospheric circulation in governing the spatial distribution of aerosols in the SEAS during the pre-monsoon phase of ARMEX -II.

4.2 ARMEX -II

The ARMEX was a large scale field campaign dedicated to meteorological and oceanographic observations coordinated by Department of Science and Technology (DST) under the Indian Climate Research Programme (ICRP). The main focus of this experiment was to understand the dynamics of monsoon genesis over the SEAS. It was carried out in two parts. The first part of this campaign (ARMEX – I) was conducted in 2002 and the second part (ARMEX – II) in 2003, both around the south west monsoon season. ARMEX-II itself had two phases; one during the pre-monsoon period (referred as first phase) intended for studying the warm pool phenomenon and the other (referred as second phase), at the beginning of the monsoon, mainly for the study of convective systems over the Arabian Sea [Rao, 2005].

The first phase of ARMEX-II was from March 14 to April 10, 2003 in which aerosol measurements were conducted onboard Sagar Kanya (SK190). The cruise track of SK190 is shown in Fig.4.1. This cruise covered an oceanic area around 500 km × 750 km,

bound by 7.5° - 12.5° N and 70° - 77.5° E (referred hereafter as the ARMEX domain). During this phase, the ship was stationed at around 9.2° N, 74.5° E (hereafter referred as Time Series Location, TSL) from March 23 to April 06, 2003 to facilitate time series observations on meteorological and aerosol parameters from a fixed position where the probability of occurrence of warm pool (before the onset of summer monsoon) was considered to be highest.

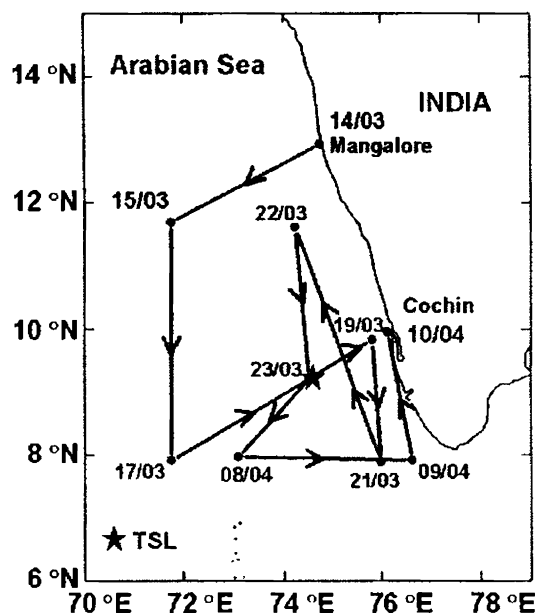


Fig.4.1. Cruise track of Sagar Kanya during the first phase of ARMEX-II, SK190 (March 14 – April 10, 2003)

4.3 Data used for the study

Measurements on the spatial distribution of AOD and the size segregated mass concentration of aerosols in the ambient air were made on board Sagar Kanya at an altitude of about 10m above the sea level (over the deck). Spectral AOD was measured using a hand held Microtops –II sunphotometer (Solar Light Co.) at wavelengths 0.38, 0.50, 0.675 and $0.87 \mu\text{m}$ [Moorthy *et al.*, 2005]. Utmost care was taken to collect accurate data with Microtops, following the guidelines laid down for its operation as detailed in Sect.2.3.3 of Chapter 2. During the 28 days of the campaign, AOD could be measured on 24 days (favoured by clear sky condition). The average values of AOD measured on each day is assigned to the mean position of the ship on that day.

Size segregated aerosol mass concentration was measured using a Quartz Crystal Microbalance (QCM) cascade impactor (model PC-2, California measurements Inc.) in 10

successive size bins with 50% cut-off diameters at 25, 12.5, 6.4, 3.2, 1.6, 0.8, 0.4, 0.2, 0.1 and $0.05\mu\text{m}$. The flow rate of this instrument was maintained at 240 ml min^{-1} and the samplings were done at 5-8 min intervals, depending on the aerosol loading in the atmosphere. In order to preserve the instrument calibration, the QCM was operated only during the period when the atmospheric relative humidity (RH) was less than 78%. The operation of QCM was interrupted whenever the wind speed relative to the ship decreased below 4 ms^{-1} to prevent any contamination by stagnant particles from ship's exhaust [Moorthy *et al.*, 2005].

Level 3 Collection 005 MODIS data on spectral AOD, fine mode fraction (FMF) and aerosol mass concentration from Aqua and Terra at a particular location are optimally combined to represent the daily mean aerosol properties at that location. The details of the data and the procedure for combining Aqua and Terra data are described in Chapter 2, Section 2.2.7. Wind field and RH at different atmospheric levels (1000 – 400 hPa) are obtained from NCEP reanalysis.

4.4 Comparison of AOD and Angstrom exponent from MODIS with cruise measurements

Among the seven MODIS spectral channels, the wavelengths 0.55, 0.66 and $0.865\mu\text{m}$ are close to the Microtops wavelengths at 0.50, 0.675 and $0.87\mu\text{m}$ respectively and lie within this range. In order to make a realistic comparison of the AODs from the two instruments, the Microtops measured AODs ($\tau_{\text{Microtops}}$) are adjusted (or normalized) to the nearest MODIS wavelengths [using Eq.(3.1) in Chapter 3] using the Angstrom exponent (α) derived from Microtops AODs at the wavelengths 0.50, 0.675 and $0.87\mu\text{m}$ through a logarithmic regression [Chapter 1, Eq.(1.27)]. Thus the Microtops measured AOD at 0.50 is normalized to 0.55 μm , 0.675 to 0.66 μm and 0.87 to 0.865 μm .

Figure 4.2 shows a scatter plot of the Microtops measured AOD at $0.55\mu\text{m}$ (adjusted from $0.50\mu\text{m}$) and MODIS retrieved AOD at $0.55\mu\text{m}$ along with the corresponding standard deviations. Daily average of Microtops measured AOD is taken along the horizontal axis and the corresponding mean value of MODIS measured AOD over a grid size of $1^\circ \times 1^\circ$ box which encompasses the mean position of ship on that day is taken along the vertical axis. Horizontal and vertical bars represent the respective standard deviations. A mean regression line established using these values is also shown in the figure. The

relation and regression coefficients estimated for the three MODIS wavelengths are summarized in Table.4.1.

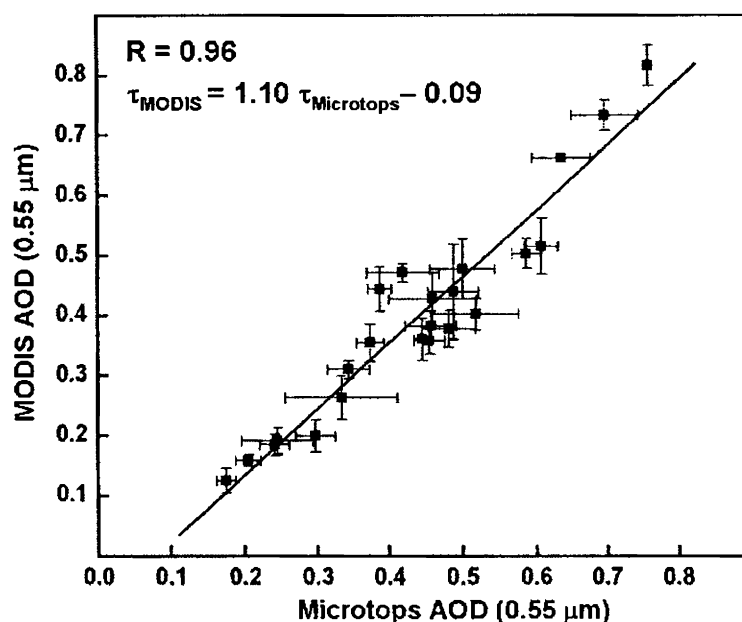


Fig.4.2. Scatter plot showing the comparison of MODIS derived daily mean AOD (at 0.55 μm) with that from Microtops (at 0.55 μm adjusted from 0.50 μm). Horizontal bars are the standard deviations of the Microtops measurements and the vertical bars are the standard deviations of MODIS derived AOD. Correlation coefficient and regression relation are also shown in the figure.

The non-zero intercepts in the regressions result from an improper representation of surface reflectance in the MODIS retrieval procedure while the deviation of slopes from unity indicates a systematic bias arising mostly from instrument calibration error and/or inappropriate choice of the aerosol model in the MODIS retrieval algorithm [Chu *et al.*, 2002; Remer *et al.*, 2005; Tripathi *et al.*, 2005]. The low scatter of points from the regression line in Fig.4.2 as well as the high correlations in Table.4.1 for the three wavelengths indicate good agreement of MODIS derived AOD with the ship borne measurements.

The intercepts though small (less than 0.1), are negative in all the three cases. This would imply a small over correction for the surface reflectance in this region in all the three MODIS spectral channels [Misra *et al.*, 2008]. For the values of ‘a’ in Table 4.1, MODIS underestimates the AOD when it is low and over estimates when it is high. The cross over occurs around 0.9, 0.12 and 0.17 (AOD values) respectively at wavelengths 0.55, 0.66 and 0.865 μm. For the measured range of AODs, MODIS underestimates the AOD at 0.55 μm

by 0.04, and overestimates at 0.66 μm and 0.865 μm by 0.05 and 0.04 respectively. Because of this, the α derived from MODIS will be smaller than that estimated from the spectral AOD measurements using Microtops.

Table 4.1. The correlation coefficients and regression relations between MODIS derived AOD and that from Microtops, at different wavelengths.

Wavelength (μm)	Correlation Coeff. (R)	Regression relation ($\tau_{\text{MODIS}} = a \tau_{\text{Microtops}} + b$)	
		a	b
0.55	0.96	1.10	-0.09
0.66	0.97	1.25	-0.03
0.865	0.97	1.41	-0.07

Figure 4.3 shows a time series plot of the mean and the standard deviation of α determined from MODIS (α_{MODIS}) derived AODs at 0.55, 0.66 and 0.865 μm and those estimated from the Microtops ($\alpha_{\text{Microtops}}$) AODs at 0.50, 0.675 and 0.87 μm . It can be clearly

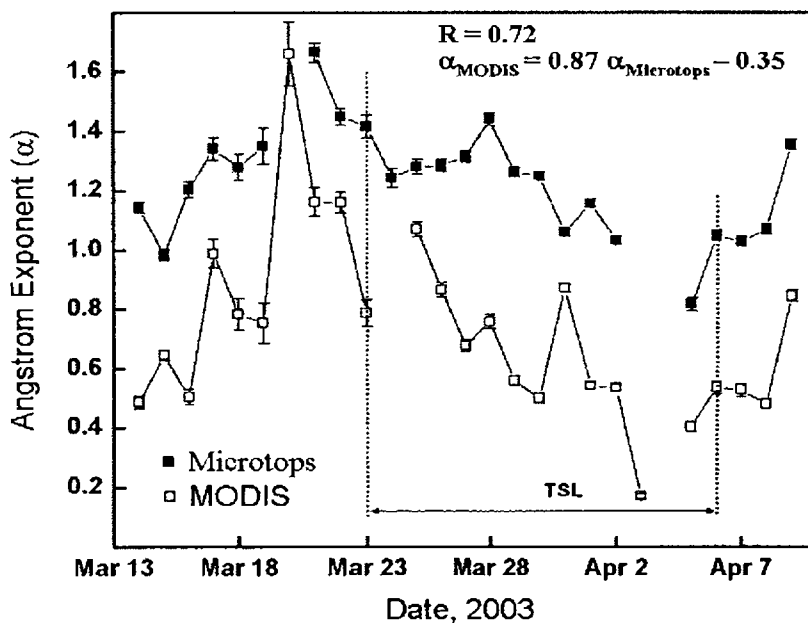


Fig.4.3. Time series plot of the daily mean and standard deviation of Angstrom exponent from MODIS derived AODs at 0.55, 0.66 and 0.865 μm wavelengths and those obtained from Microtops measured AODs at 0.50, 0.675 and 0.87 μm wavelengths. The correlation coefficient and the regression relation are also shown in the figure. The range marked with TSL denotes the period when the ship was stationary at the time series location.

seen that the daily variations of the two Angstrom exponents are more-or-less similar (with a correlation coefficient 0.72), but α_{MODIS} is always less than $\alpha_{\text{Microtops}}$. On an average this difference is ~ 0.37 . The possibility of attributing this difference to the difference in the spectral bands used in the two measurements is further examined by suitably interpolating the Microtops measured AOD values to MODIS wavelengths. Accordingly, each individual AOD measured by Microtops on a day (between 0.50 and 0.87 μm) is normalized to the nearest wavelengths of MODIS (between 0.55 and 0.865 μm) and the values of $\alpha_{\text{Microtops}}$ are re-estimated. The difference in values of $\alpha_{\text{Microtops}}$ reduced on an average only by ~ 0.07 which is far short of the mean difference of ~ 0.37 . This shows that the difference in α between MODIS and Microtops must be due to the errors in the retrieval of AOD by MODIS.

4.5 Comparison of mass concentration measurements

MODIS provides column integrated mass concentration derived from the optical depth at 0.55 μm , FMF and the modelled extinction coefficients for small and large particles [Remer *et al.*, 2005]. This is used as a measure of aerosol mass loading at a particular location. As the present campaign having the data on size segregated aerosol mass concentration measured using the QCM, the agreement between the two is examined in different size regimes.

A time series plot of MODIS derived columnar mass concentration along with the surface mass concentration of coarse mode particles (size range 1.6 to 25 μm) measured by QCM is shown in Fig.4.4. These two quantities show a significant positive correlation ($R = 0.81$) indicating that the mass concentration provided by MODIS represents mostly the mass loading of coarse size particles. This is quite expected since mass concentration in most of the situations is decided by the larger size particles while the number concentration is mainly determined by the sub-micron size particles. Thus the MODIS measured column integrated mass concentration over the ARMEX domain is mostly governed by the coarse particles near the surface.

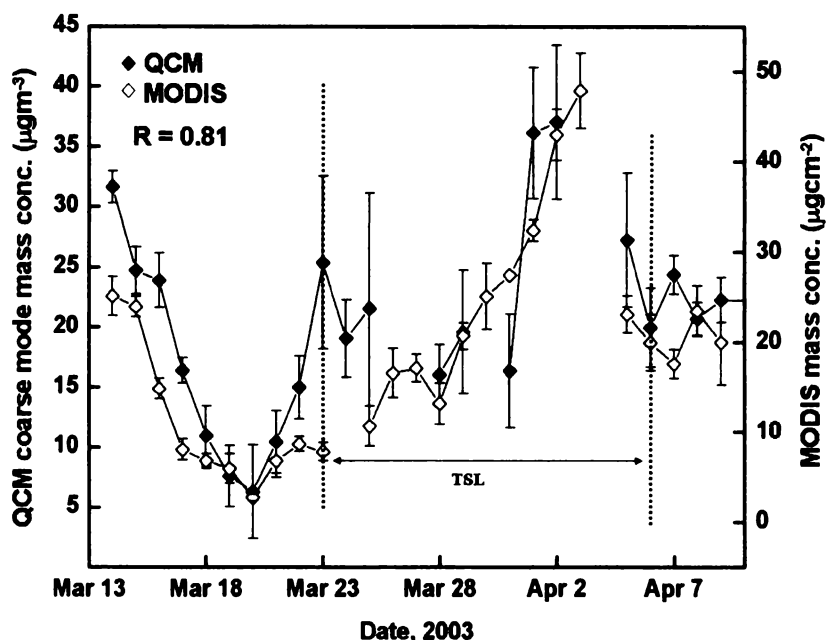


Fig.4.4. Comparison of MODIS derived integrated mass concentration with QCM measured coarse mode mass concentration (along with standard deviations) during the first phase of ARMEX-II along the cruise track. The time series during the TSL period is marked in the figure.

4.6 Role of atmospheric circulation in the spatial distribution of AOD

The mean ocean surface wind field from QuikSCAT over the Arabian Sea, during the campaign period is shown in Fig.4.5. The mean wind variables such as convergence and

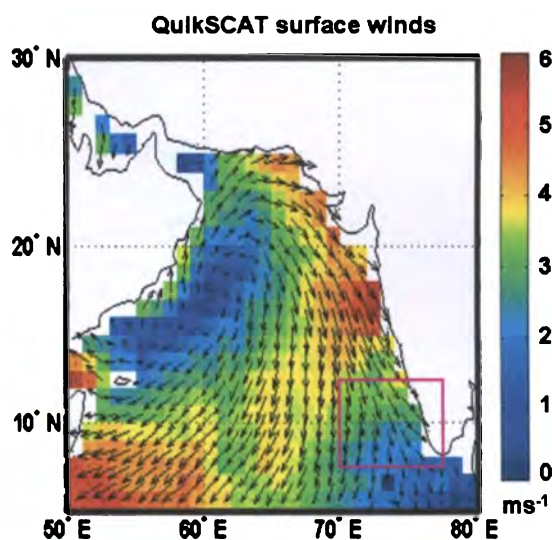


Fig.4.5 Spatial distribution of QuikSCAT surface wind over the Arabian Sea averaged for the first phase of ARMEX II. The rectangular box shown in the figure is the ARMEX domain.

vorticity, at two altitudes (925 and 700 hPa levels) computed from NCEP winds, in the geographical region, 5° - 30°N and 50° - 90°E are presented in Fig.4.6. The rectangular box in these figures represents the ARMEX domain (7.5° - 12.5°N, 70° - 77.5°E) in the SEAS. As can be noticed in Fig.4.5, the ocean surface wind is very low ($< 4 \text{ ms}^{-1}$) over the ARMEX domain, but moderately high in the upwind region.

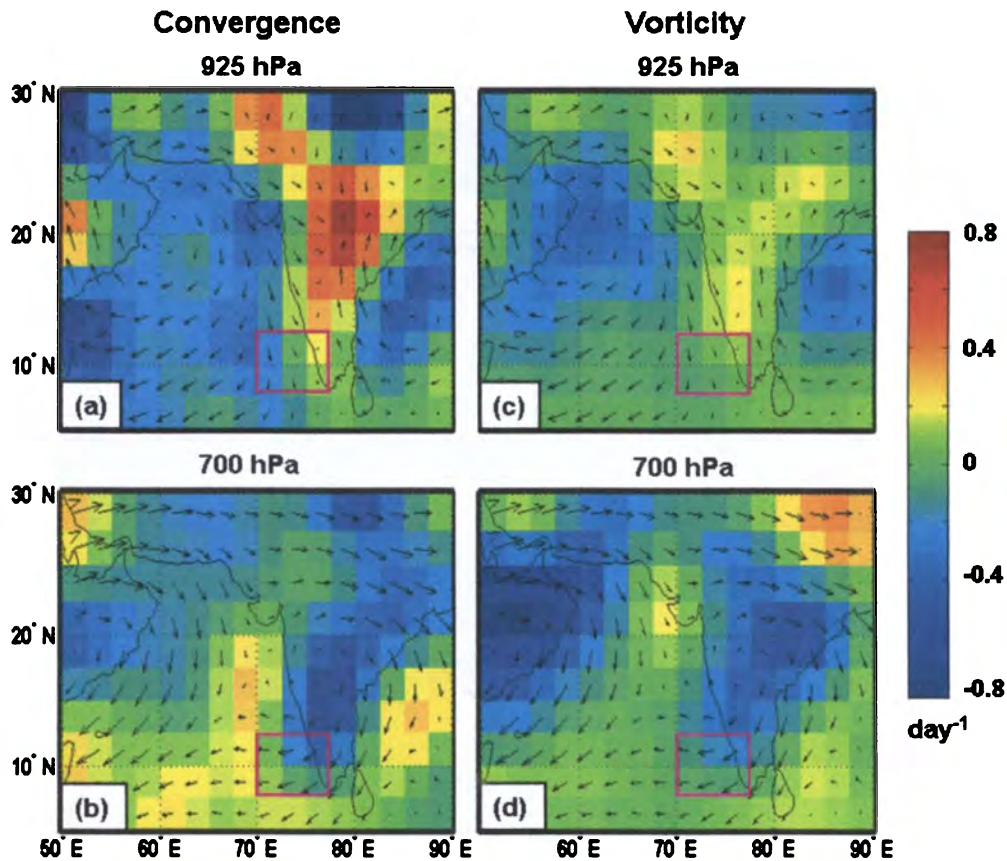


Fig.4.6. Average spatial distribution of wind convergence at 925 hPa (a) wind convergence at 700 hPa (b) vorticity at 925 hPa (c) and vorticity at 700 hPa (d) derived from NCEP reanalysis winds during the first phase of ARMEX –II. The rectangular box shown in the map is the ARMEX domain.

The high pressure (indicated by large negative vorticity) in Fig. 4.6(c) at the 925 hPa level prevailing in the north western quarter of the Arabian Sea drives an anticyclonic flow from the Arabian Desert. Attracted by the low pressure over the Indian peninsula [indicated by a slight positive vorticity, in Fig.4.6(c)], this flow speeds up after traversing through the northern Arabian sea and turns southward along the west coast and decelerates as it reaches the southern end of the Indian Peninsula. The wind field at 925 hPa level also

shows a fairly strong convergence at the south western quarter of the Indian land mass [Fig.4.6(a)] which intrudes into the ARMEX domain across the coastal boundary.

At the higher altitude (700 hPa level), the wind speed in general is relatively high. The westerly flow originating (around 22° - 27°N) from Arabia, turns southward in the mid Arabian Sea [Fig.4.6(c)] without reaching the SEAS. But the westerly winds from the latitudes north of 27°N flow a long distance, turn southward near the eastern part of the Indian subcontinent and sweep over the western Bay of Bengal and reach the SEAS after crossing the southern part of the peninsula. The anticyclone at 925 hPa level over the western Arabian Sea is moved westward over to the Arabian land mass at 700 hPa. Similarly, the anticyclone at 925 hPa over the Bay of Bengal has also shifted on to the Indian peninsula at 700 hPa [Fig.4.6(c) and (d)]. The wind convergence which nearly covered the entire Indian landmass in the lower altitude (925 hPa) is replaced by a divergence at higher altitude (700 hPa) as seen in Fig.4.6(b).

Figure 4.7 shows the mean spatial distribution of AOD over the Arabian Sea for the campaign period derived from daily MODIS Level 3 data. The high AOD in the north/north

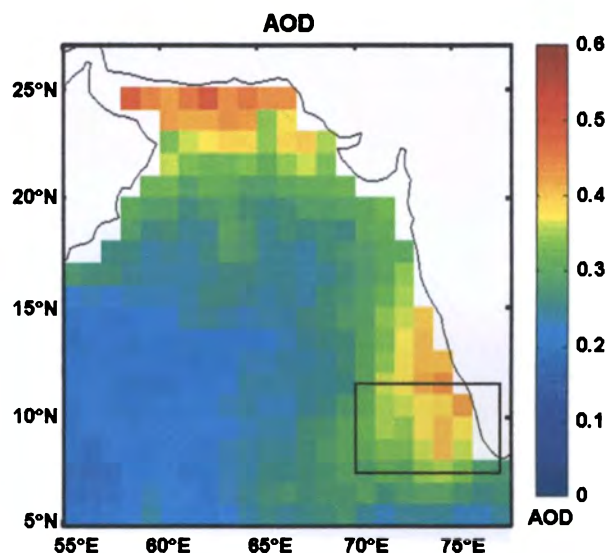


Fig.4.7. Mean spatial distribution of AOD from MODIS over the Arabian Sea during the first phase of ARMEX-II. The rectangular box shown in the figure is the ARMEX domain.

western Arabian Sea is mostly due to direct transport of dust by winds blowing from the adjacent arid regions. This can occur even for low wind speeds ($\leq 5 \text{ ms}^{-1}$) if it is in the appropriate direction [McTainsh, 1980; d'Almeida et al., 1991]. On the other hand, the

increased AOD in the SEAS is mostly due to the accumulation of aerosols by the prevailing convergence at lower altitude [Fig.4.6(a)]. Note that, an increase in aerosol mass concentration near the surface reported in this region during the INDOEX was also mainly attributed to wind convergence [Parameswaran *et al.*, 2001] near the west coast. From the wind pattern at 925 hPa [Fig.4.6(a) and (c)], the origin of these aerosols can be traced back to arid regions of Arabia. Besides wind convergence, wind induced sea salt aerosols and anthropogenic aerosols from the Indian west coast might also contribute to the high AOD observed in this region.

Wind field at 700 hPa [Fig.4.6(b)] show the possibility of advection of aerosols from the continental regions in north western and central parts of India, the Indo Gangetic Plane as well as the east coast of Peninsular India towards the SEAS. However, the contributions from these regions could rather be marginal because of the prevailing wind divergence at this level over the SEAS, favouring dispersal of aerosols rather than accumulation. Earlier studies by Moorthy *et al.*, [2005] using HYSPLIT (Hybrid Single Particle Lagrangian Integrated Trajectory) back trajectories also showed that over the ARMEX site, the aerosols in the lower atmosphere (500 to 1800m) are influenced by the direct transport from West Asian regions, western India and west coast of India. On the other hand, the aerosols at higher levels (above 1800 m) are advected from north west India, central India and Bay of Bengal through long winding trajectories (spending 4 to 7 days). As the time taken for this advection is very large, the contribution by this transport to the observed aerosol system will be relatively small.

As AOD can also be influenced by RH when it exceeds $\sim 70\%$ [Parameswaran, 1996] the effect of this also is to be considered for the analysis. Figure 4.8 shows the mean NCEP vertical profile of RH over the ARMEX domain during the campaign. As seen from this profile, the value of RH is mostly less than $\sim 50\%$ except at the lowest altitude where it exceeds 70%. This shows that the RH induced growth of aerosols (hygroscopic growth) could be marginally significant only at very low altitudes (near the surface) and almost negligible above ~ 300 m.

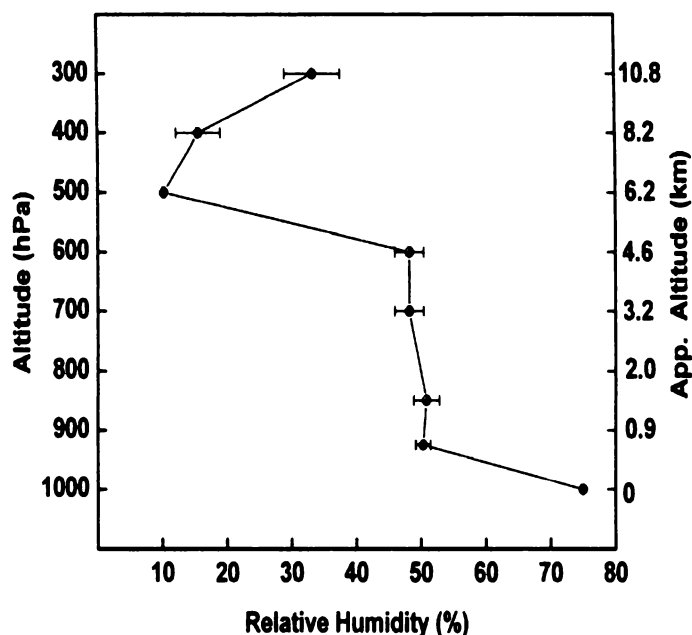


Fig. 4.8. Mean relative humidity from NCEP at different atmospheric altitudes during the first phase of ARMEX-II over the ARMEX domain, along with their standard deviations. Note that the altitude scale on the left axis is shown in pressure levels and the corresponding approximate values in km are shown on the right axis.

4.7 Temporal characteristics of AOD during ARMEX -II

Values of AOD at $0.55 \mu\text{m}$ from MODIS and Microtops (adjusted from $0.50 \mu\text{m}$) along with the FMF from MODIS at the mean positions of the ship on different days along the ship track are shown in Fig.4.9. During the TSL period, the ship was stationary at

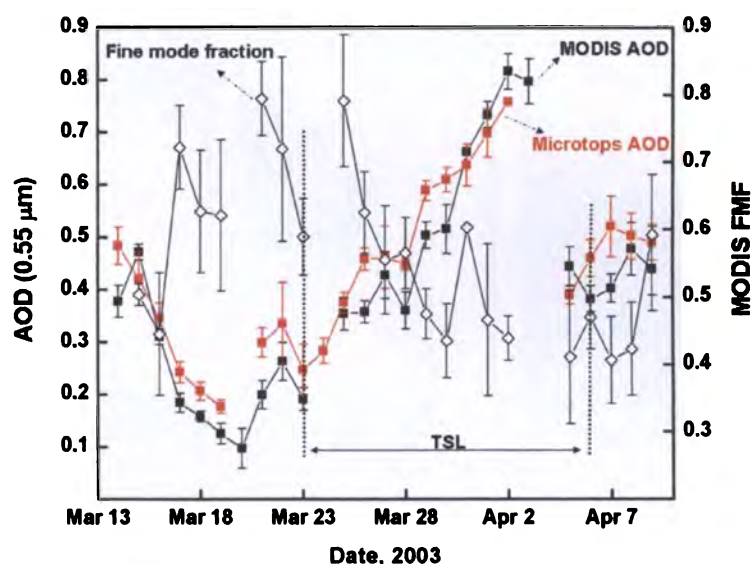


Fig.4.9. Time series plot of AOD from Microtops and MODIS and FMF from MODIS and their standard deviations, during the first phase of ARMEX-II campaign along the cruise track. Time series during the TSL period is marked in the figure.

9.2°N, 74.5°E. It can be seen that the temporal variation of FMF in general, is in opposite phase with that of AOD. A fairly good agreement between the time sequence of FMF in this figure and that of Angstrom exponent shown in Fig.4.3 is observable.

A close examination on the spatial distribution of AOD from MODIS over the Arabian Sea reveals that most of the prominent variations recorded on the ship could be associated with the southward migration of clusters of aerosols along the west coast of peninsular India. This aspect is studied in detail by examining the time evolution of the spatial pattern of MODIS derived AOD during the period when the AOD measured on the ship showed pronounced day-to-day variations. Figure 4.10 shows the AOD distribution from MODIS on some selected days between March 14 and April 06, 2003 when significant AOD variations were observed on the ship. The location of the ship is indicated by a star '☆' symbol.

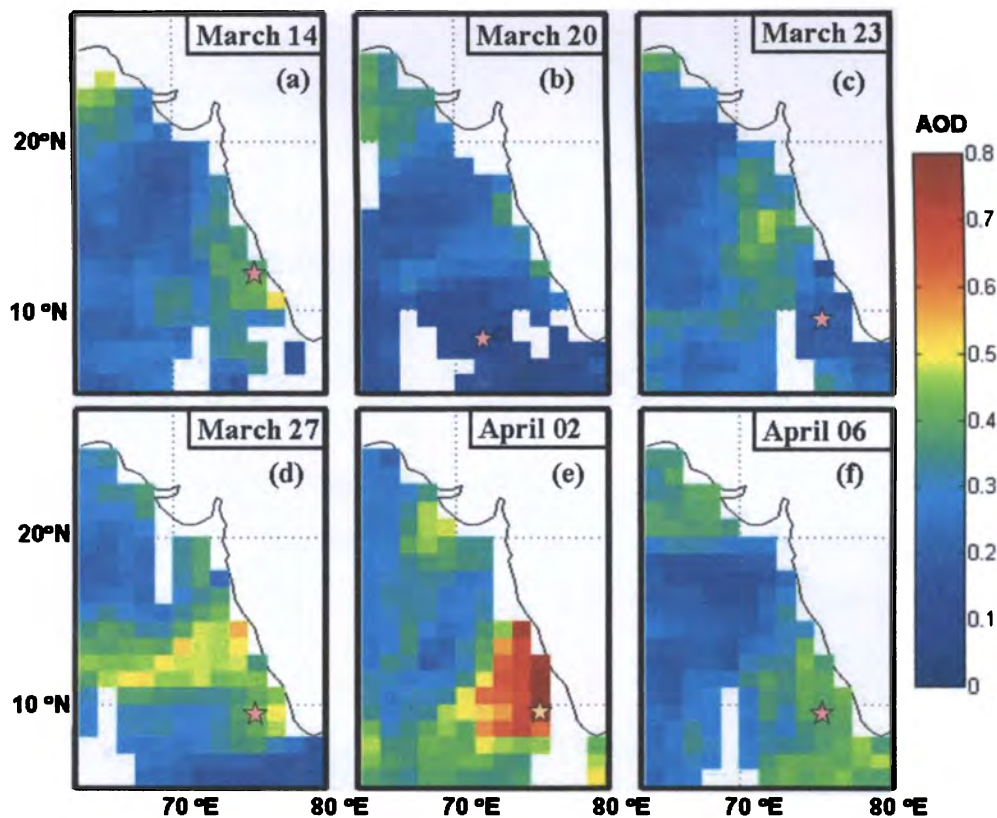


Fig.4.10. Spatial distribution of AOD from MODIS over the Arabian Sea on March 14 (a) March 20 (b) March 23 (c) March 27 (d) April 02 (e) and April 06, 2003 (f) depicting the movement of aerosol clusters along the west coast of India, during the first phase of ARMEX-II. 'Star' denotes the mean position of Sagar Kanya on the respective dates.

The moderately high AOD seen in Fig.4.9, at the start of the cruise (from Mangalore) on March 14 is due to the presence of a weak aerosol cluster in the vicinity of the ship [Fig.4.10(a)]. Subsequently, this cluster moves (southwards) away from the ship and disperses in 4-5 days after reaching the southern end of the land mass. Associated with this movement, the AOD measured on the ship reduces and remains more or less low till March 20. Meanwhile, another aerosol cluster that formed around $\sim 17^\circ$ N by March 20 [Fig.4.10(b)] starts moving southwards parallel to the west coast to approach the ship which was stationed at the TSL. During its movement the cluster also intensifies. As it nears the ship by March 23 [Fig.4.10(c)], the AOD on the ship starts increasing [Fig.4.9]. The AOD on the ship reaches its peak value (> 0.8) on April 02 [Fig.4.9] when the cluster has almost totally engulfed the ship [Fig.4.10(e)]. On subsequent days, as the cluster moves out further, the AOD on the ship decreases [Fig.4.9]. After reaching the tip of the Indian peninsula by \sim April 06 the cluster disperses [Fig.4.10(f)]. Thus the time variation of AOD observed on the ship is closely linked to the dynamics of the southward migrating aerosol clusters along the west coast of Indian peninsula.

A striking feature in Fig.4.9 is the high values of AOD nearly synchronising with the low values of FMF and α (Fig.4.3). This is possible only if the particles constituting the aerosol plume are predominantly coarse mode, which is likely if the cluster consist of mineral dust or sea-salt particles produced in the high wind regime near the north western coast of India. Considering the wind speed dependence of sea salt production reported by various authors [*Blanchard and Woodcock, 1980; Moorthy and Satheesh, 2000; Smirnov et al., 2003; Satheesh et al., 2006b*], its contribution to the observed high values of AOD would not be substantial since sea surface winds over the Indian west coast on an average are not strong enough [Fig.4.5]. This suggests that the cluster is mostly composed of mineral dust originating from the arid parts of Arabia.

4.8 Influence of circulation and RH on the day-to-day variation of AOD over the ARMEX domain

Motivated by the above observations, which showed a close association between wind field and AOD variations, a detailed investigation is carried out to establish the role of circulation parameters (wind speed and convergence) and RH on the observed variation of AOD over the ARMEX region. For this, daily AOD values at $0.55 \mu\text{m}$ from MODIS along

with wind field and RH from NCEP reanalysis are utilized. The four parameters considered for this exercise are

(1) Change in AOD per day

$$V_1 = \tau_2 - \tau_1 \quad (4.1)$$

where τ_2 corresponds to AOD in a pixel of the ARMEX domain on a given day and τ_1 that on the previous day. In a pair of successive days, only those pixels for which data is available on both the days are considered for computing V_1 .

(2) Horizontal surface (1000 hPa) wind speed

$$V_2 = \sqrt{[u(1000\text{hPa})]^2 + [v(1000\text{hPa})]^2} \quad (4.2)$$

where u and v refer to meridional and zonal components of vector wind.

(3) Column integrated aerosol flux convergence

The accumulation of aerosols due to wind convergence is expressed through an appropriate physical quantity - the convergence of aerosol flux which is the product of aerosol concentration and wind. Column integrated aerosol flux convergence is defined by

$$V_3 = - \int_0^{z_u} \left\{ \frac{\partial}{\partial x} [\beta(z)u(z)] + \frac{\partial}{\partial y} [\beta(z)v(z)] \right\} dz \quad (4.3)$$

where z corresponds to altitude and z_u is the upper limit of integration (equivalent to 400 hPa here) and β is the aerosol extinction coefficient (a measure of aerosol concentration) related to MODIS derived AOD (τ) as

$$\beta(z) = \frac{\tau}{H_a} \exp\left(-\frac{z}{H_a}\right) \quad (4.4)$$

where H_a is the aerosol scale height which governs the rate of decrease of β with altitude. By varying H_a , the weightage given to the altitude extent for the influence of wind to the aerosol flux can be varied. Larger the values of H_a , higher the altitude up to which the wind would affect aerosol flux. For the present analysis, the value of H_a is varied from 0.5 to 4 km (0.5, 1, 2, 3 and 4 km).

4) Relative humidity

Since RH exceeds ~ 70% only in the lowest altitude (Fig.4.8), its value in this level alone is considered for the present analysis. It is therefore assumed that the RH at the higher altitudes does not cause any hygroscopic growth of the aerosols. This variable at 1000 hPa is named as V_4 .

Making use of the above four variables, partial correlations of V_1 with the other variables (V_2 , V_3 and V_4) are estimated. Partial correlation is an index for the dependence between the two parameter (say V_1 and V_2 as typical example) in the absence of any influence from the other variables (V_3 and V_4 in the present case).

The partial correlation between the variables 'a' and 'b' is thus defined as [Spiegel and Stephens, 2000; Gupta, 2005],

$$R_{ab.cd} = \frac{R_{ab,d} - R_{ac,d} \cdot R_{bc,d}}{\sqrt{(1 - R_{ac,d}^2)(1 - R_{bc,d}^2)}} \quad (4.5)$$

where each $R_{xy,z}$ is the partial correlation between 'x' and 'y' in the absence of 'z' given by

$$R_{xy,z} = \frac{R_{xy} - R_{xz} R_{yz}}{\sqrt{(1 - R_{xz}^2)(1 - R_{yz}^2)}} \quad (4.6)$$

where R_{xy} , R_{xz} etc. represent the cross correlations between 'x' and 'y', 'x' and 'z', etc. Since the NCEP reanalysis variables are available only at $2.5^\circ \times 2.5^\circ$ resolution, the AOD data from MODIS is degraded to this resolution. Details of aerosol flux convergence computations incorporating AOD from MODIS (taking care of the blank pixels) and wind field from NCEP-as well as the integration over the altitude required for the computation of V_3 [Eq.(4.3)] are detailed in Chapter 2 (Sect. 2.7.1). The quantities V_1 , V_2 , V_3 and V_4 are averaged over the ARMEX domain (excluding the land and coastal pixels) for each day during the campaign period (except for the first day for which V_1 is not defined). Since the physical mechanisms represented by V_2 , V_3 and V_4 operate in a continuous manner, these quantities are further averaged over the two days in each successive pair.

4.8.1 Discussion of the results

When the partial correlations of V_1 with V_2 , V_3 and V_4 (i.e., $R_{12,34}$, $R_{13,24}$ and $R_{14,23}$ respectively) are computed for the TSL period during when the event of AOD enhancement linked with the passage of the aerosol cluster took place, both V_3 and V_4 show significant correlation with V_1 . This shows that the AOD variation is significantly influenced by wind convergence and RH (near the surface). The estimated partial correlations for different values of H_a during the TSL period are presented in Table. 4.2.

Table 4.2. Variation of partial correlation coefficients $R_{12,34}$, $R_{13,24}$ and $R_{14,23}$ computed for different aerosol scale heights during the TSL period over the ARMEX domain.

Scale height H_a (km)	Partial correlation with surface wind ($R_{12,34}$)	Partial correlation with convergence ($R_{13,24}$)	Partial correlation with RH ($R_{14,23}$)
0.5	< 0.1	0.55	0.27
1	< 0.1	0.69	0.52
2	< 0.1	0.64	0.48
3	< 0.1	0.49	0.28
4	< 0.1	0.42	0.21

Among the three partial correlations, $R_{13,24}$ and $R_{14,23}$ are significant while the $R_{12,34}$ is totally insignificant. The values of $R_{13,24}$ and $R_{14,23}$ increase with increase in H_a and attain maximum values, 0.69 ($p < 0.02$) and 0.52 ($p < 0.1$) respectively for $H_a = 1$ km and subsequently decreases with further increase in H_a .

Increase in the value of H_a , in effect includes the contribution of winds from higher altitudes in the flux convergence calculation. The initial increase of $R_{13,24}$ with increase in H_a indicates that convergence in winds close to the surface is inadequate for explaining the observed modulation of AOD. At the same time, the decrease of $R_{13,24}$ for H_a above 1 km indicates that the weightage of winds from higher altitudes (through convergence) is unimportant as far as the AOD variations are concerned. Thus for an optimum value of $H_a \sim 1$ km, the winds in the altitude region above the surface up to around 1 km, in the form of flux convergence, significantly influence the observed AOD variations. Figure 4.11 depicts

the time series of AOD change per day and flux convergence over the domain for $H_a = 1$ km. These two parameters show a fairly good correspondence during the TSL period.

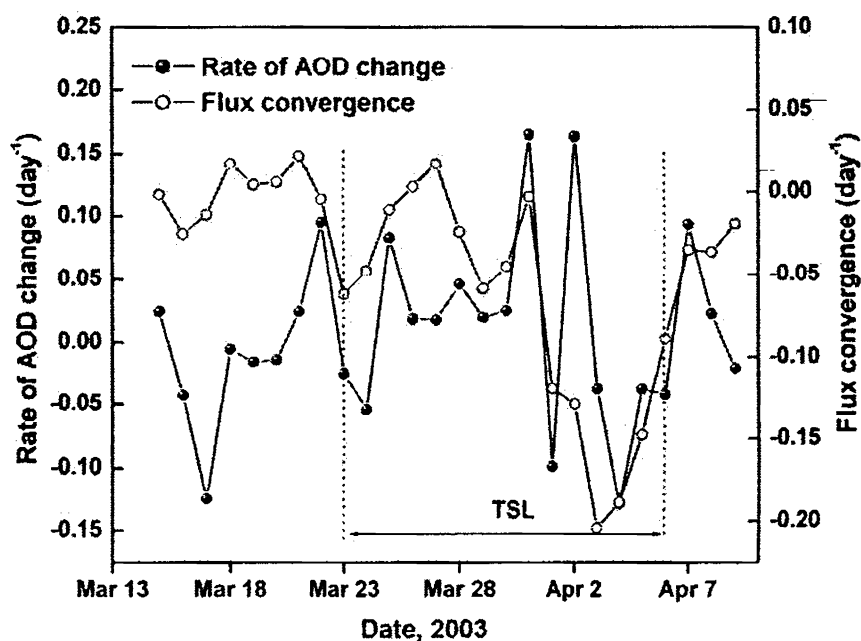


Fig.4.11. Time series plot showing the rate of AOD change along with the flux convergence computed for aerosol scale 1 km height averaged over the ARMEX domain, during the first phase of ARMEX-II. Time series during the TSL period is marked in the figure.

The partial correlation $R_{14,23}$ also shows an increase with increase in H_a from 0.5 to 1 km, which is followed by a decrease for further increase in H_a , exactly similar to the case for $R_{13,24}$ shown in Table. 4.2. This can be attributed to the fact that the interference from flux convergence on the partial correlation of AOD change with RH decreases as H_a increases from 0.5 to 1 km and increases for further increase in H_a . This analysis shows that the AOD variation is mainly influenced by flux convergence in the altitude region below ~ 1 km as well as RH near the surface.

The mean vertical wind over the ARMEX domain during the TSL period is presented in Fig.4.12. An important feature to be noticed in this figure is the change in the vertical wind above 925 hPa. An updraft prevailing in the lower altitude changes to a downdraft at levels above 925 hPa. This change in wind direction leads to confinement of aerosols below ~ 1 km.

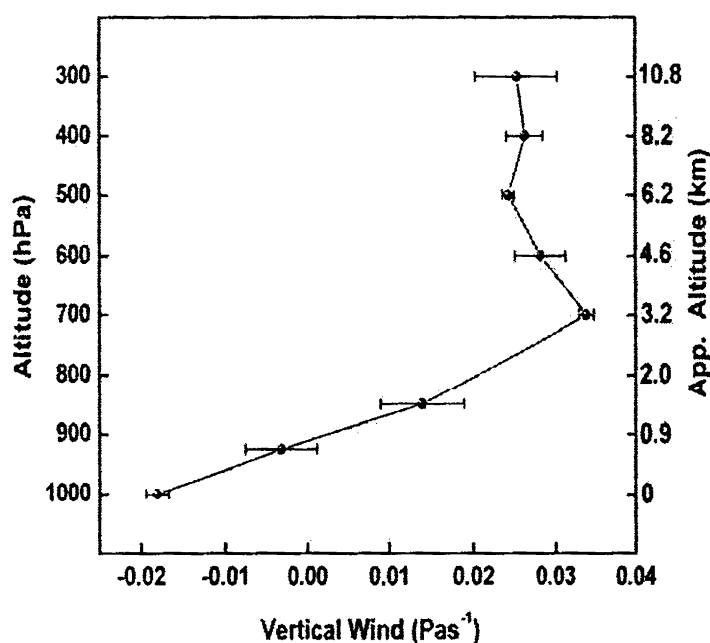


Fig.4.12. Mean vertical wind from NCEP at different atmospheric altitudes along with the standard deviation, during the TSL period over the ARMEX domain. Note that the altitude scale on the left axis is shown in pressure levels and the corresponding approximate values in km are shown on the right axis.

The low value of $R_{12,34}$ in Table.4.2 indicates that the influence of local surface wind in modulating the AOD over the ARMEX domain is insignificant. But the moderate correlation of AOD with RH ($R_{14,23}$) is an indirect indicator for the presence of wind generated hygroscopic marine aerosols over the ARMEX domain inspite of the prevailing low surface wind speeds [Fig.4.5]. In order to investigate this feature, the wind field in the vicinity of the ARMEX domain is examined in detail.

A perusal of Fig.4.5 reveals a region of relatively high wind speed in the upwind direction (north/north west of the ARMEX domain). The surface wind in this region is high particularly during the TSL period. Figure 4.13 shows the distribution of QuikSCAT winds averaged over the period, March 29 – April 01, 2003, when the wind speeds over the eastern Arabian Sea reached it peak value of $\sim 7 - 8 \text{ ms}^{-1}$. These high wind speeds are conducive for the production of sea-salt aerosols. This *in situ* generated sea-salt aerosols are further transported in the downwind direction by the prevailing wind. This aspect is investigated in detail by considering a zone, $12.5^\circ - 20^\circ\text{N}$ and $67.5^\circ - 75^\circ\text{E}$ over the high wind region (indicated by the purple border box in Fig.4.13). The correlation between the surface wind speed at this location with the AOD over the ARMEX domain is calculated for different time lags. The time sequences of QuikSCAT wind speed (in the purple box)

and the AODs averaged over the ARMEX domain (black box) are presented in Fig.4.14. It can be seen that the correlation attains a maximum value ~ 0.66 corresponding to a time lag of two days.

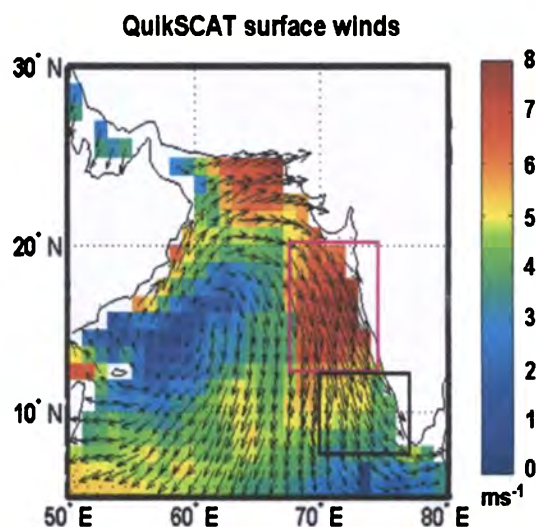


Fig.4.13. QuikSCAT surface winds averaged for the period March 29 – April 01, 2003 during the TSL period. The purple border box encloses the high wind speed region in the upwind direction from the ARMEX domain indicated by black border box.

Now, considering the mean wind speed of 4.5 ms^{-1} observed over the high wind region during the TSL period, the time required for an aerosol cluster to travel from the

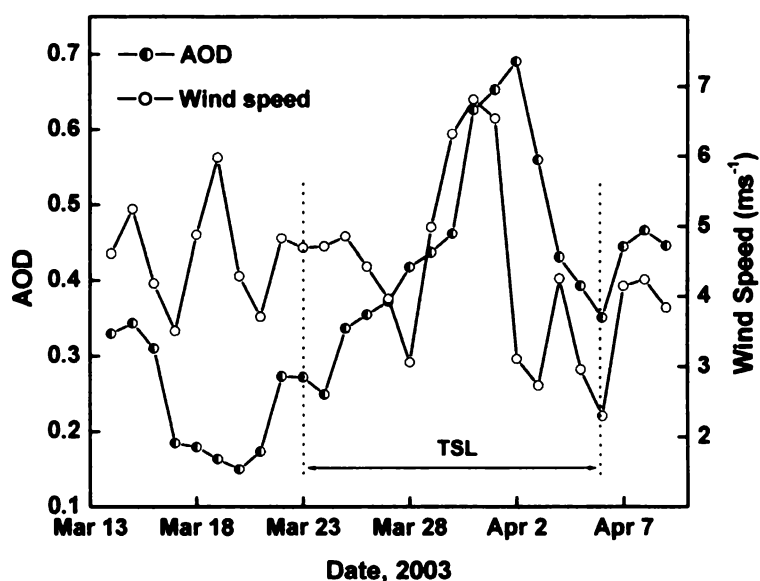


Fig.4.14. Time sequence of MODIS derived AOD averaged over the ARMEX domain and wind speed averaged over the high wind speed region in the upwind direction. Time series during the TSL period is marked in the figure.

location of high wind speed (middle of the purple bordered box in Fig.4.13) to the ship's location (in TSL) is around two days. This indicates the possibility of marine aerosols generated in the high wind region subsequently transported by the prevailing wind also contributing to the observed AOD variations over the ARMEX domain. However, this contribution to the observed AOD may not be substantial as the wind speed in the upwind domain (purple box) is rather moderate.

4.9 Summary

A comparison of MODIS derived spectral AOD with the Microtops measurements collected onboard the ship during the ARMEX-II campaign yields good agreement with correlation coefficients 0.96 – 0.97 and mean deviations around 0.04. The Angstrom exponents computed from the spectral AODs (of MODIS and Microtops) also shows a good correlation of 0.72. This indicates that the MODIS derived AOD compares favourably with direct measurements.

This chapter mainly deals with an investigation on the mechanism of aerosol transport over the South East Arabian Sea (SEAS) during ARMEX-II period (March 14 – April 10, 2003) and the role played by wind field and relative humidity (RH) in the observed AOD modulation at the Time Series Location (TSL). Studies on the spatial distribution of AOD from MODIS during ARMEX-II reveals that the episodic enhancement and decay of AOD observed over the study region during the TSL period (March 23 to April 06, 2003) is caused by the southward migration of an intensifying aerosol cluster along the west coast and its subsequent dispersal at the southern tip of the Indian peninsula. The decrease of Angstrom exponent and fine mode fraction coinciding with this event reveals that this aerosol cluster is dominated by coarse mode particles. The prevailing wind system during the campaign period over the Indian land mass and the adjoining oceanic region indicates that the most probable factor contributing the aerosols within the cluster is the mineral dust transported from the arid regions of Arabia through the lower altitude winds which converges over the SEAS. At the same time, transport at higher altitudes seems unlikely, since these winds have to travel long distance through the central India and the Bay of Bengal to reach the ARMEX domain, losing considerable amount of coarse mode aerosols on its way. Added to this, the presence of a divergence at the upper level over the SEAS is not conducive for the accumulation of aerosols at higher altitudes.

The influence of circulation variables (wind convergence and surface wind speed) and relative humidity on the day-to-day variation of AOD over the ARMEX domain is investigated further using NCEP reanalysis winds, RH and MODIS data. A partial correlation analysis is employed to examine the influence of each of these parameters (aerosol flux convergence, surface wind speed and surface RH which are treated as independent variables) on the observed AOD variations (treated as the dependent variable). When the entire period is considered, none of these variables shows any notable influence on AOD variations. However, when the analysis is confined to the TSL period, while the ship was stationary at $\sim 9.2^{\circ}\text{N}$, 74.5°E , the observed time variation of AOD is found to be significantly influenced by flux convergence at low altitudes (partial correlation, 0.69). During this period, RH near the surface also appears to affect the AOD variation to some extent (though not as strongly as the flux convergence), notwithstanding the fact that the surface wind speed over the domain is rather small.

Even though the aerosol production due to local surface winds at the TSL is negligible (because of very low wind speeds), relatively large wind speed over a domain in the upwind direction is conducive for aerosol generation. The wind speed at this location shows a good correlation ($R=0.66$) with AOD measured over the ARMEX domain with a time lag of two days, showing the influence of transport dynamics. This, along with the moderate partial correlation of AOD with RH indicates that, during the TSL period the contribution of wind generated hygroscopic marine aerosols from the high wind area to the total aerosol load over the ARMEX domain may not be insignificant. However, as the wind speeds are rather moderate, this contribution is not substantial as far as the total AOD over the ARMEX domain is concerned. The main contributor to the observed high AOD during the TSL period, thus remains to be mineral dust originating from the arid regions of Arabia.

These factors along with the close correspondence between MODIS column mass concentration and the QCM measured coarse mode mass concentration onboard the ship suggests that the aerosol plume encountered during the TSL period, is mostly composed of coarse mode mineral dust particles which is more or less confined to the lower atmospheric altitudes (< 1 km).

Chapter 5

Influence of circulation parameters on aerosol distribution over the Bay of Bengal during the pre-monsoon period: ICARB (Phase I)

5.1 Introduction

Surrounded by land mass with diverse natural and anthropogenic activities on all the three sides, the Bay of Bengal (BoB) is a unique oceanic region conducive for studying the intrusion of continental aerosols in to the pristine oceanic environment through various pathways. The physical and chemical properties of aerosols and their abundance in this region show significant variations with changes in meteorological conditions and seasonal changes in the synoptic circulation [*Satheesh et al.*, 2006a] over the continent.

Major efforts for aerosol studies over the BoB commenced with the ship cruise in 2001 which was followed by a few other short term campaigns in 2003 [*Satheesh et al.*, 2006a]. An aerosol observatory was set up in 2002 over the island location, at Port Blair (11.63°N, 92.71° E), mainly to address the seasonal, annual, interannual and long term variations in aerosol properties over the BoB and to identify the physical processes responsible for these variations [*Moorthy et al.*, 2003]. These ground based observations along with satellite measurements revealed strong anthropogenic influence on the aerosol properties over this oceanic region [*Satheesh et al.*, 2001; *Moorthy et al.*, 2003; *Ramachandran and Jayaraman*, 2003; *Vinoj et al.*, 2004b]. Studies based on satellite data

(NOAA and MODIS) showed that the influence of continental aerosols is maximum during the pre-monsoon period [Nair *et al.*, 2003; Satheesh *et al.*, 2006a]. These studies further revealed that the three major regions influencing the aerosol system over the BoB are the central and east coast of India, China/East Asia and Arabia [Satheesh *et al.*, 2006a].

In 2006, ISRO-GBP organized a major field experiment, ICARB (Integrated Campaign for Aerosols, gases and Radiation Budget) in which simultaneous observations on aerosols were carried out from the Indian land mass and the surrounding oceanic regions including the BoB during the pre-monsoon season [Moorthy *et al.*, 2008]. These observations yielded a wealth of data that enables a detailed understanding of aerosol properties and the influencing features of related transport dynamics.

5.2 Integrated Campaign for Aerosols, gases and Radiation Budget (ICARB)

ICARB was an exhaustive field campaign ever carried out over the Indian region. This included aerosol measurements over the Indian landmass using a network of ground stations, ship cruises over the adjoining oceans and aircraft sorties in the lower atmosphere. The main theme of the campaign was to investigate the spatio-temporal heterogeneity of aerosols, influence of long-range transport and regional meteorology on aerosol properties, the nature of aerosol vertical distribution and finally, the impact of aerosols on regional radiative forcing [Moorthy *et al.*, 2008]. The cruise measurements were made onboard ORV Sagar Kanya, in two phases: the first phase over the BoB (SK223 A), from March 18 to April 12, 2006 and the second phase over the Arabian Sea (SK223 B) from April 18 to May 11, 2006.

The work presented in this chapter deals with an investigation on the aerosol transport mechanism as well as the role of atmospheric circulation in modulating the aerosol properties over the BoB during the first phase of ICARB. An attempt is also made to study the spatial distribution of aerosol source strength over the BoB using the flux continuity equation. The geographical domain considered for this study is enclosed within 10° - 22.5° N and 80° - 95° E (referred hereafter as the study domain). The cruise track over the BoB during the campaign (SK223 A) is presented in Fig.5.1

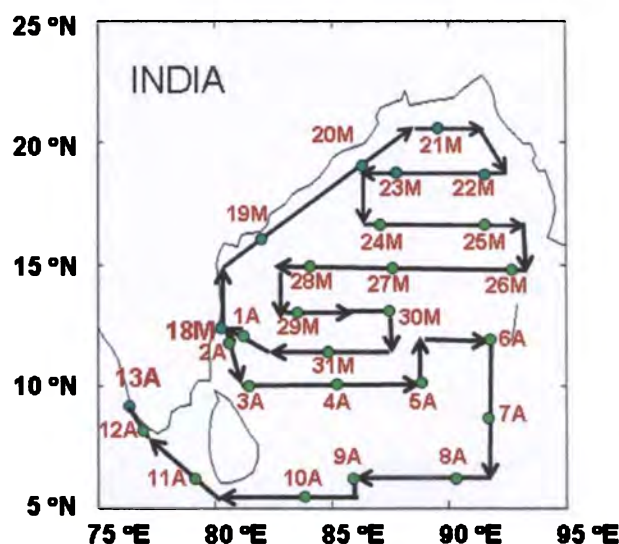


Fig.5.1. Cruise track of SK223 A over the BoB from March 18 to April 12, 2006. Green dots represent the position of the ship every 5:30 UTC. Dates are marked near the points with suffix 'M' for March and 'A' for April.

5.3 Data

Spectral AOD measurements were carried out onboard Sagar Kanya on all the days using a Microtops sunphotometer (Solar Light Co.) at the wavelengths 0.34, 0.44, 0.50, 0.675 and 0.87 μm from \sim 07:00 to 17:00 IST at \sim 20 minutes interval avoiding cloudy conditions (Chapter 2, Sect.2.3).

The $1^\circ \times 1^\circ$ AOD and FMF data from Terra and Aqua satellites are optimally averaged to obtain the daily mean values from MODIS (Chapter 2, Sect.2.2.7). The NCEP reanalysis wind fields at seven pressure levels from 1000 to 400 hPa are used to examine the prevailing aerosol transport mechanism. QuikSCAT data on ocean surface wind (averaged over the descending and ascending passes) is used to assess the *in situ* production of marine aerosols over the study domain.

For studying the influence of transport dynamics, a clear understanding on the altitude distribution of aerosols is very crucial. The space borne Lidar onboard CALIPSO (Cloud Aerosol Lidar and Infra-red Pathfinder Satellite Observations) provides the vertical structure of aerosol extinction (Chapter 1, Sect.1.9.2.17) at regular intervals. Being a member of A-Train satellites, CALIPSO follows MODIS Aqua satellite in the same track with a lag of \sim 2 minutes. As CALIPSO is operational only since mid-June 2006, a mean aerosol extinction profile at 0.532 μm is generated by averaging the extinction over the

study domain during the March – April period for the years 2007 and 2008. This profile is normalized with respect to the columnar AOD measured by MODIS at the same location, for getting the information on the prevailing altitude structure of aerosols on a particular day at the specific location. Details of this procedure are presented in Sect.5.8.2.

5.4 Comparison of AOD from MODIS with ship measurements

Before examining the aerosol transport and the related dynamics over the BoB, the quality of MODIS derived AOD over the study domain during the pre-monsoon period is assessed by comparing it with ground-based direct measurements. The Level 3 daily AOD (at 0.55 μm) from MODIS at $1^\circ \times 1^\circ$ grids encompassing the cruise track are averaged to derive the daily mean AOD corresponding to the mean position of the ship. A comparison is carried out between this mean AOD (τ_{MODIS}) and the daily mean ship borne Microtops measurements ($\tau_{\text{Microtops}}$). As the 0.55 μm channel is not available in Microtops, the AOD at 0.50 μm is adjusted (or normalized) to 0.55 μm using the Angstrom exponent [Chapter 3, Eq.(3.1)] derived from the Microtops spectral AODs through a logarithmic regression. Figure 5.2 shows a scatter plot between the two AOD measurements and their respective standard deviations. This plot shows a very good agreement between the two AOD values. A linear correlation established between the two yields a correlation coefficient of 0.85, which is significant at $p < 0.01$ level. The standard deviation between the two measurements is 0.09. MODIS underestimates the AOD on an average, by 0.07. A least square fit of these values yields a linear regression with slope 0.86 and intercept -0.03 .

A similar comparison between Microtops AOD and that from Terra alone [Aloysius *et al.*, 2008] yielded a lower value for the intercept (-0.005) and a higher value for the slope (0.98) with a standard deviation of 0.06 and a mean underestimate of 0.01 for MODIS derived AOD. These values show that the agreement between the two AOD values is better than that obtained by optimally combining the Aqua and Terra, discussed above. But since optimally combined data has the advantage of maximum spatial coverage (necessary for meeting the basic requirement for the study of transport dynamics) they (τ_{MODIS}) are used for the present study even though its agreement with the Microtops measurements is marginally inferior.

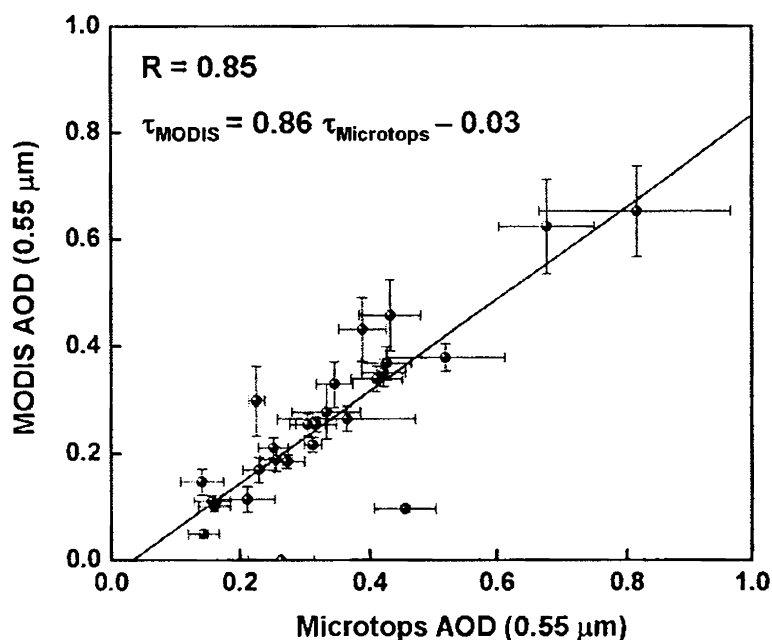


Fig.5.2. Scatter plot of AODs from MODIS and Microtops (0.55 μm) and their standard deviations. Correlation coefficient and the regression relation are shown in the figure.

5.5 Circulation variables and spatial distribution of aerosols over the BoB

A detailed investigation is carried out to study the AOD distribution over the BoB and its contribution from fine (particle radius $< 0.1 \mu\text{m}$) and coarse (particle radius $> 0.1 \mu\text{m}$) mode particles. The AOD due to fine mode particles are estimated by multiplying the total AOD with the FMF. The difference between AOD and fine mode AOD gives the coarse mode AOD. The spatial distribution of total AOD and fine mode and coarse mode AODs (fmAOD and cmAOD respectively) during the first phase of ICARB over the BoB are presented in Fig.5.3(a) and Fig.5.3(b) respectively. In order to highlight the contrast between the three cases, a two times expanded colour scale is used for Fig.5.3(b).

During the study period, AOD data is available for 20-25 days over most of the BoB region except in the south eastern corner ($\sim 5^\circ\text{-}12^\circ\text{N}$, $88^\circ\text{-}95^\circ\text{E}$) where data is available for only 10 to 20 days. The mean standard deviation of AOD presented in Fig.5.3(a) is $\sim 10\%$. Values of AOD in general, are large near the Head BoB and along the east coast of peninsular India. The contribution of fine mode is much larger ($\sim 60 - 70\%$) than that of coarse mode in most of the regions, except over the Head BoB where both the contributions

are nearly equal. Large fraction of fine mode implies significant advection of continental/anthropogenic particles from the adjoining continents.

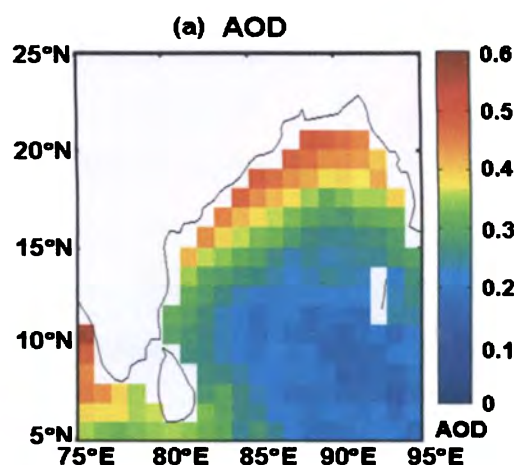


Fig.5.3(a). Mean spatial distribution of AOD over the BoB during the first phase of ICARB, obtained from MODIS.

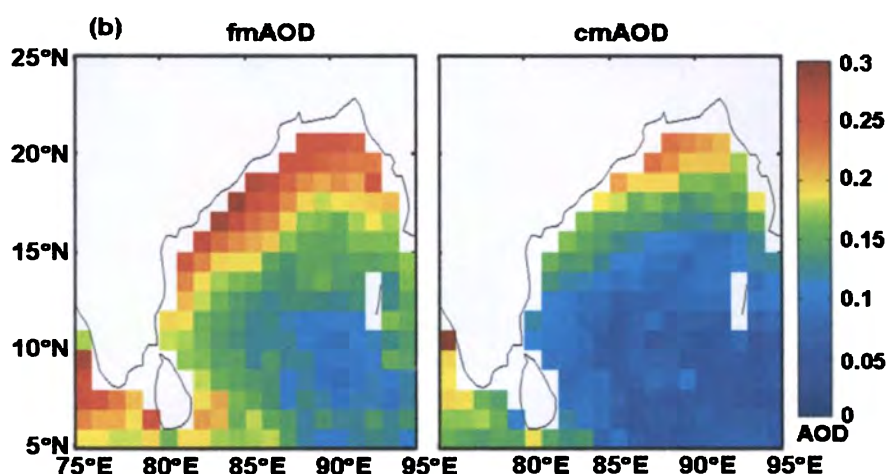


Fig.5.3(b). Mean spatial distribution of fine mode AOD (fmAOD) and coarse mode AOD (cmAOD) over the BoB during the first phase of ICARB, obtained from MODIS.

High aerosol loading near the east coast of peninsular India during the winter and pre-monsoon period and an increase in its encompassed area from November to April have been reported in a few earlier studies based on satellite data [Nair *et al.*, 2003; Aloysius *et al.*, 2006; Satheesh *et al.*, 2006b; Parameswaran *et al.*, 2008]. Ship-based campaigns have also revealed large abundance of sub-micron particles over the BoB, compared to that over the Arabian Sea and the Indian Ocean [Satheesh *et al.*, 2001; Ramachandran and Jayaraman, 2003; Vinoj *et al.*, 2004b]. These observed aerosol features and temporal

variations were attributed to seasonal changes in lower tropospheric circulation (without much quantitative support).

In the present study, the QuikSCAT measured ocean surface wind and the NCEP reanalysis wind at different altitudes are examined to delineate the influence of the wind field on the spatial distribution of AOD over the BoB and its day-to-day variations during the campaign period. Figure 5.4(a) shows the mean NCEP winds at 925 hPa level (~ 700 m) over the Indian subcontinent and the surrounding oceanic regions during the campaign period. Figure 5.4(b) shows the mean surface wind over the BoB derived from the QuikSCAT data. The region enclosed by the rectangular box (10° - 22.5° N, 80° - 95° E) is the study domain.

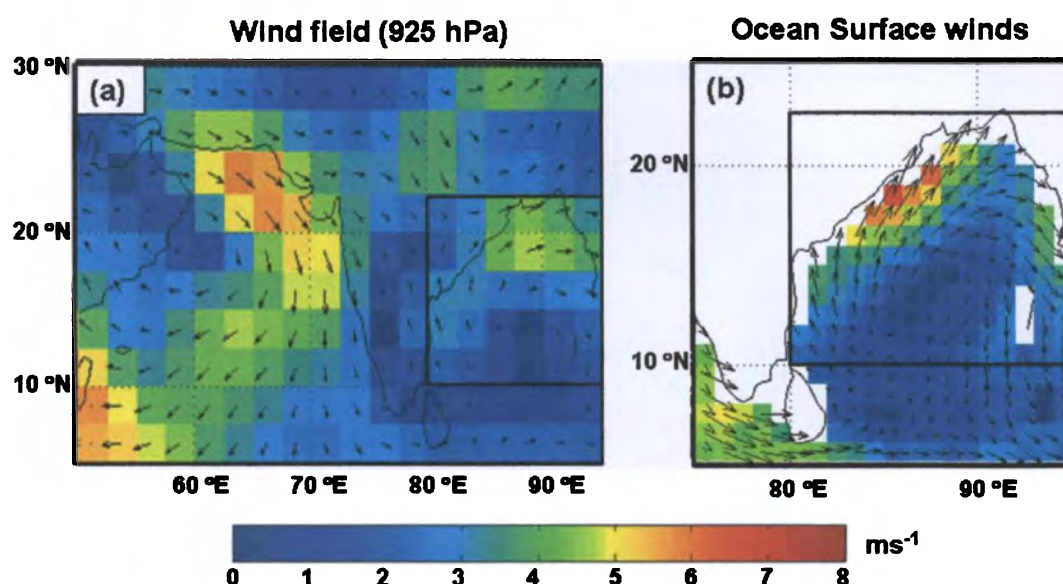


Fig.5.4. Mean spatial distribution of wind field at 925 hPa over India and the surrounding oceanic regions from NCEP reanalysis (a) and surface wind from QuikSCAT over the BoB (b) during the first phase of ICARB. The area contained by the rectangular box in both the figures is the study domain.

Being direct measurement, the QuikSCAT wind over the ocean, is superior to NCEP reanalysis. As seen in Fig.5.4, over the Indian landmass the wind speed is rather small, but near the east coast over the BoB, it is relatively high ($\sim 7\text{ms}^{-1}$) suggesting the possibility of *in situ* generation of sea-salt aerosols. But, it is not high enough to cause an increase in AOD over the entire region as much as what is observed. In this context it is highly essential to look for other factors, which could be responsible for the increase in AOD along the east coast and Head BoB.

Figure 5.5 shows the vorticity and convergence estimated from the NCEP winds at 925 and 700 hPa levels. The low altitude vorticity [Fig. 5.5(a)] shows the presence of a strong anticyclone over the north western Arabian Sea. The strong winds associated with this anticyclone can inject particles from the Arabian deserts and from the arid regions in the north western parts of India over to northern and central India, which will be transported

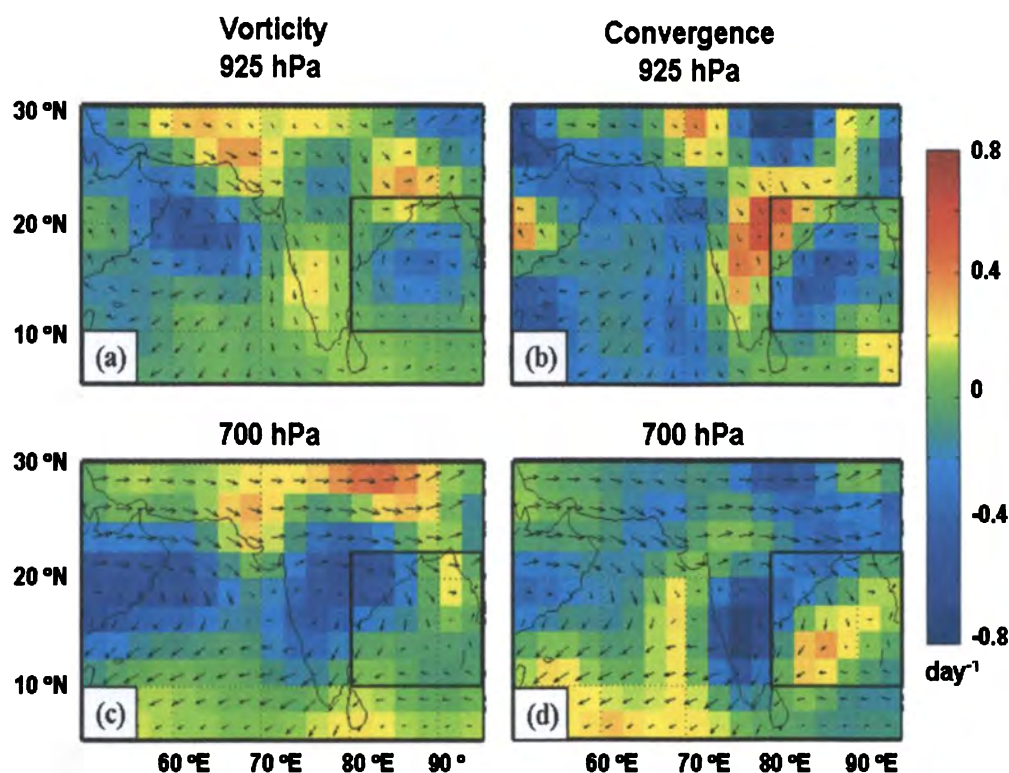


Fig.5.5. Spatial distribution of vorticity at 925 hPa (a) convergence at 925 hPa (b) vorticity at 700 hPa (c) and convergence at 700 hPa (d) averaged for the first phase of ICARB.

further towards the eastern part of peninsular India. In this location attracted by the low pressure the wind converges [Fig. 5.5(a) and (b)], leading to an accumulation of the particles. However, the high pressure (anticyclone) and divergence prevailing over the BoB [Fig.5.5(a) and (b)] prevent a direct entry of these particles over to the BoB. But the south westerly winds along the regions of northern Andhra Pradesh and Orissa, where the observed surface aerosol mass concentration is high [Niranjan *et al.*, 2008], can carry aerosols to the north western parts of the BoB.

The updrafts associated with the cyclonic circulation in the lower altitude in the western and eastern parts of the Indo Gangetic Plain as well as the updrafts along the West Asian regions [Fig.5.5(a)] can lift particles to higher altitudes. Subsequently the prevailing

wind transport these aerosols over to the BoB through higher altitudes [Fig.5.5(c) and (d)]. The wind convergence in this altitude over the BoB [Fig.5.5(d)] and the anticyclone extending from the peninsula [Fig.5.5(c)] favours the accumulation and downdraft of aerosols in this location leading to subsidence and subsequent spreading along the east coast by the low level divergence [Fig. 5.5(b)]. Thus, the circulation variables which drive, accumulate and disperse aerosols appear to play a crucial role in determining the spatial distribution of AOD over the BoB.

5.6 Aerosol transport over the BoB

Realizing the possibility of transport of aerosols from the Indian land mass to BoB (as discussed in the previous section), an attempt is made to explore the finer details of the associated mechanism. A vertical cross section of the atmosphere in a diagonal direction from Central India through the Gangetic plain to the mid-BoB, as shown in Fig.5.6(a) and (b), is considered for this analysis. The nature of the vertical wind and the strength of horizontal convergence at different levels on this vertical plane are indicated respectively in these two figures.

As stated, a major part of the horizontal advection of air from the continent to the BoB is through higher altitudes. Figure 5.6(a) shows a subsidence (in vertical wind) from higher altitudes and an updraft at lower altitudes over the land (marked by region A). This leads to confinement of particles around 700 – 600 hPa level. The divergence at these altitudes [Fig.5.5(d) and the region marked B in Fig.5.6(b)] and direction of the horizontal winds guide these particles towards the ocean where the wind convergence [Fig.5.5(d) and the region marked C in Fig.5.6(b)] traps them and are brought all the way down by the subsidence [region marked D, in Fig.5.6(a)].

From the above and the discussions in Sect. 5.5, the aerosols transported to the BoB appear to originate from West Asia, north western and central India, and coastal areas of central eastern India. The mechanisms responsible for the aerosol production in these regions are dust storms, industrial emissions and biomass burning (as part of regional agricultural activities during the pre-monsoon period) [Dey *et al.*, 2004; Girolamo *et al.*, 2004; Sing *et al.*, 2004]. Thus, the aerosols over the BoB will be a mixture of fine and coarse particles. However, the abundance of coarser particles will be relatively low as they get lost during the long-range transport before reaching the BoB.

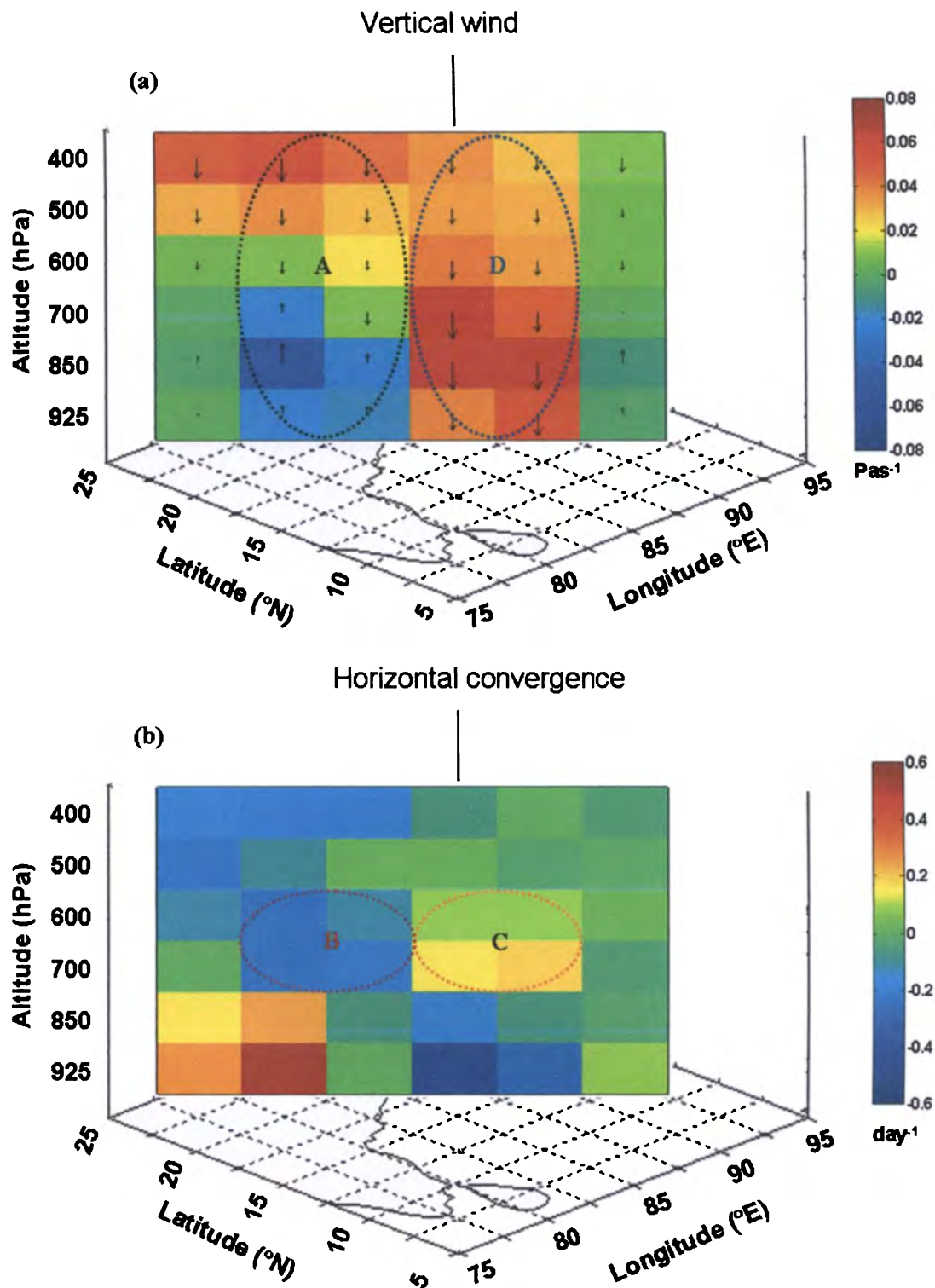


Fig.5.6. Vertical cross section of vertical wind (a) and horizontal convergence (b) along a vertical cross section from Central India through the Gangetic plane to mid-BoB

5.7 An episodic AOD event during the campaign

Figure 5.7 shows the spatial distribution of AOD over the BoB on five consecutive days from March 21 – 25, 2006, when the spatial pattern exhibits a marked deviation from the normal value. On March 21, the AOD over the entire region is rather moderate with a highest value ~ 0.35 , slightly off from the east coast of peninsular India. On the next day, the AOD along the east coast, north of $\sim 16^\circ\text{N}$ shows an increase, > 0.5 . By March 23, this develops into a large cluster of aerosols with high AOD values covering a significant portion over the north western BoB. On March 24, this cluster further intensifies (with AOD reaching as high as 0.7) and moves eastward detaching from the main land. Subsequently on March 25, the cluster suddenly weakens. The value of AOD over the entire northern BoB region decrease to the normal background level that prevailed before the cluster event. This is a typical event in which a large cluster of aerosol is advected from Indian subcontinent over to the BoB.

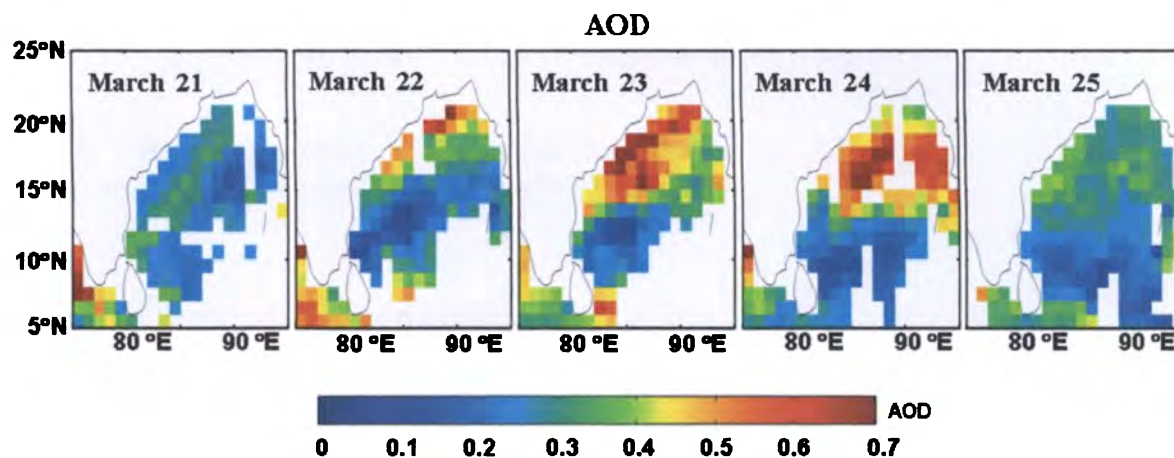


Fig.5.7. Spatial distribution of AOD over the BoB during March 21 – 25, 2006 showing the movement of an intense aerosol cluster from India to the BoB.

To examine the nature of the particles in this cluster, the fine and coarse mode components of the measured AOD are separated using the FMF from MODIS. These are presented in Fig.5.8 for the five days from March 21 to March 25, 2006. As can be seen, the fine mode AOD is significantly larger than the coarse mode within the cluster, indicating that the cluster is mostly composed of particles in the sub-micron size range.

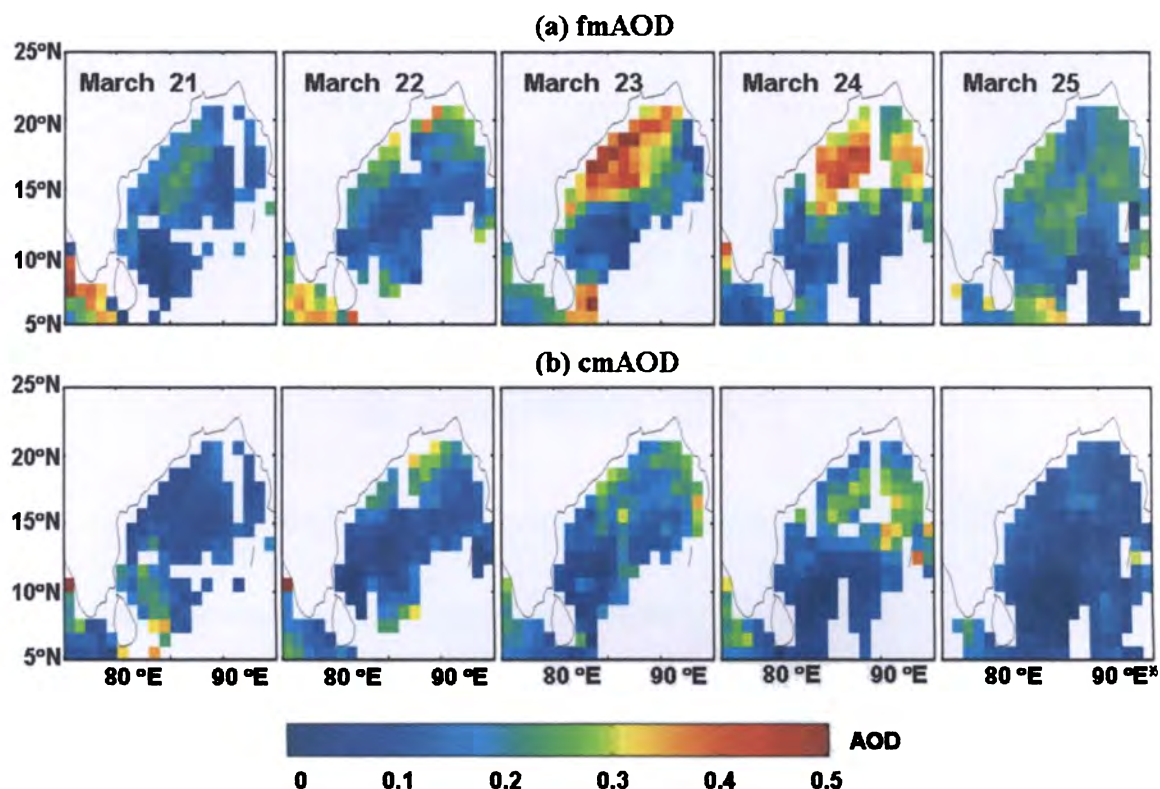


Fig.5.8. Spatial distribution of fine mode contribution to AOD (a) and coarse mode contribution to AOD (b) for the days March 21 – 25, 2006.

5.7.1 Influence of transport dynamics on the aerosol distribution over the BoB during the episode

The day-to-day variation of wind field and the associated features like convergence and vorticity are examined in detail to understand the role of transport in the observed evolution of the aerosol cluster during the episode. For this, the amount of *in situ* component also has to be accounted in the observed AOD. The mean surface wind from QuikSCAT during the episode, presented in Fig.5.9, shows that the maximum mean wind speed in the east coast is $\sim 5\text{ms}^{-1}$, which is too small to contribute anything substantially to the measured AOD (through sea-salt production).

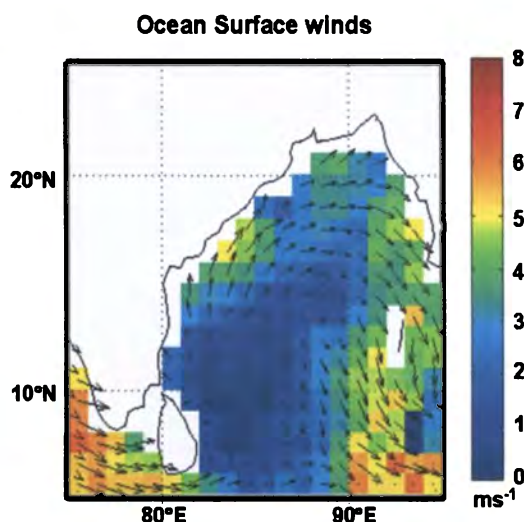


Fig.5.9. QuikSCAT surface winds averaged for March 22 – 24, 2006.

While the wind near the surface remains more or less steady, at higher altitudes (at ~ 700 hPa) it undergoes a significant change during this event. In fact, the event was mainly triggered by these changes at higher levels. Figures 5.10 and 5.11 respectively show the vorticity and convergence at 700 hPa over the Indian subcontinent and the adjoining oceanic regions during the period, March 20 to 25, 2006. The anticyclonic circulation positioned over the western Arabian Sea prior to this episode, shifts eastwards and merges with a weaker anticyclone over the land, intensifies and occupies almost the whole of the central India by March 24 [Fig.5.10]. Accordingly, the wind around this anticyclone induces a strong flow of dust laden air from west Asia to the east coast. Along with this, the convergence over the BoB [Fig.5.11], after an initial weakening, starts building up from March 22, which gives rise to an aerosol cluster by gathering the dust particles and other pollutants from the Indian landmass over the BoB at higher altitudes (700 hPa). On March 23 and 24, as this wind flow becomes stronger, the cluster intensifies and starts migrating eastwards. But the sudden weakening of the convergence on March 25, causes the cluster to disperse bringing down the AOD to its background level [Fig.5.7 and 5.8].

This epoch clearly shows the influence of transport dynamics in the formation, movement and dispersal of aerosol clusters which leads to temporal changes in the spatial distribution of aerosol loading.

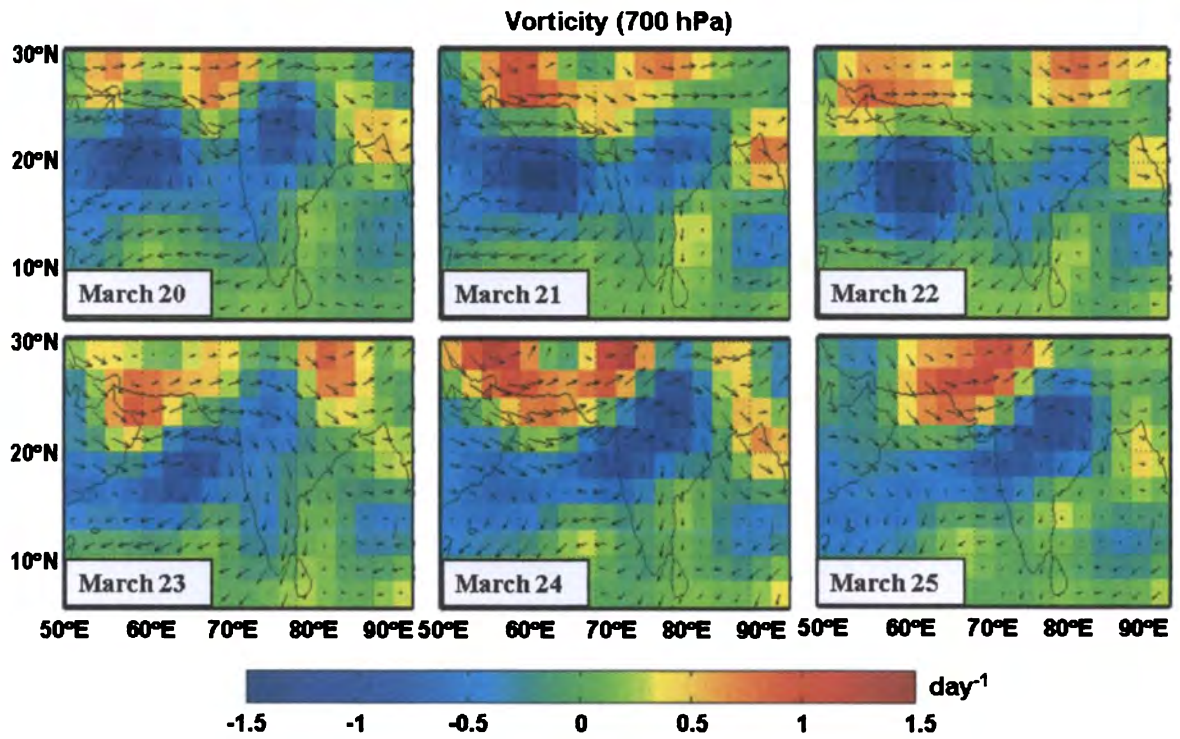


Fig.5.10. Mean distribution of wind vorticity at 700 hPa computed from NCEP reanalysis winds on different days from March 20 -25, 2006

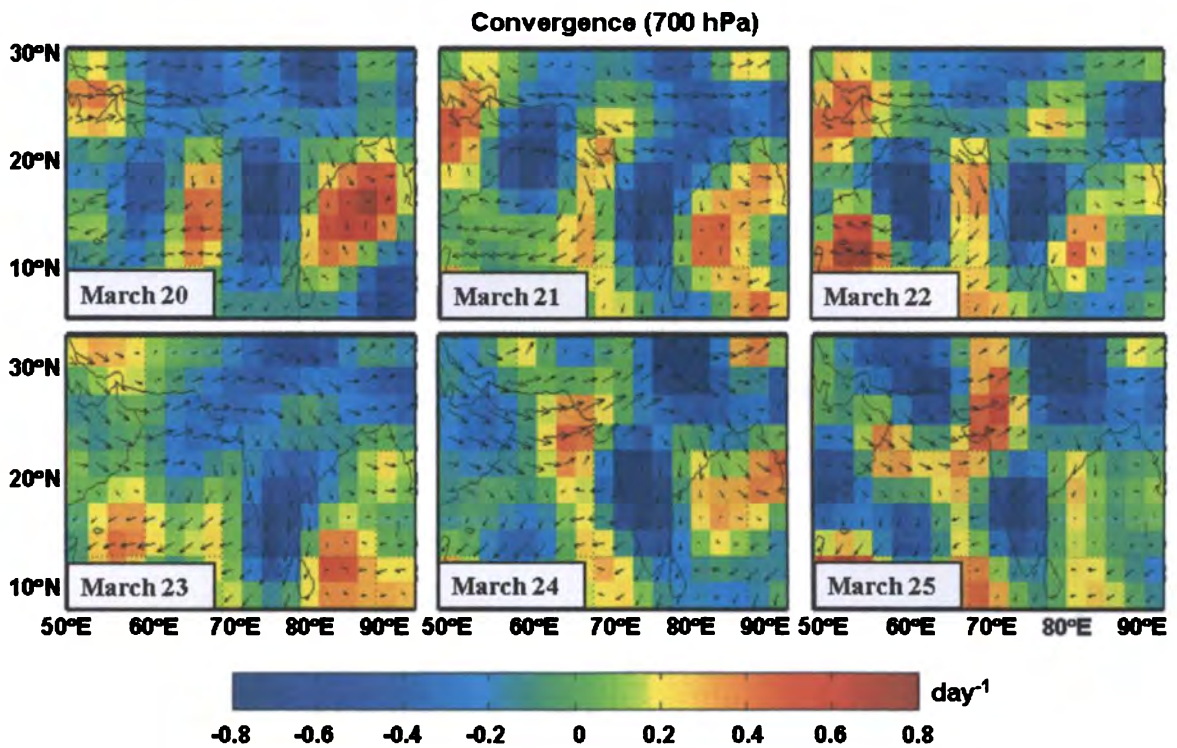


Fig. 5.11. Mean distribution of wind convergence at 700 hPa computed from NCEP reanalysis winds on different days from March 20 – 25, 2006.

5.8 Influence of wind convergence and vorticity on AOD perturbation

5.8.1 Estimation of aerosol flux convergence and flux vorticity

From the above, it is clear that the wind convergence, vorticity and vertical winds at different altitudes are decisive in determining the variations of aerosol distribution over the BoB. This aspect is examined in detail through a quantitative comparison of the temporal variations (day-to-day) of AOD with the corresponding variations in the wind parameters in that region.

Since the temporal changes in aerosol concentration is governed not only by the wind field but also by the ambient distribution of aerosols, aerosol flux convergence (f_{ac}) and aerosol flux vorticity (f_{av}) are considered as the appropriate circulation variables for this study. These variables are respectively defined as,

$$f_{ac} = -\nabla \cdot (\beta \mathbf{V}) \quad (5.1)$$

and

$$f_{av} = -\hat{k} \cdot \nabla \times (\beta \mathbf{V}) \quad (5.2)$$

where \mathbf{V} is the vector wind (obtained here from NCEP reanalysis) at a given atmospheric altitude, \hat{k} is the unit vector in the vertical direction and β is the altitude dependent aerosol extinction coefficient. To compute these parameters for different altitudes, the vertical profile of β is essential. This is derived from CALIPSO data.

5.8.2 Aerosol extinction profile derived from CALIPSO

Since CALIPSO was not operational at the time of ICARB campaign, the aerosol extinction profile is determined by averaging the CALIPSO measured day-time profiles over the study domain during the pre-monsoon months March and April (which covers the ICARB period) of the years 2007 and 2008. The basic data at 120 m vertical resolution is appropriately averaged to get a mean value of β corresponding to the NCEP pressure levels. These layer averaged extinction coefficients are further normalized by dividing the value at each level by the column integrated extinction (i.e. for unit AOD) to generate a normalized

mean profile. This normalized profile of extinction coefficient along with standard deviation is shown in Fig.5.12 (the integral from top to bottom is unity).

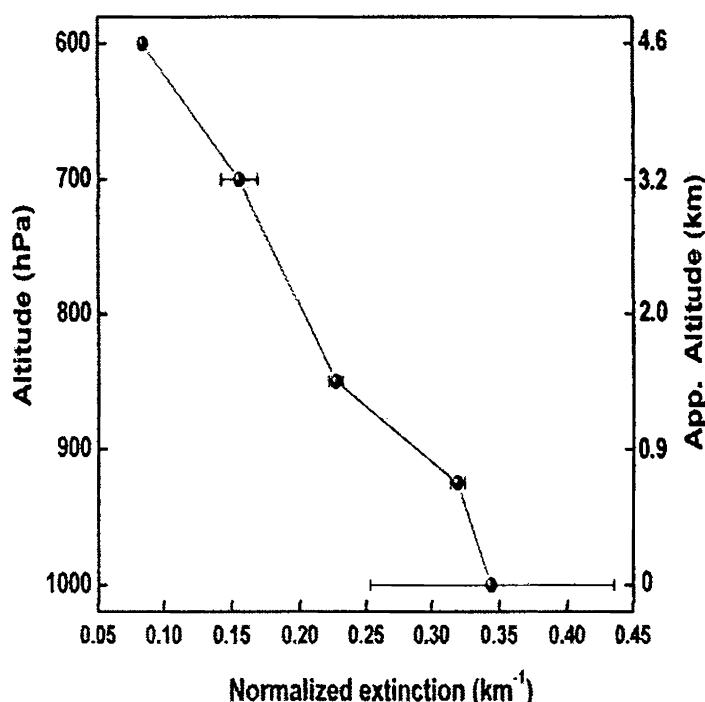


Fig. 5.12. Normalized mean vertical extinction profile of aerosols and the standard deviations derived from CALIPSO day time passes for the months March and April of 2007 and 2008 over the BoB. Note that the altitude scale on the left axis is shown in pressure levels and the corresponding approximate values in km are shown on the right axis.

As can be seen from Fig.5.12, the value of normalized aerosol extinction decreases with increasing altitude. For computational purpose, this profile is modeled by an exponentially decreasing function of altitude as

$$\beta_N(z) = \frac{1}{H_a} \exp\left(-\frac{z}{H_a}\right) \quad (5.3)$$

where β_N is the normalized extinction at any altitude and H_a is the scale height. The value of H_a estimated through a least square fit of Eq.(5.3) to the observed profile (shown in Fig.5.12) works out to be 3.3 km. This value is adopted to represent the fractional variation of aerosol extinction with altitude. By multiplying this profile with the measured AOD from MODIS, the altitude profile of extinction coefficient is obtained for each case.

5.8.3 Association of AOD modulation with wind convergence and vorticity

The day-to-day variation in AOD ($\delta\tau$) [using Eq.(4.1), Chapter 4], the flux convergence (f_{ac}) and flux vorticity (f_{av}) at the different levels (from 1000 hPa to 400 hPa) using Eq.(5.1) and (5.2) are estimated for each grid size $2.5^\circ \times 2.5^\circ$. Since the two physical processes operate continuously over the two successive days which are used to estimate $\delta\tau$, they are averaged for those two days. The altitude profile of aerosol extinction required for this computation is modelled using Eq.(5.3) with a scale height of 3.3 km along with MODIS derived AOD as the multiplying factor.

A correlation analysis is then carried out between $\delta\tau$ and f_{ac} and f_{av} at different altitudes. The altitude variation of the correlation coefficients for both the parameters are shown in Fig.5.13. It can be seen that the correlation coefficients are low near the surface, but increase with altitude reaching a maximum of 0.64 ($p < 0.01$) at 600 hPa for f_{ac} and 0.50 ($p < 0.02$) at 500 hPa level for f_{av} .

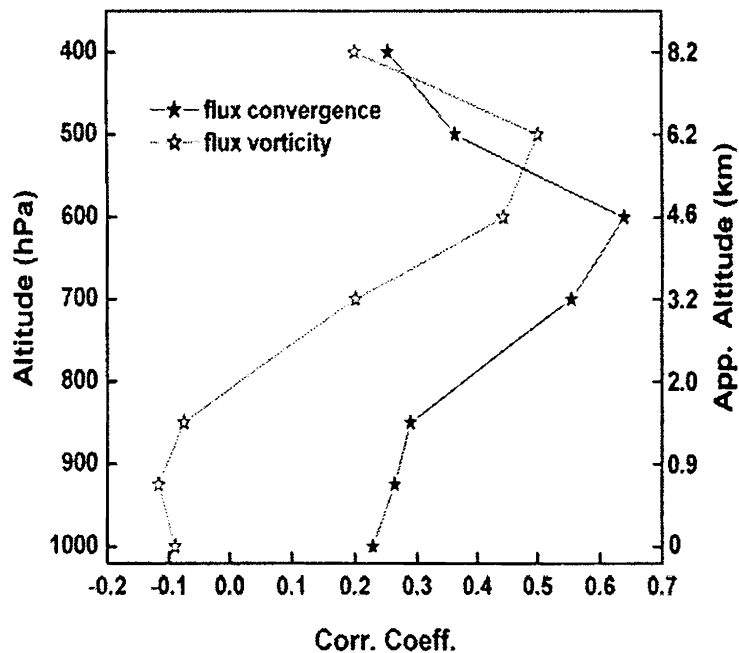


Fig.5.13. Altitude variation of coefficients of correlation between daily AOD variations and the variations in flux convergence (black solid line) and flux vorticity (dotted line) over the study domain during the first phase of ICARB. Note that the altitude scale on the left axis is shown in pressure levels and the corresponding approximate values in km are shown on the right axis.

Figure.5.14(a) and (b) respectively shows the time series plots of the f_{ac} and f_{av} for those altitudes where the correlations are maximum, along with the daily AOD change.

These figures clearly indicate that most of the variations in f_{ac} and f_{av} at 500 – 600 hPa levels matches well with the corresponding variations in $\delta\tau$. However, it would be worth in this context to note that the observed AOD variations need not entirely be due to changes in circulation parameters at a particular level (500 – 600 hPa). Rather it would also be influenced by fluxes from other atmospheric levels too, even though their significance may not be substantial [Fig.5.13]. In addition to this, the AOD changes will also depend on the strength of localized source (or sink) if they are present. Considering these factors the observed correlation of $\delta\tau$ with f_{ac} and f_{av} at higher levels can be treated as significant.

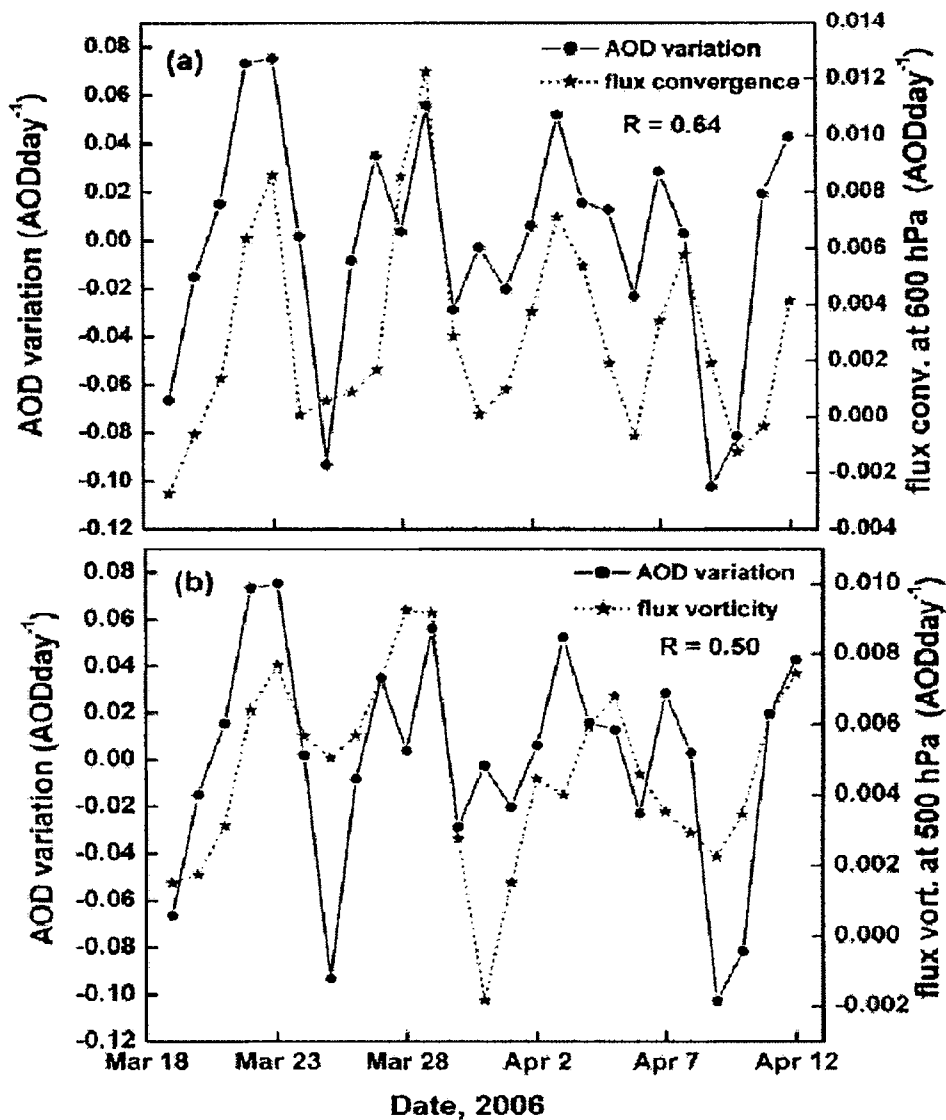


Fig.5.14. Time series plot of AOD variation along with flux convergence at 600 hPa (a) and flux vorticity at 500 hPa (b) over the study domain during the first phase of ICARB. The correlation coefficient corresponding to the linear regression between the AOD variation and flux convergence and flux vorticity are shown in the figures.

5.9 Contribution of *in situ* production on the observed AOD

From the above analysis it is quite evident that the advection of continental aerosols plays a dominant role on the aerosol loading over the BoB. Additionally, aerosols are also likely to be produced *in situ* from the sea surface (local source strength). This source strength is estimated using the flux continuity equation (Chapter 2, Sect. 2.7)

$$\frac{\partial \tau}{\partial t} + \frac{\partial}{\partial x} \left[\int_0^{\infty} \beta u \, dz \right] + \frac{\partial}{\partial y} \left[\int_0^{\infty} \beta v \, dz \right] = S(x, y, t) \quad (5.4)$$

where $\frac{\partial \tau}{\partial t}$ is the change in AOD (per day), β is the aerosol extinction coefficient, u and v are the zonal (x) and meridional (y) components of vector wind, z is the altitude, and S is the net source strength which is the resultant of actual source and sink activities. The value of β is assumed to vary exponentially with altitude according to Eq.(5.3).

The spatial distribution of estimated source strength averaged over the campaign period is presented in Fig. 5.15(a). Source strength values are expressed in AOD change per day. Positive values of S (~ 0.1) are seen along the east coast of peninsular India. Considering an uncertainty of $\sim 10\%$ associated with AOD, the estimated error for the source strength is $\sim 10\%$. Even after accounting this uncertainty, the positive values of source strength yielded from Eq.(5.4) along the east coast is quite significant. This spatial distribution of source strength also matches quite well with that of ocean surface wind speed shown in Fig.5.4(b) (indicating that the source over the east coast is associated with the wind induced sea-salt aerosols). The sea-salt AOD (τ_{ss}) is related to the wind speed (U) through the relation [Moorthy *et al.*, 1997; Moorthy and Satheesh, 2000; Vinoj and Satheesh, 2003; Satheesh *et al.*, 2006b]

$$\tau_{ss} = \tau_0 [\exp(b_{ss}U) - 1] \quad (5.5)$$

where τ_0 is the AOD at zero wind speed (indicating the background AOD) and b_{ss} is the 'wind index'. From a study carried out over the interior BoB (to minimize the influence of continental aerosols) during the same period using the MODIS derived AOD at $0.55 \mu\text{m}$ and QuikSCAT surface winds, Aloysius *et al.*, 2008 has reported the values of τ_0 and b_{ss} respectively as 0.16 and 0.08. The τ_{ss} estimated with these values and QuikSCAT measured

winds at $1^\circ \times 1^\circ$ grid sizes, using Eq.(5.5) over the study domain is presented in Fig.5.15(b). It is quite interesting to note that the overall pattern of S in Fig. 5.15(a) and τ_{ss} in Fig.5.15(b) match well with each other, supporting the accuracy of the estimation of S .

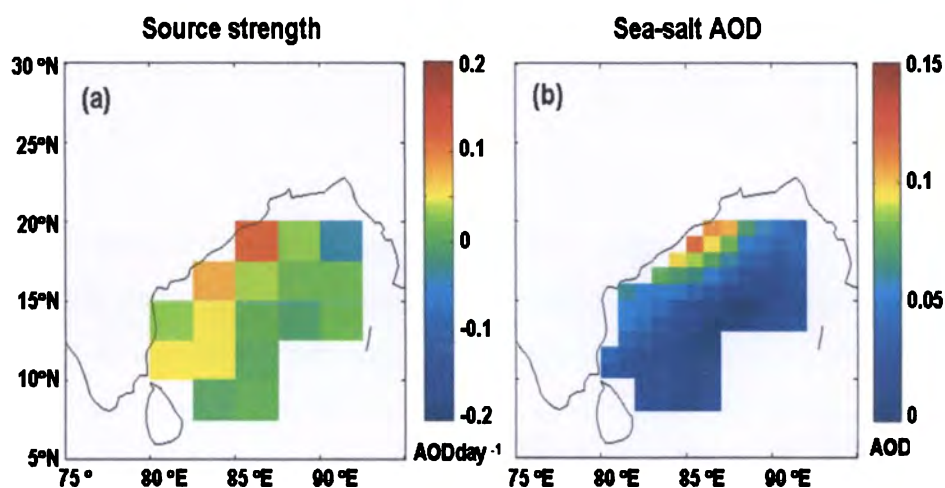


Fig.5.15. Spatial pattern of aerosol source strength estimated using aerosol flux continuity equation (a) and *in situ* produced AOD from sea-salt, estimated based on QuikSCAT surface wind speed (b) over the BoB during the first phase of ICARB

5.10 Summary

Mean spatial distribution of AOD over the BoB during the ICARB reveals significant advection of continental aerosols over to the BoB and all along the east coast of peninsular India. The relative contribution of fine particles to the total AOD is high over the entire BoB except over the Head BoB where both fine and coarse particle contribution is more or less equal. Relatively low values of QuikSCAT measured ocean surface wind in this region shows that the possibility of *in situ* production contributing to the high values of AOD is very small. An analysis of the aerosol transport dynamics using NCEP winds at different altitudes brings out clearly the mechanism of aerosol advection to the BoB region. Though the anticyclonic circulation prevailing in the lower altitudes (~ 925 hPa) prevent a direct transport of aerosols from the interior Indian landmass across the coast, the winds at higher altitudes (~ 700 hPa) accelerated by anticyclonic circulation over the Indian subcontinent is conducive for the flow of aerosol particles to the BoB. The wind convergence at higher altitude over the BoB favours the accumulation of these particles which are subsequently brought down to lower altitudes by vertical downdraft. Strong

updrafts over the central and eastern coastal India lift particles from the surface and connect them to the prevailing upper level westerly flow which takes these particles towards the BoB. But, at lower altitudes, only those particles near the east coast of peninsular India are advected over to the BoB. Thus both fine and coarse particles from the dust laden West Asian regions, north western and central India, and coastal areas of central eastern India contribute to the aerosol burden over the BoB through higher altitudes in the lower troposphere (3 – 4 km).

A detailed analysis of the daily AOD over the BoB reveals an interesting event of aerosol enhancement and decay during a period from March 22 – 25, 2006. This event is triggered by the eastward shift of a higher altitude anticyclone over the north western Arabian Sea, its intensification and subsequent merger with the weaker anticyclone over the central Indian land mass. The winds associated with the anticyclone drive a strong flow of dust laden air from west Asia and the pollution aerosols from the Indian land mass over to the northern BoB, where they accumulate due to a short term strengthening of higher altitude wind convergence leading to the formation of an aerosol cluster. This aerosol cluster drifts eastwards and attains high values of AOD by March 24. But the sudden weakening of the convergence (by the next day) causes the cluster to disperse bringing down the AOD to very low values.

An estimation of the influence of circulation variables on the AOD over the BoB is made by comparing the day-to-day AOD changes with the changes in flux convergence and flux vorticity at different altitudes. The CALIPSO derived aerosol extinction profiles averaged during the months of March and April in 2007 and 2008 is used for modeling the aerosol altitude structure. It reveals that on an average, the flux convergence at 600 hPa and flux vorticity at 500 hPa are well correlated with the observed day-to-day variations in AOD over the BoB. Mean aerosol source strength computed with the flux continuity equation indicates the presence of aerosol source along the east coast of peninsular India, mainly associated with the ocean surface winds ($\sim 7\text{ms}^{-1}$ on an average). However, the contribution of this *in situ* production is very small compared to the observed AOD over the BoB. This strongly suggests that the influence of aerosol advection is the prime governing factor for the observed high AOD over the BoB during the pre-monsoon period.

Chapter 6

Transport dynamics of aerosols over the Arabian Sea during the pre-monsoon period: ICARB (Phase II)

6.1 Introduction

Studies on aerosol distribution over the Arabian Sea have shown that advection of particles from the Indian subcontinent is quite significant during the pre-monsoon period. This is particularly true over the southern part of the Arabian Sea [*Nair et al.*, 2008; *Parameswaran et al.*, 2008]. Long range transport of aerosols (mineral dust) from the arid regions of Arabia, also contributes to the aerosol loading in this region (a typical example of which is discussed in Chapter 4), even though this contribution is well pronounced during the summer (south west) monsoon period. In contrast, the aerosol loading over the northern Arabian Sea is mostly due to direct (short range) transport of aerosols from the Arabian land mass [*Nair et al.*, 2005; *Parameswaran et al.*, 2008].

The main objective of the second phase of the ICARB (SK223 B) was to address the aerosol properties over the Arabian Sea during the pre-monsoon period. While the ARMEX-II campaign conducted during the pre-monsoon period of 2003 was focused mostly on the aerosol distribution over a small geographical region (south eastern part) over the Arabian Sea (Chapter 4), the study envisaged in the second phase of the ICARB was more exhaustive and hence it covered almost the entire Arabian Sea spanning over a region 9° - 22° N in latitude and 58° - 76° E in longitude extending over the period from April 18 to

May 11, 2006. Figure.6.1 shows the cruise track during this campaign. Simultaneous observations using a variety of instruments were involved during this campaign.

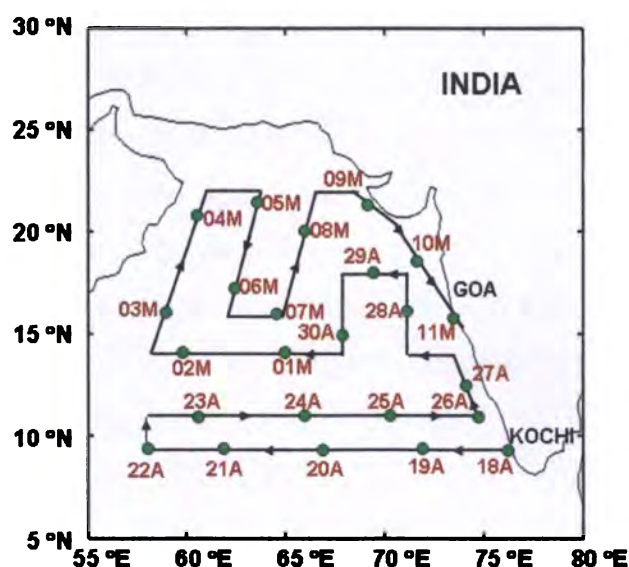


Fig.6.1. Cruise track of SK223 B over the Arabian Sea during the second phase of ICARB (April 18 – May 11, 2006). Green dots denote the position of the ship every 5:30 UTC. Dates are marked near the points with suffix 'A' and 'M' representing the months April and May respectively

While ship borne instruments made direct measurements of aerosols along the cruise track, space borne remote sensors (satellite) monitored daily distribution of aerosols over the Arabian Sea. In this chapter, a detailed study on the dynamics of aerosol transport over the Arabian Sea during ICARB (April 18 – May 11, 2006) using MODIS derived AOD data and NCEP reanalysis wind field is attempted. The temporal variation of the spatial distribution of aerosols and its association with atmospheric circulation over this oceanic region is examined on a day-to-day basis to delineate the influence of atmospheric dynamics on aerosol features.

6.2 A comparison of MODIS derived AOD with cruise measurements over the Arabian Sea

Before proceeding to a detailed analysis, as a prelude, the MODIS derived AOD over the Arabian Sea is compared with direct measurements onboard SK223 B, using Microtops sunphotometer. The Microtops measured AOD at 0.50 μm wavelength is normalized to 0.55 μm using the Angstrom exponent obtained through the regression analysis of the spectral AOD measurements at the wavelengths 0.44, 0.50, 0.675 and 0.87 μm (as detailed

in Chapters 4 and 5). Figure 6.2 shows a time series plot of the AODs derived from MODIS (optimally combined from Terra and Aqua) and Microtops at a common wavelength, 0.55 μm . In this figure, the MODIS data shown are averages of the AOD measurements over the grids traversed by the ship on each day and the corresponding standard deviations, while the Microtops data are the daily mean of *in situ* measured AOD and its standard deviations. As can be seen, the agreement between the two is quite satisfactory. A correlation analysis performed between the two yields a value, 0.89 ($p < 0.01$) for the coefficient, with a root mean square difference of 0.06. The regression relation between the MODIS and Microtops AODs is given in Fig.6.2. The MODIS derived AOD is slightly underestimated, with an average bias < 0.01 . Note that this is well within the uncertainty limits reported by *Remer et al.* [2005] for MODIS.

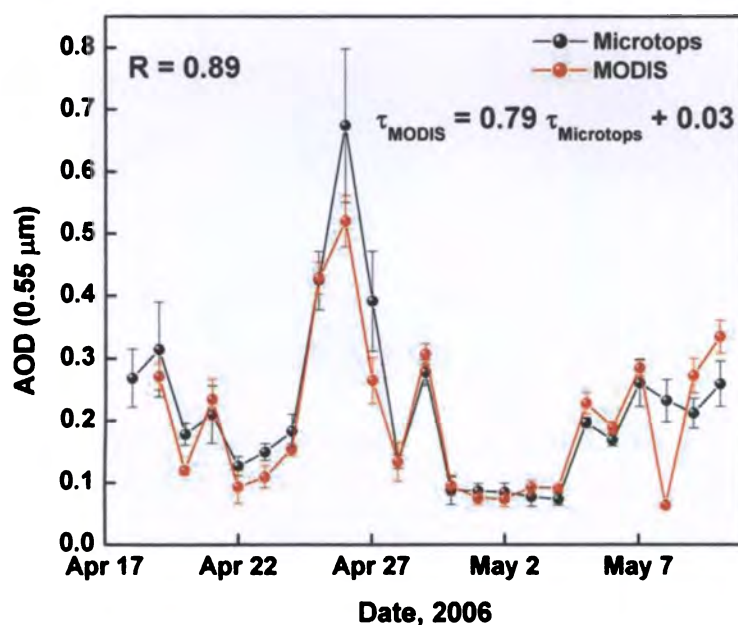


Fig.6.2. Time series plot showing the comparison between daily AOD values at 0.55 μm derived from MODIS and Microtops. The correlation coefficient and the linear regression relation are shown in the figure.

It must be noted here that a similar inter-comparison was carried out during the ARMEX-II period and the results are discussed in Chapter 4. That comparison however, was performed over a smaller geographical region, while the present comparison covers a wider geographical region over the Arabian Sea.

6.3 Spatial distribution of AOD over the Arabian Sea during the campaign

Mean spatial distribution of AOD and its contribution from fine mode and coarse mode particles (fmAOD and cmAOD respectively) over the Arabian Sea during the campaign are shown in Fig.6.3(a) and Fig.6.3(b) respectively. A distinct region where AOD values are significantly high can be seen over the SEAS (South East Arabian Sea) along the west coast of the Indian peninsula, notwithstanding for a small region of high AOD in the northern Arabian Sea [Fig.6.3(a)]. Note that, this pattern compares fairly well with that observed during the ARMEX-II period in the year 2003 [Chapter 4, Fig.4.7] except that the area encompassed by the high AOD in the northern Arabian Sea was relatively large.

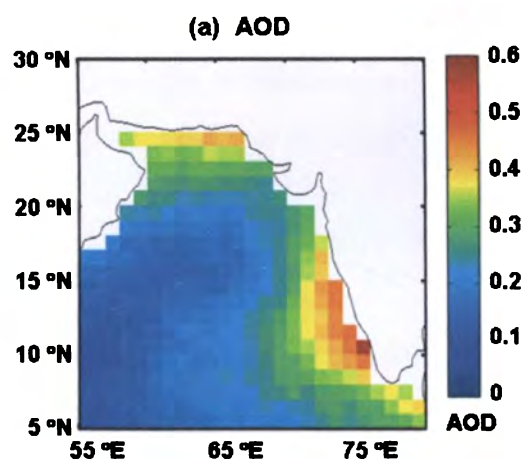


Fig.6.3(a). Mean spatial distribution of MODIS derived AOD over the Arabian Sea during the second phase of ICARB.

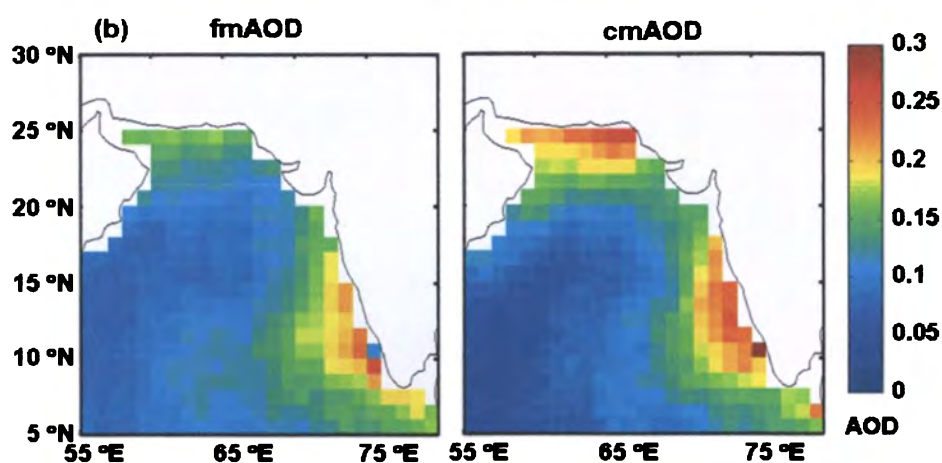


Fig.6.3(b). Mean spatial distribution of fine mode AOD (fmAOD) and coarse mode AOD (cmAOD) derived from MODIS over the Arabian Sea during the second phase of ICARB

Figure 6.3(b) shows that while the coarse particles are primarily responsible for the high AOD over the northern Arabian Sea, the contribution from both fine and coarse particles are nearly the same for the observed high over the SEAS. However, the westward spread of AOD in the SEAS is more for the fine mode [Fig.6.3(b)]. More than 60% of the total AOD in the Arabian coast as well as that over the northern parts of the Arabian Sea is contributed by coarse particles (probably consisting of both mineral dust and sea-salt particles). This reduces to ~ 50% over the SEAS region, where the aerosol loading is the largest. On the other hand, over the mid Arabian Sea and the south western parts where the AOD is very low, fine particle contribution is as high as ~ 60 -70%. On an average, over the Arabian Sea major contribution to the observed AOD comes from the coarse particles (mostly of natural origin), which is in contrast to the case observed over the BoB, where the (anthropogenically produced) small size particles were dominating. The aerosol mass concentration measured near the surface onboard the ship during the campaign also showed a dominance of coarse mode particles [Nair *et al.*, 2008].

6.4 Influence of circulation on the spatial distribution of AOD

The role of sea surface wind in the spatial distribution of aerosols is examined using QuikSCAT data. Figure 6.4 shows the mean ocean surface wind field during the campaign period over the Arabian Sea. On an average, the wind speed over the Arabian Sea is larger

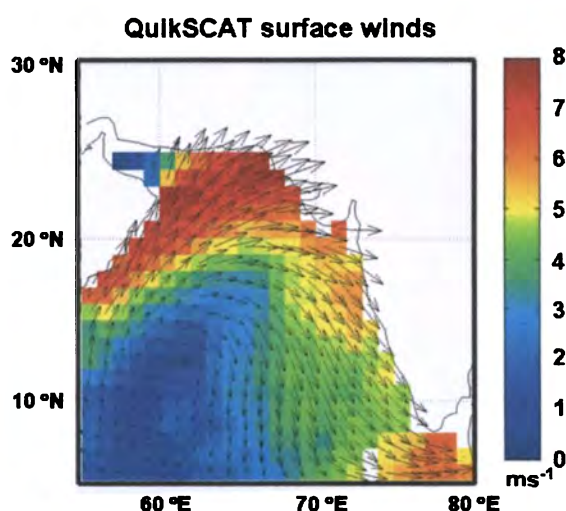


Fig.6.4. Spatial distribution of QuikSCAT ocean surface winds averaged for the second phase of ICARB.

than that over the BoB during the first phase of the ICARB (Chapter 5, Fig.5.4). The wind speed is moderately high particularly over the northern/north western parts of the Arabian Sea and near the southern tip of the Indian peninsula and is relatively low over its south eastern and central parts. Because of this, the *in situ* production of sea-salt aerosols over the Arabian Sea in general, would be relatively greater than that over the BoB.

Figure.6.5(a) and (b) shows the relevant circulation variables: convergence, vorticity and vertical winds (from NCEP reanalysis) at two altitudes, 925 and 700 hPa levels over the Arabian Sea averaged for the campaign period. Even though the general features are nearly the same as that during the ARMEX-II (Fig.4.6), significant deviations are observable on finer scales. The anticyclonic vorticity at 925 hPa in Fig 6.5(a) over the central Arabian Sea

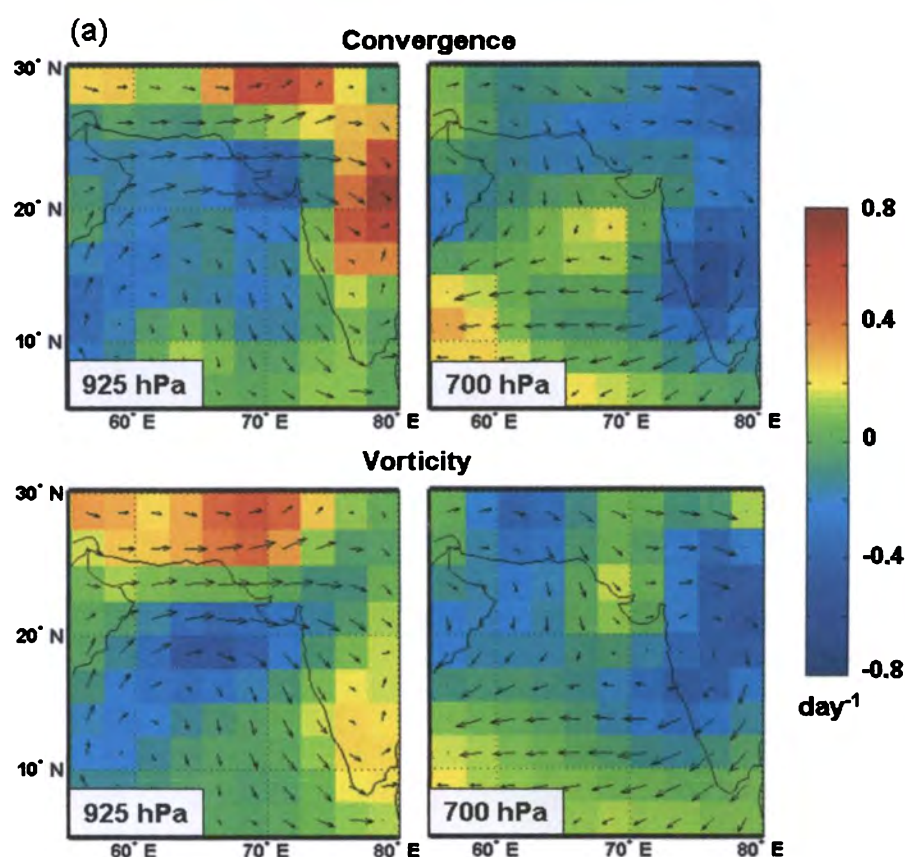


Fig.6.5(a). Mean spatial distribution of convergence and vorticity at 925 and 700 hPa averaged during the second phase of ICARB.

supports a localized high pressure system, which is in agreement with the surface wind field shown in Fig.6.4. Unlike a similar anticyclonic system causing the flow of dust particles from Arabia southwards along the Indian west coast that prevailed over the Arabian Sea during the ARMEX-II period [Figs 4.6(c)], the wind pattern during ICARB is more

favourable for driving the particles directly into the north Indian landmass. The influence of this can be observed in the spatial distribution of AOD [Fig.6.3(a)], with relatively small values over the central Arabian Sea compared to that during the ARMEX-II [Fig.4.7]. High value of AOD over the northern Arabian Sea is due to the advection of dust particles directly from the Arabian land mass by the lower altitude winds. Over and above, the *in situ* production of marine sea-salt particles by the moderately strong surface wind [Fig.6.4] is also significant during the ICARB.

At higher altitudes, in the latitude range 25° - 30° N, the westerly winds from the west Asia splits into two branches as it approaches the Indian subcontinent. While one branch proceeds directly towards the northern and central parts of the Indian subcontinent and takes a curved path over the peninsula to become north easterly as it crosses the western ghats to reach the south eastern parts of the land mass, the other branch turns southwards at the northern Arabian Sea and changes to south westward flow along the Arabian coast.

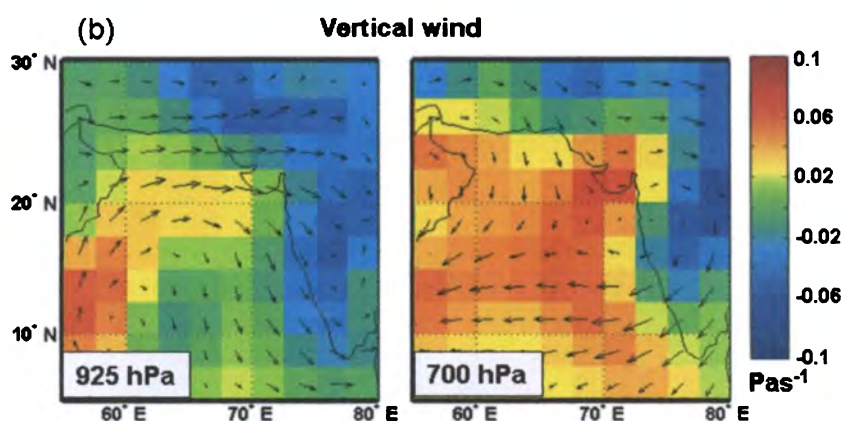


Fig.6.5(b). Mean spatial distribution of vertical wind at 925 and 700 hPa averaged during the second phase of ICARB.

In the case of vertical winds [Fig.6.5(b)], an updraft is seen in the lower altitudes over the northern and central parts of Indian subcontinent while it is downdraft over the Arabian Sea at high altitudes. This feature is favourable for uplifting aerosols from the northern and central India to higher altitudes and the transport towards the central and western Arabian Sea, where the higher level convergence [Fig.6.5(a)] favours their accumulation and subsequent subsidence [Fig.6.5(b)] by the downdraft.

Over the SEAS, the observed high values of AOD can mainly be attributed to the accumulation of aerosols by the low level wind convergence [Fig.6.5(a)]. Aerosols are

brought to SEAS through westerly winds blowing from the northern parts of Arabian Sea which turn north westerly in the west coast of peninsular India and flow southwards along the industrialized regions. Accordingly, aerosols in this region which contains both coarse and fine particles in nearly equal amount [Fig.6.3(b)] could be a mixture of dust from the West Asia, *in situ* produced sea-salt, and particles of industrial effluvia from the Indian subcontinent. In contrast, over the central and south western Arabian Sea, as the upper level wind is favourable for the transport of fine anthropogenic particles from the Indian land mass [Fig. 6.5(a) and (b)], fine particles dominate the aerosol system [Fig. 6.3(b)] at this location.

6.5 Variations in aerosol distribution during the campaign

The spatial pattern of AOD over the Arabian Sea, during the campaign period shows a gradual but well defined change on a day-to-day basis. To examine these variations the whole campaign period is divided into two halves; the first half (FH) extending from April 18 to 30, 2006 and the second half (SH) extending from May 1 to 11, 2006. The distributions of AOD as well as its fine and coarse mode contributions averaged for the two halves are presented in Fig.6.6(a) and Fig.6.6(b) respectively.

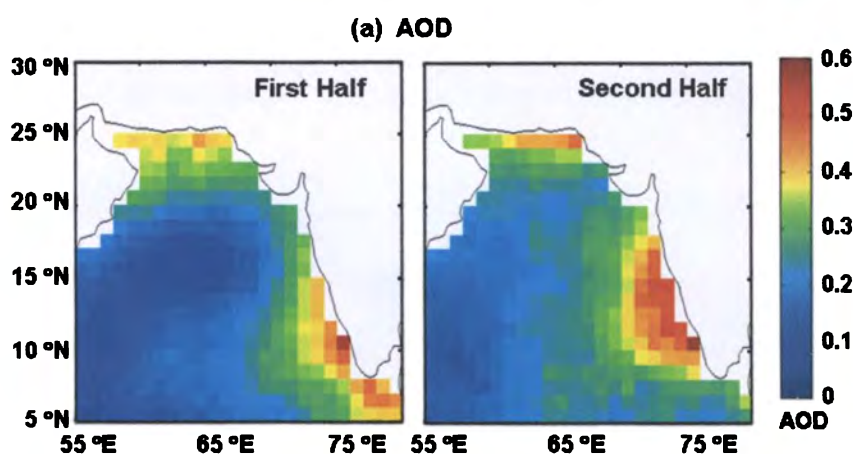


Fig.6.6(a). Spatial distribution of AOD averaged during the first half (April 18 to 30, 2006) and second half (May 1 to 11, 2006) of the second phase of ICARB

A general increase in AOD is clearly observed in the SH with respect to the FH especially, over the central and eastern Arabian Sea (between $\sim 10^\circ - 20^\circ\text{N}$ and $60^\circ - 75^\circ\text{E}$) and to a certain extent over the northern parts of the Arabian Sea along the Pakistan coast

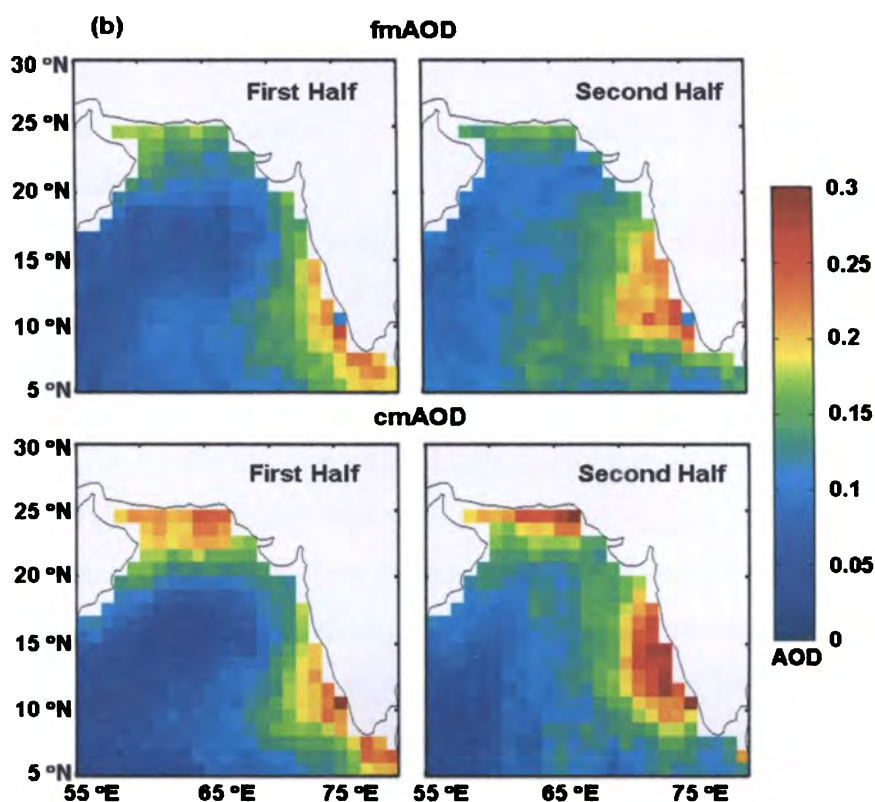


Fig.6.6(b). Mean spatial distribution of fine mode AOD and coarse mode AOD over the Arabian Sea during the first and second halves of the second phase of ICARB

[Fig. 6.6(a)]. The difference in the total AOD, and its fine mode and coarse mode components between the two halves (SH minus FH) are presented in Fig.6.7. It can be seen

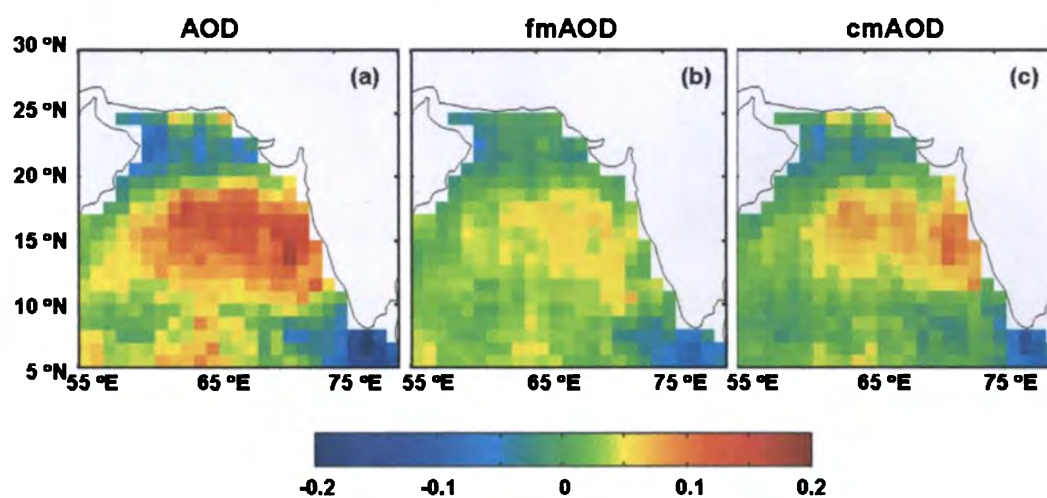


Fig. 6.7. Change in AOD (a) fine mode AOD (b) and coarse mode AOD (c) from first half to second half of the second phase of ICARB

that, over the central and eastern Arabian Sea, the increase in AOD is contributed mainly by coarse particles even though the contribution from fine particles is not insignificant, but over the northern Arabian Sea (close to the Pakistan coast) it is mostly governed by the coarse mode particles.

To examine the transport dynamics responsible for these changes, the difference in atmospheric circulation during the FH and SH are examined in detail. The mean surface wind field obtained from QuikSCAT during the two halves are presented in Fig. 6.8. In the northern Arabian Sea, while the wind field remains more-or-less the same in the two halves, the wind speed close to the Pakistan coast shows an increase during the SH. The observed increase in AOD (by ~ 0.1) in this region [Fig.6.7] during the SH can then be attributed to the increase in mean wind speed over the sea surface. But in spite of a decrease in wind speed in the west coast of India [Fig.6.8], the AOD shows an increase during SH [Fig.6.7]. This could only be attributed to a significant change in some features of the transport dynamics. To investigate this aspect, the circulation features like convergence and vorticity are examined in detail.

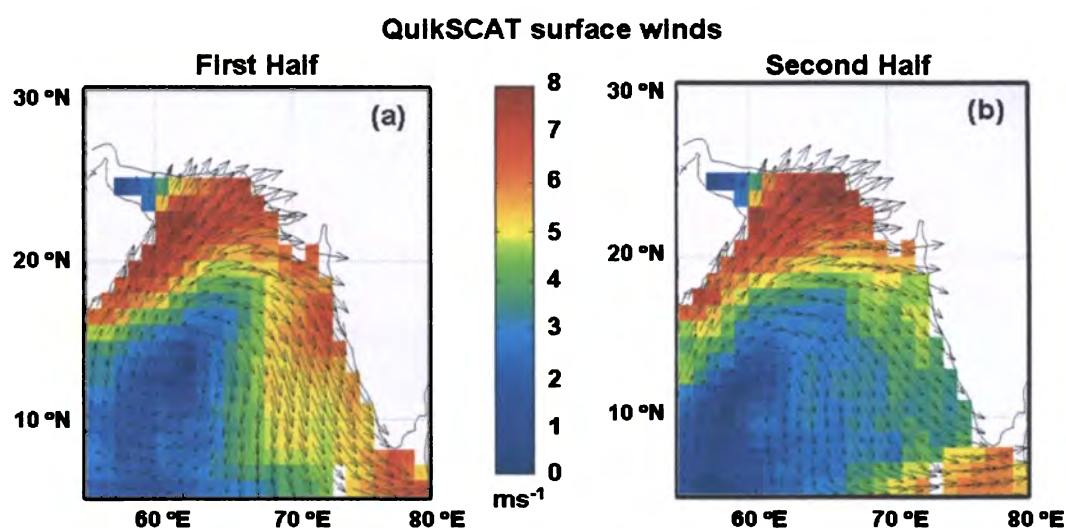


Fig.6.8. Spatial distribution of ocean surface winds averaged during the first half (a) and second half (b) of the second phase of ICARB

Figure 6.9(a) and (b) shows the spatial distribution of circulation variables (convergence, vorticity and vertical wind) over the Arabian Sea computed from the NCEP winds at 925 and 700 hPa. A notable difference can be seen in these variables between the two halves. The centre of the anticyclonic circulation located in the mid Arabian Sea as seen in the surface winds during the FH, shifts towards south west in the SH [Fig 6.8]. This allows the coarse particles from the Arabia and the northern land masses to spread more

westwards in the central and eastern Arabian Sea. Moreover, as the wind at lower altitudes over the Arabian Sea show greater convergence at the eastern end during the SH [Fig. 6.9(a)], the conditions are favourable for more accumulation of aerosols over this region.

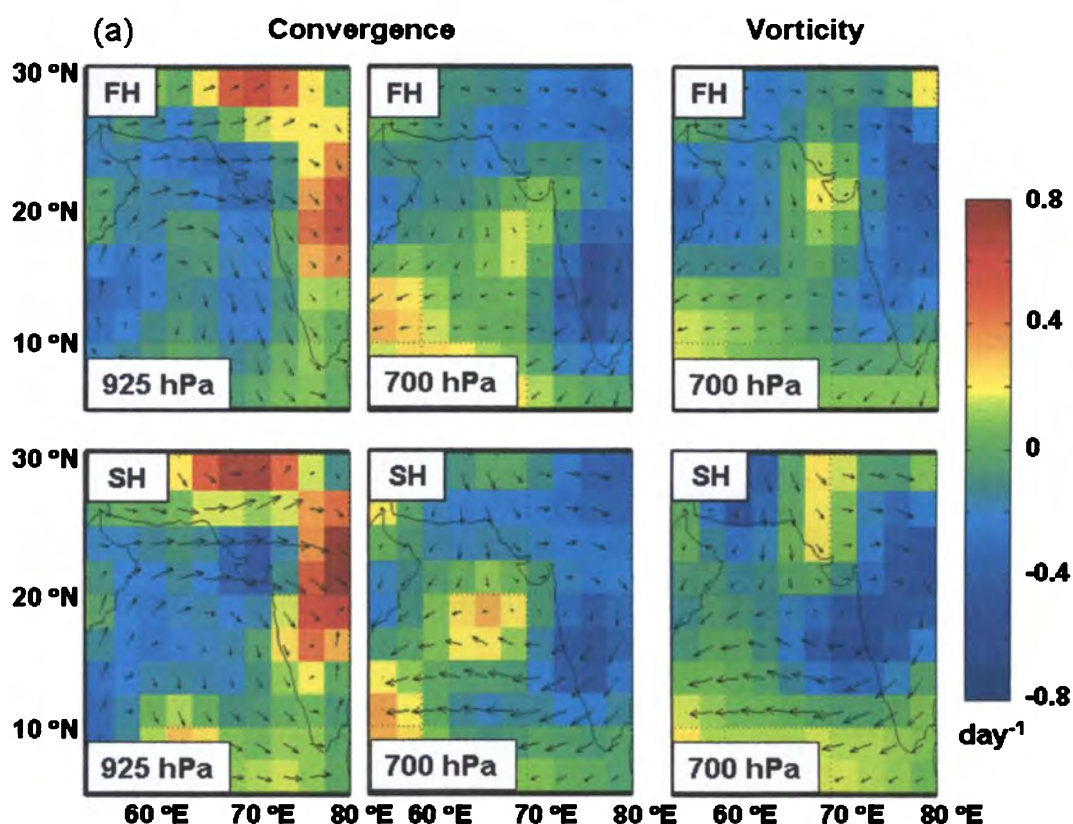


Fig. 6.9(a). Spatial distribution of mean horizontal wind convergence at 925 and 700 hPa levels along with the vorticity at 700 hPa, during the first (FH) and second (SH) halves of the second phase of ICARB

The updraft [Fig.6.9(b)] over the land mass, north and east of the Arabian Sea also is stronger in the SH than that during the FH. This is favourable for the uplift of more aerosols from continent to higher altitudes. In addition to this, the weak anticyclonic circulation at the higher altitudes, over the Indian peninsula near the west coast also strengthens during the SH [Fig.6.9(a)], which leads to increased influx of aerosols over to the central Arabian Sea. The winds associated with this anticyclone and the northerly winds from the southern Pakistan meet to form a region of wind convergence in the central (15° - 20° N in latitude and 60° -70° E in longitude) and south western Arabian Sea [Fig. 6.9(a)]. This favours an increased accumulation of particles from the continent over to the central and south western Arabian Sea during the SH leading to the observed increase in AOD [Fig 6.7] at these regions.

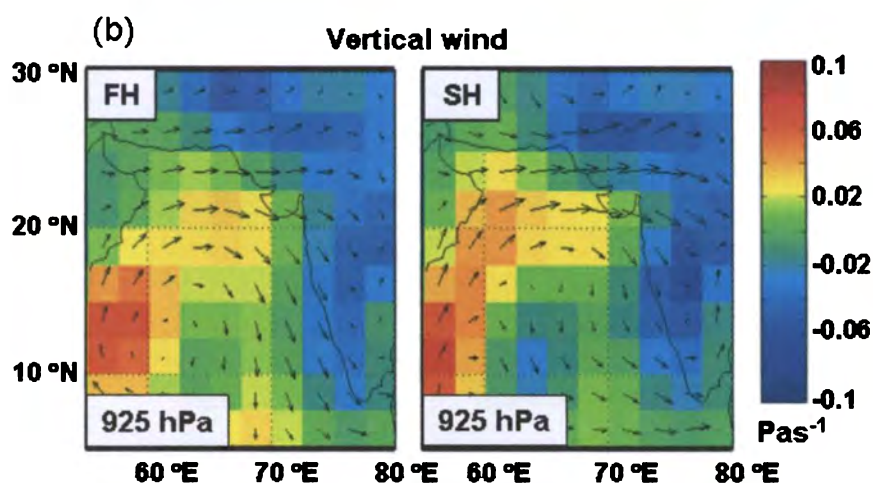


Fig.6.9(b). Spatial distribution of mean vertical wind at 925 hPa level during the first (FH) and second (SH) halves of the second phase of ICARB

This analysis clearly shows that the difference in the spatial pattern of AOD from the FH to SH is due to change in prevailing transport dynamics.

6.6 An observational evidence for the influence of transport dynamics on the spatial distribution of AOD: Cluster movement, a case study

An interesting episode, leading to the formation of a localized aerosol cluster over the northern Arabian Sea and its southward drift along the west coast of the Indian peninsula due to the transport dynamical features during the study period is discussed in this section. An aerosol cluster characterized by a localized peak in AOD (> 0.6) appears near the Mumbai coast (19°N , 73°E) on April 22, 2006. Subsequently it moves towards south along the west coast of peninsular India with an average speed of $\sim 200 \text{ km day}^{-1}$ reaching the southern tip by \sim April 28 where, after remaining for nearly two days it finally weakens and disperses. This event observed in the daily distribution of AOD from MODIS could also be observed in the values of AOD measured onboard the ship, when the cluster moved across the ship's location. Figure 6.10 shows the spatial distribution of AOD on different days from April 19 – 30, 2006 over the Arabian Sea. The gradual development of the aerosol cluster, southward migration and the final decay is sequenced in this figure. The location of the ship at 5:30 UTC on each day is shown by a star (\star) mark in these figures. The circle indicates roughly the position of the cluster on each day.

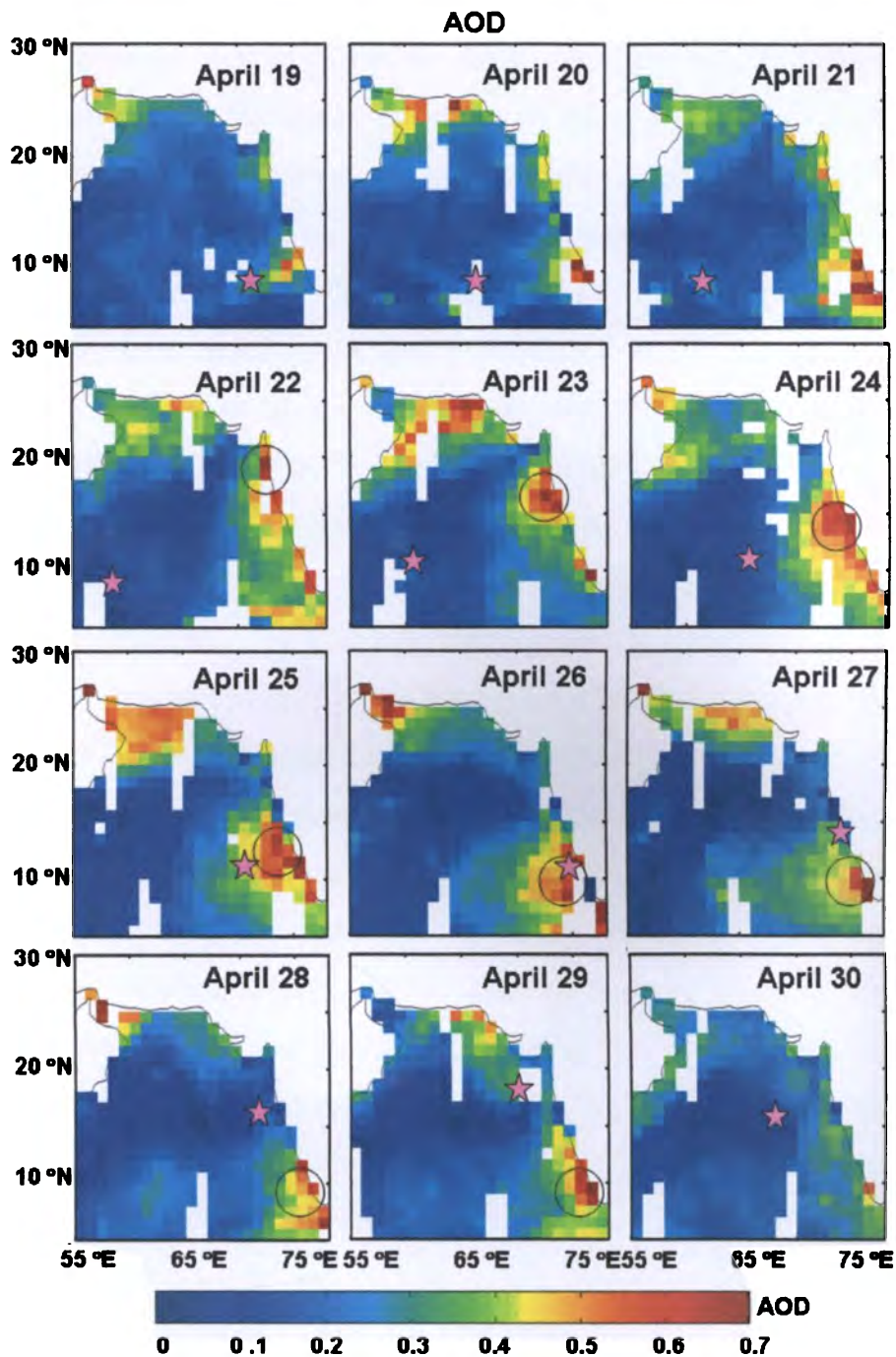


Fig.6.10. Spatial distribution of AOD on different days from April 19 – 30, 2006 depicting the movement of the aerosol cluster, which is marked with a circle. Star denotes the position of Sagar Kanya at 5:30 hrs UTC on the corresponding days.

To start with, the time series of AOD measured onboard the ship is examined during the second half of April 2006. As seen from Fig.6.2, the Microtops measured AOD show a gradual decrease from April 19 through 22, though with some fluctuations in between, due to the passage of small aerosol patches across the ship's position as can be seen in Fig.6.10.

On April 22, 2006 when the major aerosol cluster appears first close to Maharashtra coast, the ship is quite far in the western part of the Arabian Sea, and measured value of AOD (~ 0.1) is very small. As the ship moves towards (east) the west coast of India, the cluster drifts toward south along the west coast. On April 25, when the cluster meets the ship near the west coast, the AOD measured on the ship shows a significant increase [Fig.6.2] with values exceeding 0.4. By April 26, when the ship is almost within the core of the cluster, the measured AOD also reaches the peak value (~ 0.7).

On subsequent days as the ship moves further northwards and the cluster moves southwards, the AOD measured on the cruise decreases and subsequently reaches a low value (< 0.2) by April 28, 2006. The aerosol cluster which is moving southwards finally reaches the southern tip of the peninsula and disperses by April 30, 2006. Meanwhile the ship sails further northwards, to meet another relatively small aerosol patch (with low AOD value) over the northern part of the Arabian Sea on April 29. Because of the influence of this patch the AOD over the ship shows a small increase [Fig.6.2]. Subsequently as the ship sails towards south west over a region where the MODIS measured spatial pattern shows a relatively clean environment, the measured AOD onboard also shows a low value (on April 30). Thus the time series of AOD measured over the ship matches well with the MODIS observed variations in the spatial map of AOD and the movement of the aerosol cluster.

To know the nature of particles within the aerosol cluster (observed during the episode from April 22 – 28, 2006) and their possible source (of generation), the distribution of coarse and fine mode components of AOD computed from MODIS data are examined. The spatial maps of coarse and fine mode AODs on alternate days from April 23 to 27, 2006 are presented in Fig.6.11(a) and (b) respectively. This figure shows that during the initial phase, the aerosol cluster is dominated by the coarse mode particles. But, as the cluster reaches the southern tip, where it remains nearly stationary for more than a day (from \sim April 27 to 29, 2006), the contribution of fine mode increases at the expense of coarse mode. In other words, as the cluster moves towards south along the west coast its coarse mode content progressively gets depleted and the fine mode content (supplied by the anthropogenic activities along the coast) increases.

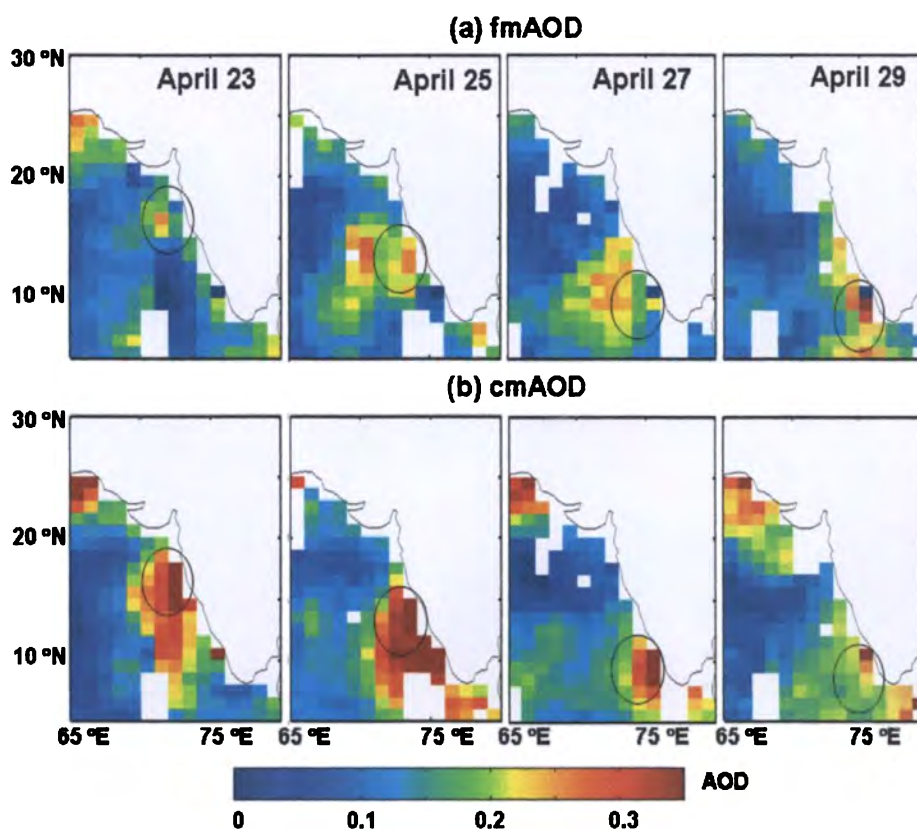


Fig.6.11. Spatial distribution of fine mode AOD (a) and coarse mode AOD on alternate days from April 23 – 29, 2006 during the episode of aerosol cluster

6.6.1 Role of dynamics in the formation, drift and dispersal of the aerosol cluster

6.6.1.1 Formation of the cluster

A close scrutiny of the daily wind pattern and circulation variables on different days, during the period of the episode reveals that on certain days the spatial pattern of wind parameters deviate significantly from the mean pattern, especially at higher altitudes. Figure 6.12(a) – (c) show respectively the two day averages of AOD distribution, before (April 19 and 20, 2006), during (April 21 and 22, 2006) and after (April 23 and 24, 2006) the formation of the aerosol cluster near the coast of Maharashtra. Similarly, Fig.6.12(d) – (f) and (g) - (i), show respectively the corresponding wind vorticity and wind convergence at 700 hPa level. A two day average is considered mainly because of the fact that, based on the spatial pattern of AOD on different days, it is seen that the time taken for the development of a major cluster from a small localized AOD fluctuation is of the order of two days.

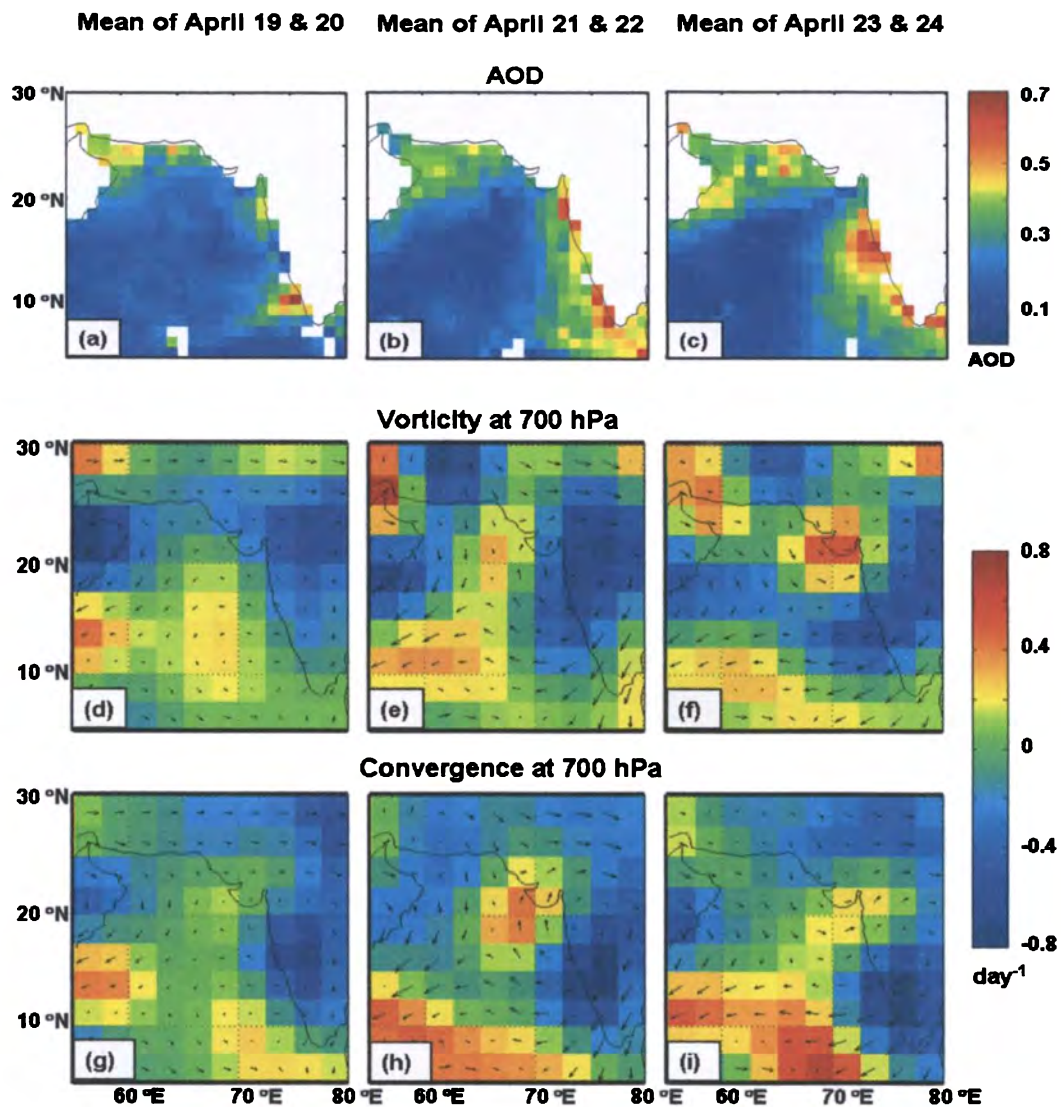


Fig. 6.12. Spatial distribution of AOD averaged over for April 19 and 20 (a) April 21 and 22 (b) and April 23 and 24, 2006 (c), vorticity at 700 hPa averaged over April 19 and 20 (d) April 21 and 22 (e) and April 23 and 24, 2006 (f), and convergence averaged over April 19 and 20 (g) April 21 and 22 (h) and April 23 and 24, 2006 (i) over the Arabian Sea.

As can be seen from Fig. 6.12 (d) to (f), the formation of the cluster can be associated with the short term strengthening of an anticyclonic circulation over the west coast of the peninsular region. The high winds associated with the anticyclone accelerate particle flow from the Indian land mass towards the west coast. On entering the Arabian Sea as wind turns northwards to meet the north westerlies from south Pakistan, at the meeting points of the winds, a convergence develops and intensifies during April 21 to 22, 2006 [Fig 6.12 (g) to (i)]. However, based on Fig. 6.13, an intense convergence does not

exist at altitudes above and below 700 hPa level, which favours the proposition that the short term enhancement of the anticyclonic circulation over the continent and the subsequent convergence of winds at ~ 700 hPa level is mainly responsible for the formation of the aerosol cluster around ~ 3 km altitude, off the Maharashtra coast.

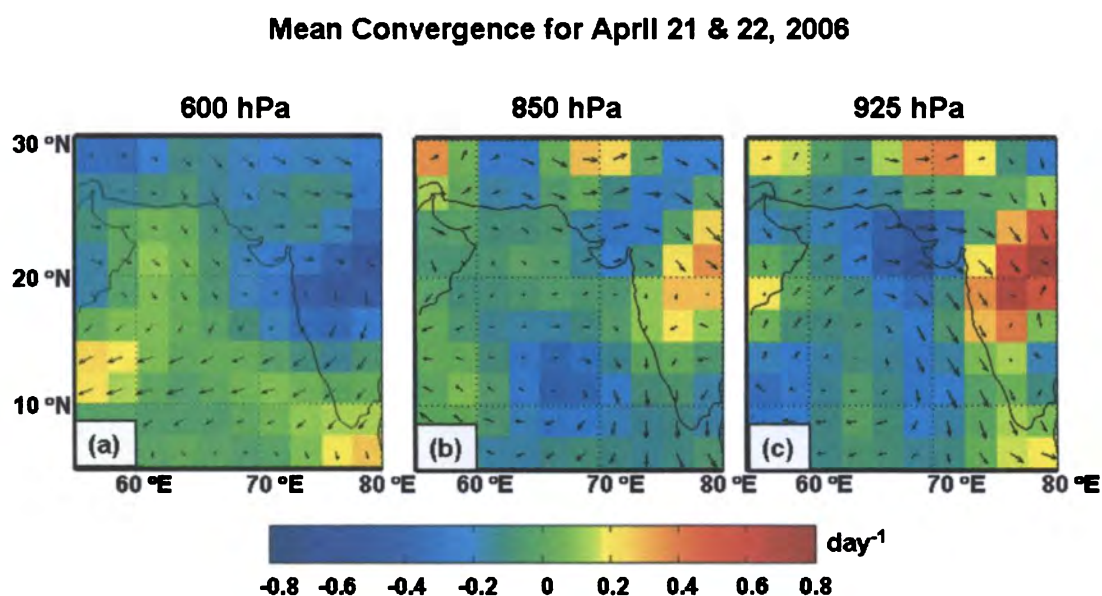


Fig.6.13. Spatial distribution of wind convergence at altitudes 600 hPa (a), 850 hPa (b) and 925 hPa (c) averaged for April 21 and 22, 2006.

The spatial distribution of the vertical winds at 925 hPa, just before the formation of the cluster (April 19 and 20, 2006) shows a strong updraft (Fig.6.14) over the Indian land

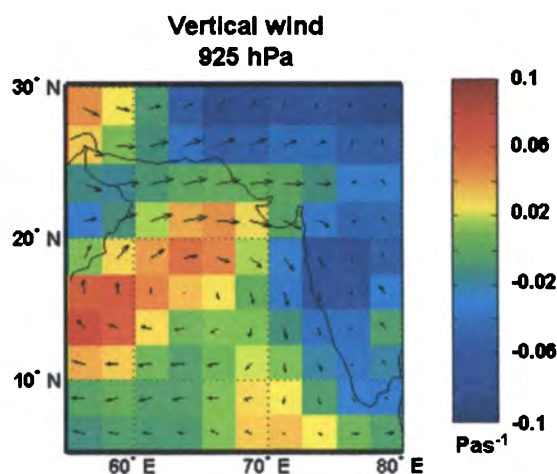


Fig.6.14. Spatial distribution of vertical wind at 925 hPa over the Arabian Sea averaged for April 19 and 20, 2006

mass, especially the Thar Desert and over the dry regions of Pakistan. This strongly suggests that the dust laden air uplifted from these regions and reaching the west coast through higher altitude wind, has copiously contributed to the coarse particle abundance in the cluster particularly, during the initial phase of its evolution, even though the contribution from locally produced sub-micron particles (anthropogenic) from Maharashtra *sumo toto* is not negligible [Fig.6.11].

6.6.1.2 Movement of the cluster along the west coast

From April 22, the aerosol cluster formed off the Maharashtra coast slowly drifts [Fig.6.10] towards south along the west coast. For sustaining the cluster all through its movement, the wind convergence along its path should be sufficiently strong. But as seen in Fig 6.5(a) in the latitudes south of $\sim 17.5^\circ$ N, the winds at 700 hPa are diverging and the direction is not conducive for the southward movement of the cluster. This necessitates one to examine the altitude structure of the wind field.

The wind convergence at 700, 850 and 925 hPa levels averaged during the period, April 22 – 28, 2006 is presented in Fig.6.15(a), (b) and (c) respectively. The encircled

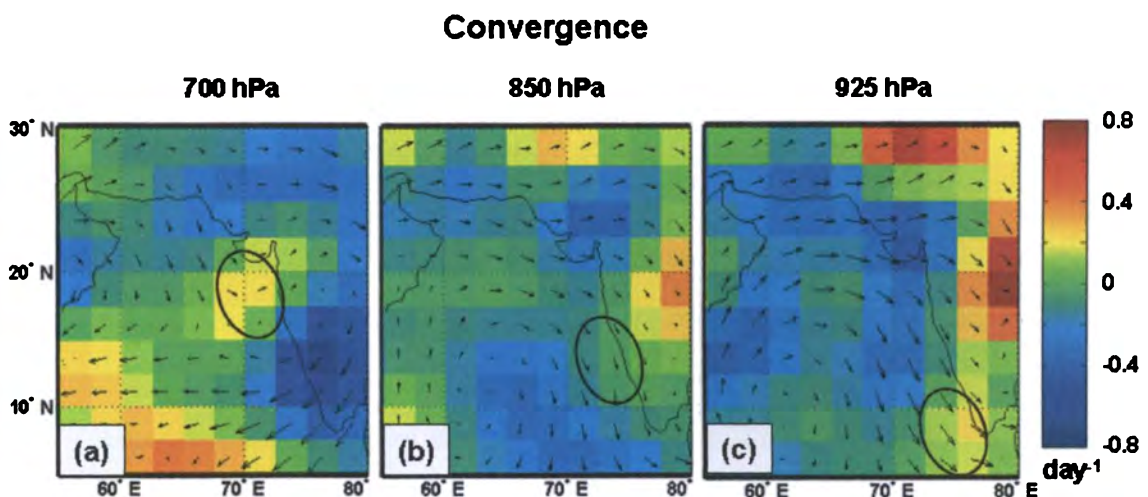


Fig.6.15. Mean spatial distribution of convergence at altitudes 700 (a), 850 (b) and 925 hPa (c) respectively during the cluster movement (April 22 – 28, 2006).

regions in these figures are the locations where the convergence is maximum (near the west coast) at the respective altitudes. It is quite interesting to note that the position of the cluster

on April 22 and 23 [Fig. 6.10] nearly coincides with that of the encircled region in Fig.6.15(a). Same is true on the subsequent days as can be seen from Fig. 6.15(b) and 6.15(c). This shows that the position of the convergence maximum descends in altitude (from 700 to 925 hPa level) as the cluster moves southwards.

On examining the altitude profile of mean vertical wind in different latitude bands [Fig.6.16], each of 5° in width from 5° to 20°N, in the longitude region of 70° to 77.5°E

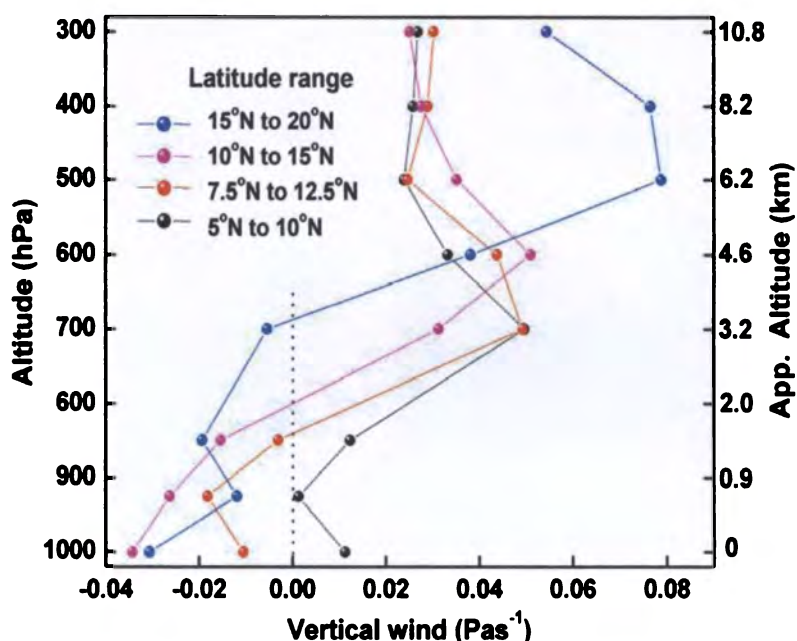


Fig. 6.16. Mean vertical wind profile over different latitudinal regions between 5° to 20°N, averaged over the longitude belt, 70° to 77.5° E, along the path of the aerosol cluster. Note that the altitude scale on the left axis is shown in pressure levels and the corresponding approximate values in km are shown on the right axis.

(the path in which the aerosol cluster moved), it can be seen that altitude at which the vertical wind reverses its direction descends continuously as the cluster moves from north to south. These features of circulation dynamics strongly suggest that the position of the wind convergence that confines the aerosols, descends in altitude progressively as the cluster moves towards south.

6.6.1.3 Dispersal of the cluster

On reaching the southern tip of the Indian peninsula, the aerosol cluster persists nearly for two days (from April 28 to 29) and subsequently disperses very fast (within a day). Figure 6.17 (a) and (b) respectively show the two day average of wind convergence

and vorticity at 925 hPa over the Arabian Sea before and during the days when the aerosol cluster dispersed. The left panels are the averages for the days April 27 and 28, 2006, when the cluster is near the southern tip of the peninsula and the right panels are the averages over the next two days, when the cluster got dispersed. It can be seen from Fig 6.17(a) that as the anticyclone over the Arabian Sea weakens on April 29 and 30, the low pressure near the southern tip of the peninsula declines. This feature leads to a perceptible decrease in prevailing convergence [Fig.6.17 (b)] near the southern tip of the peninsula, leading to the dispersal of the cluster.

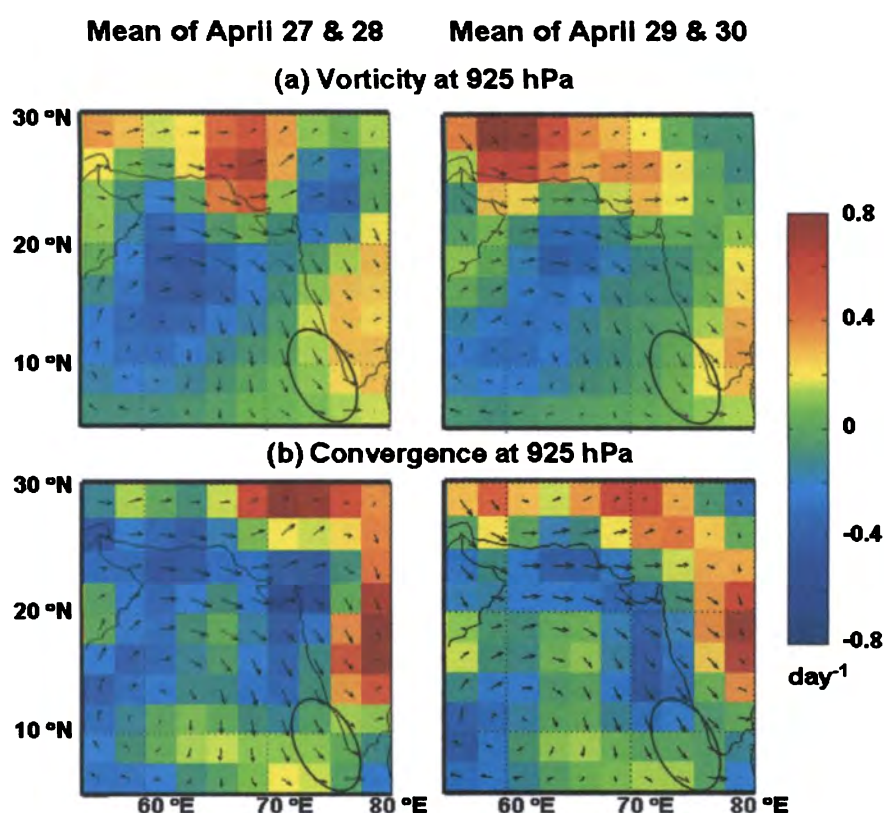


Fig. 6.17. Spatial distribution of vorticity at 925 hPa averaged for April 27 and 28 and for April 29 and 30, 2006 (a) and vorticity at 925 hPa averaged for April 27 and 28 and for April 29 and 30, 2006 (b)

The above analysis clearly shows that the transport dynamics plays a major role in the generation, movement and dispersal of the observed aerosol cluster during this episode, delineating the importance of the atmospheric circulation in the spatial distribution of aerosols.

6.6.2 Evidences from Lidar observations in support of the transport dynamics of aerosol cluster

In the above, the exhaustive analysis of the wind system has brought out the fact that the aerosol cluster descended in altitude as it drifted southwards. This hypothesis is further checked using the altitude profile of aerosols measured near Trivandrum (8.5° N, 77° E) with an air-borne Lidar and ground-based Lidar measurements from Pune (18.5° N, 73.7° E). Lidar studies carried out at Pune during ICARB by *Raj et al.*, [2008] have reported the presence of an elevated aerosol layer at about 3 – 3.5 km altitude during the campaign period, which is in good agreement with the altitude of strong convergence identified in the present analysis (of wind field). It is also important to note that the existence of such an elevated aerosol layer over the Arabian Sea was reported during the Indian ocean experiment (INDOEX) conducted in the period, January to March, 1999 [*Leon et al.*, 2002; *Welton et al.*, 2002], which was considered as the manifestation of upper level transport of continental aerosols from Arabia, eastern Pakistan and the Thar desert where the dust storm activity is very frequent during this period [*Sikka*, 1997; *Jha and Krishnamurthy*, 1998; *Rajeev et al.*, 2000].

During ICARB, aircraft sorties were carried out from different locations to study the altitude structure of aerosols [*Moorthy et al.*, 2008]. A Micro Pulse Lidar (MPL) was carried onboard an aircraft exclusively for this purpose. Air sorties were conducted over to the Arabian Sea on April 23, 2006 around 20:00 IST from Trivandrum up to a distance of ~ 350 km from the coast. The mean altitude structure of aerosol extinction coefficient obtained from this sortie is presented in Fig. 6.18(a). The spatial distribution of AOD from MODIS and the convergence at 925 hPa from NCEP for the same day are also shown in Fig. 6.18(b) and (c) respectively. For generating the AOD map, the Aqua (equatorial crossing time, 13:30 LMT) data on April 23, 2006 and Terra (equatorial crossing time, 10:30 LMT) data on April 24, 2006 are averaged to arrive at a mean distribution for ~ 23:30 LMT on April 23, 2006 [Fig.6.18(b)]. A small aerosol cluster near the Trivandrum coast can be seen along with the major cluster (the dynamics of which is discussed in Sect.6.6) positioned near the Goa coast. The altitude profile of aerosol extinction [Fig.6.18 (a)] shows a pronounced peak below 1 km where according to Fig. 6.15(c) and 6.18(c), the

convergence is maximum. These Lidar observations at Pune and Trivandrum thus suggest that the elevated layer of aerosols descends in altitude as the cluster migrates towards south.

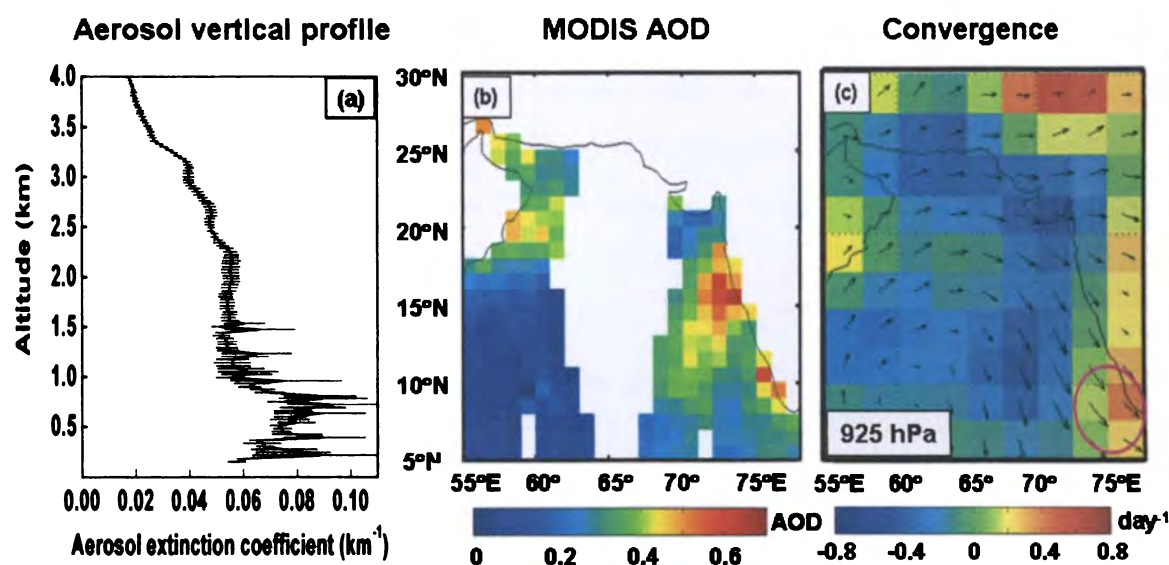


Fig. 6.18. Mean vertical profile of aerosol extinction coefficient over the Arabian Sea obtained within 350 km off the coast from Trivandrum, measured using air-borne MPL on April 23, 2006 at ~20:00 hrs IST (a) average of AOD data from Aqua on April 23, 2006 at ~ 13:30 LMT and Terra on April 24, 2006 at ~ 10:30 LMT, representing the AOD distribution at ~ 23:30 LMT on April 23, 2006 (c) wind convergence at 925 hPa on April 23, 2006. The circled region in (c) indicates the region where the convergence is the maximum in the western coast of peninsular India on April 23, 2006.

6.6.3 Supporting evidence from aerosol chemical analysis for the source of aerosols in the cluster

With the wind field features discussed in the section 6.4, it is highly suggestive that the aerosols in the cluster consist mainly of dust particles from the arid regions of north western India, southern Pakistan and Arabia (especially, in the formative stage) and also a fraction of fine particles from the industries along the west coast of India (which dominates in the later stages of the cluster). Chemical analysis is the most potential tool for source apportionment. The chemical constitution of the aerosol cluster is examined using the data on the chemical composition of aerosols collected onboard Sagar Kanya. This analysis shows [George *et al.*, 2008] abundance of crustal and pollution components in the aerosol samples collected from the location of the cluster. The daily mean concentration of the main crustal components (Aluminum and Iron) and the anthropogenic component (Sulphates) on different days from April 22 to 28, 2006 are presented in Table.6.1 along

with the mean position of the ship on these days [Fig.6.10]. It can be seen from this table that as the ship approaches the aerosol cluster, the mass concentrations of Aluminium, Iron and sulphates increase steadily, reaching a peak values on April 26 and 27, when the cluster is closer to the ship. But the anthropogenic component is much larger than the crustal components. Subsequently, as the ship moves away, the concentration of all these components reduces. This indicates that the cluster was composed of crustal particles as well as anthropogenic pollutants. Note that, the ship meets the cluster during the later phase of its evolution, when the fine mode anthropogenic contribution (sulphates) dominates over the coarse mode mineral dust (Aluminum and Iron).

Table 6.1. Daily mean concentration of the main crustal components (Aluminium and Iron) and anthropogenic component (Sulphates) obtained from the chemical analysis of aerosol samples collected onboard Sagar Kanya, during the period April 22 to 28, 2006.

Date	Ship's mean position		Aluminium (μgm^{-3})	Iron (μgm^{-3})	Sulphates (μgm^{-3})
	Latitude ($^{\circ}$ N)	Longitude ($^{\circ}$ E)			
22/04/2006	10.06	58.34	0.321	0.366	3.723
24/04/2006	11.00	64.87	0.418	0.425	3.056
25/04/2006	11.08	71.39	0.406	0.487	4.334
26/04/2006	11.20	74.50	0.928	1.103	6.007
27/04/2006	13.97	73.93	1.021	1.059	7.579
28/04/2006	15.28	71.50	0.231	0.208	3.419

6.7 Influence of wind convergence on AOD variations

6.7.1 Estimation of flux convergence

As seen from above, the spatial distribution of AOD is strongly influenced by the wind convergence in the lower troposphere. In order to assess this relationship more quantitatively, a correlation analysis is performed between the daily wind convergence at different altitudes and the corresponding variations in AOD over the oceanic part of the domain (5° - 25° N and 55° - 77.5° E). Appropriate variable considered for this analysis is the flux convergence defined by,

$$f_{ac} = -\nabla \cdot (\beta V) \quad (6.1)$$

where β is the aerosol extinction coefficient at a particular altitude and V is the vector wind at that level. For the computation of f_{ac} , it is essential to know the altitude structure of aerosols over the study domain during the period of analysis. This is derived from CALIPSO data.

6.7.2 Aerosol extinction profile from CALIPSO

Following the procedure adopted for the BoB region (Chapter 5, Sect.5.8.2), altitude profiles of aerosol extinction from CALIPSO (during the day time) over the study domain (oceanic part within the region $5^\circ - 25^\circ\text{N}$ and $55^\circ - 77.5^\circ\text{E}$) are averaged for the April – May period of 2007 and 2008 to arrive at a mean profile. From this profile, the extinction coefficients at the pressure levels of NCEP are sealed out. Integrating this altitude profile from the base to top, the AOD is estimated. The profile is further normalized by dividing the value of β at different levels by this value of AOD. Figure 6.19 shows the mean altitude profile of aerosol extinction coefficient thus obtained normalized with respect to the AOD,

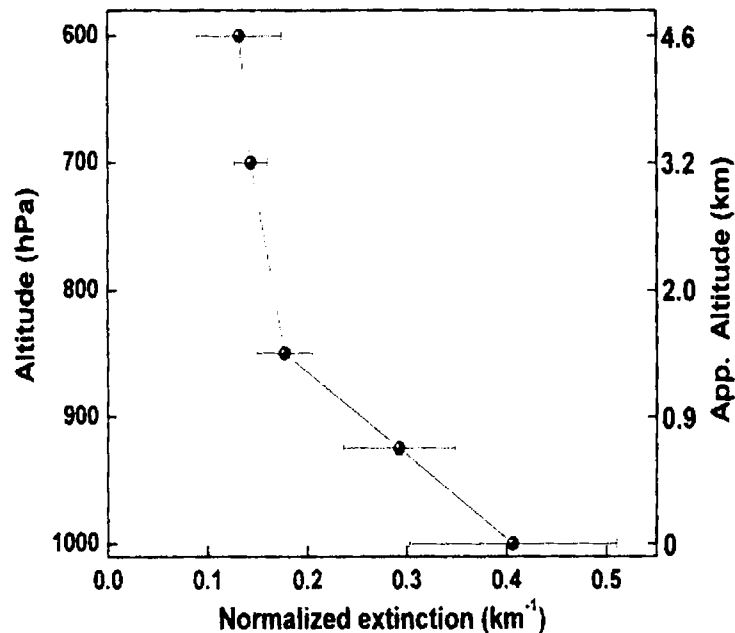


Fig.6.19. Vertical profile of normalized extinction coefficient derived from CALIPSO day time passes over the domain ($5^\circ - 25^\circ\text{N}$, $55^\circ - 77.5^\circ\text{E}$) averaged for the months April and May of 2007 and 2008. Note that the altitude scale on the left axis is shown in pressure levels and the corresponding approximate values in km are shown on the right axis.

along with the standard deviations. Following the procedure adopted in Chapter 5, Sect.5.8.2, this profile is approximated in terms of a model in the form

$$\beta_n(z) = \frac{1}{H_a} \exp\left(-\frac{z}{H_a}\right) \quad (6.2)$$

where β_n is the normalized aerosol extinction coefficient at an altitude z and H_a is the scale height whose value obtained through the best fit of the observed profile is found to be 4.3 km. Multiplying Eq.(6.2) with the AOD from MODIS, the altitude profile of aerosol extinction coefficient at every pixel in the domain is reconstructed.

6.7.3 Association between the day-to-day variations in AOD and wind convergence

Using the mean aerosol extinction profile and the NCEP winds, daily flux convergence is computed at different altitudes [Eq.(6.1)] for a grid size of $2.5^\circ \times 2.5^\circ$ over the study domain on all the individual days during the campaign period. The pixel wise flux convergence and change in AOD from the first day to the next in successive pairs (Chapter 4, Sect.4.8) over the study domain are then averaged to estimate the daily mean values. The altitude variation of the correlation between the AOD change (from one day to the next) and flux convergence (average for the two days), shown in Fig.6.20, maximizes at

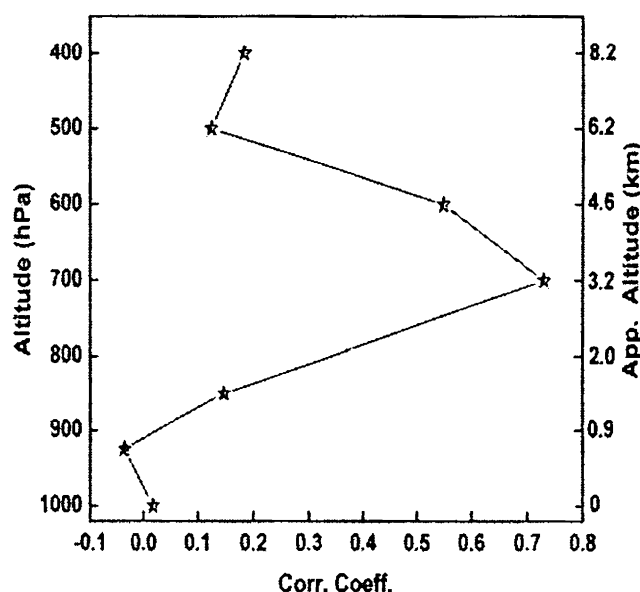


Fig.6.20. Correlation coefficients between day-to-day AOD variations and flux convergence at different altitudes. Note that the altitude scale on the left axis is shown in pressure levels and the corresponding approximate values in km are shown on the right axis.

700 hPa, with a value of 0.73 for the correlation coefficient, which is significant at >99% level of significance. Above and below this level, the correlation decreases very fast. Figure 6.21 shows a time series plot of the day-to-day change in AOD and the corresponding variation in flux convergence at 700 hPa level (at which the correlation is maximum). These two parameters show a very good correspondence with each other, which suggests that the variation in flux convergence around 3 km (corresponding to 700 hPa) is the major factor influencing the observed variation of mean AOD over the Arabian Sea.

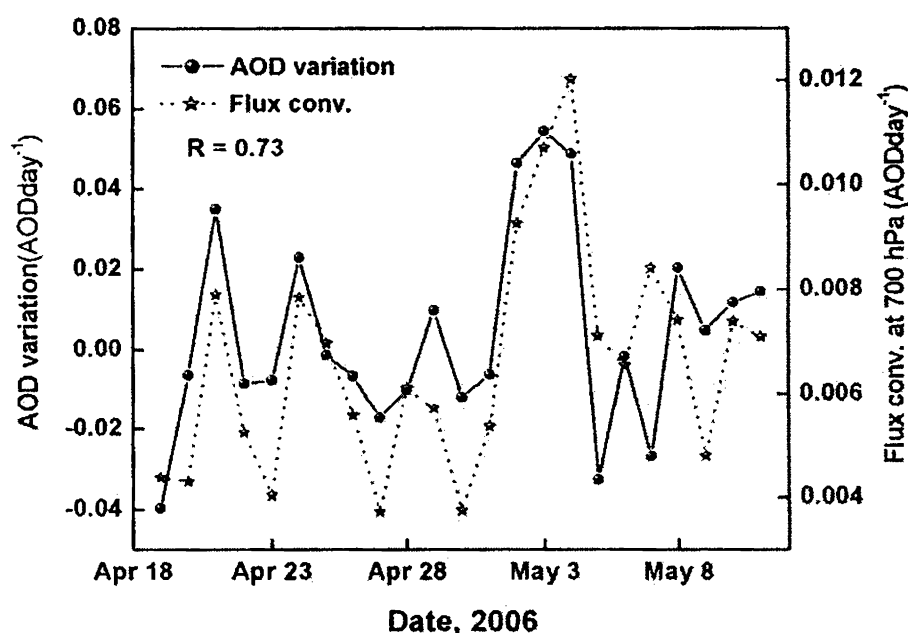


Fig.6.21 Time series plot of day-to-day AOD variation and flux convergence at 700 hPa over the domain (oceanic part over 5° - 25°N and 55° - 77.5°E) in the Arabian Sea during the second phase of ICARB. The coefficient corresponding to the correlation between the two is shown in the figure.

6.8 Estimation of aerosol source strength over the Arabian Sea

Even though a major share of the AOD observed over this oceanic region is due to aerosol advection from the surrounding land mass, the contribution from *in situ* production may not be totally negligible since the surface winds are not too low at many places. To identify the sources of possible sea-salt production over the Arabian Sea, the aerosol flux continuity equation is solved by introducing the MODIS AOD data, NCEP winds and the altitude profile of aerosol extinction. Figure 6.22 shows the distribution of source strength (expressed in AODday⁻¹) over the Arabian Sea, averaged for the entire campaign period.

This shows that the aerosol source strength is quite significant over the north eastern Arabian Sea (close to the coast of Pakistan) and to a lesser extent near the Mumbai coast. Over the north eastern Arabian Sea region, aerosol source nearly coincides with the high wind ($> 7\text{ms}^{-1}$) region close to the coast, seen in QuikSCAT ocean surface winds [Fig.6.4], suggesting that the marine sea-salt generation is the most probable mechanism for the observed increase in AOD. On the other hand, the source strength along the Arabian coast is low compared to the north eastern part, even though the wind speed is quite significant. This could be due to the inadequacies in the vertical aerosol extinction model or due to the presence of some strong aerosol removal processes. Vertical downdraft could be one factor responsible for such an aerosol loss. It is worth noting that, the vertical downdraft in the lower altitude over this region, in fact is much stronger than that over the north eastern parts [Fig 6.5(b)].

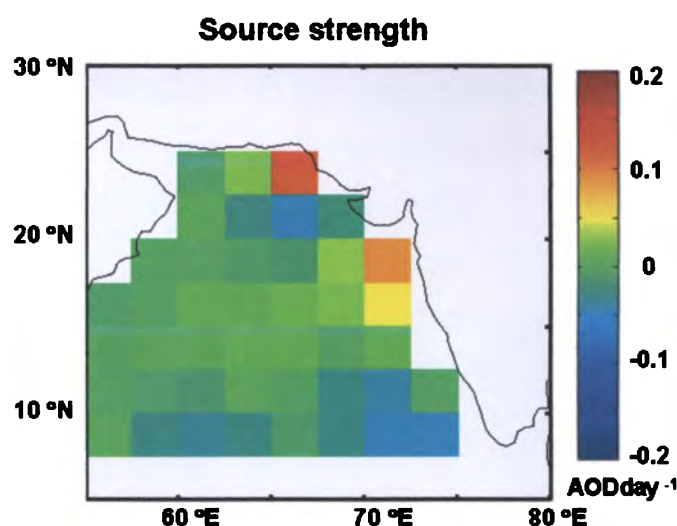


Fig.6.22. Mean source strength distribution over the Arabian Sea during the second phase of ICARB.

Relatively weak but the well discernible source seen near the Mumbai coast cannot be ascribed to marine aerosol production alone since the wind speeds here are not sufficiently strong [Fig.6.4]. Aerosol source at this location then should mainly be due to some anthropogenic activities, as this region is highly industrialized and has a few offshore oil rigs (Mumbai high, at 19°N and 71°E), which constantly give out emissions like smoke and soot [Das and Mohan, 2003].

6.9 Summary

The mean spatial distribution of AOD derived from MODIS over the Arabian Sea during the second phase of ICARB (April 18 – May 11, 2006) shows high values over the northern and south eastern Arabian Sea. In the northern Arabian Sea, more than ~ 60% contribution to AOD is from coarse particles, while in the eastern parts on an average, both fine and coarse particles contribute more or less equally. Over the mid Arabian Sea and the south western parts, even though the AOD values are low, the fine particles contribute to more than 60%. The dynamics of aerosol transport during this period is investigated using the NCEP reanalysis winds at different altitudes and the QuikSCAT derived ocean surface wind. QuikSCAT surface wind indicates that the marine aerosol production over the Arabian Sea is quite substantial in its northern part. Besides, dust transport from the arid regions of Arabia is an additional mechanism which contributes to the observed high AOD in this region. The lower altitude wind originating from the northern part of the Arabian Sea, after flowing along the industrialized west coast of peninsular India converges over the south eastern Arabian Sea and gives rise to the high aerosol loading in this region. The updraft in vertical wind over the land, north and east of the Arabian Sea, suggests the possibility for an uplift of aerosol particles to higher altitudes where they are further transported towards the Arabian Sea and subsequently brought down by the downdraft prevailing in this region.

A close examination of aerosol distribution on a day-to-day basis reveals significant variability in AOD during the campaign period. A comparison of AOD distribution between the first (April 18 -30, 2006) and second (May 1 – 11, 2006) halves of the campaign shows higher values of AOD over the central, eastern and north eastern parts of the Arabian Sea during the second half. Over the central and eastern parts, the increase in AOD is caused mainly by coarse particles even though the contribution from fine particles is not insignificant. Over the north eastern Arabian Sea, the increase in AOD is mainly caused by the influence of coarse particles. Since there is an increase in the surface winds over this region during the second half, the increase in the contribution of coarse particles could be due to enhanced generation of sea-salt. Over the central and eastern part of the Arabian Sea, the increase in AOD is due to the southward shift of an anticyclonic

circulation in the central Arabian Sea, which spreads the particles coming from Arabia more towards these two regions. In the eastern parts, the intensification of lower altitude convergence during the second half adds to the enhancement in AOD. Over and above, the anticyclonic system over the Indian peninsula (at higher altitudes) strengthens during the second half and accelerates the particle flow from the Indian land mass towards the central and south western parts of the Arabian Sea, where the higher altitude convergence (and subsequent downdraft) also becomes quite significant.

Analysis of small scale features on the daily AOD distribution reveals an interesting episode of aerosol cluster formation on the west coast of peninsular India near to the Maharashtra coast on April 22, 2006 and its subsequent movement towards south up to the tip of the peninsula where it remains for more than a day and then decays rapidly by April 30, 2006. This cluster, though initially was composed mostly of coarse particles, picks up anthropogenic particles from the industrialized west coast of India during its southward transport to become fine particle dominated, by the time it reaches the southern end. Winds at different altitudes are examined to seek the exact cause for the cluster formation. This investigation shows that, it is a short term intensification of the wind convergence at ~ 700 hPa near the Maharashtra coast, resulting from the strengthening of the anticyclone over the peninsular India that leads to the accumulation of aerosols and subsequent formation of the cluster. The downward shift of the convergence maximum and the altitude of the vertical wind reversal along the path of the cluster indicate that the cluster descends in altitude as it moves towards south. The presence of an elevated layer at about 3 – 3.5 km reported by Lidar observation at Pune and the detection of an aerosol peak at lower altitude (<1 km) at Trivandrum during this period further provide an observational support for this inference. An abrupt weakening of the lower level anticyclone over the Arabian Sea and the convergence in the south eastern Arabian Sea finally leads to the quick dispersal of the aerosol cluster near the southern tip of peninsular India. Chemical analysis of the aerosol samples collected during the ICARB shows enhancement in the crustal components (like Aluminum and Iron) and anthropogenic components (sulphates) in the cluster, when it is closer to the ship. But the anthropogenic component is higher than the crustal component indicating the predominance of fine particles when it approaches the southern end of the Indian peninsula.

A correlation analysis between the day-to-day variations in AOD and the flux convergence at different altitudes over the Arabian Sea suggests that the flux convergence around 3 km is the most influencing factor for the observed modulation in AOD. Estimation of source strength using the aerosol flux continuity equation reveals the presence of prominent sources over the north eastern Arabian Sea (along the Pakistan coast) and near the Mumbai coast. Sea-salt production by surface winds is found to be the prime process for the aerosol generation in the north eastern Arabian Sea. Near the Mumbai coast, where the wind speed is rather low, the weak sea-salt production, coastal industrial activities and off-shore oil rigs together contribute to the aerosol source.

Chapter 7

Summary and Future Scope

7.1 Summary

The Indian subcontinent, with its unique location over the globe, is a region highly influenced by the aerosols brought in from the surroundings through long range transport, in addition to the locally generated aerosols. The diverse nature of aerosol sources and the constantly changing transport pathways are the major factors responsible for the large variability in aerosol properties and their spatial distribution observed in this region. The present study mainly focuses on this very important, but relatively less explored aspect of aerosol science, the dynamics of aerosol transport. The role of transport in the spatial distribution and the temporal variability of aerosols are examined in detail at different sites over the Indian region. A brief summary of each chapter, the major outcomes of the research work and the scope for further investigations are described hereafter.

Chapter 1 provides an overview of atmospheric aerosols, their generation mechanisms, physical and optical properties and possible radiative impacts. This chapter contains a brief introduction on various techniques employed in aerosol measurements with special emphasis on the space-borne remote instrumentation. A brief review of the space-borne aerosol sensors and their utility for studying aerosol transport dynamics are also included in this chapter. This chapter concludes with an outline on the objectives of the present study.

A description of various sensors and the data products used for this study are presented in **Chapter 2**. This includes aerosol products from MODIS (onboard Terra and Aqua satellites), spectral AOD from Microtops, reanalysis winds and atmospheric humidity from NCEP, and ocean surface winds from QuikSCAT. MODIS has the advantage of having seven spectral channels for retrieving aerosol properties over the land and the ocean. This data includes information on AOD and aerosol size distribution. With the combined data from Terra and Aqua, the spatial coverage accomplished by MODIS is beyond comparison with any other sensor. The different algorithms adopted for aerosol retrieval over the land and the oceans are described in this chapter. The working principle of Microtops sunphotometer whose AOD data is utilized for assessing the accuracy of MODIS retrieved AOD, is also discussed. NCEP reanalysis provides information on different meteorological parameters like wind and relative humidity (globally) at different pressure levels. MODIS derived aerosol parameters and NCEP data are effectively utilized to investigate the role of atmospheric circulation (convergence, vorticity and up/downdrafts) and relative humidity on the day-to-day variation of AOD. Further, by incorporating the wind and AOD data into an aerosol flux continuity equation, major sources/sinks of aerosols can be identified. These methodologies are described in this chapter. A major source of aerosols over the ocean is the in-situ production of sea-salt by ocean surface winds. In the present study, QuikSCAT derived winds are used for estimating sea-salt production over the ocean. The method of detection of ocean surface winds by QuikSCAT sensor is also described in this chapter.

Subsequent four chapters are devoted for explaining the study of aerosol transport dynamics at different locations (over the land and the ocean) at different periods of the year, carried out as part of this research work. Aerosol flux continuity equation is used to delineate the major sources of aerosol in different contexts and the results evolved from the studies are presented.

Chapter 3 deals with the spatio-temporal variations of aerosol distribution over the Ganga Basin during the winter period, when ISRO-GBP Land Campaign-II was carried out in this region in December, 2004. The main objective of this campaign was the characterization of aerosols over the Indo-Gangetic Plain during the winter season when the occurrences of fog and haze are very frequent all along this region. The role of transport dynamics governing the day-to-day variations of AOD in this region is examined in detail

and the major findings are described in this chapter. Prevailing low pressure and the wind convergence in the lower troposphere (below 1 km) during the winter months are found to be conducive for the increased aerosol loading in this region. Wind convergence is the main mechanism responsible for the day-to-day variation in AOD. By solving the flux continuity equation with AOD data from MODIS and NCEP winds, with an appropriate sink model, realistic information on the prevailing aerosol sources over the Ganga basin are delineated. Emission from thermal power plants located in this region is found to be a major mechanism for aerosol generation in this region.

A detailed study on the aerosol transport over the South East Arabian Sea (SEAS) during the pre-monsoon period of 2003 (when the Arabian Sea Monsoon Experiment, ARMEX-II was conducted over this oceanic region, March 14 – April 10, 2003) and its influence on the time variation of the spatial distribution of AOD in this region are discussed in **Chapter 4**. The high value of AOD observed over the SEAS, during this period is mainly caused by the accumulation of aerosols in the lower troposphere due to the wind convergence in this region. Short term temporal variation in AOD in this region is caused by the drifting of aerosol clusters from north to south along the Indian west coast. On reaching the southern end of the peninsula, these clusters get dissipated. The episodic enhancement and decay of AOD observed onboard Sagar Kanya, during the campaign could be well correlated with the temporal evolution of a southward moving prominent aerosol cluster. The fine mode fraction (FMF), Angstrom exponent, QCM measured surface mass concentration and the prevailing wind system reveals that this cluster is mainly composed of mineral dust transported from the Arabian deserts. A partial correlation analysis of the day-to-day variation in AOD with flux convergence, surface wind speed and relative humidity shows that the episodic enhancement and decay in the AOD can be mainly attributed to the variations in wind convergence in the lower troposphere (below ~ 1 km), over the SEAS. The analysis also indicates that in addition to the dust particles, marine aerosols produced in the upwind region advected over to the ARMEX domain also contributes to a certain extent for the observed AOD variations.

Chapter 5 deals with the mechanism of aerosol transport over the Bay of Bengal (BoB) during the pre-monsoon season. This study is carried out as a part of the first phase of ICARB campaign under the ISRO-GBP during March 18 – April 12, 2006 period. During this campaign, measurements on different aerosol parameters were carried out. The

aerosol loading is found to be largest in the northern and north western parts of BoB, which decreases towards the central and southern parts. Aerosols over the BoB are mostly composed of fine mode particles except near the Head BoB where the contribution from fine and coarse particles is more-or-less the same. A detailed analysis of wind field reveals that the fine and coarse particles from West Asia, north western and central India and the Indian east coast are the principal contributors to the high aerosol loading over the BoB. Even though the prevailing anticyclonic circulation near the surface (over the BoB) impedes the direct flow of aerosols from the main land to the BoB, winds at higher altitudes over the main land (~3 km) is conducive for the aerosol transport over to the BoB. The prevailing wind convergence at these altitudes over the BoB favours an accumulation of particles and subsequent subsidence due to the prevailing downdraft. A quantitative comparison of the day-to-day variation in AOD during the campaign period with the circulation parameters reveals that the wind convergence and vorticity around 500 – 600 hPa level are the main factors governing the variations in AOD. A detailed analysis of an episode involving the formation and decay of an aerosol cluster during March 22 - 25, 2006 reveals that a short lived variation in atmospheric circulation features over the Arabian Sea, the Indian land mass and the BoB are mainly responsible for the observed AOD variation over the northern BoB region. In-situ production of aerosols over the BoB estimated using the flux continuity equation shows weak sources along the east coast of India, which agrees well with the spatial distribution of the contribution of sea-salt estimated from QuikSCAT sea surface wind speed.

Transport dynamics of aerosols over the Arabian Sea during the pre-monsoon period (second phase of ICARB, April 18 – May 11, 2006) is detailed in **Chapter 6**. The high AOD over the northern parts of the Arabian Sea is mainly due to coarse particles. The most probable sources of these particles are sea-salt aerosols generated by sea surface wind and the direct transport of soil dust from the arid regions of Arabia. On the other hand, the high values of AOD over the south eastern Arabian Sea can be attributed to the influence of transport dynamics. The soil dust advected from the arid regions of Arabia by the north/north westerly wind, mixed with the anthropogenic emissions from the industrialized west coast (of India), accumulated by the convergence prevailing over the south eastern Arabian Sea is mainly responsible for the significant increase in AOD observed in this region. Analysis of AOD during the campaign shows the formation of an intense aerosol

cluster, off Maharashtra coast, which moves southward on the subsequent days and disperses finally near the tip of the Indian peninsula. The genesis of the cluster is triggered by a short term intensification of an anticyclone at higher altitudes and subsequent convergence near the west coast of Indian peninsula. A detailed analysis of prevailing transport reveals that the cluster descends to lower altitudes as it moves southwards under the influence of wind field in all the three dimensions. The descending of aerosol cluster in altitude is further supported by the direct measurements on the altitude distribution of aerosols measured over Pune and Trivandrum. The aerosol cluster found to be initially dominated by coarse particles, becomes fine mode dominated as it reaches the southern tip of the peninsula (where it gets dissipated). The chemical analysis of aerosol particles just before its dispersal reveals significantly large amount of anthropogenic aerosols along with measurable contribution of crustal aerosols. It is also found that the day-to-day variation in AOD over the Arabian Sea in general, is predominantly governed by the wind convergence at altitudes around 3 km. Estimation of aerosol source strength reveals significant contribution from the north eastern Arabian Sea near Pakistan coast due to the sea-salt production by the surface winds. The anthropogenic contribution from the industrial emissions along the west coast including the emissions from 'Mumbai High' is responsible for the source observed near the Mumbai coast. However, the sea-salt contribution is rather small in this region.

The present study clearly brings out the influence of transport dynamics on the aerosol distribution over the Indian region at a few selected geographically distinct locations. Over the Bay of Bengal the dominant pathway of aerosol transport during the pre-monsoon period is through higher altitudes (~ 3 km); directed from the Indian main land. In contrast, the aerosol pathways over the Arabian Sea during the same period are quite complex. They are directed from geographically different environments around the ocean through different altitudes. However in general, the day-to-day variability of AOD at both these regions is significantly influenced by the features of atmospheric circulation especially, the wind convergence at higher altitudes (around 3 km). Over the Ganga Basin during the winter period, the wind convergence at lower altitudes (< 1 km) governs the short term variations in AOD, while the mean AOD distribution at this location is mainly governed by the local anthropogenic sources.

7.2 Scope for future investigation

The thesis highlights the role of transport dynamics in the spatial distribution of aerosols and their temporal variabilities. This theme opens up a new phase in the study of aerosols and has broadened the areas for further investigations.

A critical requirement for the investigation of aerosol transport is the altitude distribution of aerosol concentration over the domain of interest during the period of study. In the present study, due to the non availability of realistic (measured) aerosol profiles, either model profiles are used or profiles are generated over the study domain for the corresponding seasons from the available CALIPSO data during a later period. The lack of realistic profiles could possibly introduce uncertainties in the estimated source strength. A more realistic estimation could have been achieved if CALIPSO data for the campaign periods was available. This emphasizes the need of well-coordinated campaigns (similar to ICARB) in future, during which extensive profile measurements are also available. Over and above, the present study should be extended to other regions and other seasons and for more duration. This will be useful in addressing other complex features such as the influence of inter-seasonal (annual) and inter-annual variabilities in transport dynamics on aerosol distribution and source strength.

By introducing appropriate aerosol parameters and source distribution along with reanalysis data into regional climate models, numerical experiments could be carried out to identify the physical processes involved in the transport of aerosols influencing regional weather and climate.

References

- Abdou, W., D. Diner, J. Martonchik, C. Bruegge, R. Kahn, B. Gaitley, and K. Crean, (2005), Comparison of coincident MISR and MODIS aerosol optical depths over land and ocean scenes containing AERONET sites, *J. Geophys. Res.*, 110, D10S07, doi: 10.1029/2004JD004693.
- Ackerman, S., K.I. Strabala, W.P. Menzel, R.A. Frey, C.C. Moeller, and L.E. Gumley (1998), Discriminating clear sky from clouds with MODIS, *J. Geophys. Res.*, 103, 32 139 – 32 140.
- Ackerman, A. S., O.B. Toon, D.E. Stevens, A.J. Heymsfield, V. Ramanathan, E.J. Welton (2000), Reduction of tropical cloudiness by soot, *Science*, 288, 5468,1042-1047.
- Ahmad, Z. and R. S. Fraser (1982), An Iterative Radiative Transfer Code For Ocean-Atmosphere Systems, *J. Atmos. Sci.*, 39, 656-665.
- Albrecht, B. A. (1989), Aerosols, cloud microphysics, and fractional cloudiness, *Science*, 245, 1227-1230.
- Ali, K., G. A. Momin, S. Tewari, P. D. Safai, D. M. Chate, and P. S. P. Rao (2004), Fog and precipitation chemistry at Delhi, north India, *Atmos. Environ.*, 38, 4215–4222.
- Aloysius M., M. Mohan, K. Parameswaran (2006), Aerosol optical depth modulations by lower tropospheric meteorological fields, *Proc. SPIE*, 6408, doi:10.1117/12.694082.
- Aloysius, M., M. Mohan, S.S. Babu, V.S. Nair, K. Parameswaran, and K.K. Moorthy (2008), Influence of circulation parameters on the AOD variations over the Bay of Bengal during ICARB, *J. Earth Syst. Sci.*, 117, S1, 353 – 360.
- Andreae, M. O., and P. J. Crutzen (1997), Atmospheric aerosols: Biogeochemical sources and role in atmospheric chemistry, *Science*, 276 (5315), 1052-1058.
- Angstrom, A. (1929), On the atmospheric transmission of Sun radiation on dust in the air, *Geogr. Ann.*, 11, 156.– 166.
- Angstrom, A. (1964), The parameters of atmospheric turbidity, *Tellus*, 16, 64– 75.
- Ansmann, A., I. Mattis, U. Wadinger, F. Wagner, J. Reichardt, and T. Deshler (1997), Raman Lidar observations of particle optical depth, effective radius, mass and surface area over Central Europe at 53.4°N, *J. Atmos. Sci.*, 54, 2630 – 2641.
- Antuna, J.C., L.W. Thomson, and J.E. Barnes (2002) , Lidar validation of SAGE II aerosol measurements after the 1991 Mount Pinatubo eruption, *J. Geophys. Res.*, 107, D14, 10.1029/2001JD001441, ACL 3.

- Arimoto, R. (2001), Eolian dust and climate: relationships to sources, tropospheric chemistry, transport and deposition, *Earth-Sci. Rev.*, Vol. 54 (1-3), 29–42.
- Ball, W. P., R. R. Dickerson, B. G. Doddridge, J. W. Stehr, T. L. Miller, D. L. Savoie, and T. P. Carsey (2003), Bulk and size segregated aerosol composition observed during INDOEX 1999: Overview of meteorology and continental impacts, *J. Geophys. Res.*, 108 (D10), 8001, doi:10.1029/2002JD002467.
- Barkan, J., P. Alpert, H. Kutiel, and P. Kishcha (2005), Synoptics of dust transportation days from Africa toward Italy and central Europe, *J. Geophys. Res.*, 110, D07208, doi:10.1029/2004JD005222.
- Baron, P.A., and K. Willeke (2001), *Aerosol measurement - Principles, techniques and applications*, Second edition, John Wiley & sons, Inc., New York
- Bellouin, N., O. Boucher, J. Haywood, and M. S. Reddy (2005), Global estimate of aerosol direct radiative forcing from satellite measurements, *Nature*, 438, 1138– 1141, doi:10.1038/nature04348.
- Blanchard, D.C., and A.H. Woodcock (1957), Bubble formation and modification in the sea and its meteorological significance, *Tellus*, 9, 145 – 158.
- Blanchard, D.C. (1963), The electrification of the atmosphere by particles from bubbles in the sea, *Progr. Oceanogr.*, 1, 71 – 202.
- Blanchard, D.C., and A.H. Woodcock (1980), The production concentration and vertical distribution of the sea salt aerosols, *Ann. N. Y. Acad. Sci.*, 338, 330 –347, 1980.
- Blanchard, D. C. (1983), The production, distribution, and bacterial enrichment of the sea-salt aerosol, in *Air-Sea Exchange of Gases and Particles*, edited by P. S. Liss and W. G. N. Slinn, D. Reidal Publishing Co., Dordrecht, Holland, pp. 299-405.
- Bodhaine, B. A., N.B. Wood, E.G. Dutton, and J.R. Slusser (1999), On Rayleigh optical depth calculations, *J. Atmos. Ocean. Technol.*, 16(11), 1854– 1861.
- Bohren, C.F., and D.R. Huffman (1983), *Absorption and scattering of light by small particles*, Wiley, N.Y.
- Bond, T. C., D.G. Streets, K.F. Yarber, S.M. Nelson, J.-H. Woo, and Z. Klimont (2004), A technology based inventory of black and organic carbon emissions from combustion, *J. Geophys. Res.*, 109, D14203, doi:10.1029/2003JD003697.
- Bovensmann, H., J.P., Burrows, M. Buchwitz, J. Frerick, S. Noël, V. V. Rozanov, K.V. Chance, and A.P.H. Goede (1999), SCIAMACHY: Mission Objectives and Measurement Modes, *J. Atmos. Sci.*, 56, 127–150.
- Brumberger, H., et al. (1968), Light scattering, *Sci. Technol.*, pp. 34 – 60.

Byers, H.R. (1965), *Elements of cloud physics*, University of Chicago Press, Chicago.

Cakmur, R. V., R.L. Miller, J. Perlwitz, I. V. Geogdzhayev, P. Ginoux, D. Koch, K. E. Kohfeld, I. Tegen and C. S. Zender (2006), Constraining the magnitude of the global dust cycle by minimizing the difference between a model and observations, *J. Geophys. Res.*, 111, D06207.

Chameides, W. L., et al., A case study of the effects of atmospheric aerosols and regional haze on agriculture: An opportunity to enhance crop yields in China through emission controls?, *Proc. Nat. Acad. Sci.*, 96(24), 13,626– 13,633, 1999.

Chandra, S., S.K. Satheesh, and J. Srinivasan (2004), Can the state of mixing of black carbon aerosols explain the mystery of 'excess' atmospheric absorption?, *Geophys. Res. Lett.*, 31, 2004, doi:10.1029/2004GL020662.

Charlson, R.J. and M.J. Pilat (1969), Climate: The influence of aerosols, *J. Appl. Meteorol.*, 8, 1001 – 1002.

Charlson, R.J., J. Langner, and H. Rodhe (1990), Sulphate aerosol and climate, *Nature*, 348, 22.

Charlson, R.J., S.E. Schwartz, J.M. Hales, R.D. Cess, J.A. Coakley Jr., J.E. Hansen, and D.J. Hofmann (1992), Climate forcing by anthropogenic aerosol, *Science*, 255, 423 – 430.

Chen, W-T, R. Kahn, D. Nelson, K. Yau, and J. Seinfeld (2008), Sensitivity of multi-angle imaging to optical and microphysical properties of biomass burning aerosols. *J. Geophys. Res.*, 113, D10203, doi:10.1029/2007JD009414.

Chin, M., R.A. Kahn, L.A. Remer, H. Yu, D. Rind, G. Feingold, P.K. Quinn, S.E. Schwartz, D.G. Streets, P. Decola, R. Halthore (2009), Atmospheric aerosol properties and climate impacts, Synthesis and assessment product 2.3, *Report by the U.S climate change science program and the subcommittee on global change research*.

Chu, D. A., Y.J. Kaufman, C. Ichoku, L.A. Remer, D. Tanre, and B.N. Holben (2002), Validation of MODIS aerosol optical depth retrieval over land, *Geophys. Res. Lett.*, 29(12), 10.1029/2001GL013205.

Chung, C.E., V. Ramanathan and J.T. Kiehl (2002), Effects of the South Asian absorbing Haze on the Northeast Monsoon and Surface-Air Heat Exchange, *J. Clim.*, 2462-2476.

Clarke, A. D., and J. Noone (1985), Measurements of soot aerosol in Arctic snow, *Atmos. Environ.*, 19, 2045– 2054.

Coakley, Jr., J.A., R.D. Cess, and F.B. Yurevich (1983), The effect of tropospheric aerosols on the earth's radiation budget: A parameterization for climate models, *J. Atmos. Sci.*, 40, 116 – 138.

- Coakley, J. A. Jr, R. L. Bernstein, P.A. Durkee (1987), Effect of ship stack effluents on cloud reflectance, *Science*, 237, 953–956.
- Cox, C., and W. Munk (1954), Statistics of the sea surface derived from sun-glitter, *J. Mar. Res.*, 13, 198 – 208.
- d'Almeida, G.A., and L. Schutz (1983), *J. Clim., Appl. Meteorol.*, 22, 233.
- d'Almeida, G.A., P. Koepke, and E.P. Shettle (1991), *Atmospheric Aerosols: Global Climatology and Radiative Characteristics*, A. Deepak Publishing, Hampton, Va.
- Das, I., M. Mohan, and K.K. Moorthy (2002), Detection of marine aerosols with IRS P4 - Ocean Colour Monitor, *Proc. Indian Acad. Sci.*, 111, No.4, 425 – 435.
- Das, I. (2004), *Characterisation of marine aerosols using satellite data*, Ph.D. Thesis, Gujarat University.
- Das, I., and M. Mohan (2003), Detection of marine aerosols using ocean colour sensors, *Mausam (Special Issue)*, 54, 1, 327 – 334.
- Deepak, A., and G. P. Box (1982), Representation of aerosol size distribution data by analytic models, in *Atmospheric aerosols: Their formation, optical properties and effects*, pp. 79-110, Spectrum Press, Hampton, Virginia.
- de Graaf, M., and P. Stammes (2005), SCIAMACHY Absorbing Aerosol Index – calibration issues and global results from 2002 – 2004, *Atmos. Chem. Phys.*, 5, 2385 – 2394.
- Deirmendjian, D. (1969), *Electromagnetic scattering on spherical polydispersions*, Elsevier, New York.
- Devara, P.C.S., P.E. Raj, and S. Sharma (1994), Remote sensing of atmospheric aerosol in the nocturnal boundary layer using lidar, *Environ. Pollut.*, 85, 97 – 102.
- Dey, S., S.N. Tripathi, R.P. Singh, and B.N. Holben (2004), Influence of dust storms on aerosol optical properties over the Indo – Gangetic basin, *J. Geophys. Res.*, 109, doi: 10.1029/2004JD004924.
- Dey, S., and S. N. Tripathi (2007), Estimation of aerosol optical properties and radiative effects in the Ganga basin, northern India, during the wintertime, *J. Geophys. Res.*, 112, D03203, doi:10.1029/2006JD007267.
- Diner, D., J. Beckert, T. Reilly, et al. (1998), Multiangle Imaging Spectro-Radiometer (MISR) description and experiment overview, *IEEE Trans. Geosci. Remote Sens.*, 36, 1072-1087.

Ding, K., and H. R. Gordon (1995), Analysis of the influence of oxygen A-band absorption on atmospheric correction of ocean color imagery, *Appl. Opt.*, 34, 2068-2080.

Di Sarra, A., T. Di Iorio, M. Cacciani, G. Fiocco, and D. Fua (2001), Saharan dust profiles measured by lidar at Lampedusa, *J. Geophys. Res.*, 106, 10,335– 10,347.

Dubovik, O., B.N. Holben, T.F. Eck, A. Smirnov, Y.J. Kaufman, M.D. King, D. Tanre, and I. Slutsker (2002a), Variability of absorption and optical properties of key aerosol types observed in world wide locations, *J. Atmos. Sci.*, 59, 590–608.

Dubovik, O., B.N. Holben, T. Lapyonok, A. Sinyk, M.I. Mishchenko, P. Yang, and I. Slutsker (2002b), Non-spherical-aerosol retrieval method employing light scattering by spheroids, *Geophys. Res. Lett.*, 29(10), 1415, doi:10.1029/2001GL014506.

Dubovik, O., A. Sinyuk, T. Lapyonok, et al. (2006), Application of light scattering by spheroids for accounting for particle nonsphericity in remote sensing of desert dust, *J. Geophys. Res.*, 111, D11208, doi:10.1029/2005JD006619.

Duce R.A., et al. (1979), Wet and dry deposition of trace metals and halogens in the marine environment, paper presented at Symposium on the budget and cycles of trace gases and aerosols in the atmosphere, *Comm. on Atmos. Chem. Global Pollut.*, Boulder.

Duce, R.A., et al. (1980), Long range atmospheric transport of soil dust from Asia to the tropical north Pacific: temporal variability, *Science*, 209, 1522 – 1524.

Duce R.A. (1995), Sources, distributions, and fluxes of mineral aerosols and their relationship to climate, in *Dahlem workshop on aerosol forcing of climate*, edited by R.J Charlson and J. Heitzenberg, pp – 43 – 72, John Wiley, New York, 1995.

Duncan, B. N., R. V. Martin, A. C. Staudt, R. Yevich, and J. A. Logan (2003), Interannual and seasonal variability of biomass burning emissions constrained by satellite observations, *J. Geophys. Res.*, 108(D2), 4100, doi:10.1029/2002JD002378.

Dutton, E. G., P. Reddy, S. Ryan, and J. J. DeLuisi (1994), Features and effects of aerosol optical depth observed at Mauna Loa, Hawaii: 1982– 1992, *J. Geophys. Res.*, 99, 8295– 8306.

Eck, T., B.N., Holben, J. Reid, O. Dubovik, A. Smirnov, N. O'Neill, I. Slutsker and S. Kinne (1999), Wavelength dependence of the optical depth of biomass burning, urban and desert dust aerosols, *J. Geophys. Res.*, 104 (D24), 31 333 – 31 349.

Eck, T.F., B.N. Holben, O. Dubovik, A. Smirnov, P. Goloub, H.B. Chen, B. Chatenet, L. Gomes, X.-Y. Zhang, S.-C. Tsay, Q. Ji, D. Giles, and I. Slutsker (2005), Columnar aerosol optical depth at AERONET sites in central eastern Asia and aerosol transport to the tropical mid-Pacific, *J. Geophys. Res.*, 110, D06202, doi: 10.1029/2004JD005274.

Edlén, B. (1966), The refractive index of air, *Metrologia*, 2, 71–80.

- El-Askary, H., R. Gautam, R.P. Singh, and M. Kafatos (2004), Monitoring dust storms over Indo- Gangetic basin, *J. Indian Soc. Rem. Sens.*, 32 (2), 121 – 124.
- El-Askary, H., R. Gautam, R.P. Singh, and M. Kafatos (2006), Dust storm detection over the Indo-Gangetic basin using multi sensor data, *Adv. Space Res.*, 37, 728 – 733.
- Evans, K.F and G.L. Stephens (1991), A new polarized atmospheric radiative transfer model, *J. Quant. Spectrosc. Radiat. Transfer*, 46 (5), 413 – 423.
- Farlow, N.H., and G.V. Ferry (1979), Latitudinal variations of stratospheric aerosols, *J. Geophys. Res.*, 84, 733 – 743.
- Feingold, G., R. Boers, B. Stevens, and W. R. Cotton (1997), A modelling study of the effect of drizzle on cloud optical depth and susceptibility, *J. Geophys. Res.*, 102 (D2), 13527-13534.
- Fisher, R.A. (1970), *Statistical methods for research workers*, 14th edition, Oliver and Boyd Edinburgh, Tweeddale Court.
- Fitzgerald, J.W., and W.A. Hoppel (1988), Numerical simulation of the evolution of the particle size distribution in the marine boundary layer, *Atmospheric aerosols and nucleation*, Lecture notes in physics series, edited by Wagner, P.E., and G. Vali, 309, Springer-Verlag, Berlin.
- Fitzgerald, J.W. (1991), Marine aerosols: A review, *Atmos. Environ.*, 25, 533 – 545.
- Formenti, P., M.O. Andreae, T.W. Andreae, E. Galani, A. Vasaras, C. Zerefos, *et al.* (2001), Aerosol optical properties and large-scale transport of air masses: observations at a coastal and a semiarid site in the eastern Mediterranean during summer 1998, *J. Geophys. Res.*, 106, 9807–9826.
- Fraser, R. H., R. A. Ferrare, Y. J. Kaufman, and S. Mattoo (1989), Algorithm for atmospheric corrections of aircraft and satellite imagery, *Tech. Memo. 100751*, NASA Goddard Space Flight Cent., Greenbelt, Md.
- Freilich, *SeaWinds Algorithm Theoretical Basis Document*, NASA, ftp://podaac.jpl.nasa.gov/pub/ocean_wind/quikscat/doc/atbd-sws-01.pdf.
- Gabriel, R., O.L. Mayol-Bracero, and M.O. Andreae (2002), Chemical characterization of submicron aerosol particles collected over the Indian Ocean, *J. Geophys. Res.*, 107 (D19), 8005, doi:10.1029/2000JD000034.
- Gao Y., Y.J. Kaufman., D. Tanre, D. Kolber, and P.G. Falkowski (2001), Seasonal distribution of Aeolian iron fluxes to the global ocean, *Geophys. Res. Lett.*, 28, 29 – 32.
- Gao, B.-C., Y. J. Kaufman, D. Tanre', and R.-R. Li (2002), Distinguishing tropospheric aerosols from thin cirrus clouds for improved aerosol retrievals using the

ratio of 1.38- μm and 1.24- μm channels, *Geophys. Res. Lett.*, 29(18), 1890, doi:10.1029/2002GL015475.

Garg, A., P.R. Shukla, S. Bhattacharya, and V.K. Dadhwal (2001), Subregion (district) and sector SO₂ and NO_x emissions for India: Assessment of inventories and mitigation flexibility, *Atmos. Environ.*, 35, 703 – 713.

Gatebe, C. K., M.D. King, et al. (2001), Sensitivity of off-nadir zenith angles to correlation between visible and near-infrared reflectance for use in remote sensing of aerosol over land, *IEEE Trans. Geosci. Remote Sens.*, 39(4), 805– 819.

Gautam, R., N. C. Hsu, M. Kafatos, and S.-C. Tsay (2007), Influences of winter haze on fog/low cloud over the Indo-Gangetic plains, *J. Geophys. Res.*, 112, D05207, doi:10.1029/2005JD007036.

Geogdzhayev, I. V., M. I. Mishchenko, W. B. Rossow, B. Cairns, and A. A. Lacis (2002), Global two-channel AVHRR retrievals of aerosol properties of the ocean for the period of NOAA-9 observations and preliminary retrievals using NOAA-7 and NOAA- 11 data. *J. Atmos. Sci.*, 59, 262–278.

George, S.K. (2008), *Chemical composition of atmospheric aerosols over geographically distinct environments*, Ph.D. Thesis, University of Kerala.

Girolamo, L., T.C. Bond, D. Bramer, D.J. Diner, F. Fettinger, R.A. Kahn, J.V. Martonchik, M.V. Ramana, V. Ramanathan, and P.J. Rasch (2004), Analysis of multi-angle imaging spectroradiometer (MISR) aerosol optical depths over greater India during winter 2001 - 2004, *Geophys. Res. Lett.*, 31, L23115, doi: 10.1029/2004GL021273.

Gobbi, G. P., F. Barnada, R. Giorgi, and A. Santacasa (2000), Altitude-resolved properties of a Saharan dust event over the Mediterranean, *Atmos. Environ.*, 34, 5119– 5127.

Goloub, P., J.L. Deuze, M. Herman, D. Tanre, I. Chiapello, B. Roger, and R.P. Singh (2001), Aerosol remote sensing over land using the space-borne polarimeter, POLDER, in *Current Problems in atmospheric radiation*, edited by W.L. Smith, and Yu. M. Timofeyev, pp. 113 – 116, A. Deepak Publishing, Hampton, Virginia.

Gordon, H.R., and Wang, M. (1994), Retrieval of water-leaving radiance and aerosol optical thickness over the oceans with SeaWiFS: A preliminary algorithm, *Appl. Opt.*, 33, 443-452.

Griggs, M. (1975), Measurements of atmospheric aerosol optical thickness over water using ERTS-1 data, *J. Air Pollut. Control Assoc.*, 25, 625 – 626, 1975.

Griggs, M. (1979), Satellite observations of atmospheric aerosols during the EOMET cruise, *J. Atmos. Sci.*, 36,695-698.

- Gupta, S.P. (2005), *Statistical methods*, pp. 1110 – 1118, Sultan Chand and Sons, Educational publishers, New Delhi,
- Gustafsson, O., M. Krusa, Z. Zencak, R. J. Sheesley, L. Granat, E. Engstrom, P.S. Praveen, P.S.P. Rao, C. Leck, and H. Rodhe (2009), Brown clouds over South Asia: Biomass or fossil fuel combustion?, *Science*, 323, 495 – 498.
- Habib, G., C. Venkataraman, M. Shrivastava, R. Banerjee, J. Stehr, and R. Dickerson (2004), New methodology for estimating biofuel consumption in India: Atmospheric emissions of black carbon and sulphur dioxide, *Global Biogeochem. Cyc.*, 18, GB3007, doi:10.1029/2003GB002157.
- Hall, D.O., F. Rosilloccale, J. Wood (1994), Biomass utilization in households and industry: energy use and development, *Chemosphere*, 29, 1099–1119.
- Hamonou, E., P. Chazette, D. Bali, F. Dulac, X. Schneider, F. Galani, G. Ancellet, and A. Papayanis (1999), Characterization of the vertical structure of the Saharan dust transport to the Mediterranean basin, *J. Geophys. Res.*, 104 (D22), 256– 270.
- Hanel, G. (1976), The properties of atmospheric aerosol particles as functions of relative humidity at thermodynamic equilibrium with surrounding moist air, *Adv. Geophys.*, 19, 73- 188.
- Hansen, E.J., and L.D. Travis (1974), Light scattering in planetary atmospheres, *Space Sci. Rev.*, 16, 527–610.
- Hansen, J., M. Sato, and R. Ruedy (1997), Radiative forcing and climate response, *J. Geophys. Res.*, 102, 6831 – 6864.
- Harrison, R.M., and R.E. van Grieken (1998), *Atmospheric particles*, IUPAC series on analytical and physical chemistry of environmental systems, Vol.5, John Wiley and Sons Ltd, England.
- Hart, W.D., J.D. Spinhirne, S.P. Palm, and D. Hlavka (2005), Height distribution between cloud and aerosol layers from the GLAS space borne lidar in the Indian Ocean Region, *Geophys. Res. Lett.*, 32, L22S06, doi:10.1029/2005GL023671.
- Haywood, J.M., and K.P. Shine (1997), Multi-spectral calculations of the direct radiative forcing of tropospheric sulphate and soot aerosols using a column model, *Q. J. Roy. Meteorol. Soc.*, 123, 1907 – 1930.
- Haywood, J. M. and V. Ramaswamy (1998), Global sensitivity studies of the direct radiative forcing due to anthropogenic sulfate and black carbon aerosols, *J. Geophys. Res.*, 103, 6043–6058.
- Haywood, J.M., V. Ramaswamy, and B.J. Soden (1999), Tropospheric aerosol climate forcing in clear sky satellite observations over the oceans, *Nature*, 283, 1299-1302.

- Haywood, J. R., and O. Boucher (2000), Estimates of the direct and indirect radiative forcing due to tropospheric aerosols: A review, *Rev. Geophys.*, 38(4), 513 – 543.
- Heath, D.F., A.J. Krueger, H.R. Roeder, and B.D. Henderson (1975), The solar backscatter ultraviolet and total ozone mapping spectrometer (SBUV/TOMS) for Nimbus, *Opt. Eng.*, 14, 323 – 331.
- Heitzenberg, J., R.J. Charlson, A.D. Clarke, et al. (1997), Measurements and modeling of aerosol single scattering albedo: Progress, problems and prospects, *Beitr. Phys. Atmos.*, 70, 249 – 263.
- Heitzenberg, J., F. Raes, S.E. Schwartz, et al. (2002), Tropospheric Aerosols, in *Atmospheric Chemistry in a changing world – An integration and synthesis of a decade of tropospheric chemistry research*, edited by G. Brasseur, R.G. Prinn, and A.A.P. Pszenny, Springer: Berlin, Germany.
- Herman, J.R., and D. Larko (1994), Low ozone amounts during 1992 – 1993 from Nimbus 7 and Meteor 3 total ozone mapping spectrometer, *J. Geophys. Res.*, 99, 3483 – 3496.
- Herman J.R., P.K. Bhartia, O. Torres, C. Hsu, C. Seftor, and E. Celarier (1997), Global distribution of UV-absorbing aerosol from Nimbus-7/TOMS data, *J. Geophys. Res.*, 102, 16 912 – 16 922.
- Hewitt, C.N., and A.V. Jackson (2003), *Handbook of Atmospheric Science: Principles and Applications*, University of Leeds, Blackwell Science Ltd., A Blackwell Publishing company, Australia.
- Hinds, W. (1999), *Aerosol technology*, 2nd Ed, John Wiley & Sons, Inc., New York.
- Hobbs, P.V., J.S. Reid, R.A. Kotchenruther, R.J. Ferek, and R. Weiss (1997), Direct radiative forcing by smoke from bio-mass burning, *Science*, 275, 1776 – 1778.
- Hobbs, P. V. (2000), *Introduction to Atmospheric Chemistry*, 262 pp., Cambridge University Press.
- Hoff, R.M., S. P. Palm, J. A. Engel-Cox, and J. Spinhirne (2005), GLAS long-range transport observation of the 2003 California forest fire plumes to the northeastern US, *Geophys. Res. Lett.*, 32, L22S08, doi:10.1029/2005GL023723.
- Hoffman, D.J (1988), *Aerosols and climate*, Ed. P.V. Hobbs and M. P. McCormick, pp 195, A Deepak publishing.
- Hoffman, R.N. and S.M. Leidner (2005), An introduction to the near-real-time QuikSCAT data, *Weather and Forecasting*, 20, 476-493.
- Holben, B.N., T.F. Eck, I. Slutsker, D. Tanre, J.P. Buis, A. Setzer, E. Vermote, J.A. Reagan, Y.J. Kaufman, T. Nakajima, F. Lavenu, I. Jankowiak, and A. Smirnov

(1998), AERONET – A federated instrument network and data archive for aerosol characterisation, *Rem. Sens. Environ.*, 66, 1-16.

Holben, B.N., D. Tanre, A. Smirnov, T.F. Eck, I. Slutsker, N. Abuhassan, W.W. Newcomb, J.S. Schafer, B. Chatenet, F. Lavenu, Y.J. Kaufman, J.V. Castle, A. Setzer, B. Markham, D. Clark, R. Frouin, R. Halthore, A. Karnieli, N.T. O'Neill, C. Pietras, C., R.T. Pinker, K. Voss, and G. Zibordi (2001), An emerging ground- based aerosol climatology: aerosol optical depth from AERONET, *J. Geophys. Res.*, 106,12 067 – 12 097.

Hoppel, W. A., J.W. Fitzgerald, G.M. Frick, R.E. Larson, and E.J. Mack (1990), Aerosol size distributions and optical properties found in the marine boundary layer over the Atlantic Ocean. *J. Geophys. Res.*, 95,3659 – 3686.

Hovis, W.A., D.K. Clark, F. Anderson, et al. (1980), Nimbus-7 Coastal Zone Color Scanner: system description and initial imagery, *Science*, 210, 60–63.

Husar, R. B., J.M. Prospero, and L.L Stowe (1997), Characterization of tropospheric aerosols over the oceans with the NOAA advanced very high resolution radiometer optical thickness operational product, *J. Geophys. Res.*, 102, 16 889–16 909.

Ichoku, C., L. Robert, Y.J. Kaufman, L.A Remer, R-R. Li, V. J. Martins, B.N. Holben, N. Abuhassan, I. Slutsker, T.F. Eck, and C. Pietras (2002), Analysis of the performance characteristics of the five-channel Microtops II Sun photometer for measuring aerosol optical thickness and precipitable water vapor, *J. Geophys. Res.*, Vol. 107, D13, 10.1029/2001JD001302.

Ichoku, C., L. A. Remer, Y. J. Kaufman, R. Levy, D. A. Chu, D. Tanre, and B. N. Holben (2003), MODIS observation of aerosols and estimation of aerosol radiative forcing over southern Africa during SAFARI 2000, *J. Geophys. Res.*, 108(D13), 8499, doi:10.1029/2002JD002366.

Ichoku, C., L. A. Remer, and T. F. Eck (2005), Quantitative evaluation and intercomparison of morning and afternoon MODIS aerosol measurements from Terra and Aqua, *J. Geophys. Res.*, 110, D10S03, doi:10.1029/2004JD004987.

Ignatov, A. and L. Stowe (2002), Aerosol retrievals from individual AVHRR channels: I. Retrieval algorithm and transition from Dave 5 to 6S radiative transfer model, *J. Atmos. Sci.*, 59, 313 – 334.

Intergovernmental Panel on Climate Change (IPCC) (2001), *Climate change 2001: The Scientific Basis*, edited by Houghton, et al., Cambridge Univ. Press, New York, pp. 896.

Intergovernmental Panel on Climate Change (IPCC), (2007), *Climate change 2007: The scientific basis*, In: Solomon, S. (Ed.), *Contribution of Working Group I to the Fourth Assessment Report of the Intergovernmental Panel on Climate Change*, Cambridge Univ. Press, New York.

- Jacobson, M. Z. (2001), Strong radiative heating due to mixing state of black carbon in the atmospheric aerosols, *Nature*, 409, 695– 697.
- Jaenicke, R. (1980), Atmospheric aerosols and climate, *J. Atmos. Sci.*, 11, 577 – 588.
- Jaenicke, R. (1984), Physical aspects of atmospheric aerosol, in *Aerosols and their climatic effects*, Gerber, H.E and A. Deepak (Eds), pp. 7- 34, A. Deepak Publishing, Hampton, Va.
- Jaenicke, R. (1993), Tropospheric aerosols, in *Aerosol-cloud-climate interactions*, edited by P.V. Hobbs, 1 – 31, Academic Press, San Diego.
- Jain, M.K., S.R.K. Iyengar, and R.K. Jain (1993), *Numerical methods for scientific and engineering computation*, pp. 249 – 251, Wiley Eastern Limited.
- Jayaraman, A. S. Ramachandran, Y.B. Acharya, and B.H. Subbaraya (1995), Pinatubo volcanic aerosol layer decay observed at Ahmedabad (23°N), India using Nd YAG backscatter Lidar, *J. Geophys. Res.*, 100, 23 209 – 23 214.
- Jethva, H., S. K. Satheesh, and J. Srinivasan (2005), Seasonal variability of aerosols over the Indo-Gangetic basin, *J. Geophys. Res.*, 110, D21204, doi:10.1029/2005JD005938.
- Jethva, H., S. K. Satheesh, and J. Srinivasan (2007), Assessment of second generation MODIS aerosol retrieval (Collection 005) at Kanpur, India, *Geophys. Res. Lett.*, 34, L19802, doi:10.1029/2007GL029647.
- Jha, B., and T.N Krishnamurthi (1998), Real-time meteorological reanalysis atlas during pre-INDOEX Field Phase –98, Scientific Rep., *FSU Rep. 98 – 08*, Tallahassee, FL 32306-4520.
- Jha, B., and T. N. Krishnamurti (1999), Real-time meteorological atlas during the INDOEX-1999, Scientific Rep., *FSU Rep. 99-09*, Tallahassee, FL 32306 - 4520.
- Junge, C.E. (1963), Air chemistry and radioactivity, *Int. Geophys. Ser.*, Academic, New York, Vol. 4, pp. 382.
- Junge, C.E. (1972), Our knowledge of the physio-chemistry of aerosols in the undisturbed marine environment, *J. Geophys. Res.*, 77, 27, 5183 – 5200.
- Kahn, R., P. Banerjee, D. McDonald, and D. Diner (1998), Sensitivity of multiangle imaging to aerosol optical depth, and to pure-particle size distribution and composition over ocean, *J. Geophys. Res.*, 103, 32195-32213.
- Kalashnikova, O., and R. Kahn (2006), Ability of multiangle remote sensing observations to identify and distinguish mineral dust types: Part 2. Sensitivity over dark water, *J. Geophys. Res.*, 111:D11207, doi:10.1029/2005JD006756.

- Kalnay, E., M. Kanamitsu, R. Kistler, W. Collins, et al. (1996), The NCEP/NCAR Reanalysis 40-year Project, *Bull. Am. Meteorol. Soc.*, 77, 437–471.
- Kalivitis, N., E. Gerasopoulos, M. Vrekoussis, G. Kouvarakis, N. Kubilay, N. Hatzianastassiou, I. Vardavas, and N. Mihalopoulos (2007), Dust transport over the eastern Mediterranean derived from Total Ozone Mapping Spectrometer, Aerosol Robotic Network, and surface measurements, *J. Geophys. Res.*, 112, D03202, doi:10.1029/2006JD007510.
- Kaufman, Y.J., D. Tanre, H.R. Gordon, T. Nakajima, J. Lenoble, R. Frouin, H. Grassl, B.M. Herman, M.D. King, and P.M. Teillet (1997a), Passive remote sensing of tropospheric aerosol and atmospheric correction for the aerosol effect, *J. Geophys. Res.*, 102, 16 815 – 16 830.
- Kaufman, Y.J., D. Tanre, L.A. Remer, E.F. Vermote, A. Chu, and B.N. Holben (1997b), Operational remote sensing of tropospheric aerosol over land from EOS moderate resolution imaging spectroradiometer, *J. Geophys. Res.*, 102, 17 051 – 17 068.
- Kaufman, Y. J., A. E. Wald, L. A. Remer, B-C. Gao, R-R. Li, and L. Flynn (1997c), The MODIS 2.1- μm channel – Correlation with visible reflectance for use in remote sensing of aerosol, *IEEE Trans. Geosci. Remote Sens.*, 35(5), 1286–1298.
- Kaufman, Y. J. and R.S. Fraser (1997), Confirmation of the smoke particles effect on clouds and climate, *Science*, 277, 1636–1639.
- Kaufman, Y.J., P.V. Hobbs, V. Kirchhoff, et al. (1998), Smoke, Clouds, and Radiation – Brazil (SCAR-B) Experiment, *J. Geophys. Res.*, 103 (D24), 31 783 – 31 808.
- Kaufman, Y., D. Tanre', and O. Boucher (2002), A satellite view of aerosols in the climate system, *Nature*, 419, doi:10.1038/nature01091.
- Kaufman, Y. J., O. Boucher, D. Tanre', M. Chin, L. A. Remer, and T. Takemura (2005), Aerosol anthropogenic component estimated from satellite data, *Geophys. Res. Lett.*, 32, L17804, doi:10.1029/2005GL023125.
- Kent, G.S., P.H. Wang, and K.M. Skeens (1997), Discrimination of cloud and aerosol in the Stratospheric and Gas Experiment III occultation data, *App. Opt.*, 36, 8639 – 8649.
- Kent, G.S., C.R. Trepte, and P.L. Lucker (1998), Long-term Stratospheric Aerosol Gas Experiment I and II measurements of upper tropospheric aerosol extinction, *J. Geophys. Res.*, 103, D22, 28 863 – 28 874.
- Kidder, S.G., and T.H. Vonder Haar (1995), *Satellite meteorology an introduction*, Academic Press.
- Kiehl, J. T. and B.P. Briegleb (1993), The relative roles of sulfate aerosols and greenhouse gases in climate forcing, *Science*, 260, 311–314.

Kiehl, J.T., V. Ramanathan, J.J. Hack, A. Huffman, and K. Swett (1999), The role of aerosol absorption in determining the atmospheric thermodynamic state during INDOEX (abstract), *EOS Trans. AGU*, 80 (46), Fall Meet. Suppl., 184.

King, M.D., Y.J. Kaufman, D. Tanre', and T. Nakajima (1999), Remote sensing of Tropospheric Aerosols from Space: Past, Present, and Future, *Bull. Am. Meteorol. Soc.*, 80, 2229 – 2259.

Kirimoto, T. and R.K. Moore (1985), Scanning wind-vector scatterometers with two pencil beams, *Proc. Conf. on Rem. Sens. Oceans Atmos.*, NASA Conf. Pub., 2303, 89- 97.

Kleidman, R. G., N. T. O'Neill, L. A. Remer, Y. J. Kaufman, T. F. Eck, D. Tanre', and B. N. Holben (2005), Comparison of Moderate Resolution Imaging Spectroradiometer (MODIS) and aerosol robotic network (AERONET) remote-sensing retrievals of aerosol fine mode fraction over ocean, *J. Geophys. Res.*, 110, D22205, doi:10.1029/2005JD005760.

Koepke, P. (1984), Effective reflectance of oceanic white caps, *Appl. Opt.*, 23, 1816 – 1824.

Koren, I., J. H. Joseph, and P. L. Israelevich (2003), Detection of dust plumes and their sources in northeastern Libya, *Can. J. Remote Sens.*, 29(6), 792–796.

Koren, I., L. A. Remer, Y. J. Kaufman, Y. Rudich, and J. V. Martins (2007), On the twilight zone between clouds and aerosols, *Geophys. Res. Lett.*, 34, L08805, doi:10.1029/2007GL029253.

Kramer, H.J. (1994), *Observation of the Earth and its environment*, Springer-Verlag, New York.

Krishnamurti, T. N., A. Chakraborty, A. Martin, W. K. Lau, K.-M. Kim, Y. Sud, and G. Walker (2009), Impact of Arabian Sea pollution on the Bay of Bengal winter monsoon rains, *J. Geophys. Res.*, 114, D06213, doi:10.1029/2008JD010679.

Lau, K.-M., M. K. Kim, and K. M. Kim (2006), Asian summer monsoon anomalies induced by aerosol direct forcing: The role of the Tibetan plateau, *Clim. Dyn.*, 26, 855–864, doi:10.1007/s00382-006-0114-z.

Lau, K.-M., V. Ramanathan, G.-X. Wu, Z. Li, S.C. Tsay, C. Hsu, R. Sikka, B. Holben, D. Lu, G. Tartari, M. Chin, P. Koidelova, H. Chen, Y. Ma, J. Huang, K. Taniguchi, and R. Zhang (2008), The joint aerosol-monsoon experiment- A new challenge for monsoon climate research, *Bull. Am. Meteorol. Soc.*, 89, 369 – 383, doi:10.1175/BAMS-89-3-369.

Lee, T., et al. (2006), The NPOESS VIIRS day/night visible sensor, *Bull. Am. Meteorol. Soc.*, 87, 191-199.

Lelieveld, J., P. J. Crutzen, V. Ramanathan, et al. (2001), The Indian Ocean Experiment: Widespread air pollution from South and Southeast Asia, *Science*, **291**, 1031–1036.

Leon, J.-F., P. Chazette, J. Pelon, F. Dulac and H. Randriamiarisoa (2002), Aerosol direct radiative impact over the INDOEX area based on passive and active remote sensing, *J. Geophys. Res.*, **107**, D19, 10.1029/2000JD000116.

Leroy, M., J. L. Deuze, F. M. BrCon, O. Hautecoeur, M. Herman, J. C. Buriez, D. Tanrt, S. Bouffies, P. Chazette, and J. L. Roujean (1997), Retrieval of atmospheric properties and surface bidirectional reflectances over land from POLDER ADEOS, *J. Geophys. Res.*, **102**, 17 023 – 17 037.

Levy, R.C., L.A. Remer, D. Tanré, Y.J. Kaufman, C. Ichoku, B.N. Holben, J.M. Livingston, P.B. Russell and H. Maring (2003), Evaluation of the MODIS retrievals of dust aerosol over the ocean during PRIDE, *J. Geophys. Res.*, **108**, (D14), 10.1029/2002JD002460.

Levy, R. C., L. A. Remer, and Y.J. Kaufman (2004), Effects of neglecting polarization on the MODIS aerosol retrieval over land, *IEEE Trans. Geosci. Remote Sens.*, **42**(11), 2576-2583.

Levy, R.C., L.A. Remer, J.V. Martins, Y.J. Kaufman, A. Plana-Fattori, J. Redemann, and B. Wenny (2005), Evaluation of the MODIS aerosol retrieval over ocean and land during CLAMS, *J. Atmos. Sci.*, **62** (4), 974 – 992.

Levy, R. C., L. A. Remer, S. Mattoo, E. Vermote, and Y. J. Kaufman (2007), Second generation algorithm for retrieving aerosol properties over land from MODIS spectral reflectance, *J. Geophys. Res.*, **112**, D13211, doi:10.1029/2006JD007811.

Li, F., and V. Ramanathan (2002), Winter to summer monsoon variation of aerosol optical depth over the tropical Indian Ocean, *J. Geophys. Res.*, **107**, 4284, doi: 10.1029/2001JD000949.

Li, R.-R., Y. J. Kaufman, B.-C. Gao, and C. O. Davis (2003), Remote sensing of suspended sediments and shallow coastal waters, *IEEE Trans. Geosci. Remote Sens.*, **41**, 559– 566.

Liu, Z., D. Liu, J. Huang, M. Vaughan, I. Uno, N. Sugimoto, C. Kittaka, C. Trepte, Z. Wang, C. Hostetler, and D. Winker (2008), Airborne dust distributions over the Tibetan Plateau and surrounding areas derived from the first year of CALIPSO lidar observations, *Atmos. Chem. Phys. Discuss.*, **8**, 5957– 5977.

London, J., R. D. Bojkov, S. Oltmans, and J. I. Kelley (1976), Atlas of the global distribution of total ozone July 1957– June 1967, *NCAR Tech. Note 133+STR*, pp. 276, National Centre for Atmospheric Research, Boulder.

- Lubin D., J.-P. Chen, P. Pilewskie, V. Ramanathan, and F.P. J. Valero (1996), Microphysical examination of excess cloud absorption in the tropical atmosphere, *J. Geophys. Res.*, 101, 16 961 – 16 972.
- Lungu, T., Ed., (2001): *QuikSCAT science data product user's manual, overview and geophysical data products*, Version 2.2, Jet Propulsion Laboratory, Pasadena, CA, 95 pp. [JPL D-18053].
- Luo, C., N. Mahowald, and C. Jones (2004), Temporal variability of dust mobilization and concentration in source regions, *J. Geophys. Res.*, 109, D20202, doi:10.1029/2004JD004861.
- Mackay, G., M.D. Steven, and J.A. Clark (1998), An atmospheric correction procedure for the ATSR-2 visible and near-infrared land surface data, *Int. J. Remote Sens.*, 19, 2949-2968.
- Malm, W. C., J. F. Sisler, D. Huffman, R. A. Eldred, and T. A. Cahill (1994), Spatial and seasonal trends in particle concentration and optical extinction in the United States, *J. Geophys. Res.*, 99(D1), 1347-1370.
- Martins, J. V., D. Tanre, L.A. Remer, Y. Kaufman, S. Mattoo, and R. Levy (2002), MODIS Cloud screening for remote sensing of aerosols over oceans using spatial variability, *Geophys. Res. Lett.*, 29(12), 8009, doi:10.1029/2001GL013252.
- Martonchik, J., D. Diner, R. Kahn, M. Verstraete, B. Pinty, H. Gordon, and T. Ackerman (1998), Techniques for the Retrieval of aerosol properties over land and ocean using multiangle data, *IEEE Trans. Geosci. Remote Sens.*, 36, 1212-1227.
- Masouka, E., A. Fleig, R.E. Wolfe, and F. Patt (1998), Key characteristics of MODIS data products, *IEEE Trans. Geosci. Remote Sens.*, 36, No.4, 1313 – 1323.
- Massie, S.T., O. Torres, and S.J. Smith (2004), Total Ozone Mapping Spectrometer (TOMS) observations of increase in Asian aerosol in winter from 1979 – 2000, *J. Geophys. Res.*, 109, D18211, doi: 10.1029/2004JD004620.
- McCartney, E.J. (1976), *Optics of the atmosphere*, John Wiley & Sons, New York.
- McClatchey, R.A., R.W. Fenn, J. E. A. Selby, F.E. Volz and J.S. Garing (1972), *Optical properties of the atmosphere*, AFCRL – 72- 0497, US Airforce Geophysical Laboratory, Hanscom Mass.
- McCormick, R.A. and J. H. Ludwig (1967), Climate modification by atmospheric aerosols, *Science*, 156 (3780), 1358 – 1359.
- McCormick, M.P., P. Hamill, T.J. Pepin, W.P. Chu, T.J. Swissler, L.R. McMaster (1979), Satellite studies of the stratospheric aerosol, *Bull. Am. Meteorol. Soc.*, 1038 – 1046.

- McTainsh, G. H. (1980), Harmattan dust deposition in northern Nigeria, *Nature*, 286, 587–588.
- Meehl, G.A., J.M. Arblaster, and W.D. Collins (2007), Effects of black carbon aerosols on the Indian monsoon, *J. Climate*, 21, doi:10.1175/2007JCL1777.1, 2869 – 2882.
- Menon, S., J. Hansen, L. Nazarenko, and Y. Lou (2002), Climatic effects of black carbon aerosols in China and India, *Science*, 297, 2250 – 2253.
- Middleton, N.J. (1986), A geography of dust storms in south west Asia, *Int. J. Climatol.*, 11, 3247 – 3267.
- Miller, R. L., I. Tegen, and J. Perlwitz (2004), Surface radiative forcing by soil dust aerosols and the hydrologic cycle, *J. Geophys. Res.*, 109 (D4), art. no. D04203, 1–8.
- Mircea, M., M. C. Facchini, S. Decesari, F. Cavalli, L. Emblico, S. Fuzzi, A. Vestin, J. Rissler, E. Swietlicki, G. Frank, M. O. Andreae, W. Maenhaut, Y. Rudich, and P. Artaxo (2005), Importance of the organic aerosol fraction for modeling aerosol hygroscopic growth and activation: a case study in the Amazon Basin. *Atmos. Chem. Phys.*, 5, 3111–3126.
- Mishchenko, M.I., and L.D. Travis (1997), Satellite retrieval of aerosol properties over the ocean using polarization as well as intensity of reflected light, *J. Geophys. Res.*, 102, 16 989 – 17 013.
- Mishchenko, M.I., I. V. Geogdzhayev, B. Cairns, W. B. Rossow, and A. A. Lacis (1999), Aerosol retrievals over the ocean by use of channels 1 and 2 AVHRR data: Sensitivity analysis and preliminary results, *Appl. Opt.*, 38, 7325–7341.
- Mishchenko, M. I., I.V. Geogdzhayev, L. Liu, J.A. Ogren, A.A. Lacis, W.B. Rossow, J.W. Hovenier, H. Volten, and O. Muoz (2003), Aerosol retrievals from AVHRR radiances: effects of particle nonsphericity and absorption and an updated long-term global climatology of aerosol properties, *J. Quant. Spectrosc. Radiat. Transfer*, 79/80, 953–972.
- Mishchenko, M., B. Cairns, G. Kopp, et al. (2007), Accurate monitoring of terrestrial aerosols and total solar irradiance: Introducing the glory mission, *Bull. Am. Meteorol. Soc.*, 88, 677 - 691.
- Misra, A., A. Jayaraman, and D. Ganguly (2008), Validation of MODIS derived aerosol optical depth over Western India, *J. Geophys. Res.*, 113, D04203, doi: 10.1029/2007JD009075.
- Mitchell Jr., J.M. (1970), A preliminary evaluation of atmospheric pollution as a cause of the global temperature fluctuation of the past century, In Fred Singer, S. (Ed.), *Global Effects of Environmental Pollution*, pp. 139–155, Springer-Verlag, New York,.

- Molina, L. T., and M. J. Molina (1986), Absolute absorption cross sections of ozone in the 185- to 350-nm wavelength range, *J. Geophys. Res.*, 91, 14,501–14,508.
- Moller, D. (1984), Estimation of the global man-made sulphur emission, *Atmos. Environ.*, 18, 19-27.
- Monahan, E.C. (1971), Oceanic white caps and sea state, *J. Phys. Oceanogr.*, 1, 139 – 144.
- Monahan, E.C., D.E. Spiel, and K.L. Davidson (1986), A model for marine aerosol generation via white caps and wave disruption, *Oceanic white caps*, Riedel, Hingham, M.A., U.S.A.
- Moorthy, K.K, S.K. Satheesh, and B.V.K. Murthy (1997), Investigations of marine aerosols over the tropical Indian ocean, *J. Geophys. Res.*, 102, 18827 – 18842.
- Moorthy, K.K., and A. Saha (2000), Aerosol study during INDOEX: Observations of enhanced aerosol activity over the Mid Arabian Sea during the northern winter, *J. Atmos. Sol. Terr. Phys.*, 62, 65 – 72.
- Moorthy, K.K., and S.K. Satheesh (2000), Characteristics of aerosols over a remote island, Minicoy in the Arabian Sea: Optical properties and retrieved size characteristics; *Q. J. R. Meteorol. Soc.*, 126, 81 – 109.
- Moorthy, K. K., A. Saha, B.S.N. Prasad, K. Niranjana, D. Jhurry, P.S. Pillai (2001), Aerosol optical depths over peninsular India and adjoining oceans during the INDOEX campaigns: Spatial, temporal, and spectral characteristics, *J. Geophys. Res.*, 106(D22), 28 539–28 554.
- Moorthy K K, S.S. Babu, and S.K. Satheesh (2003), Aerosol optical depth over the Bay of Bengal: Role of transport, *Geophys. Res. Lett.*, 30, No 5, doi: 10.1029/2002GL016520 1249.
- Moorthy, K.K., S. S. Babu, and S.K. Satheesh (2005), Aerosol characteristics and radiative impacts over the Arabian Sea during the inter monsoon seasons: Results from ARMEX field Campaign, *J. Atmos. Sci.*, 62, 192 – 206.
- Moorthy, K. K., S. K. Satheesh, S. S. Babu, and C. B. S. Dutt (2008), Integrated Campaign for Aerosols, Gases and Radiation Budget (ICARB): An overview, *J. Earth Syst. Sci.*, 117, 243–262.
- Morys, M., F.M. Mims III, S. Hagerup, S. E. Anderson, A. Baker, J. Kia, and T. Walkup (2001), Design, calibration, and performance of MICROTOPS II handheld ozone monitor and sun photometer, *J. Geophys. Res.*, 106 (D13), 14 573 – 14 582.
- Moulin, C., C.E. Lambert, and U. Dayan, et al. (1998), Satellite climatology of African dust transport in the Mediterranean atmosphere, *J. Geophys. Res.*, 103, 13 137–13 143.

Mukai, S., I. Sano, and A. Toigo (1998), Removal of scattered light in the earth troposphere, *Earth Planets Space*, 50, 595 – 601.

Nair, P. R., and K. K. Moorthy (1998), Effects of changes in atmospheric water vapour content on physical properties of aerosols at a coastal location, *J. Atmos. Solar Terr. Phys.*, 60, 563 – 572.

Nair, S. K., K. Rajeev, and K. Parameswaran (2003), Winter time regional aerosol distribution and the influence of continental transport over the Indian Ocean, *J. Atmos. Solar Terr. Phys.*, 65, 149– 165.

Nair, S.K., K. Parameswaran, and K. Rajeev (2005), Seven year of satellite observations of the mean structures and variabilities in the regional aerosol distribution over the oceanic areas around the Indian subcontinent, *Ann. Geophys.*, 23, 2011 – 2030.

Nair, V. S., K. K. Moorthy, D. P. Alappattu, P. K. Kunhikrishnan, S. George, P. R. Nair, S. S. Babu, B. Abish, S. K. Satheesh, S. N. Tripathi, K. Niranjana, B. L. Madhavan, V. Srikant, C. B. S. Dutt, K. V. S. Badarinath, and R. R. Reddy (2007), Wintertime aerosol characteristics over the Indo-Gangetic Plain (IGP): Impacts of local boundary layer processes and long-range transport, *J. Geophys. Res.*, 112, D13205, doi:10.1029/2006JD008099.

Nair, V.S., K. K. Moorthy, S. S. Babu, K. Narasimhalu, L.S.S. Reddy, R.R. Reddy, K.R. Gopal, V. Sreekanth, B.L. Madhavan, and K. Niranjana (2008), Size segregated aerosol mass concentration measurements over the Arabian Sea during ICARB, *J. Earth Sys. Sci.*, 117, S1, 315 – 323.

Nair,P.R., S.K. George, K. Parameswaran, M. Aloysius, D. P. Alappattu, M. Mohan, P.K. Kunhikrishnan (2009), Short-term changes in the aerosol characteristics at Kharagpur (22°19'N, 87°19'E) during winter, *J. Atmos. Solar Terr. Phys.*, 71, 1771– 1783.

Nakajima, T., A. Higurachi, K. Kawamoto, and J.E. Penner (2001), A possible correlation between satellite-derived cloud and aerosol microphysical parameters, *Geophys. Res. Lett.*, 28, 1171–1174.

Niranjana, K., V. Sreekanth, B.L. Madhavan, and K.K. Moorthy (2006), Wintertime aerosol characteristics at a north Indian site Kharagpur in the Indo-Gangetic plains located at the outflow region into Bay of Bengal, *J. Geophys. Res.*, 111, D24209, doi: 10.1029/2006JD007635.

Niranjana, K., V. Sreekanth, B.L. Madhavan, T. Anjana Devi, and B. Spandana (2008), Temporal characteristics of aerosol physical properties at Vishakapatnam on the east coast of India during ICARB-signatures of transport onto Bay of Bengal, *J. Earth Sys. Sci.*, 117, S1, 421- 427.

Novakov, T., D.A. Hegg, and P.V. Hobbs (1997), Airborne measurements of carbonaceous aerosols on the East Coast of the United States, *J. Geophys. Res.*, 102, 30023–30030.

O'Dowd, C. D., and M.H. Smith (1993), Physicochemical properties of aerosols over the north-east Atlantic: Evidence for wind-speed related submicron sea-salt aerosol production, *J. Geophys. Res.*, 98(D1), 1137 – 1149.

O'Dowd, C. D., M.H. Smith, J. A. Lowe, B. M. Davison, C. N. Hewitt, and R. M. Harrison (1996), New particle formation in the marine environment, *Proc. 14th International Conference on Nucleation and Atmospheric Aerosols*, Helsinki, Eds. Kulmala and Wanger, pp. 925-929, Pergamon Press.

O'Neill, N.T., T.F. Eck, A. Smirnov, B.N. Holben, and S.Thulasiraman (2003), Spectral discrimination of coarse and fine mode optical depth, *J. Geophys. Res.*, 108(D17), 1198 4559, doi:10.1029/2002JD002975.

Pacyna, J. M. (1986), Atmospheric trace elements from natural and anthropogenic sources, in *Toxic Metals in the Atmosphere*, edited by J. O. Nriagu and C. I. Davidson, pp. 33-52, Wiley, New York.

Parameswaran, K., and G. Vijayakumar (1994), Effect of atmospheric relative humidity on aerosol size distribution, *Ind. J. Rad. Space Phys.*, 23 175 -188.

Parameswaran, K. (1996), Effect of relative humidity on light scattering by poly-disperse aerosols, *Ind. J. Radio Space Phys.*, 25, 64 – 73.

Parameswaran, K., K. Rajeev, and K.S. Gupta (1997), An observational study of night time aerosol concentrations in the lower atmosphere at a tropical coastal station, *J. Atmos. Solar Terr. Phys.*, 59, No. 14, 1727 – 1737.

Parameswaran, K. (1998), Atmospheric aerosols and their radiative effects, *Proc. Indian Nat. Sci. Acad.*, 64 A (3), 245 – 266.

Parameswaran, K., P. R. Nair, and R. Rajan (2001), Aerosol loading in the atmospheric boundary layer at Trivandrum coast and in the adjoining oceanic environment during the FFP and IFP of the INDOEX, *Cur. Sci.*, Vol. 80, 151 – 165.

Parameswaran, K., S.K. Nair, and K. Rajeev (2008), Impact of aerosols from the Asian continent on the adjoining oceanic environments, *J. Earth Sys. Sci.*, 117, No.1, 83 – 102.

Parungo, F., B. Kopcewicz, C. Nagamoto, R. Schnell, P. Sheridan, C. Zhu, and J. Harris (1992), Aerosol particles in the Kuwait oil fire plumes—Their morphology, size distribution, chemical composition, transport, and potential effect on climate, *J. Geophys. Res.*, 97, 15 867– 15 882.

Perry, K.D., T.A. Cahill, R.A. Elred, D.D. Dutcher and T.E. Gill (1997), Long-range transport of North African dust to the eastern United States, *J. Geophys. Res.*, 102, 11 225 – 11 238.

Pincus, R., and M. Baker (1994), Precipitation, solar absorption, and albedo susceptibility in marine boundary layer clouds, *Nature*, 372, 250-252.

Porter, J.N., and A.D. Clarke (1997), Aerosol size distribution models based on in situ measurements, *J. Geophys. Res.*, 102, D5, 6035 – 6045.

Porter, J.N., M. Miller, C. Pietras, and C. Motell (2001), Ship-based Sun Photometer measurements using Microtops Sun photometers, *J. Atmos. Oceanic Tech.*, Vol. 18, 765 – 774.

Prasad, A.K., R.P. Singh, and M. Kafatos (2006), Influence of coal based thermal power plants on aerosol optical thickness in the Indo-Gangetic basin, *Geophys. Res. Lett.*, 33, L05805, doi : 10.1029/2005GL023801.

Prospero, J.M., and R.T. Nees (1977), Dust concentration in the atmosphere of the equatorial North Atlantic: Possible relationship to the Sahelian drought, *Science*, 196, 1196 – 1198.

Prospero, J.M., R.A. Glaccum, and R.T. Nees (1981), Atmospheric transport of soil dust from Africa to South America, *Nature*, 289, 570 – 572.

Prospero, J.M., R.J. Charlson, V. Mohnen, R. Jaenicke, C. Delany, J. Moyere, W. Zoller, and K. Rahn (1983), The atmospheric aerosol system: an overview, *Rev. Geophys. Space Phys.*, 21 (7), 1607 – 1629.

Prospero, J.M., and R.T. Nees (1986), Impact of North African drought and El Nino on mineral dust in the Barbados trade winds, *Nature*, 320, 735 – 738.

Prospero, J. M. (1996), The atmospheric transport of particles to the Ocean, in *Particle Flux in the Ocean*, edited by V. Ittekkot, P. Schäfer, S. Honjo and P.J. Depetris, pp. 19-52, John Wiley & Sons, Chichester.

Prospero, J. M. (2002), The Chemical and Physical Properties of Marine Aerosols: An Introduction; In: *Chemistry of Marine Water and Sediments*, edited by A. Gianguzza, E. Pellizzetti and S. Sammarano, pp 35–82, Springer-Verlag Berlin, Heidelberg.

Prospero, J. M., P. Ginoux, O. Torres, et al. (2002), Environmental characterization of global sources of atmospheric soil dust identified with the Nimbus 7 Total Ozone Mapping Spectrometer (TOMS) absorbing aerosol product, *Rev. Geophys.*, 1, art. no. 1002, 1– 22.

Prospero, J. M. (2003), Global dust transport over the oceans: The link to climate, *Geochimica Et Cosmochimica Acta*, 67 (18), A384.

Prospero, J. M., and P. J. Lamb (2003), African droughts and dust transport to the Caribbean: Climate change implications, *Science*, 302, 1024– 1027.

Pruppacher, H. R., and J. D. Klett (1978), *Microphysics of clouds and precipitation*, D. Reidal Publishing Co., USA.

Quinn, P. K., D. J. Coffman, T. S. Bates, T. L. Miller, J. E. Johnson, E. J. Welton, C. Neusuess, M. Miller, and P. J. Sheridan (2002), Aerosol optical properties during INDOEX 1999: Means, variability, and controlling factors, *J. Geophys. Res.*, 107(D19), 8020, doi:10.1029/2000JD000037.

Quinn, P. K., G. Shaw, E. Andrews, E.G. Dutton, T. Ruoho-Airola, and S.L. Gong (2007), Arctic haze: current trends and knowledge gaps, *Tellus*, 59B, 99–114.

Raj, P.E., S.K. Saha, S.M. Sonbawne, S.M. Deshpande, P.C.S. Devara, Y.J. Rao, K.K. Dani, and G. Pandithurai (2008), Lidar observation of aerosol stratification in the lower troposphere over Pune during pre-monsoon season of 2006, *J. Earth Sys. Sci.*, 117 (S1), pp 293 – 302.

Rajeev, K., V. Ramanathan, and J. Meywerk (2000), Regional aerosol distribution and its long range transport over the Indian Ocean, *J. Geophys. Res.*, 105, D2, 2029 – 2043.

Rajeev, K., S.K. Nair, K. Parameswaran, and C.S. Raju (2004), Satellite observations of the regional aerosol distribution and transport over the Arabian Sea, Bay of Bengal, and Indian Ocean, *Indian J. Mar. Sci.*, 33, 11–29.

Ramachandran, S., and A. Jayaraman (2003), Spectral aerosol optical depths at Bay of Bengal and Chennai: I- measurements, *Atmos. Environ.*, 37, 1941 – 1949.

Ramanathan, V., P.J. Crutzen, J. Lelieveld, A.P. Mitra, et al. (2001), Indian Ocean Experiment: An integrated analysis of the climate forcing and the effects of the great Indo-Asian haze, *J. Geophys. Res.*, 106, 28371 – 28398.

Ramanathan, V., and M.V. Ramana (2005), Persistent, wide spread, and strongly absorbing haze over the Himalayan foothills and the Indo – Gangetic basin, *Pure Appl. Geophys.*, 162, 1609 – 1626, doi: 10.1007/s00024 – 005 – 2685 – 8.

Ramanathan, V., C. Chung, D. Kim, T. Bettge, L. Buja, J. T. Kiehl, W. M. Washington, Q. Fu, D. R. Sikka, and M. Wild (2005), Atmospheric Brown Clouds: Impacts on South Asian Climate and Hydrological Cycle, *Proc. Nat. Acad. Sci* 102(15), 5326-5333.

Ramanathan, V., and Y. Feng (2009), Air pollution, greenhouse gases and climate change: Global and regional perspectives, *Atmos. Environ.*, 43, 37 – 50.

Rao, S. (2005), Arabian Sea Monsoon Experiment: An overview, *Mausam*, 56, 1-6.

Rast, M., J.-L. Bezy, and S. Bruzzi (1999), The ESA Medium resolution Imaging Spectrometer MERIS – a review of the instrument and its mission, *Int. J. Remote Sens.*, 20, 1682 – 1701.

Reddy, M.S., and C. Venkataraman (2002), Inventory of aerosol and sulphur dioxide emissions from India: I. Fossil fuel combustion, *Atmos. Environ.*, 36, 677 – 697.

Reddy, M. S., and O. Boucher (2004), A study of global cycle of carbonaceous aerosols in the LMDZT general circulation model, *J. Geophys. Res.*, 109, D14202, doi:10.1029/2003JD004048.

Redemann, J., P.B. Russel, and P. Hamil (2001), Dependence of aerosol light absorption and single-scattering albedo on ambient relative humidity for sulfate aerosols with black carbon cores, *J. Geophys. Res.*, 106, 27 485 – 27 495.

Remer, L. A., A.E. Wald, et al. (2001), Angular and seasonal variation of spectral surface reflectance ratios: Implications for the remote sensing of aerosol over land, *IEEE Trans. Geosci. Remote Sens.*, 39(2), 275–283.

Remer, L.A., D. Tanre, Y.J. Kaufman, C. Ichoku, S. Mattoo, R. Levy, D.A. Chu, B.N. Holben, A. Dubovik, A. Smirnov, J.V. Martins, R –R., Li, and Z. Ahmad (2002), Validation of MODIS aerosol retrieval over ocean, *Geophys. Res. Lett.*, 29(12), 10.1029/2001GL013204.

Remer, L.A., Y.J. Kaufman, D. Tanre, S. Mattoo, D.A. Chu, J.V. Martins, R-R. Li, C. Ichoku, R.C. Levy, R.G. Kleidman, T.F. Eck, E. Vermote, and B.N. Holben (2005), The MODIS aerosol algorithm, products and validation, *J. Atmos. Sci.*, 62, 947 – 973.

Remer, L.A., D. Tanre, Y.J. Kaufman, R.C. Levy, and S. Mattoo (2006), Algorithm for remote sensing of tropospheric aerosols from MODIS: Collection 005, Algorithm Theoretical Basis Document, NASA Goddard Space Flight Centre, Greenbelt, Md (Available at http://modis-atmos.gsfc.nasa.gov/reference_atbd.php).

Remer, L. A., R.G. Kleidman, R.C. Levy, Y.J. Kaufman, D. Tanre, S. Mattoo, J.V. Martins, C. Ichoku, I. Koren, H. Yu, and B.N. Holben (2008), Global aerosol climatology from the MODIS satellite sensors, *J. Geophys. Res.*, 113, D14S07, doi:10.1029/2007JD009661.

Robock, A. (2000), Volcanic eruptions and climate, *Rev. Geophys.*, 38, 191–219.

Rood, M. J., D.S. Covert, and T.V. Larson (1987), Hygroscopic properties of atmospheric aerosol in Riverside, California, *Tellus*, 39b, 383–397.

Rosenfeld, D. (1999), TRMM observed first direct evidence of smoke from forest fires inhibiting rainfall, *Geophys. Res. Lett.*, 26, 3105– 3108.

Rosenfeld, D. (2000), Suppression of rain and snow by urban and industrial pollution, *Science*, 287, 1793-1796.

Santer, B.D., K.E. Taylor, T. M. L. Wigley, T.C. Johns, et al. (1996), A search for human influence on the thermal structure of the atmosphere, *Nature*, 382, 39 – 46.

Satheesh, S. K., K.K. Moorthy, and I. Das (2001), Aerosol spectral optical depths over Bay of Bengal, Indian Ocean and Arabian Sea, *Curr. Sci.*, 81 1617 – 1625.

Satheesh, S.K. (2002), Aerosol radiative forcing over land: effect of surface and cloud reflection, *Ann. Geophys.*, 20, 2105–2109.

Satheesh, S.K., and J. Srinivasan (2002), Enhanced aerosol loading over Arabian Sea during the pre-monsoon season: Natural or anthropogenic?, *Geophys. Res. Lett.*, 29, 1874, doi:10.1029/2002GL015687.

Satheesh, S. K., J. Srinivasan, and K. K. Moorthy (2006a), Spatial and temporal heterogeneity in aerosol properties and radiative forcing over Bay of Bengal: Sources and role of aerosol transport, *J. Geophys. Res.*, 111, D08202, doi:10.1029/2005JD006374.

Satheesh, S. K., J. Srinivasan, and K.K. Moorthy (2006b), Contribution of sea-salt to aerosol optical depth over the Arabian Sea derived from MODIS observations, *Geophys. Res. Lett.*, 33, L03809 doi: 10.1029/2005GL024856.

Satheesh, S. K., K. K. Moorthy, S. S. Babu, V. Vinoj, and C. B. S. Dutt (2008), Climate implications of large warming by elevated aerosol over India, *Geophys. Res. Lett.*, 35, L19809, doi:10.1029/2008GL034944.

Shaw, G. E., J. A. Reagan, and B. M. Herman (1973), Investigation of atmospheric extinction using direct solar radiation measurements made with a multiple wavelength radiometer, *J. Appl. Meteorol*, 12, 374–380.

Sikka, D.R. (1997), Desert climate and its dynamics, *Curr. Sci.*, 72 (1), 35 – 46.

Singh, R.P., S. Dey, S.N. Tripathi, V. Tare, and B. Holben (2004), Variability of aerosol parameters over Kanpur, northern India, *J. Geophys. Res.*, 109, D23206, doi: 10.1029/2004JD004966.

Slinn, S. A., and W. G. N. Slinn (1980), Predictions for particle deposition on natural-waters, *Atmos. Environ.*, 14(9), 1013 – 1016, doi:10.1016/0004-6981(80)90032-3.

Smirnov, A., B.N. Holben, T.F. Eck, O. Dubovik, and I. Slutsker (2003), Effect of wind speed on columnar aerosol properties at Midway island, *J. Geophys. Res.*, 108, D24, 4802, doi: 10.1029/2003JD003879.

Smith, K R (2000), National burden of disease in India from indoor air pollution, *Proc. Nat. Acad. Sci.*, 97, 13286-13293.

- Sokolik, I. N., and O.B. Toon (1996), Direct radiative forcing by anthropogenic airborne mineral aerosol, *Nature*, 381, 681–683.
- Soufflet, V., D. Tanre, A. Royer, and N.T. O'Neill (1997), Remote sensing of aerosols over boreal forest and lake water from AVHRR data, *Remote Sens. Environ.*, 60, 22–34.
- Spiegel, M.R., and L.J. Stephens (2000), *Theory and problems of statistics*, 3rd Edition, pp 345 – 349, Tata McGraw-Hill publishing limited, New Delhi.
- Spinhirne, J. D., S. P. Palm, W. D. Hart, D. L. Hlavka, and E. J. Welton (2005), Cloud and aerosol measurements from GLAS: Overview and initial results, *Geophys. Res. Lett.*, 32, L22S03, doi:10.1029/2005GL023507.
- Stowe, L., A. Ignatov, and R. Singh (1997), Development, validation, and potential enhancements to the second generation operational aerosol product at NOAA/NESDIS, *J. Geophys. Res.*, 102, 16 923–16 934.
- Streets, D. G., K. F. Yarber, J.-H.Woo, and G. R. Carmichael (2003), Biomass burning in Asia: Annual and seasonal estimates and atmospheric emissions, *Global Biogeochem. Cyc.*, 17(4), 1099, doi:10.1029/2003GB002040.
- Streets, D. G., T. C. Bond, T. Lee, and C. Jang (2004), On the future of carbonaceous aerosol emissions, *J. Geophys. Res.*, 109, D24212, doi:10.1029/2004JD00490.
- Tang, I.N., and H.R. Munkelwitz (1977), Aerosol growth studies, III, Ammonium bisulphate aerosols in a moist atmosphere, *J. Aerosol. Sci.*, 8, 321 – 330.
- Tang, I.N., H.R. Munkelwitz, and J.G. Davis (1977), Aerosol growth studies—II. Preparation and growth measurements of monodisperse salt aerosols, *J. Aerosol Sci.*, 8, 149–159.
- Tang, I.N. (1980), Deliquescence properties and particle size change of hygroscopic aerosols, in *Generation of aerosols*, edited by K. Willeke, Chapter 7, Butterworth, Stoneham, Mass.
- Tanre, D., Y.J. Kaufman, M. Herman, and S. Mattoo (1997), Remote sensing of aerosol properties over oceans using the MODIS/EOS spectral radiances, *J. Geophys. Res.*, 102, 16 971 – 16 988.
- Tare, V., S.N. Tripathi, N. Chinnam, A.K. Srivastava, S. Dey, V.P. Kanawade, A. Agarwal, S. Kishore, R.B. Lal, and M. Sharma (2006), Measurements of atmospheric parameters during Indian Space Research Organization Geosphere Biosphere Program Land Campaign II at a typical location in the Ganga Basin: 2. Chemical properties, *J. Geophys. Res.*, 111, D23210, doi:10.1029/2006JD007279.
- Tegen, I., and I. Fung (1995), Contribution to the mineral aerosol load from land surface modification, *J. Geophys. Res.*, 100, 18 707 – 18 716.

Tegen, I., P. Hollrig, M. Chin, I. Fung, D. Jacob, and J. Penner (1997), Contribution of different aerosol species to the global aerosol extinction optical thickness: Estimates from model results, *J. Geophys. Res.*, 102(D20), 23895-23915.

Tegen, I., and R.A. Miller (1998), General circulation model study on the inter-annual variability of soil dust aerosol, *J. Geophys. Res.*, 103 (D20), 25 975–25 995.

Teillet, P. (1990), Rayleigh optical depth comparisons from various sources, *Appl. Opt.*, 29, 1897– 1900.

Tomasi, C., V. Vitale, A. Lupi, C. Di Carmine, M. Campanelli, A. Herber, R. Treffeisen, et al. (2007), Aerosols in polar regions: A historical overview based on optical depth and in situ observations, *J. Geophys. Res.*, 112, D16205, doi:10.1029/2007JD008432.

Torres, O., P.K. Bhartia, J.R. Herman, Z. Ahmad, and J. Gleason (1998), Derivation of aerosol properties from satellite measurements of backscattered ultraviolet radiation: Theoretical basis, *J. Geophys. Res.*, 103, 17 099–17 110.

Torres, O., P.K. Bhartia, J.R. Herman, A. Sinyuk, P. Ginoux, and B. Holben (2002), A long term record of aerosol optical depth from TOMS observations and comparison to AERONET measurements, *J. Atmos. Sci.*, 59, 398–413.

Torres, O., P. K. Bhartia, A. Sinyuk, E. Welton, and B. Holben (2005), Total Ozone Mapping Spectrometer measurements of aerosol absorption from space: Comparison to SAFARI 2000 ground based observations, *J. Geophys. Res.*, 110, D10S18, doi:10.1029/2004JD004611.

Tripathi, S.N., S. Dey, A. Chandel, S. Srivastava, R.P. Singh, and B.N. Holben (2005), Comparison of MODIS and AERONET derived aerosol optical depth over the Ganga Basin, India, *Ann. Geophys.*, 23, 1093 – 1101.

Tripathi, S. N., V. Tare, N. Chinnam, A.K. Srivastava, S. Dey, et al. (2006), Measurements of atmospheric parameters during Indian Space Research Organization Geosphere Biosphere Programme Land Campaign II at a typical location in the Ganga basin: 1. Physical and optical properties, *J. Geophys. Res.*, 111, D23209, doi:10.1029/2006JD007278.

Tsunogai, S., O. Saito, R. Yamada, and S. Nayaka (1972), Chemical composition of oceanic aerosols, *J. Geophys. Res.*, 77, 5283 – 5291.

Tucker, C. J., H. E. Oregne, and W. W. Newcomb (1991), Expansion and contraction of the Sahara desert from 1980 to 1990, *Science*, 253, 299–301.

Twomey, S. (1974), Pollution and planetary albedos, *Atmos. Environ.*, 8, 1251 – 1256.

Twomey, S. (1977), The influence of pollution on the shortwave albedo of clouds, *J. Atmos. Sci.*, 34, 1149 – 1152.

- Vaveka, M., K. Hameri, T. Puhakka, et al. (2000), Effects of meteorological processes on aerosol particle size distribution in an urban background area, *J. Geophys. Res.*, 105, 9807–9821.
- Veihelmann, B., P. F. Levelt, P. Stammes, and J. P. Veefkind (2007), Simulation study of the aerosol information content in OMI spectral reflectance measurements, *Atmos. Chem. Phys.*, 7, 3115–3127.
- Vigroux, E. (1953), Contribution a` l'e`tude expe`rimentale de l'absorption de l'ozone, *Ann. Phys.*, 8, 709–762.
- Vinoj, V., and S.K. Satheesh (2003), Measurement of aerosol optical depth over Arabian Sea during summer monsoon season, *Geophys. Res. Lett.*, Vol. 30, No. 5, 1263, doi: 10.1029/2002GL016664.
- Vinoj, V., S. K. Satheesh, S. S. Babu, and K. K. Moorthy (2004a), Large aerosol optical depths observed at an urban location in southern India associated with rain-deficit summer monsoon season, *Ann. Geophys.*, 22, 3073–3077.
- Vinoj, V., S. S. Babu, S. K. Satheesh, K.K. Moorthy, and Y. J. Kaufman (2004b), Radiative forcing by aerosols over the Bay of Bengal region derived from shipborne, island-based, and satellite (Moderate-Resolution Imaging Spectroradiometer) observations, *J. Geophys. Res.*, 109, D05203, doi:10.1029/2003JD004329.
- Wang, C.S. and R.L. Street (1978), Measurements of spray at an air-water interface, *Dyn. Atmos. Oceans*, 2, 141 – 152.
- Welton, E.J., K.J. Voss, P.K. Quinn, P.J. Flatau, K. Markowicz, J.R. Campbell, J.D. Spinhirne, H.R. Gordon, and J.E. Johnson (2002), Measurements of aerosol vertical profiles and optical properties during INDOEX 1999 using micropulse lidars, *J. Geophys. Res.*, 107, D19, 8019, doi: 10.1029/2000JD000038.
- Wen, G., A. Marshak, and R. F. Cahalan (2006), Impact of 3D clouds on clear sky reflectance and aerosol retrieval in a biomass burning region of Brazil, *Geosci. Remote Sens. Lett.*, 3, 169 – 172, doi:10.1109/LGRS.2005.861386.
- Wen, G., A. Marshak, R. F. Cahalan, L. A. Remer, and R. G. Kleidman (2007), 3D aerosol-cloud radiative interaction observed in collocated MODIS and ASTER images of cumulus cloud fields, *J. Geophys. Res.*, 112, D13204, doi:10.1029/2006JD008267.
- Wentz, F. J. and D. K. Smith (1999), A model function for the ocean-normalized radar cross section at 14 GHz derived from NSCAT observations, *J. Geophys. Res.*, 104, 11499–11514.
- Westphal, D., and O. Toon (1991), Simulations of microphysical, radiative and dynamical processes in a continental-scale forest fire smoke plume, *J. Geophys. Res.*, 96 (D12), 22 379 – 22 400.

- Whelpdale, D.M. (1982), Dry and wet deposition, In *Chemistry of the unpolluted and polluted troposphere*, edited by H.W. Georgii and W. Jaeschke, D. Reidel, 375 – 391.
- Whitby, K. T. (1978), The physical characteristics of sulphur aerosols, *Atmos. Environ.*, 12, 135-159.
- Wilson, T. R. S. (1975), Salinity and major elements of seawater, in *Chemical Oceanography*, 2nd ed., edited by J.-P. Riley and G. Skirrow, pp. 365-413, Academic Press, Orlando, FL.
- Winker, D.M., J.R. Pelon, and M.P. McCormick (2003), The CALIPSO mission: space borne lidar for observation of aerosols and clouds, *Proc. SPIE*, 4893, 1- 11.
- Winker, D. M., W. H. Hunt, and M. J. McGill (2007), Initial performance assessment of CALIOP, *Geophys. Res. Lett.*, 34, L19803, doi:10.1029/2007GL030135.
- Winter, B., and P. Chylek (1997), Contribution of sea salt aerosol to the planetary clear sky albedo, *Tellus*, 49B(1), 72-79.
- Wiscombe, W.J. (1980), Improved Mie scattering algorithms, *Appl. Opt.*, 19, 1505 – 1509.
- Woodcock, A. H. (1953), Salt nuclei in marine air as a function of altitude and wind force, *J. Meteorol.*, 10, 362-371.
- Woolf, D.K., E.C. Monahan, and D.E. Spiel (1988), Quantification of the marine aerosol produced by white caps, Preprint, Seventh Conf. on Ocean-Atmosphere Interaction, *Amer. Meteor. Soc.*, 182 – 185.
- Yu, H., Y.J. Kaufman, M. Chin, G. Feingold, L.A. Remer, T.L. Anderson, Y. Balkanski, N. Bellouin, O. Boucher, S. Christopher, P. DeCola, R. Kahn, D. Koch, N. Loeb, M.S. Reddy, M. Schulz, T. Takemura, and M. Zhou (2006), A review of measurement-based assessment of aerosol direct radiative effect and forcing, *Atmos. Chem. Phys.*, 6, 613 - 666.
- Yue, G.K., M.P. McCormick, and W.P. Chu (1986), Retrieval of composition and size distribution of stratospheric aerosols with the SAGE II satellite experiment, *J. Atmos. Oceanic Technol.*, 3, 371 – 380.
- Zhang, J., J. S. Reid, and B. N. Holben (2005), An analysis of potential cloud artifacts in MODIS over ocean aerosol thickness products, *Geophys. Res. Lett.*, 32, L15803, doi:10.1029/2005GL023254.
- Zion, P. M. (1983), Description of algorithms for processing coastal zone color scanner (CZCS) data, NASA/JPL, Pasadena, CA, *JPL Pub. 83-98*, pp. 1– 29.

List of Publications

Aloysius, M., M. Mohan, K. Parameswaran, S.K. George, and P.R. Nair (2008), Aerosol transport over the Gangetic basin during ISRO-GBP Land Campaign-II, *Ann. Geophys.*, 26, 431- 440.

Aloysius, M., M. Mohan, S.S. Babu, V.S. Nair, K. Parameswaran, and K.K. Moorthy (2008), Influence of circulation parameters on the AOD variations over the Bay of Bengal during ICARB, *J. Earth Syst. Sci.*, 117, 51, 353 – 360.

Aloysius, M., M. Mohan, S.S. Babu, K. Parameswaran, and K.K. Moorthy (2009), Validation of MODIS derived aerosol optical depth and an investigation on aerosol transport over the South East Arabian Sea during ARMEX-II, *Ann Geophys.*, 27, 2285 – 2276.

Alappattu, D.P., P.K. Kunhikrishnan, M. Aloysius, and M. Mohan (2009), A case study of atmospheric boundary layer features during winter over a tropical inland station - Kharagpur (22.32°N, 87.32°E), *J. Earth Syst. Sci.*, 118, No. 4, 281 – 293.

Nair, P.R., S.K. George, K. Parameswaran, M. Aloysius, D.P. Alappattu, M Mohan, and P.K. Kunhikrishnan (2009), Short term changes in the aerosol characteristics at Kharagpur (22° 19'N, 87° 19' E) during winter, *J. Atmos. Solar Terr. Phys.*, 71, 1771 – 1783.

Aloysius M., M. Mohan, and K. Parameswaran (2006), Aerosol optical depth modulations by lower tropospheric meteorological fields, *Proc. SPIE*, 6408 doi:10.1117/12.694082.

Aloysius M., M. Mohan, K. Parameswaran and K.K. Moorthy (2007) Generation, transport and distribution features of aerosols over Bay of Bengal during ICARB, *Emerging trends in Aerosols, technology and Applications IASTA Bulletin, ISSN 0971 – 4510*, 18, Nos. 1 &2, 318 – 320.

Symposium Presentations

Aloysius, M., M. Mohan, and K. Parameswaran, Study of Aerosol Transport over the Indian region using MODIS and NCEP Data, National Space Science Symposium (NSSS), Andhra University, Vishakapatnam, February 9 – 12, 2006.

Aloysius, M., M. Mohan, and K. Parameswaran, Aerosol transport over Gangetic basin during ISRO-GBP land campaign- II, ICARB/IGBP Annual Review, SPL, VSSC, Trivandrum, October 25-27, 2006.

Aloysius, M., M. Mohan, and K. Parameswaran, Aerosol optical depth modulation by lower tropospheric meteorological fields, SPIE Asia Pacific Remote Sensing Symposium, National Institute of Oceanography, Goa, November 13 – 17, 2006.

Aloysius M., M. Mohan, K. Parameswaran and K.K. Moorthy, Generation, transport and distribution features of aerosols over Bay of Bengal during ICARB, Indian Aerosol Science and Technology Association (IASTA), On emerging trends in Aerosols: technology and Applications, NPL, New Delhi, November 14 – 16, 2007. (Received Best Paper Award)

Aloysius, M., M. Mohan, S.S. Babu, and K. Parameswaran, Comparison of MODIS with ship-borne aerosol measurements and investigation of aerosol transport over the Arabian Sea during ARMEX-II, International symposium on Aerosol-chemistry-climate interactions (ACCLINT), PRL, Ahmedabad, November 20 – 22, 2007.

Aloysius, M., M. Mohan, M. V.S. Nair, P.A. Denny, K. K. Moorthy, P.K. Kunhikrishnan, and K. Parameswaran, Role of atmospheric circulation parameters in the transport features of aerosols over Arabian Sea during ICARB, National Space Science Symposium (NSSS), Radio Astronomy Centre, Ooty, February 26 – 29, 2008.

Mohan, M., M. Aloysius, and K. Parameswaran, Aerosol generation sources over the Ganga basin during ISRO-GBP land campaign- II, National Space Science Symposium (NSSS), Radio Astronomy Centre, Ooty, February 26 – 29, 2008.

Awards/Honours

Best paper award for poster presentation at IASTA 2007 Conference on Emerging trends in Aerosols: Technology and Applications, held at New Delhi from November 14-16, 2007 for the paper titled “Generation, transport and distribution features of aerosols over Bay of Bengal during ICARB” authored by Aloysius M., M. Mohan, K. Parameswaran and K.K. Moorthy.

